A study of stellar populations in the last 5 billion years using Integral Field Spectroscopy

Sam Vaughan

Balliol College

University of Oxford

A thesis submitted for the degree of

Doctor of Philosophy

Hilary 2019

For Dad

Up, up the long, delirious burning blue
I've topped the wind-swept heights with easy grace
Where never lark, or ever eagle flew -
And, while with silent, lifting mind I've trod
The high untrespassed sanctity of space,
Put out my hand, and touched the face of God.

John Gillespie Magee
1922-1941

Abstract

In this thesis, I study the properties of quiescent and star-forming galaxies with integral field spectroscopy. The study of quiescent galaxies focuses on inferring the low-mass end of the stellar initial mass function (IMF). To accomplish this, we make spatially resolved measurements of a number of "gravity-sensitive" absorption features in the spectra of three nearby early-type galaxies. These vary in strength between otherwise identical (low-mass) dwarf and giant stars, allowing for measurement of the dwarf-to-giant ratio and hence the low-mass IMF.

In NGC 1277 and IC 843, I use the Oxford SWIFT instrument to study the variation of these features as a function of radius. I find strong gradients in NaI0.82 absorption but flat FeH0.99 profiles in both cases, although the data cannot distinguish between chemical abundance gradients or a gradient in the IMF being the cause. I then fit models to the integrated spectrum of each galaxy, finding an IMF slope of $x = 2.27 \pm 0.17$ IC 843 and $x = 2.69 \pm 0.11$ in NGC 1277. Next, I use MUSE to make quantitative inferences about an IMF gradient in NGC 1399. I use full spectral fitting in 18 annular bins to measure a super-Salpeter IMF slope in the galaxy's centre, which is radially constant out to ~ 0.7 effective radii before becoming consistent with a Milky-Way IMF at R_e. These findings add weight to the theory of a two-stage formation process for massive elliptical galaxies.

I then introduce K-CLASH, which uses KMOS to observe star-forming galaxies in four galaxy clusters from the CLASH survey. I describe the observations, data reduction and analysis process, and present a novel probabilistic method of determining whether a target resides in a cluster or field environment. I compare and contrast the properties of field and cluster galaxies, finding that the cluster sample follow a star-formation rate "Main Sequence" relation which is offset to smaller SFR by 0.18 dex. Furthermore, I measure the size of galaxies in optical light and Hα emission and find the average ratio $r_{50_{H\alpha}}/r_{50_{R_c}}$ to be significantly smaller in cluster galaxies than in the field comparison sample. I find no significant differences in ISM conditions. These observations are evidence for environmental reduction of star-formation, although deeper observations are required to discriminate between a global effect (due to ISM heating) or outside-in processes (such as ram-pressure stripping).

Statement of Originality

The work presented in this thesis was undertaken at the Department of Astrophysics at the University of Oxford between October 2015 and March 2019 under the supervision of Professor Roger Davies. It was funded by a Science and Technologies Research Council studentship. I hereby declare that no part of this thesis has been submitted in support of another degree, diploma, certificate or other qualification at the University of Oxford or elsewhere. Except where otherwise stated, or where reference is made to the work of others, the work in this thesis is entirely my own.

The work presented in Chapters 2 and 3 are based on the peer-reviewed, published papers Vaughan et al. 2018a (Monthly Notices of the Royal Astronomical Society, Volume 475, p.1073-1092) and Vaughan et al. 2018b (Monthly Notices of the Royal Astronomical Society, Volume 479, p.2443-2456), of which I am the first author.

In Chapter 2, the code used to make an index measurement from a spectrum was written by Dr. Simon Zieleniewski (University of Oxford). The code to convolve a spectrum to a given velocity dispersion was written by Dr. Ryan Houghton (University of Oxford). The application of these tools, however, is my entirely own. The SWIFT observations were conducted by myself and Dr. Simon Zieleniewski (one night remotely and four at Mount Palomar) and Dr. Ryan Houghton (one night remotely).

In Chapter 3, the MUSE data were reduced by Dr. Simon Zieleniewski.

In Chapter 4, the fits to the K-CLASH photometric data using `MagPhys` and the calculation of the Hα Signal-to-Noise ratios were performed by Dr. Alfie Tiley (Durham University). Dr. Tiley also made Figure 4.2, which is reproduced with permission. KMOS observations were carried out by myself, Dr. Laura Prichard (Space Telescope Science Institute), Mr. Behzad Ansarinejad (Durham University) and Dr. Alfie Tiley.

Sam Vaughan

March 2019

Acknowledgements

First and foremost, I'd like to thank my supervisor, Professor Roger Davies, for all his help, encouragement and guidance throughout the last few years. I'm so grateful for the friendly, relaxed atmosphere of our meetings, and for the insights which have put everything I've been doing into context. It's been a privilege to have been your graduate student.

I'd also like to thank Dr. Ryan Houghton and Dr. Simon Zieleniewski for answering all my annoying questions, teaching me how astronomers actually do science and for being constant allies in the fight against telluric emission lines. The second half of this thesis wouldn't have been completed without Dr. Alfie Tiley. Alfie, thanks for all of your hard work to make K-CLASH a reality, and for being a good friend and mentor. I'd also like to thank everyone at Galaxy Evoluncheon (née Black Hole Lunch) for your insights and discussions throughout the years.

I wouldn't have made it to this stage without having some pretty amazing people in my life. Firstly, I'd like to thank everyone around the department for making the place so welcoming. Joe, I'm going to miss your sunny disposition. Thanks for making the office more fun- and for telling me to listen to The National. Rebecca and Chris, thanks for taking the plunge with me at Blenheim, and for waiting for me whenever I slowed you down on the bike. Ashling- if you didn't exist then they'd have to invent you. Thank you for all of your help throughout my time in Oxford, for making sure things ran so smoothly and for always being around for a chat. There are too many other people to name individually, but special mention must go to Marius, Ollie, Nicole, Becky, Kit, David, James M. and Laura.

Fliss and James, I'm so grateful to you two for for always making me laugh, and for being an oasis away from Oxford. And James, thanks for always making time to see the football- we've had some pretty great times at the Bridge. Thanks also to Tom, Leanne, Ashley and everyone else else back home. Ben, thanks for sharing the start of this research journey with me before jetting off to far-flung lands (I don't blame you). We've both come a long way from staircase 7NB. Matt, Aneesh, Stina, Ellie, Charlotte, Jacob and Adam, thanks for all of the Oxford memories, and for getting me out out of this place every once in a while. Special thanks also to Debby,

Phil, Rob, Claire, Fanny, Rahul and Leea for being such good friends. I definitely picked the right college.

I'm very grateful to my housemates Paul, Sergio, Catherine and Naomi for the years of domestic bliss. Paul and Sergio, you guys are fantastic- I have to grudgingly admit you have the better bromance. Catherine, thank you for putting up with me for so many hours each day, and for all the hours of procrastination when we couldn't face any more science. There's no one I'd have rather shared an office with. And Naomi, thank you for eating eggs at 5am, laughing at the way I say "square" and being there to shout Thunder Road all the way home. I wouldn't have had anywhere near as much fun without you. Oh, and thank you for your quick reflexes with that cup at the Christmas Party. You all have to promise to come visit me down under!

Lastly, I'd be nowhere without my family. Angus, thank you for being my brother. I couldn't be prouder of everything you've accomplished and the hard working, generous, hilarious person you've become. Mum, there really aren't enough words to describe how grateful I am for everything you've done for me. You've made me the person I am today. Thank you for being my best friend. Lordy, thank you for always being pleased to see me, and for reminding me that, sometimes, nothing else matters apart from the next throw of your ball. And finally, Dad, to whom this thesis is dedicated. Thank you for showing me how to always keep my cool, teaching me to be curious and finding humour in the bleakest of situations. And for standing out in the cold at my football matches all those years ago. I hope you'd be proud.

Sam

March 2019

Contents

List of Figures

List of Tables

1 | Introduction

In the beginning, the Universe was created. This has made a lot of people very angry, and been widely regarded as a bad move.

Douglas Adams

In this thesis, we study the properties of quiescent galaxies in the local Universe and star-forming galaxies at intermediate redshifts ($0.3 < z < 0.6$). The observational technique which links these studies is integral-field spectroscopy, the practice of capturing a spectrum of an object at multiple spatial positions simultaneously. Here, we give a short history of optical astronomy, summarise the current understanding of the processes which shape galaxies and provide some background for subsequent chapters.

1.1 A short history of optical astronomy

The interdisciplinary study of *archeoastronomy* has begun to shed light on just how important keeping track of the heavens was for early human societies. Recent work has found that mesolithic hunter-gatherers in Scotland built large-scale calendars into

the ground around 8,000 BCE to measure the phases of the moon, perhaps to track the migratory patterns of their prey (Gaffney et al., 2013). Going even further back, the ancestors of Aboriginal Australians who first landed in northern Australia before 40,000 BCE have been described as "the first astronomers" (Haynes, 1996). Whilst no written or physical record of Aboriginal astronomy exists before the invasion of Australia by the British in 1788 (e.g. see the review by Norris 2016), knowledge of the night sky was integral to the culture and education of a large number of Aboriginal communities. Some Aboriginal people knew every star in the night sky brighter than fourth magnitude (Mountford, 1976), observations of stellar colours and variability form part of Aboriginal oral traditions (e.g. Norris, 2016; Hamacher, 2018) and there is oral evidence of Aboriginal people also measuring the passage of time by studying the phases of the moon (e.g. Cairns & Harney, 2004).

The next steps forward in the field of astronomy came as a result of technological advancements in other areas. Following centuries of astronomical observations with the naked eye in ancient Greece, China and the Middle East, the first telescope was invented in 1608 by Hans Lippershey. The telescope's first use in an astronomical context came soon after when Galileo Galilei (using his own improved design) published observations of the moon in *The Starry Messenger* (*Sidereus Nuncius*). He would go on to discover the Galilean moons of Jupiter, observe sunspots and publish observations of Venus, Saturn and Neptune (Sharratt, 1996).

To achieve better magnification, however, refracting telescopes required larger and larger lenses, which were costly to make and difficult to perfect. The first *reflecting* telescope was built by Isaac Newton in 1666, although designs by James Gregory and Marin Mersenne exist from decades earlier (Watson, 2004). Mirrors were much easier to manufacture to the necessary sizes, and the ability to add silver to the surfaces of metal plates, rather than polishing the surface of the metal itself, led to the design of the first modern telescopes in the late 1800s at the Lick and Mount

Wilson observatories in California.

Until the late 1800s, astronomy entirely consisted of studying the *appearances* of objects and their positions on the sky. This was soon to change when work by Gustav Kirchhoff and Robert Bunsen began the systematic application of spectroscopy to identify the composition of materials (Kirchhoff & Bunsen, 1860). The first published examples of spectral observations of astronomical objects (other than the Sun) is Huggins & Miller (1864), who study a number of planetary nebulae (see Becker 2001 for a historical review). Soon, studying the spectra of astrophysical sources was commonplace, and would prove crucial to the most famous work of the early 20th century. At Mount Wilson, Edwin Hubble observed the doppler shifts of spectral lines in a number of nearby galaxies (as well as collating observations by Vesto Slipher and Milton Humason) and constructed the relation between recession velocity and distance– with slope known as the "Hubble constant"– to provide the first evidence of the expansion of the Universe (Hubble, 1929).

In the forthcoming decades, telescopes became bigger and spectrographs more accurate. The next great development in optical astronomy, however, did not arrive until the 24$^{\text{th}}$ of April 1990, with the launch of the *Hubble Space Telescope* (*HST*)[1]. The images received from *HST* heralded the start of an era when optical astronomy could be regularly conducted without the blurring effect of the Earth's atmosphere. Amongst its many science achievements, some standout results include observations to reduce the uncertainty in the Hubble constant to less than 3% (Freedman et al., 2001; Riess et al., 2011); the contribution of measurements of high-redshift supernovae to infer the accelerated expansion of the Universe (Riess et al., 1998; Perlmutter et al., 1999); and the discovery of supermassive black holes at the centres of nearly all massive galaxies (e.g. incontrovertible evidence of individual black holes by Harms et al. 1994 and Ferrarese et al. 1996 among others; see the review by Kormendy & Ho

[1]Or, perhaps more accurately, on January 13$^{\text{th}}$ 1994 when the Corrective Optics Space Telescope Axial Replacement (COSTAR) system was installed to correct the faulty primary mirror.

2013). *HST* also paved the way for other space based observatories (e.g. GALEX, *Planck*, *Spitzer*, *Gaia*), showing that observations from low-earth orbit (and beyond) were not only possible but could become routine.

Two further advances in instrumentation bear mentioning. The first is the introduction of adaptive optics to ground-based observatories. Adaptive optic systems and *HST* were developed with the same goal in mind– to remove the effects of astronomical seeing from observations, giving (in some cases) diffraction limited results. First proposed by Babcock (1953), but not able to be put into practice for astronomical purposes until the 1990s, adaptive optics systems work by measuring the effects of atmospheric turbulence on a bright point source, then correcting for these aberrations in real time by deforming the telescope's primary mirror. The current generation of adaptive optics on 8m class telescopes can now also utilise laser guide stars (which excite sodium atoms in the upper atmosphere) to create the necessary point source, rather than having to rely on using a bright star a few arcseconds from their target.

The second development in astronomical instrumentation– on which each chapter in this thesis depends– is the invention and development of integral field spectroscopy (and integral field units; IFUs). For many years, spectroscopy was conducted using a long slit (or even a single aperture) to obtain a spectrum with limited spatial information. IFUs allow the observer to capture spectra at multiple spatial positions at the same time, which results in a three dimensional "data cube". This data cube has two spatial dimensions and one spectral dimension, in comparison with the one spatial dimension and one spectral dimension of a long-slit spectrum, or the sole spectral dimension of a fibre observation. Integral field data is in a sense a cross between imaging and spectroscopy– the result can be thought of as an image with a spectrum at every pixel. A schematic illustrating the differences between a long-slit spectrograph and an IFU is shown in Figure 1.1.

There are three main classes of IFUs. Firstly, lenslet IFUs collect the light from

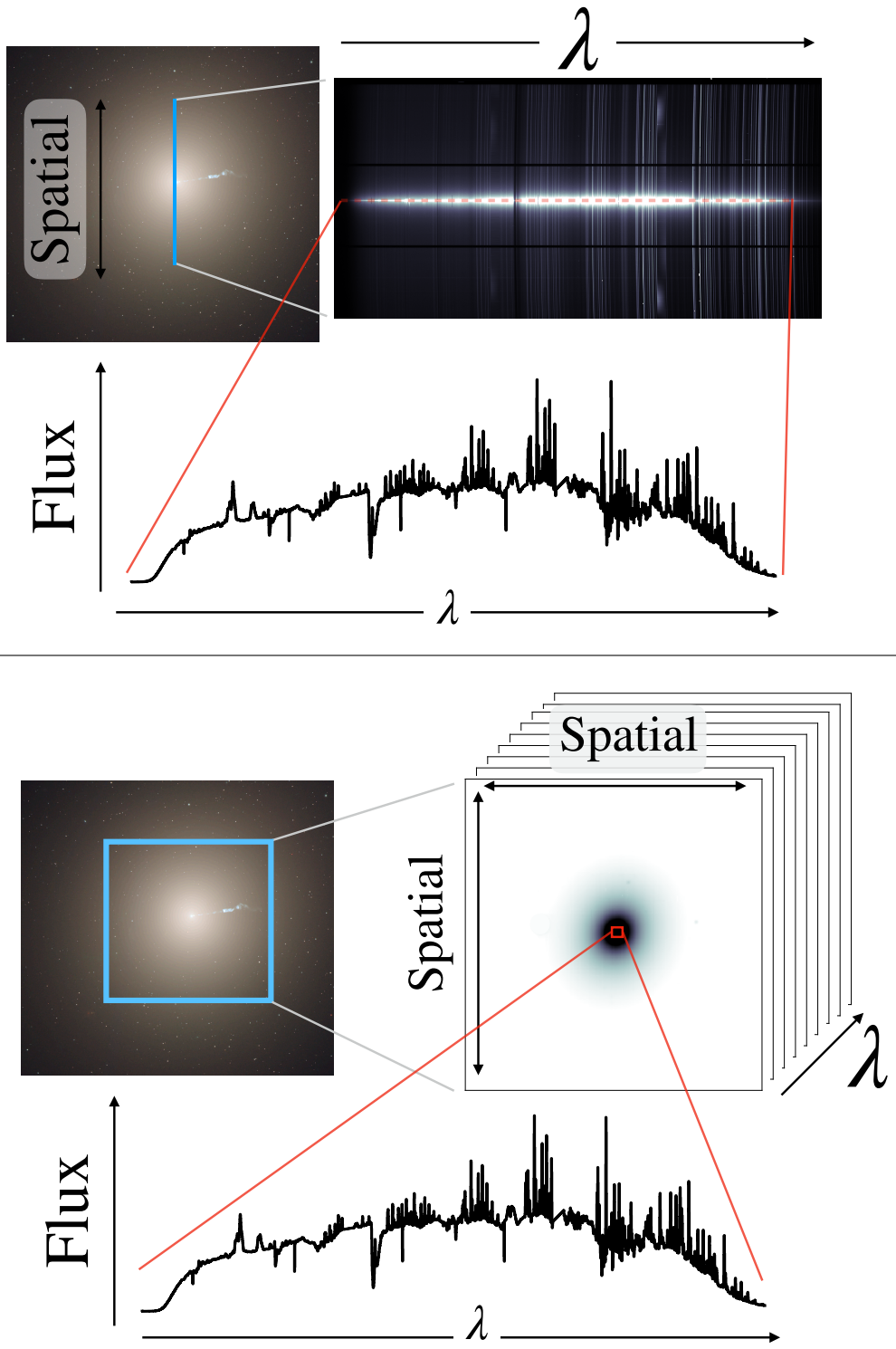

Figure 1.1: The differences between long-slit spectroscopy (top) and integral field spectroscopy (bottom). The target is shown on the left. The instrument footprint (a slit or integral field unit) is shown in blue. The right hand side shows the reduced data. In the case of a slit, this is an array with one spatial dimension and one spectral dimension. In the case of an IFU, this is an array with *two* spatial dimensions and one spectral dimension. An example spectrum (which has not been sky subtracted, telluric corrected or throughput calibrated) is shown beneath. Image credit: M87; NASA, ESA, and the Hubble Heritage Team (STScI/AURA)

an astronomical object onto an array of micro-lenses. The output from each lens is then directed onto a dispersive element (usually a grating). Whilst these designs are simple (with very high throughput), the wavelength range of the data has to be small to avoid different spectra overlapping on the detector. Examples of lenslet IFUs include OSIRIS on Keck (Larkin et al., 2006) and the (now retired) SAURON instrument on the William Herschel Telescope (Bacon et al., 2001).

Secondly, fibre IFUs sample an astronomical image using a closely-packed bundle of fibre-optic cables. The light from these fibres is then dispersed by a slit in the same way as a normal multi-object spectrograph. Fibre IFUs have the advantage of flexibility in choosing the output location of the light, compared to the fixed optical paths of other classes of IFUs. The downsides are the degradation over time of the optical fibres (which can lead to poor throughput) and the limited filling factor of the fibre bundles on the sky. Examples of fibre IFUs are the large surveys MANGA (Bundy et al., 2015) and SAMI (Croom et al., 2012).

The third class of IFUs are known as "image slicers". In this design the astronomical image hits an array of mirrors, each arranged at a slightly different angle, to segment the image into strips. The optical path is arranged such that each slice is directed onto a grating, dispersing the light in a similar manner to a long-slit spectrograph. The process is like observing with a single slit at many different parallel positions across a galaxy, but with the advantage that only one exposure is necessary to collect light from the entire object. The idea of using an image slicer to rearrange an astronomical image to pass through a slit is very old (e.g. Bowen, 1938), but it wasn't until the mid 1990s that the first image slicer IFU was developed (the "3D" instrument; Weitzel et al. 1996). Image slicers provide a high density of spectra on the detector, with few gaps in the image plane (e.g. due to the inefficient packing of optical fibres). Their downside is the expensive manufacturing costs. Examples of image slicers include SWIFT (Thatte et al. 2006; see Chapter 2), MUSE (Bacon

et al. 2010; see Chapter 3) and the multi-object IFU KMOS (Sharples et al. 2013; see Chapters 4 and 5).

1.1.1 The current cosmological paradigm

Two of the most important tenets of cosmological theories are that the Universe is, on large scales (i.e. hundreds of megaparsecs), both homogeneous and isotropic. This means that, in statistical terms, the Universe appears to be the same in all directions (isotropic) and each location in it appears to be comparable (homogenous). Taken together, these two facts form the "cosmological principle", upon which our current theory of cosmology depends. Cosmologists believe that the Universe is comprised of baryonic "normal" matter (such as protons and neutrons), cold dark matter (which only interacts gravitationally, and not with electromagnetic radiation) and dark energy (which tends to accelerate the expansion of space). The proportion of each of these components is roughly 5%, 26% and 69% respectively (Planck Collaboration et al., 2016).

13.8 billion years ago, the Universe was created out of a hot, dense singularity in an event known as the Big Bang. Immediately afterward, it underwent a short period of exponential expansion known as inflation (Guth, 1981; Linde, 1982). From here, the Universe continued to expand (at a slower rate) and cool. At this point, all of space was filled with a plasma completely opaque to light (due to the Thomson scattering of photons by free electrons). It took $\sim 400,000$ years for the Universe to cool sufficiently to allow electrons to become bound to protons in an event known as "recombination". From here, no longer impeded, photons travelled freely throughout the Universe for the first time. Today, we observe these photons as the "cosmic microwave background" (CMB) radiation, a uniform blackbody spectrum at a temperature of 2.73 K (Fixsen, 2009).

Before inflation began, the Universe is thought to have been entirely featureless

and spatially homogeneous, apart from small fluctuations of the quantum vacuum. During inflation, these fluctuations were magnified and became imprinted onto the matter density of the Universe. In the following billions of years, regions which were slight over-densities grew in mass and merged together over time, leading to the *hierarchical* formation of structure (e.g. Press & Schechter, 1974). Dark matter is collisionless, and so collects together in spheroidal "halos". Gas, on the other hand, is dissipative, which allows it to cool and sink towards the centre of its halo. Torques between individual dark matter halos during assembly can impart angular momentum to the baryons, which leads to the formation of a rotating disk of gas rather than a central pile-up. Such a disk provides the appropriate conditions from which stars can form, lighting up these dark halos and turning them into the objects we refer to as *galaxies*.

1.2 Galaxies in the local Universe

Galaxies are accumulations of gas, stars, dust and dark matter bound together by the force of gravity. We live in the Milky Way galaxy, which for many years was thought to contain all matter in the Universe. Astronomers had, however, long noted "nebulous" patches of the night sky, which looked more extended and were distinct from point-like stars. In 964 CE, for example, the Persian astronomer Abdul-Rahman al-Sufi published his "Book of the Fixed Stars" in which he described the Large Magellanic Cloud and the Andromeda galaxy (see e.g. Hafez et al., 2011, for a discussion). In 1781, whilst searching for comets, Charles Messier published his observations of over a hundred objects with "nebulosity", which we recognise today as galaxies, globular clusters and supernovae remnants, as well as things we now consider "true" nebulae (Messier, 1781). Further catalogues grew in size as telescopes improved, with the "New General Catalogue" of observations by John Dreyer and William, Caroline and

John Herschel of nearly 8,000 objects still in use today (Dreyer, 1888).

It is only remarkably recently, however, that we have understood that these "nebulae" are really galaxies like our own Milky Way at cosmological distances from Earth. Early measurements of the doppler shift of M31 (the Messier catalogue's designation for the Andromeda galaxy) were performed by Slipher (1913), who found that they implied its velocity was 300kms^{-1} towards us, "the greatest [velocity] hitherto observed". His later work also found the Sombrero Galaxy (NGC 4594) to have a radial velocity of 1000kms^{-1} away from us (Slipher, 1914). Combined with further observations of novae in M31, the tide of opinion was swinging to the current interpretation of these "spiral nebulae", with a number of papers proposing that they were in fact galaxies in their own right (Puiseux, 1912; Crommelin, 1918; Curtis, 1917; Shapley, 1919)[2]. The first true understanding of the distance to other galaxies came with Hubble (1925, 1929), who used the period-luminosity relation of Cepheid variable stars discovered by Henrietta Swan Leavitt and Edward Pickering (Leavitt & Pickering, 1912) to measure the distance to M31 and other nearby galaxies, placing them at their true position outside our own galaxy.

Edwin Hubble was also instrumental in categorising galaxies. Hubble (1926) proposed what is now known as the Hubble sequence to classify galaxies based on their visual morphologies, codifying the distinction between "elliptical" or "early-type" galaxies and "spiral" or "late-type" galaxies. The two classes have distinct properties. In general, elliptical galaxies are more massive than spirals (e.g. see the stellar mass functions of Bell et al. 2003 and Kauffmann et al. 2003a). In the local Universe, at fixed mass, elliptical galaxies are generally less likely to be star-forming, have redder

[2]Interestingly, this was not the first time that the scientific consensus was of objects residing outside the Milky Way. In the mid 1800s, Sir John Herschel published results describing how a new telescope resolved the nebulosity of the Orion Nebula into individual stars, refuting the "Shining Fluid" hypothesis that it was a nebula in our own galaxy and implying a large distance. The view that nebulae similar to Orion were outside the Milky Way held until Huggins (1865), who showed that the spectrum of Orion contained nebular emission lines, evidence that it was, in fact, made of gas. In the words of Crommelin (1918), at this point "the external galaxy view was swiftly abandoned".

optical colours, contain older stellar populations and have smaller sizes (e.g. Strateva et al., 2001; Shen et al., 2003; Kauffmann et al., 2003b; Cappellari, 2016). Furthermore, the surface brightness profiles of early and late type galaxies are different; it has been known for many years that elliptical galaxies have light profiles which follow a "de Vaucouleurs" law (de Vaucouleurs, 1953), whilst spirals are better described by a purely exponential profile (Sérsic, 1963).

It should be noted, however, that using these differences to select a "pure" sample of objects is fraught with difficulty. Selecting all "red" galaxies in a survey, for example, is *not* exactly equivalent to selecting all galaxies with elliptical morphologies, which is not entirely equivalent to selecting all "quenched" galaxies (e.g. Conselice, 2006; Bernardi et al., 2010; Schawinski et al., 2014). Astronomers have not been able to find a single physical characteristic which reliably correlates with morphology. Even the (arbitrary) definition of "red" and "blue" objects in a sample has profound implications on the conclusions which are drawn from it (Taylor et al., 2015).

1.2.1 Galaxy scaling relations

A key tool used to study the galaxy population as a whole involves looking for correlations between two (or more) galaxy properties among a large sample of objects. There are a number of well known "scaling relations" which galaxies obey, often with total stellar mass (M_*) on one axis. A key test of any cosmological simulation or theory of galaxy evolution is how well they can match these observed relationships, whilst their goal is to explain *why* such relations exist at all.

Firstly, there exists a tight correlation between a galaxy's global star formation rate (SFR) and M_* (e.g. Brinchmann et al. 2004; Noeske et al. 2007; Wuyts et al. 2011; see Speagle et al. 2014 for a compilation of literature measurements). This has come to be known as the "Main Sequence" of star formation, and has also been found to hold on *local* scales too, between the SFR surface density and stellar mass

surface density (Cano-Díaz et al., 2016). In regards to their chemical enrichment, a tight relation also exists between the gas-phase metallicity (Z) of a galaxy and M_* (Lequeux et al., 1979; Tremonti et al., 2004). Studies have also found that SFR is an important "second variable" in this relation, such that a "fundamental metallicity relation" exists in Z-SFR-M_* coordinates. (Mannucci et al., 2010). Further relations link a galaxy's size and M_* (Trujillo et al., 2004; van der Wel et al., 2014) as well as M_* and the fraction of cold gas in its interstellar medium (ISM; Baldry et al. 2008; Peeples & Shankar 2011).

On smaller scales, Magorrian et al. (1998) discovered a link between the mass of a galaxy's central supermassive black hole (SMBH) and its total stellar mass. Soon after, work by Ferrarese & Merritt (2000) and Gebhardt et al. (2000) found that the tighter relation was with the velocity dispersion of the galaxy's bulge, $\sigma_{\rm bulge}$. Since $\sigma_{\rm bulge}$ is understood to be influenced by processes which act on scales of kiloparsecs, it is intriguing that it correlates so well with the central black hole mass (which has a gravitational sphere of influence $r = GM_\bullet/\sigma^2$ on the order of tens to hundreds of parsecs; Kormendy & Ho 2013). This finding led to the idea of "feedback" by Active Galactic Nuclei (AGN), in which the central SMBH releases radiation, winds and/or jets of hot matter from near its accretion disk which heat or expel a galaxy's ISM. This, in turn, stops a galaxy's star formation and also suppresses accretion onto the black hole itself. The black hole will therefore shut down its outburst, allowing ejected gas to cool and return to the galaxy, where the cycle can start again. Whilst such a fuelling/feedback model would regulate the growth of both galaxy and SMBH, direct observational evidence for AGN feedback has been difficult to find (e.g. see the review by Fabian, 2012).

Some of the most famous scaling relations tie together a galaxy's stellar properties with its dynamics. The first studies of flat rotation curves in the outskirts of disk galaxies (van de Hulst et al., 1957; Roberts, 1966; Rubin & Ford, 1970; Bosma,

1978; Rubin et al., 1980; Bosma, 1981) coincided with discoveries of the Tully-Fisher (TF; Tully & Fisher, 1977) and Faber-Jackson (Faber & Jackson, 1976) relations. Originally, the TF related a galaxy's optical absolute magnitude with its integrated HI linewidth, but its modern use relates a galaxy's total stellar mass (or even total baryonic mass; Freeman 1999; McGaugh et al. 2000) to its peak circular rotation velocity. The Faber-Jackson relation is between central velocity dispersion, σ, and absolute magnitude. Later, Dressler et al. (1987); Djorgovski & Davis (1987) and Faber et al. (1987) showed that the Faber-Jackson relation was a special case of the "fundamental plane" of elliptical galaxies, which relates the peak velocity dispersion, σ, to the effective radius[3], r_e, and average surface brightness within r_e, μ.

Studies of the kinematics of early type galaxies have also shown that they are not, in fact, a homogenous population. The first rotation curve of an elliptical galaxy was published in Bertola & Capaccioli (1975). Soon after, Illingworth (1977) and Schechter & Gunn (1979) presented some of the first kinematic studies of large numbers of bright elliptical galaxies, showing that they exhibited far less rotation than predicted for isotropic oblate or prolate models, and must be triaxial and supported by anisotropic motion (Binney, 1978). However, Davies et al. (1983) presented evidence that *faint* ellipticals (with absolute magnitude $M_B > -20.8$) did in fact rotate rapidly. These studies used long-slit spectroscopy along the major and minor axes of their targets, but with the advent and maturity of integral field spectroscopy it became possible to make two dimensional kinematic maps of early-type galaxies (ETGs).

Emsellem et al. (2007) and Cappellari et al. (2007) introduced the λ_R parameter, which is a luminosity-weighted comparison of ordered rotation to random motion:

$$\lambda_R \equiv \frac{\langle R|V\rangle}{\langle R\sqrt{V^2+\sigma^2}\rangle}$$

Using a combination of λ_R and ϵ, a galaxy's ellipticity, a classification of *slow*

[3] r_e is the radius within which half of the total light of an object is emitted

rotators and *fast* rotators arose, which was strengthened by the larger, volume limited ATLAS^{3D} survey (Cappellari et al., 2011). These classifications tie in well with other observational differences between high mass (or bright) and low mass (or faint) ETGs (e.g. see the review by Cappellari, 2016). To summarise, ETGs less massive than $\sim 2\times10^{11}$ $M_{\odot}$ tend to have "disky" isophotes, central light profiles which rise to a cusp, younger stellar populations and appear at all values of ellipticity. Their kinematic maps are more likely to show evidence for ordered rotation from a pronounced stellar disk. These galaxies are classified as fast rotators. ETGs more massive than $\sim 2\times10^{11}$ $M_{\odot}$, on the other hand, tend to have "boxy" isophotes, depleted central light profiles and are rounder than $\epsilon \sim 0.4$. Kinematic maps of these galaxies often show no ordered rotation, with no obvious stellar disk, leading to their classification as slow rotators. The formation channels for each class of ETG are uncertain, but it is clear that two distinct pathways are necessary.

1.3 The Initial Mass Function and Spectral Energy Distribution modelling

Galaxies emit across the entire electromagnetic spectrum, from low frequency radio waves to high energy gamma rays. Taken together, a galaxy's total spectral output is known as its "spectral energy distribution" (SED). Attempting to model a galaxy's SED has a long history (e.g. Tinsley, 1968; Spinrad & Taylor, 1971; Faber, 1972), with "stellar population synthesis" (SPS) modelling the current state-of-the-art approach (see Conroy 2013 for a review).

The building blocks of SPS models are simple stellar populations (SSPs). Conceptually, SSPs are very straightforward– they model the energy output from an idealised population of stars, born from a single star formation event. An SSP is therefore a collection of stars with a single age, metallicity and abundance pattern, with masses

in proportion to a prescribed initial mass function (IMF; of which more in a moment). Using knowledge of stellar evolution, a modeller can predict the SED (or spectrum) of this single collection of stars at any point in time after their birth. Following Equation 1 in Conroy (2013), the output of an SSP can be described mathematically as:

$$f_{\rm SSP}(t, Z, \lambda) = \int_{M_{\rm low}}^{M_{\rm high}} f_{\rm star}(T_{\rm eff}(M), \log g(M)|t, Z, \lambda)\Phi(M)dM \tag{1.1}$$

Here, $f(t, Z, \lambda)$ is the flux at time t, for a star or SSP of metallicity Z, at wavelength λ. The integration is over all (zero-age Main Sequence) masses of star, usually between $M_{\rm low} = 0.08{\rm M}_{\odot}$ (the hydrogen burning limit) and 100 ${\rm M}_{\odot}$. $\Phi(M)$ is the initial mass function, which describes the distribution of stellar masses in an SSP– the proportion of massive stars to low-mass stars. The properties of each individual star (its effective temperature, $T_{\rm eff}$, and surface gravity, $\log g$) are set by the use of an empirical isochrone. An isochrone places each star in a single-age population on the Hertzsprung-Russell diagram, and tracks their evolution in Luminosity- $T_{\rm eff} - \log g$ space as the population ages.

The final ingredient to create a model of a galaxy's SED is a star formation history (SFH). The SFH describes the episodes of star formation a galaxy has undergone across its lifetime. Adding together SSPs makes it possible (in theory) to match any arbitrary SFH. For simplicity, the SFH of massive ETGs is often assumed to be a single burst– that is, the spectral energy distributions of elliptical galaxies are often modelled as SSPs. See Figure 1.2 for a graphical summary of SED modelling.

Whilst there are many sources of uncertainty in the modelling of galaxy SEDs (see e.g. Conroy et al. 2009, 2010 and Conroy & Gunn 2010 for a thorough discussion), the work in the first half of this thesis concentrates on a single one: variation of the low-mass end of the stellar IMF.

As previously mentioned, the IMF defines the number density of stars at each mass on the zero-age Main Sequence in a population, and is thus intricately linked to

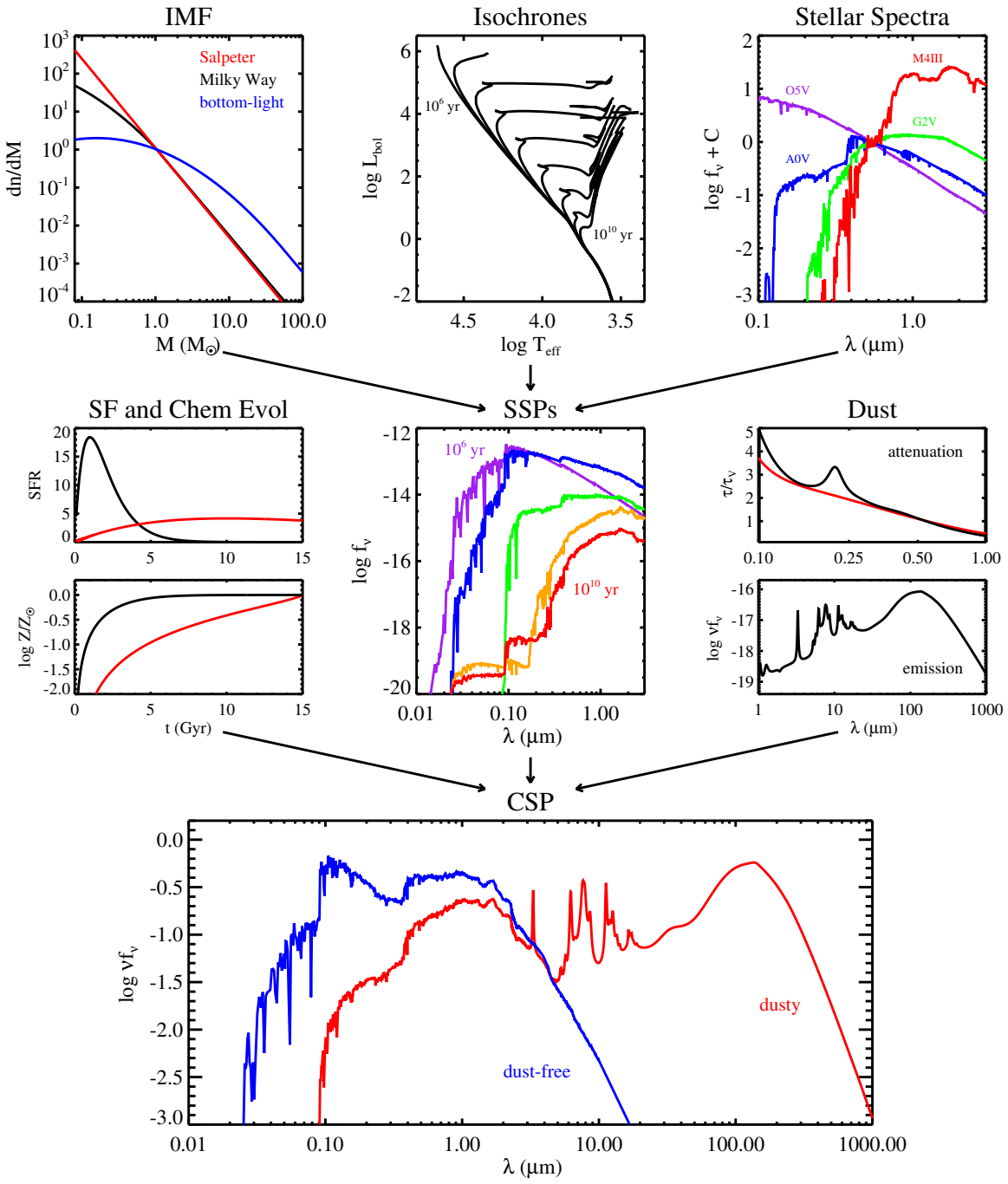

Figure 1.2: Figure from Conroy (2013). A graphical example of the various ingredients of galaxy SED modelling.

the small-scale, turbulent and not-well-understood process of star formation whilst also defining global properties for the population as a whole. The low mass end of the IMF, and hence the number of low mass stars, greatly affects the mass-to-light ratio (M/L) of a system, since a large proportion of the stellar mass in a galaxy comes from stars below 1 $M_{\odot}$. The fact that these low mass stars contribute so little to the integrated light of a population means that large changes in the M/L will not necessarily be reflected in large changes to the properties of the light itself. The high mass slope of the IMF makes a contribution to a galaxy's M/L ratio too, via stellar remnants, and also defines the importance of stellar feedback and the amount of chemical enrichment that takes place. A form for the IMF is assumed whenever a stellar mass or star formation rate is calculated, and the implications for such observational parameters if the IMF is not universal could be very serious (e.g Clauwens et al., 2016).

Historically, little evidence was found for an IMF in our galaxy which varied depending on parameters such as metallicity or environment (see Bastian et al. (2010) for a review). More recently, however, evidence has emerged for a non-universal IMF in studies of the unresolved stellar populations of ETGs. Dynamical modelling of galaxy kinematics undertaken by the ATLAS^{3D} team (Cappellari et al., 2011) and Thomas et al. (2011b) have shown that the M/L ratios of ETGs compared to the M/L ratio for a population with a Salpeter IMF diverge systematically with velocity dispersion, implying that more massive ETGs have "heavier" IMFs (e.g. Cappellari et al., 2013). Such a dynamical analysis cannot determine whether these IMFs are "bottom heavy" (more dwarf stars) or "top heavy" (more stellar remnants), however. Comparisons between stellar population synthesis models and strong gravitational lensing predict a similar IMF-σ relation (e.g. Treu et al., 2010), although massive ETGs with Milky Way-like IMF normalisation have also been found (e.g. Smith et al., 2015).

Chapters 2 and 3 use a third method of studying the IMF in extragalactic objects: using spectroscopy. To infer the IMF in an unresolved population in this manner, one has to measure the contribution of low-mass stars to the overall galaxy spectrum. This is both observationally difficult, due to the fact that stars below 0.4 $M_{\odot}$ contribute on the order of 1% of a galaxy's light for a Milky Way IMF (Conroy & van Dokkum, 2012a), but also suffers from an important degeneracy: at low spectral resolution, giants and low-mass (< 0.5 $M_{\odot}$) dwarf stars at the same effective temperature have very similar spectra, but the giants are orders of magnitude brighter. For example, M giants may have a luminosity of 10^4 $L_{\odot}$ (e.g. Zhong et al., 2015) whilst a mid M-dwarf may be only 0.01 $L_{\odot}$ (Kaltenegger & Traub, 2009). It is therefore difficult to tell whether a spectrum contains light from a large number of M-dwarf stars, implying a steep low-mass IMF, or just a small number of M-giants, leading to a more conventional mass function.

Thankfully, however, certain absorption features in the spectra of integrated stellar populations vary in strength between (otherwise identical) low mass dwarf stars and low mass giants. A measurement of the strength of these "gravity sensitive" indices gives a direct handle on the dwarf-to-giant ratio in a population, breaking the degeneracy and allowing a measurement of the low-mass IMF slope. Important far red gravity sensitive absorption features include the sodium NaI doublet at 8190Å (Keenan & Hynek, 1945; Spinrad & Taylor, 1971; Faber & French, 1980; Schiavon et al., 1997a), the calcium triplet (CaT: Cenarro et al., 2001) and Iron Hydride or the "Wing-Ford band" at 9916Å (FeH: Wing & Ford, 1969; Schiavon et al., 1997b). Studying gravity sensitive absorption features in the spectra of ETGs in this way has a long history (e.g. Spinrad & Taylor, 1971; Cohen, 1978; Faber & French, 1980; Couture & Hardy, 1993; Cenarro et al., 2003), before more recent work by van Dokkum & Conroy (2010, 2012) reignited interest in the topic.

Recent advancements in the modelling of stellar populations (e.g. Conroy & van

Dokkum, 2012a; Vazdekis et al., 2016; Conroy et al., 2018) have led to a number of studies measuring a steepening of the low-mass IMF slope with a galaxy's central velocity dispersion and/or stellar mass (e.g. Conroy & van Dokkum, 2012b; Ferreras et al., 2013; La Barbera et al., 2013; Spiniello et al., 2015b). Furthermore, studies of the variation of the IMF within galaxies (Martín-Navarro et al., 2015a,b; van Dokkum et al., 2017; Conroy et al., 2017; Parikh et al., 2018; Sarzi et al., 2018) have built up the picture of this bottom-heavy IMF (i.e. an excess of dwarf stars) being concentrated in the nuclei of massive ETGs, with Milky-Way like IMFs measured in the outskirts of these objects (although see Alton et al., 2018, who find, on average, no significant radial IMF gradient in their sample of seven nearby ETGs).

Radial measurements of the IMF and IMF-sensitive absorption features have only been presented in a handful of individual objects, and so building up a large sample of galaxies with state-of-the-art IMF determinations is important. We add to these observations in Chapters 2 and 3, with measurements of the massive local ETGs NGC 1277, IC 843 and NGC 1399.

1.4 Environmental influences on Galaxies

Whilst the Universe is homogeneous and isotropic on very large scales, this is certainly not true on the scales which are important to the evolution of galaxies. There is a wealth of observation evidence that galaxies which reside in groups or clusters have have different properties on average to those which reside in more under-dense regions (which we refer to as "the field").

For example, the classic work of Dressler (1980) presents a correlation between a galaxy's visual morphology and its local density (found by counting the 10 nearest projected neighbours of each object in the sample). As the local density of galaxies increases, the proportion of spiral galaxies decreases and the proportion of elliptical

(and S0) galaxies increases. Furthermore, an analysis of the galaxy stellar mass function as a function of environment shows that more massive galaxies are preferentially found in dense regions of space (e.g. see Blanton & Moustakas 2009 for a review). In dense regions of space, it has also been shown that the fraction of red galaxies increases (e.g. Balogh et al., 2004; Baldry et al., 2006; Pimbblet & Jensen, 2012) and the fraction of star-forming galaxies decreases (e.g. Gisler, 1978; Kauffmann et al., 2003a, 2004; Darvish et al., 2016).

The physical processes which cause the differences in galaxy properties can be broadly separated into two categories. On one hand, a number of "external" mechanisms acting on cluster galaxies (involving their interactions with the intracluster medium or other cluster members) have been suggested to quench their star formation and alter their properties. Of these, perhaps the most dramatic is ram pressure stripping (first proposed in Gunn & Gott, 1972). Galaxy clusters are the largest potential wells in the Universe, and contain vast quantities of hot gas between their constituent galaxies (e.g. see Sarazin 1986 and Kravtsov & Borgani 2012 for reviews). This intracluster medium (ICM) contains an order of magnitude more mass than is in the stars of the galaxy members, and is around a thousand times more dense than the intergalactic medium which surrounds galaxies outside clusters (e.g. Nicastro et al., 2008; Zhuravleva et al., 2013). When galaxies fall into a cluster, their motion through the ICM creates a pressure which acts on their reservoirs of gas. The force exerted can be strong enough to overcome the disk's gravitational force, leading to the gas becoming unbound from the galaxy. Spectacular examples of gas being stripped from cluster galaxies can be found at local and intermediate redshifts (e.g. Owers et al., 2012; Ebeling et al., 2014; Rawle et al., 2014; Poggianti et al., 2017), and these objects have come to be known colloquially as "Jellyfish" galaxies following Smith et al. (2010).

On the other hand, galaxy clusters are inherently special places, and the initial

conditions of galaxies which form in them are different from those which form in underdense regions of space. Since the massive clusters of today correspond to the largest overdensities in the early Universe, it has been suggested that these unique initial conditions lead to "accelerated" evolution of their members (e.g. Dressler, 1980; Kauffmann et al., 2004; Morishita et al., 2017). The question of whether internal or external drivers of galaxy evolution are most important is key to building a complete picture of the way in which galaxies change throughout their lifetimes, and a satisfactory solution currently remains out of reach.

Attempting to answer this question by studying cluster galaxies at $z = 0$ is hampered by the fact that so many of them are quiescent, evolved, and at the endpoint of their evolutionary paths. As first discussed in Butcher & Oemler (1978, 1984), galaxy clusters at $z \sim 0.5$ contain a much higher fraction of blue galaxies than today. Furthermore, of those cluster members which are not currently forming stars, a significant fraction show evidence of recently truncated star formation (from k+a spectral characteristics; Poggianti et al., 2009) at these redshifts. These observations imply that intermediate redshift clusters– which are in the process of actively transforming their members– offer a more promising route to address this problem.

Chapters 4 and 5 present the K-CLASH survey and its application to the question of the environmental processes which shape galaxies. K-CLASH uses the KMOS multi-object IFU (Sharples et al., 2013) to target galaxies in four galaxy clusters from the CLASH survey (the Cluster Lensing and Supernova survey with Hubble; Postman et al., 2012) at $0.3 < z < 0.6$. By comparing the properties of galaxies residing in these clusters with a comparison field sample along the line of sight, we aim to look for evidence (or lack thereof) of the cluster-specific effects which may lead to the differences in galaxy properties described above.

1.5 The current state of galaxy evolution

The overarching goal of the science of galaxy evolution is to present a theory to understand the various empirical observations described thus far. At its core, a good theory of galaxy evolution must explain why galaxies can be broadly subdivided into two in the ways described in Section 1.2 (i.e. to answer the question "why do galaxies appear 'bimodal'?"). To that end, there are currently two main schools of thought:

1. The first holds that all galaxies grow by forming stars in the same manner (at a rate which places them on the star-forming main sequence), until at some point they are "quenched". The process (or processes) of quenching can be external (e.g. a major merger) or internal (e.g. AGN feedback), but are distinct from the general decline in SFR with time as a galaxy ages. Such events lead to a cessation of star formation, and the galaxy transitions to become passive (e.g. Peng et al., 2010; Schawinski et al., 2014; Smethurst et al., 2015). This implies that the most important factors affecting a galaxy's properties are the quenching events which take place over its lifetime.

2. The second states that galaxy star formation rates are not "uniform until quenched", but gradually rise and fall over time as they exhaust their supplies of gas *without the need for a specific quenching mechanism*. This paradigm is the older of the two, first put forward by Tinsley (1968). Phrased another way, quenching is a symptom of the evolution of galaxies, but not necessarily informative of the process (e.g. Gladders et al., 2013; Kelson, 2014; Abramson et al., 2016). These theories generally imply that a galaxy's initial conditions are the factors which drive its evolution (e.g. the properties of its host dark-matter halo; Hearin & Watson 2013).

The difficulty in discriminating between these two theories, however, and a prob-

lem for the study of galaxy evolution in general, is that our goal is to make *longitudinal* statements. These are comments which relate to the properties of a single object changing throughout its lifetime, such as "what processes have shaped this galaxy to appear the way it does?". The only observational data we have, however, is inherently *cross-sectional*– that is, our studies only see a single snapshot of the properties of many galaxies at a number of epochs. To illustrate this point, as discussed in Abramson et al. (2016), it is obvious that none of the blue, star-forming spirals we see at $z = 0$ are the progenitors of the quenched early types at $z = 0$, despite how tempting it may be to think of galaxies 'transitioning' from the blue cloud to the red sequence across what has become known as the "green valley". Future large galaxy surveys will undoubtedly increase our *knowledge* about galaxies in the Universe, by making more observations and collecting more data. A more pressing challenge, however, is to relate these observations to theories of galaxy evolution in order to gain a greater *understanding* of the galaxy population as a whole.

1.6 This thesis

We begin this work by investigating the stellar populations of local, quiescent galaxies. Chapters 2 and 3 measure the low-mass IMF in nearby elliptical galaxies by looking for gravity-sensitive absorption features in their spectra. Chapter 2 focusses on radial measurement of a small number of these features in the galaxies NGC 1277 and IC 843. We make a quantitative measurement of the IMF in a global, integrated spectrum for each. Chapter 3 goes one step further and makes spatially resolved measurements of the IMF in NGC 1399, the massive ETG in the Fornax cluster. Each chapter ends by placing our results in context of other studies of the IMF and what our measurements imply for the formation of these objects.

In Chapter 4, we present the K-CLASH survey, which studies star-forming galaxies

at intermediate redshifts ($0.3 < z < 0.6$). This chapter discusses the goals of the survey, lays out the data reduction process, describes how our "star-forming" sample is selected and presents a measurement of the star-forming main sequence (MS). Chapter 5 uses the K-CLASH data to investigate the differences in properties of star-forming galaxies residing in high-density cluster environments, and how they differ from similar objects in the field. We accomplish this by looking for differences in the MS between field and cluster galaxies, investigating the spatial extent of star formation and studying the emission line ratios in each population. In Chapter 6, we summarise our findings and discuss avenues of future study to extend the work presented here.

In some respects, this thesis is split neatly in half. The first two chapters study stellar absorption spectra of a small number of objects at $z \sim 0$, whilst the last two chapters investigate ionised gas emission spectra in a survey of a large number of objects at $z \sim 0.5$. However, all four science chapters are linked by the experimental techniques they use. Both study spatially resolved properties of their targets, utilising integral field spectroscopy to treat galaxies as the fundamentally spatially inhomogeneous objects that they are.

2 | Radial Gradients in IMF sensitive absorption features

The work in this chapter has been published in Vaughan et al. (2018a)

2.1 Motivations

As discussed in Section 1.3, the stellar initial mass function (IMF) describes the distribution of stellar masses in a population at the moment of their formation. Put another way, the IMF can be thought of as a probability distribution function, from which the mass of each new star formed in a galaxy is drawn. Early efforts to measure the IMF were pioneered by Salpeter (1955), who used direct star counts to parameterise the IMF in the solar neighbourhood as a power law of the form $\xi(m) = km^{-x}$ with an exponent of $x = 2.35$. Using a single power law to describe the IMF has come to be called a "unimodal" description. The value of the Salpeter exponent at the high mass end has remained remarkably constant in the numerous studies of our own galaxy since, with modern day IMF parameterisations of the Milky Way incorporating a flattening at low masses: e.g Kroupa (2001) and Chabrier (2003). An IMF with a power law at masses greater than 0.6 $M_{\odot}$, a flat low-mass end and a spline

interpolation linking the two regimes is described as a "bimodal" IMF (Vazdekis et al., 1996). The high end slope of a bimodal IMF is defined by a power law index Γ_b, which is related to x via $x = \Gamma_b + 1$. An increase in Γ_b, like an increase in x, implies an increase in the dwarf-to-giant ratio and therefore an increase in the number of low mass stars.

Studies of optical and far red spectral lines have suggested correlations between the IMF and [Mg/Fe] (Conroy & van Dokkum, 2012b), metallicity (Martín-Navarro et al., 2015c), total dynamical density (Spiniello et al., 2015a) and central velocity dispersion (La Barbera et al., 2013), but importantly the agreement between spectral and dynamical IMF determination is unclear. Smith (2014) compared the IMF slopes derived using spectroscopic methods in Conroy & van Dokkum (2012b) and dynamical methods in Cappellari et al. (2013) for galaxies in common between the two studies. He found overall agreement between the two methods regarding the overarching trends presented in each study, but no correlation at all between the IMF slopes determined by each group on a galaxy by galaxy basis (see also Newman et al. 2017 for a study in three nearby strong-lens galaxies). On the other hand, Lyubenova et al. (2016) do find agreement between spectroscopic and dynamical techniques in the central regions of 27 galaxies in the CALIFA survey but only when using a bimodal IMF. Additional investigation of individual galaxies using independent IMF measurements, rather than comparison of global trends between populations, is required to understand and explain this disagreement.

A more technically challenging goal in spectral IMF measurements is determining whether IMF gradients exist within a single object. Formation pathways of ETGs predict "inside-out growth", where the centre of a massive galaxy forms in a single starburst event before minor mergers with satellites accrete matter at larger radii (e.g. Naab et al., 2009; Hopkins et al., 2009, and references therein). IMF gradients can naturally arise from such a formation history if the global IMF differs between

merger pairs, but few studies have presented evidence for such gradients to date. La Barbera et al. (2016) measure an IMF gradient in a massive ETG with central $\sigma \sim 300\text{kms}^{-1}$, whilst Martín-Navarro et al. (2015a) report IMF gradients in two nearby ETGs. Martín-Navarro et al. (2015b, hereafter MN15) also find a mild gradient in a bimodal IMF in NGC 1277, one of the objects studied in this work. Other studies make radial measurements of gravity sensitive indices but conclude in favour of individual elemental abundance gradients rather than a change in the IMF: see Zieleniewski et al. (2015), Zieleniewski et al. (2017) and McConnell et al. (2016). As we discuss in 2.7, disentangling the effects of an IMF gradient and abundance gradients is not at all straightforward.

In this chapter, we present radial observations of gravity sensitive absorption features in two galaxies. The first, NGC 1277, is a massive, compact ETG located in the Perseus cluster ($z = 0.01704$). NGC 1277 is a well studied object. It has been named as a candidate "relic galaxy" due to its similarity with ETGs at much higher redshifts (Trujillo et al., 2014), seen controversy over the mass of its central black hole (e.g. see van den Bosch et al. 2012 compared to Emsellem, 2013) and had radial measurements of its IMF gradient taken, found using optical and far red absorption indices (MN15). Their study didn't extend to measurements of the FeH index, however. MN15 found a bottom heavy bimodal IMF at all radii, measuring the slope of the IMF to be $\Gamma_b \sim 3$ (the same high-mass slope as a unimodal power law with $x = 4$) in the central regions and dropping to $\Gamma_b \sim 2.5$ ($x = 3.5$) at radii greater than 0.6 R_e.

The second galaxy, IC 843, is an edge-on ETG located on the edge of the Coma cluster ($z = 0.02457$). Thomas et al. (2007) conducted a study of the dark matter content of 17 ETGs in Coma, finding that IC 843 had an unusually high mass-to-light ratio in the R_c band with the best fitting model implying that mass follows light in this system. This result could be explained by a bottom heavy IMF, but also by a dark matter distribution where the dark matter closely follows the visible matter.

Both galaxies were chosen because the evidence for their heavy IMFs implies that the Wing-Ford band could be particularly strong in these objects.

This chapter is organised as follows. Section 2.2 summarises our observations and describes the data reduction process. We pay particular attention to the process of sky subtraction and telluric correction, which is detailed in Section 2.4. We summarise the index measurement process in 2.3 and present our radial index measurements in Section 2.5. Section 2.6 contains the quantitative measurements of the IMF in a global spectrum from each galaxy. We discuss our interpretations in Section 2.7 and draw our conclusions in Section 2.8.

2.2 Observations and Data Reduction

We used the Short Wavelength Integral Field specTrograph (Thatte et al., 2006, SWIFT) at the Palomar 200 inch telescope on January 27th 2016 and March 17th 2016 to obtain deep integral field observations of NGC 1277 and IC 843. Observations were taken in the 235 milli-arcsecond spaxel^{-1} settings, giving a field-of-view of 10.3″ by 20.9″. The wavelength coverage extends from 6300 Å to 10412 Å, with an average spectral resolution of R$\sim$4000 and a sampling of 1 Å pix^{-1}. Dedicated sky frames, offset by $\sim$100″ in declination, were observed in an OSO pattern to be used as first order sky subtraction. The seeing ranged between $\sim$1″ and 1.5″ throughout the observations. Table 2.1 lists details of the targets and observations.

The data were reduced using the SWIFT data reduction pipeline to perform standard bias subtraction, flat-field and illumination correction, wavelength calibration and error propagation. Cosmic ray hits were detected and removed using the LaCosmic routine (van Dokkum, 2001).

Differential atmospheric refraction causes the centre of the galaxy to change position within a datacube as a function of wavelength. Although the magnitude of this

Table 2.1: Targets and Observations

Galaxy	D (Mpc)	RA (J2000)	Dec (J2000)	z	R_e (kpc)	Integration Time (s)
NGC 1277	74.4	03:19:51.5	+41:34:24.3	0.01704	1.2	7 × 900
IC 843	107.9	13:01:33.6	+29:07:49.7	0.02457	4.7	9 × 900

effect is small (leading to a $\sim 1''$ shift at red wavelengths for the observations which are lowest in the sky), individual cubes were corrected by interpolating each wavelength slice to a common position. The individual observation cubes were combined using a dedicated `python` script, which linearly interpolates sub-pixel offsets between the frames.

Sky subtraction and telluric correction are very important considerations at the wavelengths of study in this chapter. They are discussed in detail in Section 2.4.

2.3 Index Measurements

2.3.1 Selected spectral features

The SWIFT wavelength range extends from 6300Å to 10412Å, covering the IMF sensitive indices NaI0.82, CaT0.86 and FeH0.99. We also make radial measurements of the TiO0.89 bandhead and the MgI0.88 absorption feature. Definitions of pseudo-continuum and absorption bands for each index, taken from Cenarro et al. (2001) and Conroy & van Dokkum (2012a), are given in Table 2.2. We use the $\mathrm{NaI}_{\mathrm{SDSS}}$ definition of the NaI 0.82 index from La Barbera et al. (2013).

The sodium feature at 0.82 μm is well studied, with a long history of measurements in the context of IMF measurements (e.g Spinrad & Taylor, 1971; Faber & French, 1980; Schiavon et al., 1997a). It is strengthened in the spectra of dwarf stars and is

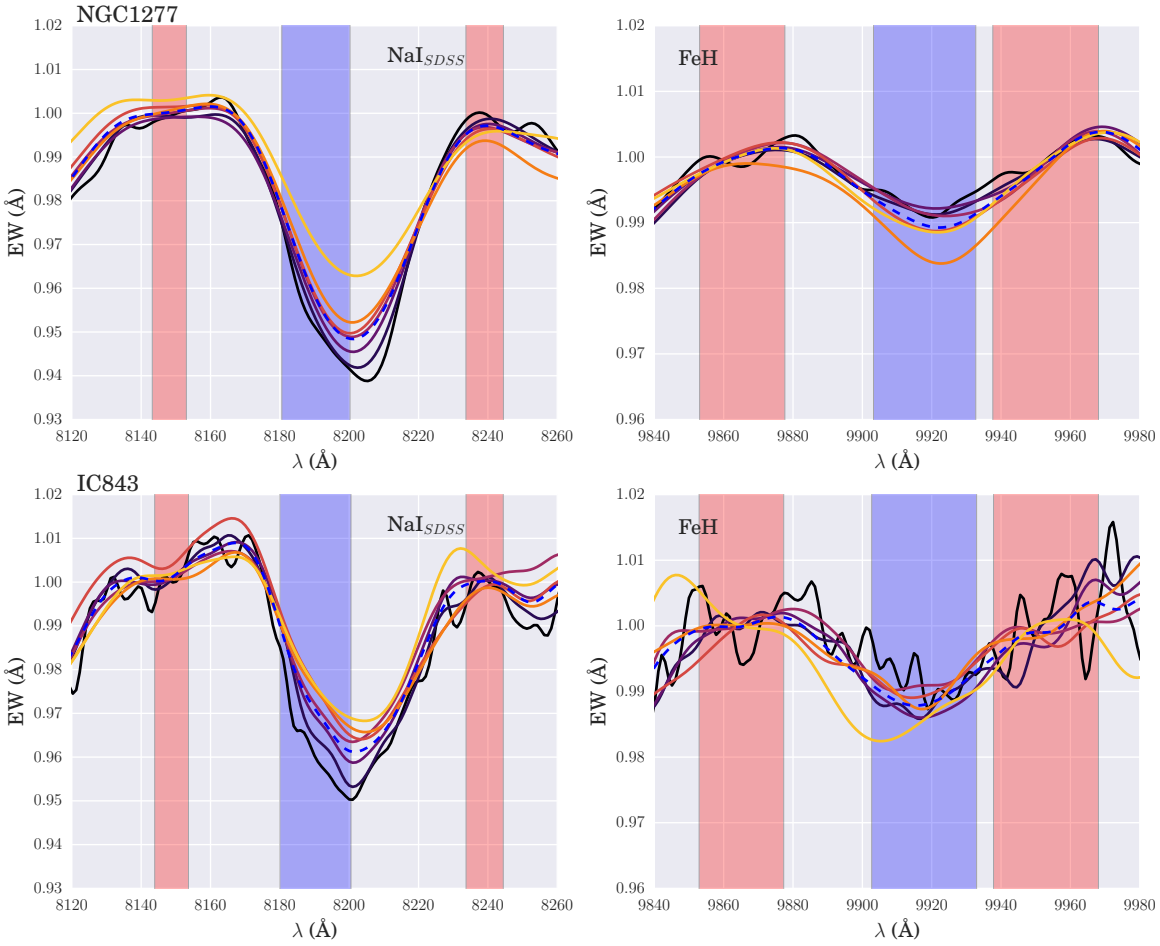

Figure 2.1: Plots of the spectra around the IMF sensitive indices NaI0.82 and the Wing-Ford band (FeH) for NGC 1277 (top) and IC 843 (bottom). Spectra are coloured from dark (central bin) to light (outskirts) and are convolved up to a common velocity dispersion of 450 kms^{-1} (NGC 1277) and 300 kms^{-1} (IC 843) for display purposes only. The dotted blue line is the global spectrum for each galaxy. Blue and red shaded regions show the index band and continuum definitions respectively.

Table 2.2: Definitions of the feature bandpass and blue and red pseudo-continuum bandpasses for each index studied in this work, from Cenarro et al. (2001) and Conroy & van Dokkum (2012a). The NaI_{SDSS} definition is from La Barbera et al. (2013). Since it is a ratio between the blue and red pseudo-continua, the TiO index has no feature bandpass definition. All wavelengths are measured in air.

Index	Blue Continuum (Å)	Feature (Å)	Red Continuum (Å)
NaI_{SDSS}	8143.0-8153.0	8180.0-8200.0	8233.0-8244.0
CaT	8474.0-8484.0	8484.0-8513.0	8563.0-8577.0
	8474.0-8484.0	8522.0-8562.0	8563.0-8577.0
	8619.0-8642.0	8642.0-8682.0	8700.0-8725.0
MgI	8777.4-8789.4	8801.9-8816.9	8847.4-8857.4
TiO	8835.0-8855.0	—	8870.0-8890.0
FeH	9855.0-9880.0	9905.0-9935.0	9940.0-9970.0

sensitive to the abundance of sodium (Conroy & van Dokkum, 2012a). The feature is a doublet in the spectra of individual stars, but the velocity dispersion in massive galaxies often blends it into a single feature.

The Wing-Ford band is a small absorption feature of the Iron Hydride molecule at 0.99μm (Wing & Ford, 1969). It is particularly sensitive to the lowest mass dwarf stars, weakens in [Na/H] enhanced populations and is relatively insensitive to α-abundance (Conroy & van Dokkum, 2012a).

The Calcium Triplet is the strongest absorption feature studied in this work, and is IMF sensitive due to the fact that it is strong in giant stars but weak in dwarfs. Its use as an IMF sensitive index was studied in Cenarro et al. (2003), where an anti-correlation between the CaT equivalent width and $\log(\sigma_0)$ was presented. Calcium is also an α element, although interestingly the Ca abundance has been shown to be depressed with respect to other α elements by up to factors of two in massive ETGs (Thomas et al., 2003). The feature also weakens in spectra with enhanced [Na/H], and is sensitive to the [Ca/H] abundance ratio.

The TiO0.89 and MgI0.88 features are both relatively insensitive to the IMF. In the models of Conroy & van Dokkum (2012a), the TiO bandhead is strongly sensitive to the α-enhancement of the population, as well as weakening with older stellar ages. It also becomes stronger with increased [Ti/Fe] and weaker with [C/Fe]. The MgI0.88 feature displays the opposite behaviour with respect to stellar age, becoming stronger as a population ages, and becomes deeper with increasing [Mg/Fe] and [α/Fe].

2.3.2 The measurement process

To attain a signal-to-noise (SN) ratio high enough to robustly measure equivalent widths, we binned the data cubes into elliptical annuli of uniform SN. We then split each annulus in half along the axis of the galaxy's rotation (such that each half contained absorption features shifted to the blue or the red) and measured the kinematics

using pPXF. Finally, each half of the same annulus was interpolated back to its rest frame and added together. This leads to a roughly constant SN in each bin for each index. Spectra of the FeH and NaI IMF sensitive indices studied in this work, for each radial bin in both galaxies, are shown in Figure 2.1.

We also make velocity and velocity dispersion measurements as a function of radius by binning the datacube to a SN ratio of 15 (for NGC 1277) or 20 (for IC 843), then extract values from a "pseudo-slit" across the cube along the major axis of each galaxy. These are shown in Figure 2.2, along with the long-slit results from MN15. Both galaxies are fast rotators, with peak rotation velocities reaching $\pm$ 300 kms^{-1} in NGC 1277 and $\pm$ 200 kms^{-1} in IC 843. The central velocity dispersion in NGC 1277 is remarkably high at $\sim$420kms^{-1}, in agreement with the values measured by MN15.

Equivalent widths are measured using the formalism of Cenarro et al. (2001), which measures indices relative to a first order error-weighted least squares fit to the pseudo-continuum in each continuum band. We propagate errors from the variance frames of each observation by making a variance spectrum for each science spectrum. All error bars in this work show 1σ uncertainties. Our measurements are shown in Tables A.1 and A.2

The equivalent widths of absorption features depend on the velocity dispersion of the spectrum they are measured from. A larger velocity dispersion tends to "wash out" a strong feature, leading to a smaller equivalent width. In order to compare measurements between different radii in the same galaxy, as well as between separate galaxies, we correct each index measurement to a common σ of 200 kms^{-1} using the same method as Zieleniewski et al. (2017).

To do this, we create an index "correction factor", $C(\sigma)$, from the simple stellar population (SSP) models of Conroy & van Dokkum (2012a, hereafter CvD12; see Section 2.5.2), which can be used to rescale a set of index measurements to a common velocity dispersion. For each index, we measure an equivalent width from the SSP

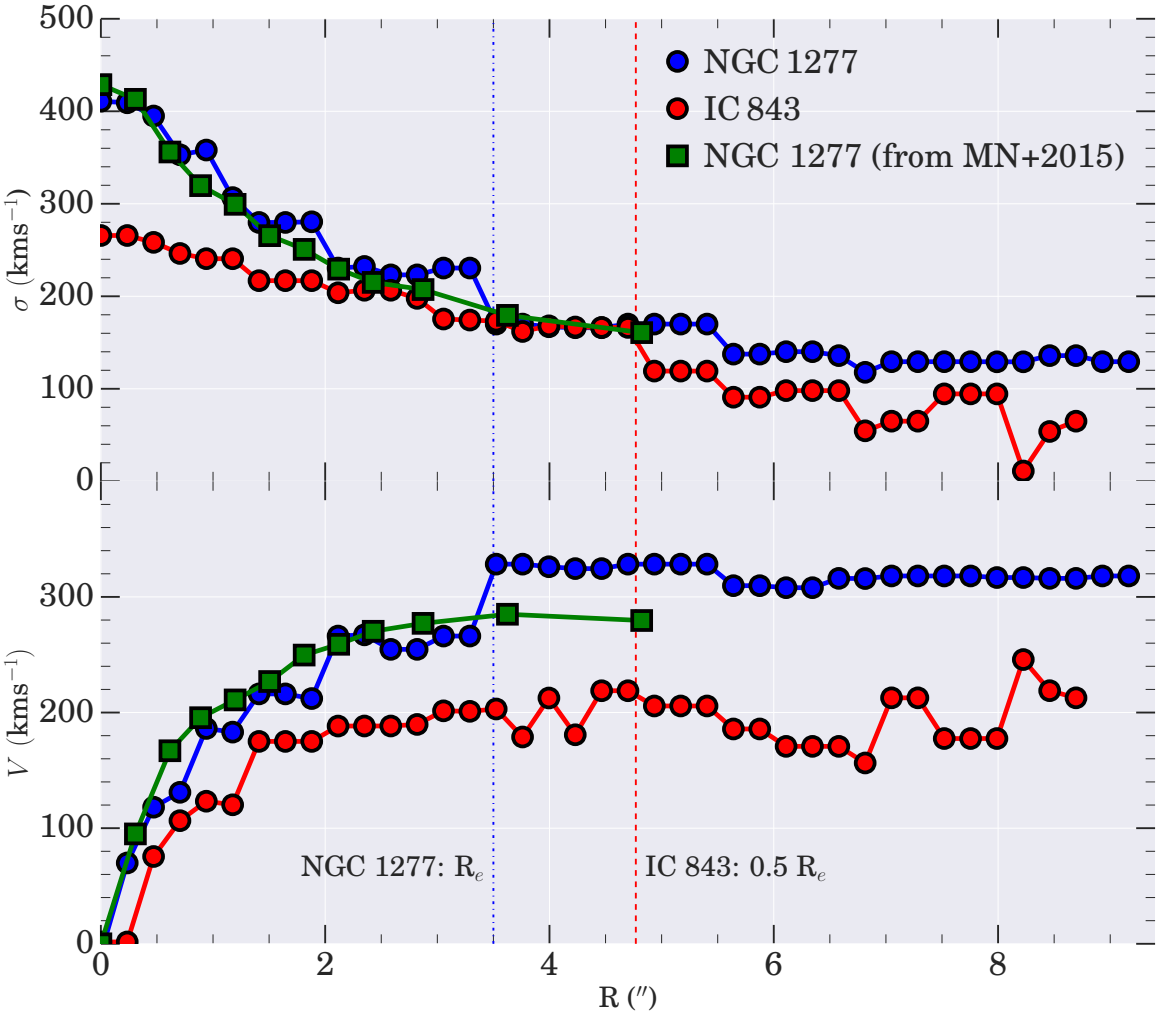

Figure 2.2: Velocity and velocity dispersion parameters for IC 843 (red) and NGC 1277 (blue). Both galaxies show large central velocity dispersions (especially NGC 1277, with σ_0=410kms^{-1}) and ordered rotation at larger radii. Green points are long-slit observations of NGC 1277 taken from MN15.

templates at a variety of velocity dispersions between 80 kms^{-1}and 410 kms^{-1}. This is repeated for each value of age, IMF slope and [α/Fe] enhancement in the CvD12 models. These form a collection of curves, $I(\sigma)$, which trace how an index responds to changes in σ.

We normalise all curves to be unity at the intrinsic velocity dispersion of the galaxy spectrum in question, σ_0. We can then define

$$C(\sigma) = I(\sigma_0)/I(\sigma) \tag{2.1}$$

using the *average* $I(\sigma)$ curve across all templates. This process is displayed graphically in Figure 2.3, reproduced with permission from Zieleniewski et al. (2017). Individual templates are shown as red and black lines, whilst the average is shown in green. The standard deviation of the templates around the average is included as an additional source of uncertainty in the final index measurement values.

2.4 Telluric Correction and Sky Subtraction

At the redshift of these galaxies, telluric absorption is prevalent around the MgI and TiO features in both objects and near the blue continuum band of the NaI feature in NGC 1277. We used the ESO tool MOLECFIT (Kausch et al., 2014) to remove it from our spectra. MOLECFIT creates a synthetic telluric absorption spectrum based on a science observation contaminated by telluric absorption. Using the radiative transfer code of Clough et al. (2005), a model line-spread function of the instrument used to observe the data and a model atmospheric profile based on the temperature and atmospheric chemical composition at the time and place of observation, a telluric spectrum is fit to the science spectra and then divided out. We use MOLECFIT between the regions $\lambda\lambda$ 7561-7768 Å, 81212-8338Å and 8931-9875 Å.

Variations in night sky emission lines occur on similar timescales to our observa-

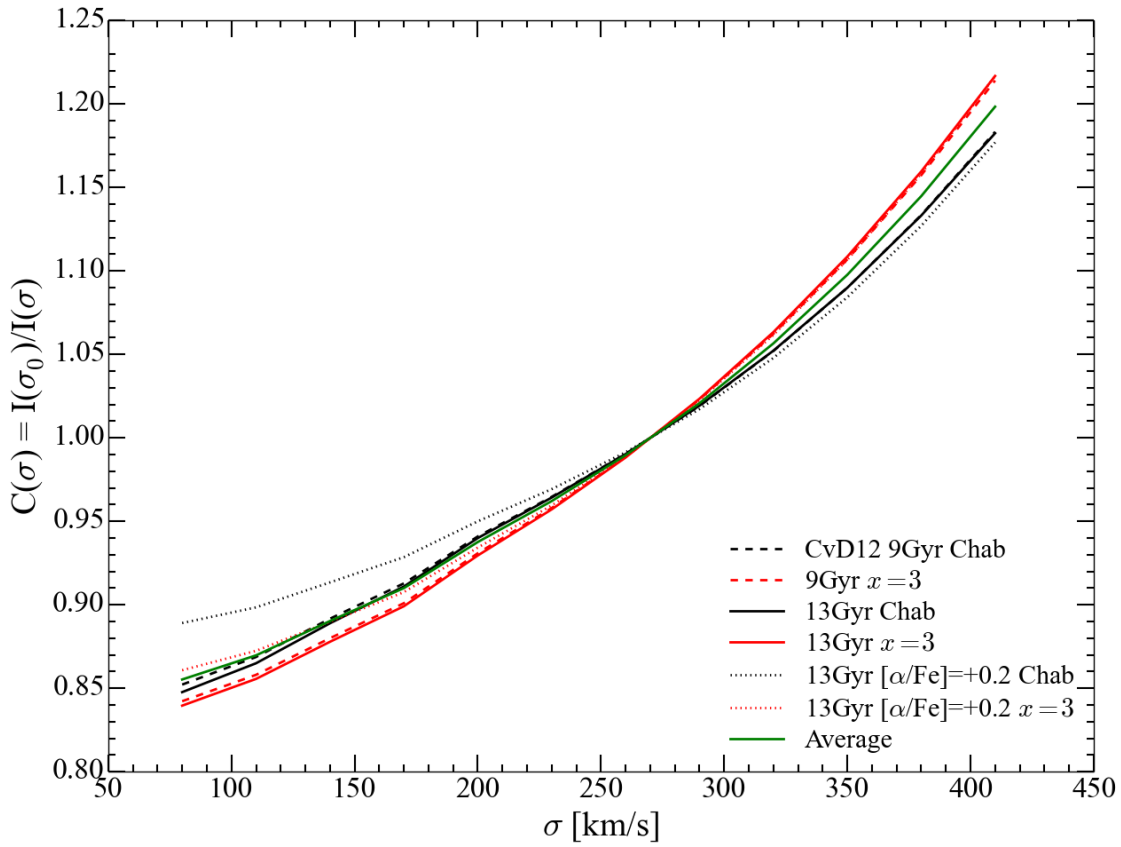

Figure 2.3: Figure A1 from Zieleniewski et al. (2017). Curves show the index correction factor, $C(\sigma)$, for the FeH index from a subset of CvD12 models. All $I(\sigma)$ curves are normalised at the galaxy velocity dispersion– here, $\sigma = 270\text{kms}^{-1}$. The correction factor at 200kms^{-1}, $C(200)$=0.93. We include the standard deviation around the average at $\sigma = 200\text{kms}^{-1}$ as an additional source of uncertainty in our final index measurement values.

tions, meaning that significant residuals from telluric emission remain after first order sky subtraction. This is especially true in the far red end of the spectrum. These residuals are the main source of systematic uncertainty in the measurement of the FeH band, and so must be accurately subtracted to ensure robust index measurements at $1\mu m$. We use two independent sky subtraction methods in this work: removing sky-lines whilst simultaneously fitting kinematics, and fitting each wavelength slice of our observation cubes with a model galaxy profile and sky image before subtracting the best fit sky model.

2.4.1 Removing Skylines with `pPXF`

The first sky subtraction technique uses the method of penalised pixel fitting (Cappellari & Emsellem 2004b; `pPXF`) to fit sky spectra to our data at the same time as fitting the stellar kinematics, as discussed in Weijmans et al. (2009) and Zieleniewski et al. (2017). This involves passing `pPXF` a selection of sky templates (as well as stellar templates) which are scaled to find the best fit linear combination to the remaining sky residuals.

The sky templates were extracted from the dedicated sky frames observed throughout the night. To account for instrument flexure, each sky template was shifted forward and backwards in wavelength by up to 2.5 pixels (2.5 Å) in 0.5 Å increments. Note that the `pPXF` sky subtraction occurs *after* first order sky-subtraction, and so we also include negatively-scaled sky spectra in the list of templates in order to fit negative residuals (which correspond to over-subtracted skylines). The sky spectra were also split into separate regions around emission lines caused by different molecular transitions, based on definitions from Davies (2007). We introduced a small number of further splits to the sky spectrum by eye, around areas where skyline residuals changed sign. Each region was allowed to vary individually in `pPXF` to achieve the best sky subtraction. A full sky spectrum, with locations of sky splits marked, is

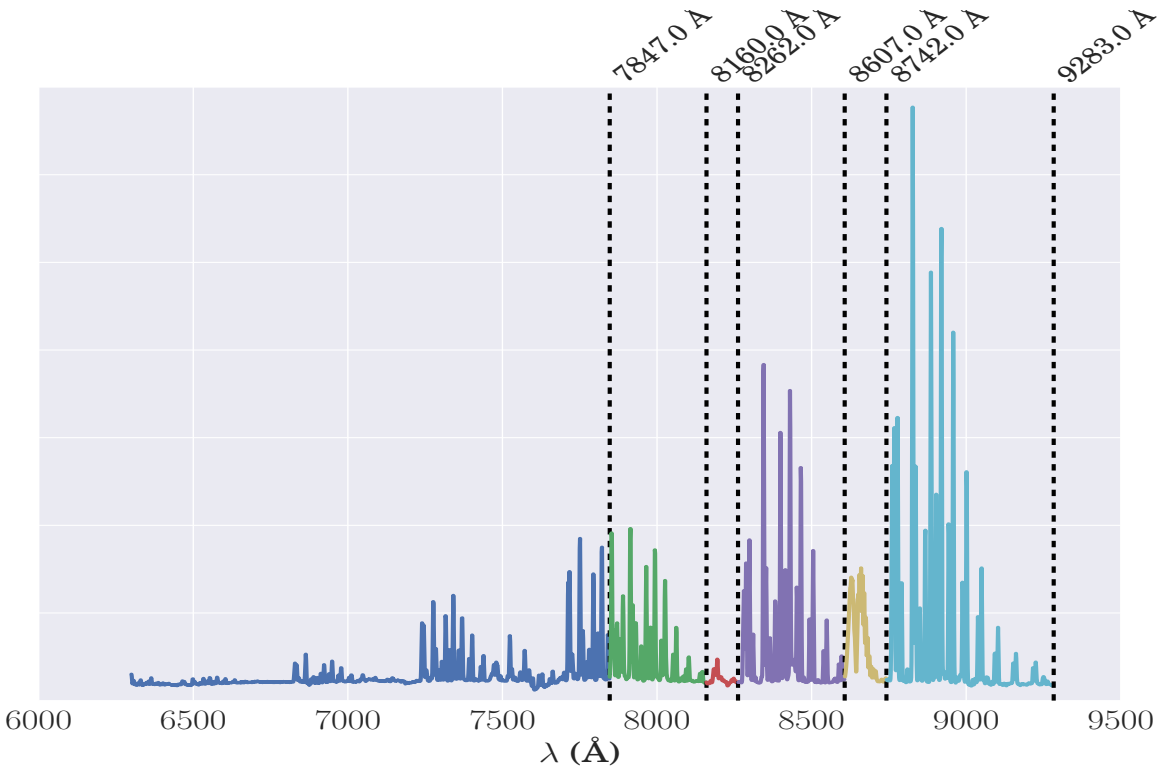

Figure 2.4: A sky spectrum from 6300 Å to 9283 Å, showing locations of split locations.

shown in Figures 2.4 and 2.5.

The area worst affected by residual sky emission is the Wing-Ford band at 9916 Å. Here, we found that changing the combination of sky splits had an impact on the quality of sky subtraction, and hence on the FeH equivalent width measurement. To quantitatively choose the set of skyline splits which gave us the best sky subtraction, we investigated the residuals of the sky subtracted spectrum around the best fitting `pPXF` template. These residuals will generally be Normally distributed around zero, with any remaining skyline residuals appearing as large positive or negative outliers. A set of residuals which have tails which deviate from a normal distribution therefore imply a poor sky subtraction.

Around FeH, there are 5 wavelengths which we decided to split the sky at; 9933 Å, 10054 Å, 10094 Å, 1013 9Å and 1.01865 Å. This leads to $2^5 = 32$ possible combinations of splits. We investigated the residuals for each of these 32 combinations, both by eye

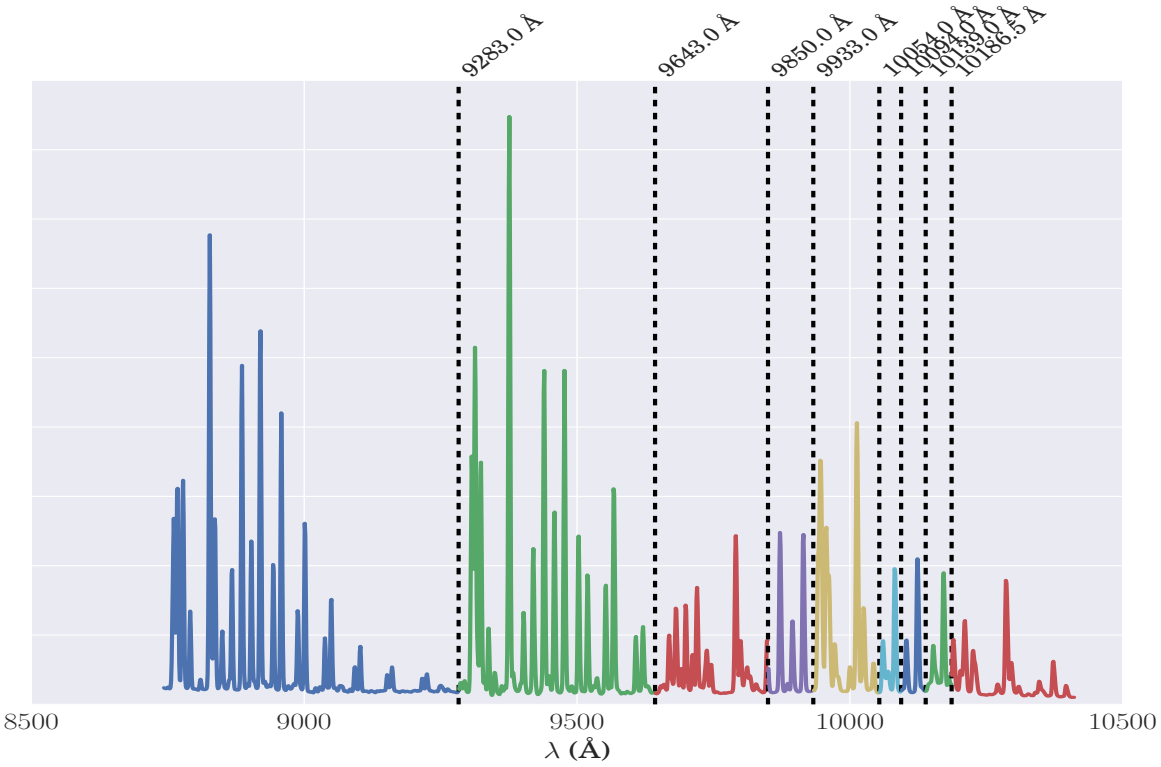

Figure 2.5: A sky spectrum centred around the Wing Ford band, showing the locations of sky splits. At the redshift of NGC 1277 and IC 843, the Wing-Ford band is observed at 10085 Å and 10160 Å respectively.

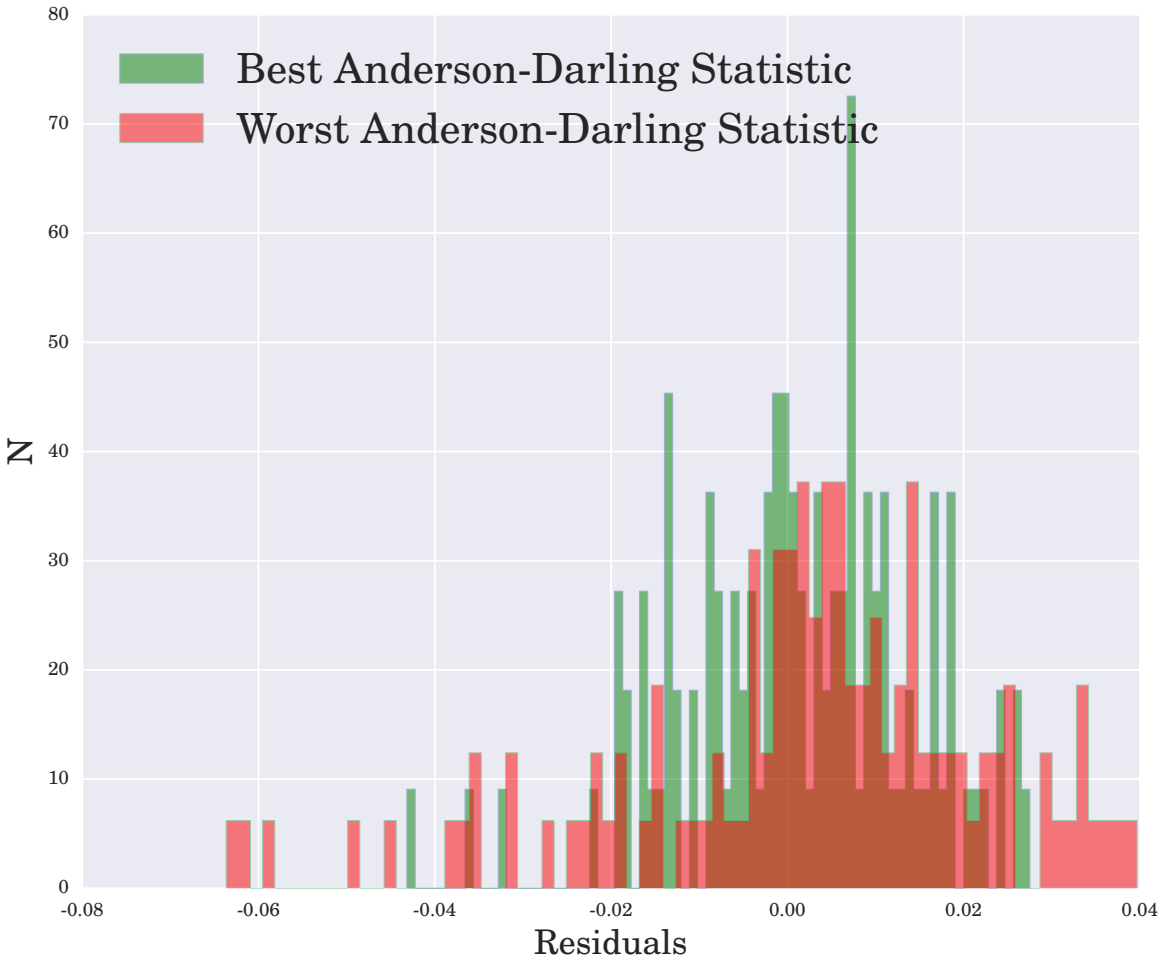

Figure 2.6: Residuals around the best fit `pPXF` template, for one of the NGC 1277 outer bins, after second order sky subtraction using `pPXF`. The two histograms correspond to two different combinations of sky line splits. The histogram in green shows the distribution with the lowest Anderson-Darling test statistic of all 32 sky split combinations, whilst the one in red shows a distribution with many outlying residuals and a large A-D statistic, corresponding to a poor second-order sky subtraction.

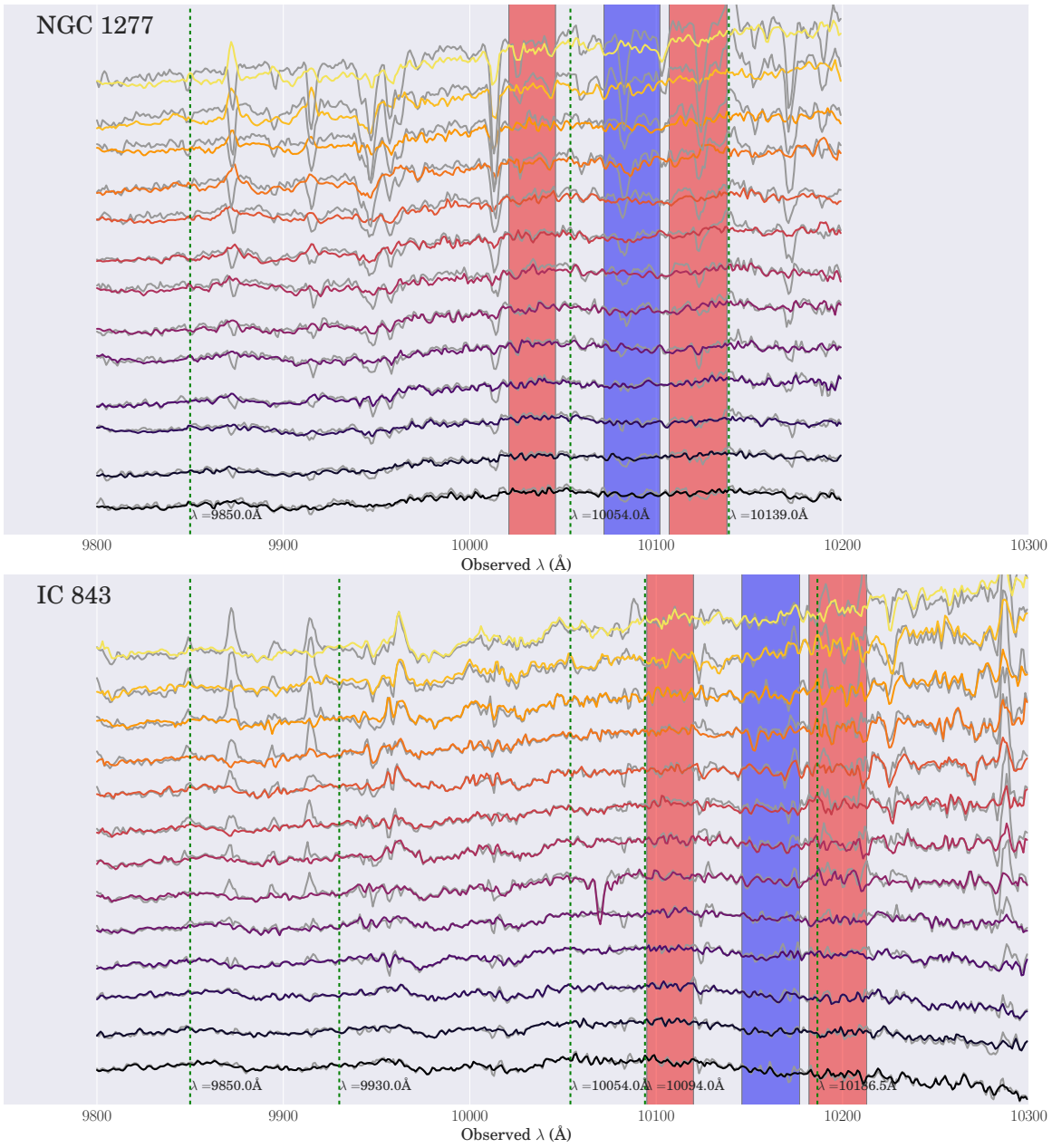

Figure 2.7: 13 spectra around the Wing-Ford band for both NGC 1277 (top) and IC 843 (bottom). These 13 spectra correspond to a central bin and 6 spectra each from the left and right sides of the galaxy. The 7 radial bins for each galaxy we use to measure index equivalent widths are formed by interpolating each of these spectra to their rest frame and adding them. The lines correspond to the spectrum in each bin before `pPXF` sky subtraction (but after first order sky subtraction; coloured grey) and afterwards (black through yellow). The spectra range from the central bin (bottom, dark) to the outermost (top, light). Green dashed line indicate the position of a cut to the sky spectrum. Blue shaded regions show the location of the FeH index whilst red shaded regions identify the location of the continuum regions.

and using an Anderson-Darling test (Anderson & Darling 1954; hereafter AD) with the null hypothesis that each sample was drawn from a normal distribution. The AD test is very similar to the more commonly used Kolmogorov-Smirnov test, but with a weighting function which emphasises the tails of each distribution more so than a KS test. For all analysis in this work we used the selection of sky splits with the lowest AD statistic, which corresponds to the residual distribution best described by a normal distribution with no outliers. A plot of the best (green) and worst (red) residual distribution for the NGC 1277 skylines is shown in Figure 2.6, whilst Figure 2.7 shows our spectra around FeH for NGC 1277 and IC 843 before and after second order sky subtraction. The spectra which, by eye, have the best sky subtraction are also those with the lowest AD statistic.

2.4.2 Median Profile Fitting

The second sky subtraction method is independent of the first. Each observation cube (which has undergone first order sky subtraction) is a combination of galaxy light and residual sky light. In each wavelength slice, sky emission corresponds to an addition of flux in all pixels whereas galaxy light is concentrated around the centre of the observation. We aim to model these two contributions in a single data cube and subtract off the best fitting sky model.

We take the median image of the data cube as the galaxy model in our fitting procedure. The sky model is a flat image at every wavelength slice; the same constant value across the IFU in each spatial dimension. Such a model assumes that the shape of galaxy light profile doesn't change over the SWIFT wavelength range of 6300 Å to 10412 Å, but is only scaled up and down as the galaxy gets brighter or dimmer and the instrument throughput varies. It should also be noted that this assumption is equivalent to saying that the median galaxy profile– which is essentially a stellar continuum map– is a good description of the equivalent width map of each feature.

This implies that spatial inhomogeneities in an index which are not represented in the stellar continuum map would not be well modelled by this description.

Using a simple least squares algorithm, we simultaneously fit the galaxy and sky model to each wavelength slice of an individual cube. We then subtract the best fit sky residuals for each cube, combine the observation cubes together and are left with an alternative sky subtracted data cube for each galaxy. These are binned and passed to `pPXF` to measure the kinematics as before, except without using the sky subtraction technique of Section 2.4.1.

The median profile fitting method leads to slightly noisier results than using `pPXF`, and as such all index measurements quoted in this chapter are derived from the first sky subtraction method. However our conclusions are unchanged regardless of which sky subtraction technique we employ. Figure 2.8 shows equivalent width measurements of the Wing Ford band from spectra which have undergone the two sky subtraction processes; subtracting skylines with `pPXF` and median profile fitting. The two methods show good agreement, implying that our FeH measurements are robust, despite the challenging nature of removing residual sky emission in the far red region of the spectrum. In particular, the global FeH measurements, on which we base a determination of the IMF in these galaxies, are entirely consistent between the two approaches.

2.5 Results

2.5.1 Radial variation in index strengths

Figure 2.9 shows the results of measuring the IMF sensitive absorption features in NGC 1277 and IC 843 as a function of radius. As discussed in Section 2.3, these measurements were taken at the intrinsic velocity dispersion of the radial bin and then corrected to 200 kms^{-1} for both galaxies. All results are equivalent widths, in

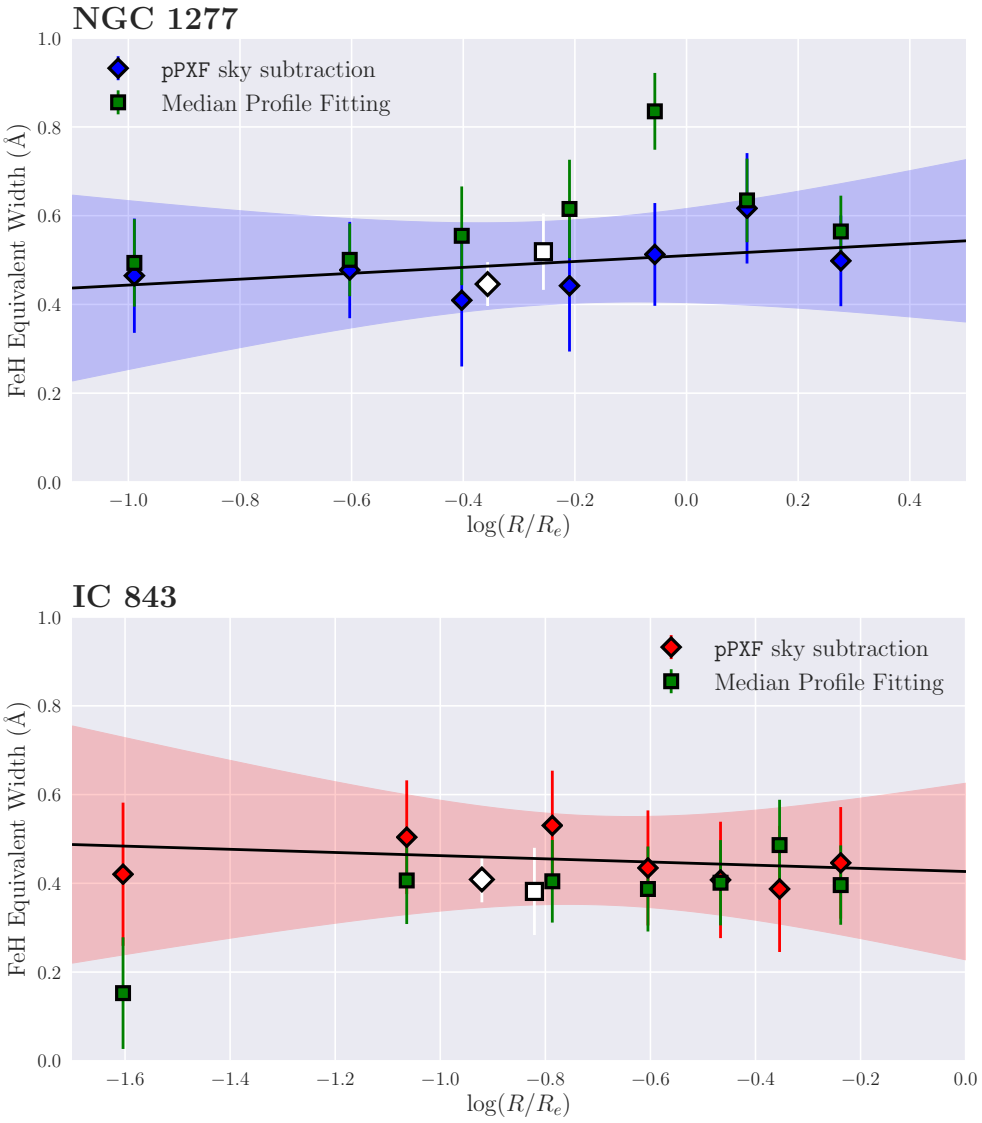

Figure 2.8: A comparison of equivalent width measurements of the Wing-Ford band, after both `pPXF` sky subtraction and median profile fitting, for NGC 1277 (top) and IC 843 (bottom). The best fit straight line for the `pPXF` sky subtraction is shown for both galaxies, as well as its one sigma uncertainty (shaded region). The two sky subtraction methods give generally good agreement, confirming the robustness of our results. In particular, the global FeH measurements are entirely consistent between the two approaches.

Table 2.3: Measured index trends with respect to $\log(R/R_e)$, with 1σ uncertainties. Units are Å/ $\log(R/R_e)$, apart from the TiO index gradient which is simply $1/\log(R/R_e)$. Index measurements are in units of Å, apart from the TiO index which is a ratio of pseudo-continua

Index	Best fit gradient		Global Index Value	
	IC 843	NGC 1277	IC 843	NGC 1277
NaI	$-0.218^{+0.11}_{-0.11}$	$-0.368^{+0.10}_{-0.10}$	0.66 ± 0.05	1.07 ± 0.05
CaT	$-0.126^{+0.28}_{-0.28}$	$-0.595^{+0.29}_{-0.30}$	7.24 ± 0.14	6.81 ± 0.13
MgI	$-0.012^{+0.09}_{-0.09}$	$0.231^{+0.12}_{-0.12}$	0.58 ± 0.04	0.56 ± 0.06
TiO	$-0.006^{+0.005}_{-0.005}$	$-0.011^{+0.005}_{-0.005}$	1.067 ± 0.002	1.073 ± 0.002
FeH	$-0.015^{+0.11}_{-0.11}$	$0.081^{+0.11}_{-0.10}$	0.41 ± 0.05	0.44 ± 0.05

units of Å and found using the formalism of Cenarro et al. (2001), except for that of TiO which is a ratio of the blue and red pseudo-continua. Table 2.3 gives the best fitting gradient, m, of the straight line fit to each index, with 1σ uncertainties from the marginal posterior of m. It also lists the measured values of each index in the integrated spectrum of each galaxy. The individual radial index measurements in both galaxies are presented in Tables A.1 and A.2.

The most significant index gradient in NGC 1277 is in NaI, which drops from 1.3 Å in the very centre to $\sim$ 0.8 Å at 1.9R$_e$. This behaviour is consistent with the findings of MN15, who found a similarly strong radial gradient in this object. We also measure negative gradients in the CaT (at a $\sim 2\sigma$ significance) and the TiO0.89 (2.75σ). The measurements of MgI0.88 index show a positive trend with radius, although the scatter in these measurements is large, possibly due to the effects of residual telluric absorption. We do not find evidence for a radial gradient in FeH0.99 in NGC 1277, with the gradient in index strength being consistent with zero.

The most significant gradient in IC 843 is also the NaI feature, albeit offset to a

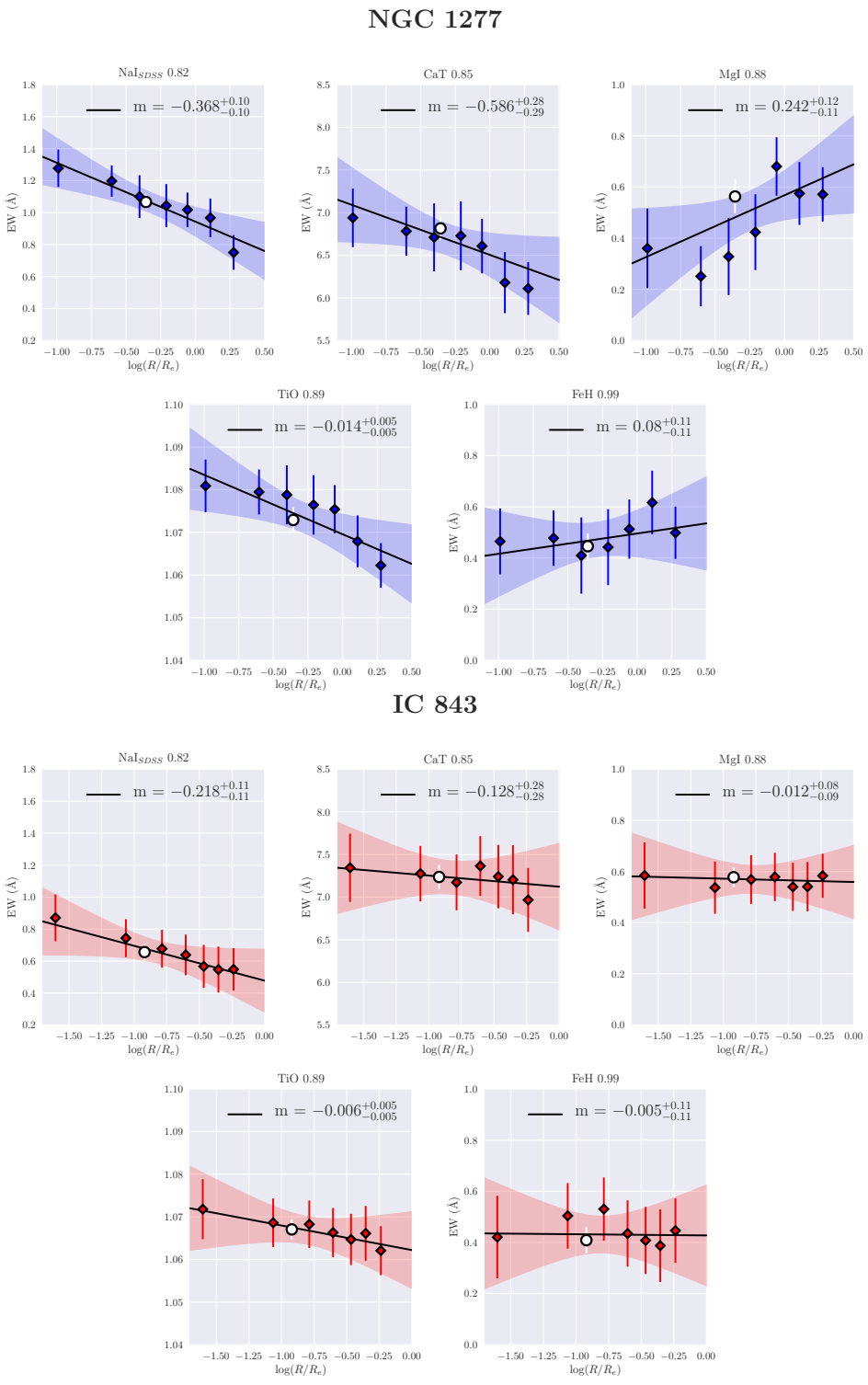

Figure 2.9: Radial measurements for each index in NGC 1277 (blue, top) and IC 843 (red, bottom). All index measurements have been corrected to a common velocity dispersion of 200kms^{-1} (see section 2.3). 1σ errors around the best fit line (encompassing uncertainty in both the gradient and intercept) are shown as shaded regions. The value of the best-fit gradient, m, is shown in each panel. The white circle shows the value of each index in the integrated spectrum of each galaxy. The individual radial index measurements for each galaxy are presented in Tables A.1 and A.2

weaker index strength. We also see a significant radial trend in TiO0.89. We measure flat radial profiles for MgI0.88, the CaT and the Wing Ford band, with all three indices having a best fit gradient fully consistent with zero.

2.5.2 Comparison to stellar population synthesis models

We now compare our measurements to two sets of simple stellar population (SSP) models. Each set models the optical and NIR spectra of a population of stars with variable ages, abundance patters and IMF slopes.

The first set are the CvD12 (Conroy & van Dokkum, 2012a) templates. These model variations in stellar age, [α/Fe], a number of individual elemental abundances and the slope of the IMF. The models are available with single-power law IMF slopes $x = 3.5$, $x = 3$, $x = 2.35$ (Salpeter) and $x = 1.8$ (which gives the same M/L ratio as the standard Chabrier (2003) IMF slope, and corresponds to a "Milky-Way" like IMF). They also include a "bottom light" IMF which is not a single power-law (from van Dokkum 2008).

Secondly, we use the E-MILES models (Vazdekis et al., 1996; Röck et al., 2016). These allow for variation in stellar metallicity, age and the slope of the IMF. La Barbera et al. (2017) have also produced the "Na-MILES" models, which are SPS templates spanning the E-MILES wavelength range with enhanced [Na/Fe] abundance ratios of up to 1.2 dex. Each set of models use single power-law IMFs.

Figure 2.10 shows a comparison of our NaI and FeH measurements to these SSP models, each convolved to 200 kms^{-1} to match our measurements. The top two panels show index predictions from the CvD12 and E-MILES libraries for changes in IMF slope from an old (13.5 Gyr for the CvD12 models, 14.125 Gyr for E-MILES) stellar population at solar metallicity, α-abundance and elemental abundance ratios. Also shown are variations in index strength with a variety of stellar population parameters included in each set of models. The bottom two panels show our measurements of

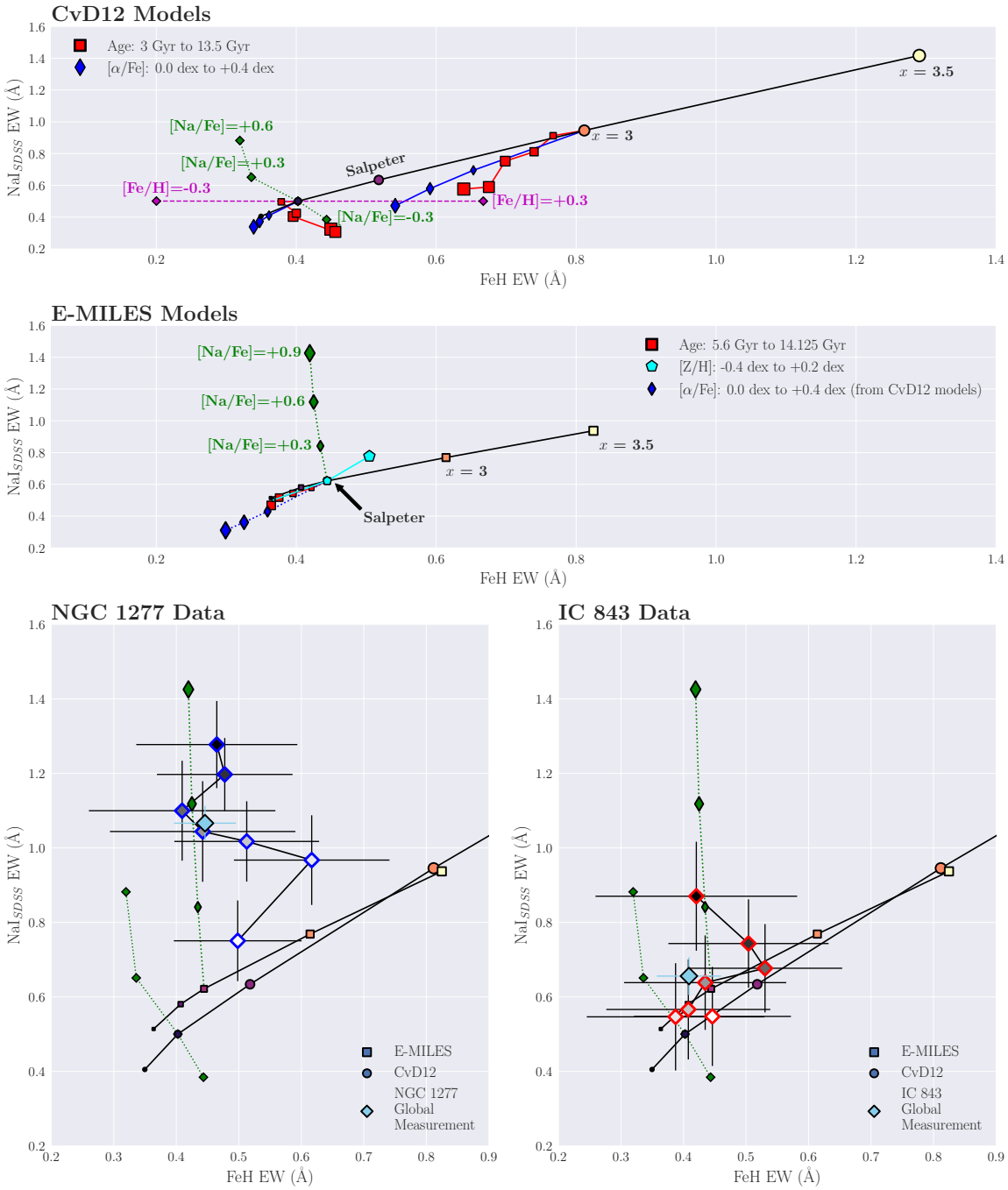

Figure 2.10: Figure caption: next page

Figure 2.10: (Previous page.) A comparison of our measurements of NaI and FeH equivalent widths to two sets of stellar population models. All equivalent widths are measured at a common velocity dispersion of 200kms^{-1}. The upper two panels show the change in FeH and NaI equivalent width with varying stellar population parameters in the CvD12 models (first panel) and E-MILES models (second panel). The black line in both panels shows index responses to varying the power-law IMF slope, x, in an old stellar population at solar metallicity, [α/Fe]=0.0 and with solar elemental abundance ratios. Note the differences in index equivalent width predictions, for the same IMF slope, between the models. Changes in [α/Fe] from solar to +0.4 dex (small to large blue diamonds), and age from 3 to 13.5 Gyr (large to small red squares) from a Chabrier and $x = 3$ IMF are shown in the top panel, for the CvD12 models. Also plotted are predictions for abundance variations of +0.6 dex to -0.3 dex in [Na/Fe] (green) and [Fe/H] (purple) from a Chabrier IMF. The second panel shows variations of the E-MILES model predictions for ages from 5.6 to 14.125 Gyr (large to small red squares), [Z/H] from -0.4 to +0.2 dex (small to large cyan pentagons) and [Na/Fe] from solar to +0.9 dex (small to large green diamonds), all from a Salpeter IMF. We also include response functions from CvD12 showing variations in [α/Fe] abundance.

The lower two panels show our resolved measurements in NGC 1277 (left, blue outline) and IC 843 (right, red outline), coloured by their radial position from the centre of the galaxy (dark) to the outskirts (light). The global measurements for both galaxies are plotted in light blue. Index predictions from the models vary from a bottom light IMF (dark colours, bottom left) to a bottom heavy IMF (light colours, top right), with equivalent IMF slopes plotted in the same colour; for example, the predictions for an IMF slope of $x = 3$ are coloured orange for both models. See Section 2.5.2 for discussion.

NGC 1277 (left) and IC 843 (right), along with CvD12 and E-MILES model predictions.

The most important elemental abundance variations in the CvD models for us here are changes in [Na/Fe] and [Fe/H]. A change in [Fe/H] of $\pm$0.3 dex has no effect on the predicted NaI equivalent width, whilst understandably leading to a large variation in FeH strength. The result of increasing [Na/Fe] is a strengthening of the NaI index combined with a weakening of the FeH equivalent width. This is due to the fact that Na is an important electron contributor in cool giant and dwarf stars, and large abundances of Na in these stellar atmospheres tends to encourage the dissociation of molecules like FeH. An α-enhanced population leads to weaker FeH

and NaI predictions, especially at steeper IMF slopes, whilst the response of the FeH index to changes in population age is found to be a function of the IMF slope. A full discussion of these effects can be found in Conroy & van Dokkum (2012a).

The E-MILES models include changes in age and metallicity. A metallicity of +0.2 dex above solar leads to increased equivalent widths for both NaI and FeH, whilst younger ages tend to weaken both indices. Interestingly, these templates predict that the FeH index is less sensitive to the effect of [Na/Fe] enhancement than the CvD12 models. We also expand the dimensionality of the E-MILES models by applying response functions for changes in [α/Fe] from the CvD12 models, in a similar way to Spiniello et al. (2015b).

Figure 2.10 also highlights a complicating factor in our interpretation of our NaI and FeH measurements: the different index predictions from the CvD12 and E-MILES models for the same value of IMF slope. The largest difference is for the most bottom heavy IMFs: the $x = 3.5$ IMF slope prediction for FeH is $\sim 37\%$ weaker in the E-MILES models compared to the CvD12, whilst the NaI predicted equivalent width is $\sim 39\%$ smaller. A large part of this difference is due to the different low-mass cutoff, m_c, assumed for the IMF in each case: 0.08 $M_\odot$ in the CvD12 models and 0.1 $M_\odot$ for E-MILES. The CvD12 models therefore have a larger number of very low-mass stars and predict stronger NaI and FeH equivalent widths.

Constraining the low-mass cut off of the IMF is a technically demanding task, with recent measurements of m_c by Spiniello et al. (2015a) and Barnabè et al. (2013) combining modelling of IMF sensitive indices with constraints from strong gravitational lensing and dynamics. Since in this work we are unable to distinguish between $m_c = 0.08\ M_\odot$ and $m_c = 0.1\ M_\odot$, we conduct our analysis and draw conclusions using both sets of SPS models.

Note that there are other key differences between the model spectra, largely due to the different ways they are computed. The two sets of models use differ-

ent isochrones for the lowest mass stars, as well as different methods to attach stars to these isochrones. Figure 2.10 shows that the response of both NaI and FeH to increases in [Na/Fe] abundance is different for the two sets of models, and at fixed [Z/H] these indices are also more sensitive to changes in [α/Fe] in the E-MILES models than CvD12. A comprehensive comparison of the IMF-sensitive features below $1\mu m$ in the two sets of models is presented in Spiniello et al. (2015b).

The measurements in both galaxies scatter around similar areas of parameter space: above a Salpeter IMF in the direction of [Na/Fe] enhancement, with the NGC 1277 points further from the model lines than IC 843. Notably, our measurements disfavour very bottom heavy single power law IMFs with x>3 in both NGC 1277 and IC 843.

2.6 IMF determination from global measurements

The next step in our analysis is to make quantitative inferences about the IMF in each galaxy using two different methods: full spectral fitting and fitting to the strength of the FeH index. Ideally, we would use both these techniques to infer radial gradients in the IMF in both galaxies. However, we find that our spectra lack the wavelength coverage to constrain some important stellar population parameters which are degenerate with IMF effects, and we must rely on previous observations from other sources to measure them (which we discuss in Section 2.6.1). We also found that the some spectra in the outer bins lacked adequate signal-to-noise to make tight constraints on the IMF. In the following section, therefore, we instead infer the IMF in a global spectrum, co-added from the entire datacube of each galaxy.

2.6.1 Full Spectral Fitting

We begin by fitting templates from the spectral library of CvD12 to the integrated spectrum from each target. This technique is discussed extensively in CvD12, and our approach is very similar. The spectral fitting covers wavelengths from 6600 Å to 10020 Å in the rest frame of each galaxy, split into four sections: 6600-7300 Å, 7600-8050 Å, 8050-9000 Å and 9680-10020 Å. The two gaps between 7300-7600 Å and 9000-9680 Å were chosen to avoid areas of residual telluric absorption. We have also carefully masked pixels contaminated by sky subtraction residuals in each spectrum. These masked regions are shaded in Figure 2.11 and 2.12.

To correct for different continuum shapes between the templates and the data, we fit Legendre polynomials to the ratio of the template and the galaxy. The order of these polynomials is defined to be the nearest integer to $(\lambda_{\rm upper} - \lambda_{\rm lower})/100$Å. We have ensured that slightly varying the order of this polynomial has negligible effect on our results, and have included the effect of this variation in the error budget for each parameter.

We allow eight parameters to vary when performing the fit: the redshift and velocity dispersion of the template; the chemical abundances [Na/Fe], [Fe/H], [Ca/Fe], [Ti/Fe] and [O/Fe]; and the single power-law IMF slope.

Ideally, the stellar age and [α/Fe] abundance would also be included as free parameters of the fit. We did not find these quantities to be well constrained by the data, however, since our wavelength coverage does not include many of the blue absorption indices sensitive to these parameters. To overcome this, we use previously published measurements of blue "Lick" indices (which are, to first order, insensitive to the IMF) from Ferré-Mateu et al. (2017) for NGC 1277 and Price et al. (2011) for IC 843 and the SPS models of Thomas et al. (2011a) to infer stellar age and [α/Fe] abundances in these objects. We then fix the values of these parameters during the

fit. The derived values are shown in Table 2.4 for both galaxies.

Note that the measurements from Ferré-Mateu et al. (2017) are spatially resolved, and we have matched these data to the aperture size used in this work. Measurements from Price et al. (2011) come from an SDSS fibre covering a diameter of 3″ in the very centre of IC 843, however, smaller than the 12″ which contribute to our global spectrum. Such a discrepancy is unavoidable, but does mean that if any radial gradients in the stellar age or [α/Fe] abundance exist in IC 843 then the parameters assumed for the global spectrum would be incorrect. Furthermore, the derived age and [α/Fe] for NGC 1277 and IC 843 were found using a different set of stellar population models than were used for the spectral fitting (the Thomas et al. 2011a models rather than those from CvD12). Small systematic offsets between the models could exist, implying that our fixed values found from the Thomas et al. (2011a) models may not be appropriate for the fitting using the CvD12 templates.

To account for this, we have also computed fits (for both galaxies) where we varied these assumed values of age and [α/Fe] abundance. The resulting change in the derived parameters are included in the error budget for each result (see Table 2.4).

The CvD12 models also allow for variation in further elemental abundances, as well as an "effective isochrone temperature" nuisance parameter, $T_{\rm eff}$. $T_{\rm eff}$ slightly changes the isochrone each galaxy template is built from, which is a proxy for varying metallicity (since variations in total [Z/H] are not modelled in the CvD12 library). Further discussion can be found in CvD12. We compute fits (at each fixed age and [α/Fe] abundance assumed above) which include all further element variations (in [C/Fe], [N/Fe], [Mg/Fe] and [Si/Fe]), as well as $T_{\rm eff}$, to ensure that the low-mass IMF slope we recover is not being driven by an elemental abundance variation we have neglected. We find that the best-fit IMF is negligibly affected in either galaxy. Any variations in the derived parameters as a result of this process are also folded into the

uncertainties reported in Table 2.4.

The fit was performed using the Markov-Chain Monte-Carlo ensemble-sampler `emcee` (Foreman-Mackey et al., 2013). We use a simple, χ^2 log-likelihood function with flat priors on each parameter. 400 "walkers" explore the posterior probability distribution, each taking 10,000 steps, giving 4×10^6 samples in total. We discard the first 8000 steps of each walker as the "burn-in" period. Each chain was inspected for convergence and we have run tests to ensure that chains which start from different areas of parameter space converge to the same result.

Results of the fitting are shown in Figures 2.11 and 2.12, with prior ranges and derived quantities shown in Table 2.4. The fits to the spectra are good, with residuals at around the 1% level for the majority of the wavelength range. The reduced χ^2 values are 0.41 and 0.95 for NGC 1277 and IC 843 respectively. We note, however, that the spectral range from 7600 to 8050 Å in IC 843 shows significant residuals. We have ensured that our conclusions for both galaxies are unaffected if we remove this region from the fit, and included the small variations in derived parameters in our error budget.

We find both galaxies to have super-solar [Na/Fe] abundances by factors of between 3 and 5, with NGC 1277 requiring greater Na enhancement than IC 843. NGC 1277 also has a more bottom heavy low-mass IMF slope than IC 843, with best fitting single power law IMF slopes of $2.69^{+0.11}_{-0.11}$ for NGC 1277 and $2.27^{+0.16}_{-0.18}$ for IC 843.

The magnitude of the [Na/Fe] enhancement in both objects is large, but it should also be noted that the spectral response to increases in [Na/Fe] between the CvD12 and E-MILES models is markedly different (as shown in Figure 2.10). This implies that the magnitude of the super-solar [Na/Fe] abundance is likely to be model dependent.

Table 2.4: Stellar population parameters for NGC 1277 and IC 843, derived from spectral fitting. The stellar age and [α/Fe] abundance (italicised) were derived from optical index measurements from Ferré-Mateu et al. (2017) (for NGC 1277) and Price et al. (2011) (for IC 843) and kept fixed during the fit. Errors are a combination of photon errors, marginalisation over changes in the fixed parameters, inclusion of further element variations, small changes in the multiplicative polynomial order and the removal of the 7600-8050 region of the spectrum. (see Section 2.6.1).

Parameter	NGC 1277	IC 843	Prior
Age (Gyr)	13^{+1}_{-3}	10 ± 3	—
[α/Fe]	0.3 ± 0.1	0.3 ± 0.1	—
σ (kms^{-1})	377^{+8}_{-8}	287^{+8}_{-7}	[0, 1000]
[Na/Fe]	$0.71^{+0.30}_{-0.26}$	$0.49^{+0.17}_{-0.17}$	[-0.3, 0.9]
[Fe/H]	$0.02^{+0.07}_{-0.07}$	$-0.10^{+0.06}_{-0.06}$	[-0.3, 0.3]
[Ca/Fe]	$-0.18^{+0.05}_{-0.04}$	$-0.20^{+0.02}_{-0.02}$	[-0.3, 0.3]
[Ti/Fe]	$-0.22^{+0.18}_{-0.17}$	$-0.02^{+0.23}_{-0.22}$	[-0.3, 0.3]
[O/Fe]	$0.001^{+0.002}_{-0.002}$	$0.00^{+0.01}_{-0.00}$	[0.0, 0.3]
IMF slope	$2.69^{+0.11}_{-0.11}$	$2.27^{+0.16}_{-0.18}$	[0.0, 3.5]

2.6.2 Index Fitting

In order to directly compare to Zieleniewski et al. (2017), we also use just the global FeH and NaI index measurements of NGC 1277 and IC 843 to make quantitative IMF statements. By interpolating the predicted FeH equivalent widths from the CvD12 and E-MILES models and comparing to our global FeH measurement, we measure global IMF slopes in each object. Appendix A.2 discusses the precise calculations in detail. We assume the same population parameters as in Section 2.6.1, as well as including the effect of the non-solar abundances found from the spectral fitting for each galaxy (see Table 2.4).

In contrast to the CvD12 models, the E-MILES models allow variation in the total metallicity, [Z/H]. Using index measurements from the same sources as before (Ferré-Mateu et al. 2017 for NGC 1277, Price et al. 2011 for IC 843), we assume a total metallicity of +0.16 dex for NGC 1277 and +0.0 dex for IC 843 in our global spectra.

To measure the effect of uncertainty in the assumed stellar population parameters for each galaxy, we modelled each parameter as a normal distribution centred on the values described above. The width of these distributions are 0.1 dex for [Z/H] and [α/Fe] and 3 Gyr for stellar age. For [Na/Fe] and [Fe/H], we use the values and errors from Table 2.4. We drew 1000 random samples from the distribution of each parameter, then recalculated the IMF slope in each case. The 16th and 84th percentiles of these samples are plotted as the blue shaded regions in Figure 2.13.

Results from this second IMF determination method show a nice agreement between the E-MILES and CvD12 stellar population models. In IC 843, the index fitting results are best fit with single power-law IMF slopes heavier than Salpeter: $x_{\mathrm{CvD}} = 2.57^{+0.30}_{-0.41}$, whilst $x_{\mathrm{E-MILES}} = 2.72 \pm 0.25$. However, the spectral fitting leads to an IMF slope shallower than Salpeter: $x_{\mathrm{SF}} = 2.27^{+0.16}_{-0.18}$ (although the results are

consistent within the error bars). For NGC 1277, the three methods agree well: $x_{\rm CvD} = 2.59^{+0.25}_{-0.48}$, $x_{\rm E-MILES} = 2.77 \pm 0.31$ and $x_{\rm SF} = 2.69^{+0.11}_{-0.11}$

Figure 2.13 shows the derived single-power law IMF slope for IC 843 and NGC 1277, plotted against their central velocity dispersion. Diamonds show the IMF slopes derived using the CvD12 stellar population models, whilst triangles show those found using the E-MILES models. Results from spectral fitting are shown as circles. Also shown are measurements from Zieleniewski et al. (2017), as well as the proposed correlations between unimodal IMF slope and σ_0 from Ferreras et al. (2013), La Barbera et al. (2013) and Spiniello et al. (2014).

Note that using values of [Na/Fe] and [Fe/H] derived by fitting the CvD12 models as corrections to the E-MILES models is not strictly correct, due to the differences in the way the models are constructed and their differing responses to changes in abundance patterns. As a first approximation, however, we have shown that doing so gives consistent results. The ideal solution would be to conduct full spectral fitting with both sets of stellar population models, and future work will investigate this further.

2.6.3 M/L values

Using these global IMF measurements, we derive V-band stellar mass-to-light values for these galaxies (in units of $\rm M_\odot/L_\odot$) . For NGC 1277, we find $(M/L)_V = 10.7^{+2.0}_{-1.4}$ from the spectral fitting, $(M/L)_V = 9.5^{+3.1}_{-2.0}$ from the CvD12 index fitting, and $(M/L)_V = 11.2^{+5.9}_{-3.3}$ for the E-MILES index fitting. For IC 843, we find $(M/L)_V = 5.1^{+0.8}_{-0.6}$ from spectral fitting, $(M/L)_V$=$7.3^{+3.4}_{-1.9}$ using CvD12 and $(M/L)_V$=$9.1^{+5.4}_{-2.9}$ using E-MILES. Combining these measurements, weighted by the inverse of their variances, gives $(M/L)_V = 10.4 \pm 1.51$ in NGC 1277 and 5.9 ± 1.72 in IC 843.

Using adaptive optics spectroscopy, Walsh et al. (2016) find $(M/L)_V = 9.3 \pm 1.6$ in the very centre of NGC 1277, whilst seeing limited observations out to $\sim 3R_e$ by

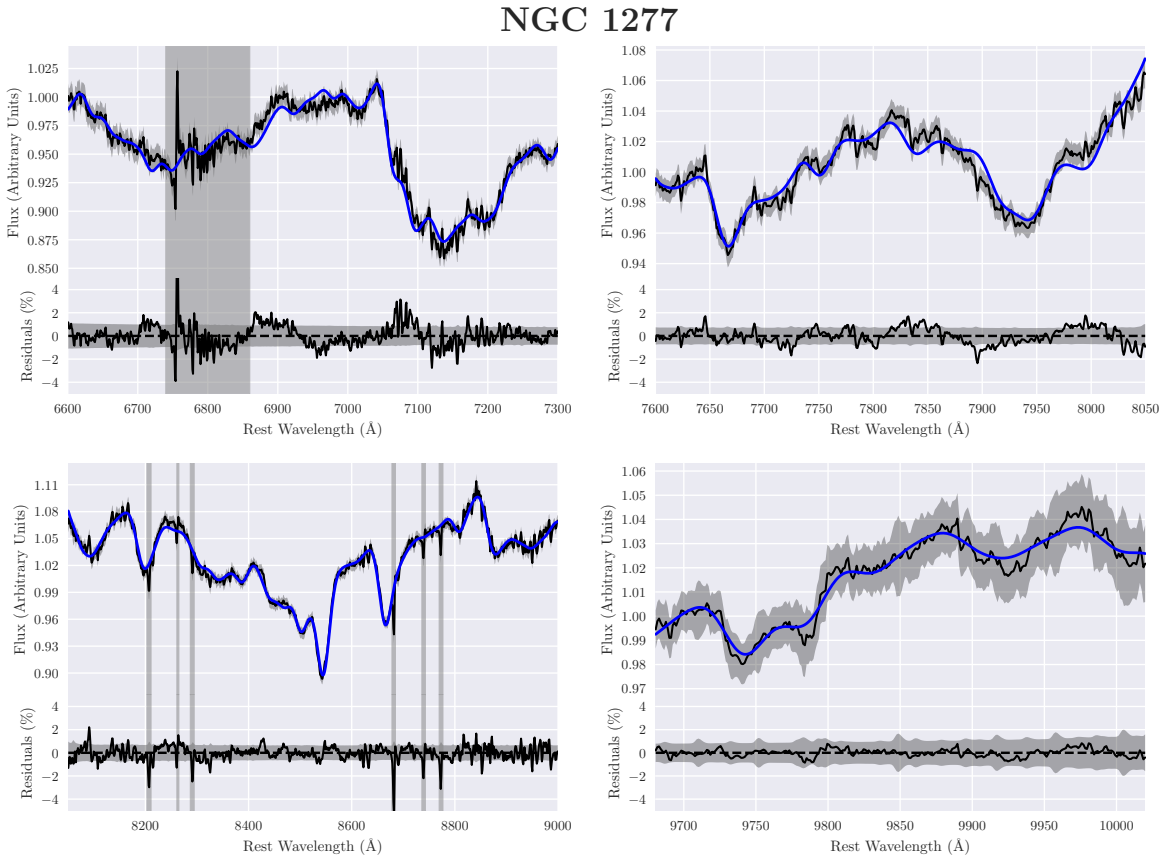

Figure 2.11: Fit to the global spectrum of NGC 1277. Within each panel, the upper plot show the data and best-fitting template whilst the lower plot shows the residuals between the data and the fit. Grey shaded regions show the noise level of the data.

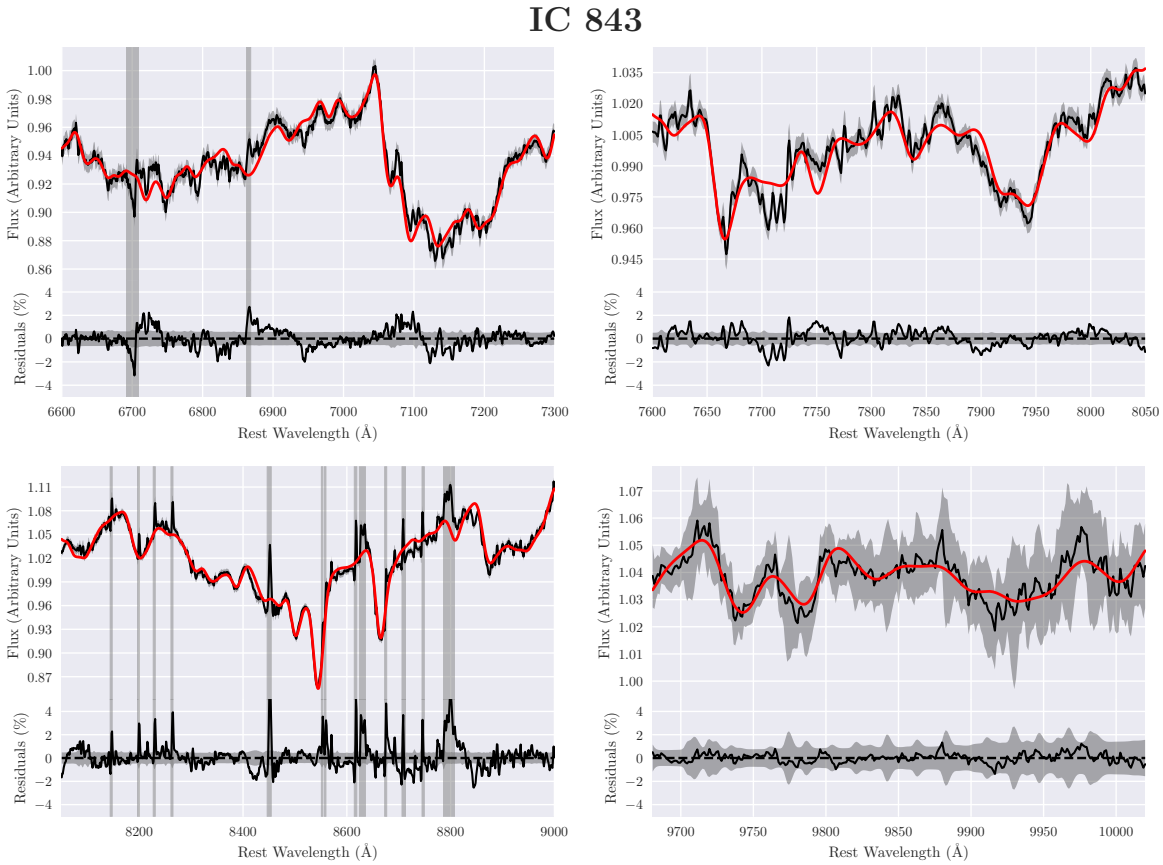

Figure 2.12: Fit to the global spectrum of IC 843: see the caption of Figure 2.11 for details.

Yıldırım et al. (2015) find $(M/L)_V = 6.5 \pm 1.5$, under the assumption of a constant stellar (M/L) with radius.

MN15 infer the V-band stellar $(M/L)_V$ ratio in NGC 1277 to be 7.5 at 1.4 R_e, rising to 11.6 in the centre, from their analysis of IMF-sensitive absorption features and the assumption of a bimodal IMF. Whilst we are unable to make such a resolved $(M/L)_V$ measurement with our data, these values are generally in agreement with our integrated measurement (which extends out to just over 2.2 R_e).

In IC 843, Thomas et al. (2007) make a dynamical measurement of the (M/L) in the R_c band, with observations extending to further than $3R_e$. They find $(M/L)_{R_c}$=10.0, as well as concluding that mass follows light in this object. Our inferred IMFs (from an integrated spectrum out to 0.65 R_e), combined with published age and metallicity measurements, lead to a final value of $(M/L)_{R_c} = 5.04 \pm 2.26$[1]. This is lower than the value from Thomas et al., despite the fact that the dynamics in this object were fit without a dark matter halo term (i.e with mass following light). This may be evidence, therefore, for a dark matter profile which closely follows the visible matter in this object.

2.7 Discussion

The main result of this work is the strong gradient in NaI0.82 absorption combined with flat profiles for FeH0.99 in both objects. The equivalent widths of FeH in both galaxies also scatter around a similar value: 0.4 Å at a velocity dispersion of 200kms^{-1}. However, whilst the FeH index values are similar between the galaxies, the measured global IMF from full spectral fitting is significantly different: $x = 2.69^{+0.11}_{-0.11}$ for NGC 1277 and $x = 2.27^{+0.16}_{-0.18}$ for IC 843.

This may imply that relying on the Wing-Ford band alone to determine the single-

[1]Found by combining the values $(M/L)_{R_c} = 4.2^{+0.6}_{-0.5}$ from spectral fitting, $8.09^{+4.1}_{-2.3}$ using the E-MILES models and $6.0^{+2.8}_{-1.6}$ using the CvD12 models

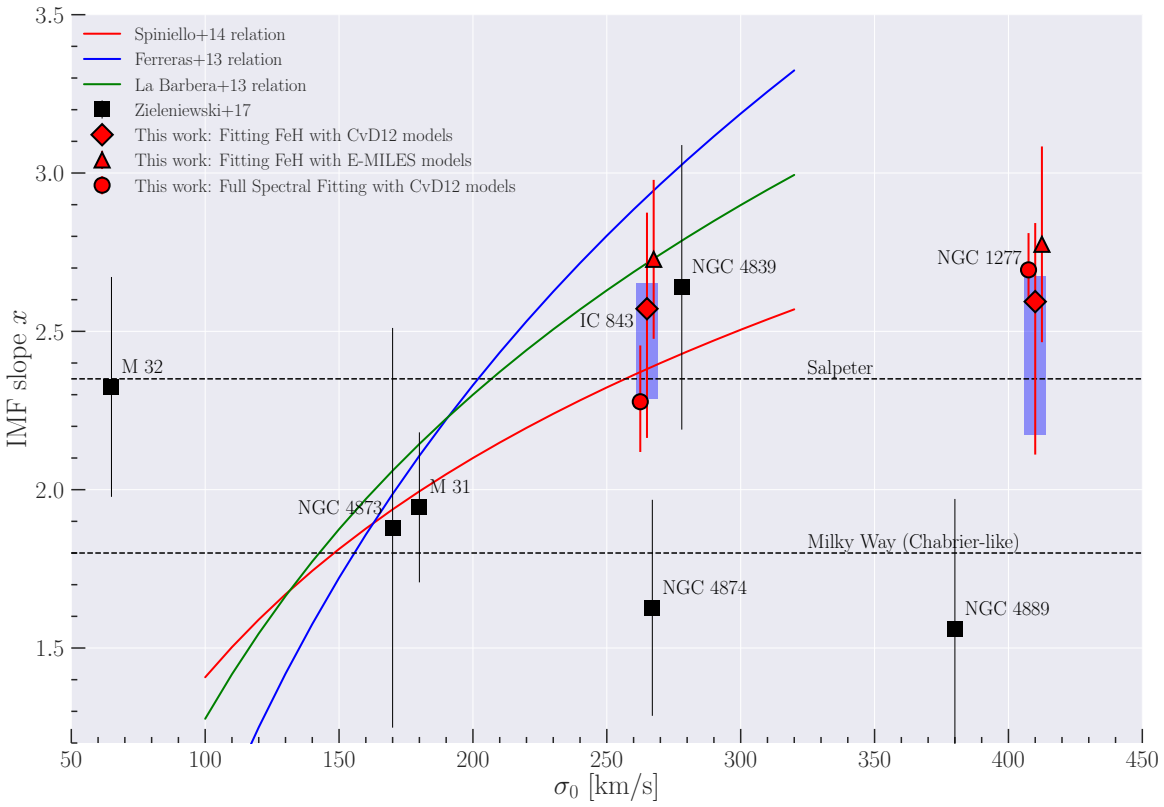

Figure 2.13: Derived IMF slope for both galaxies studied in this work, plotted against their central velocity dispersion. Discussion of the IMF slope calculation is presented in Sections 2.6.1 and 2.6.2, as well as Appendix A.2. Circles denote the values determined from spectral fitting with the CvD12 models. Diamonds correspond to the values derived by fitting the FeH index with the CvD12 stellar population models and triangles denote the values found using the E-MILES models (which are slightly offset in the x direction), following Zieleniewski et al. (2017). See section 2.6 for details. The blue shaded regions show the effect of uncertainties in the stellar population parameters assumed for each galaxy in the index fitting. They are derived by assigning a normal distribution to each parameter (centred on the appropriate values and of width 0.1 dex for [Z/H], [Fe/H], [Na/H] and [α/Fe], 1 Gyr for age), then drawing 1000 samples and calculating the IMF for each one. The blue regions denote the 16th and 84th percentiles of these samples. Red error bars combine measurement errors with stellar population uncertainties. A similarly sized uncertainty in the population parameters also applies to the E-MILES model points, but is not shown for clarity. Coloured lines show proposed unimodal IMF-σ_0 correlations from Ferreras et al. (2013), La Barbera et al. (2013) and Spiniello et al. (2014), whilst black squares are values from Zieleniewski et al. (2017). Note that measurements from Zieleniewski et al. (2017) utilise the CvD12 models only, and that this work implements an improved handling of response functions to correct for non-solar abundances.

power law IMF slope in an object could lead to different results than when utilising information from a number of gravity sensitive indices at once. However, regardless of the method used to infer the low-mass IMF slope in these objects, both these galaxies show evidence for an IMF significantly different from the IMF in the Milky Way, in agreement with previous work finding evidence for a non-universal IMF in massive early-type galaxies.

Recent work has called into question the efficacy of the Wing-Ford band as a reliable IMF indicator. Using a two-part power law to characterise the low-mass IMF, van Dokkum et al. (2017) show that the FeH equivalent width does not correlate with the IMF "mismatch" parameter, α, in their study, with some of the weakest FeH index measurements in galaxies with very bottom heavy IMFs. Furthermore, La Barbera et al. (2016) show that unimodal IMF determinations from the Wing-Ford band are in tension with unimodal IMF measurements from optical IMF sensitive indices (and use this fact to constrain the shape of the IMF in this galaxy).

2.7.1 Resolved IMF inferences

With the wavelength range used in this work, we are unable to reliably constrain some of the important stellar population parameters necessary to infer quantitative *radial* IMF measurements and disentangle the effects of IMF variation from abundance gradients. Here, however, we present a qualitative discussion of the radial trends implied by our measurements. We find that IMF gradients by themselves, with no variations in the abundances of [Na/Fe] or [Fe/H], are only marginally consistent with our radial FeH and NaI index measurements. Plausible gradients in these elemental abundances, combined with a radially constant IMF, are more consistent with the data from NGC 1277 and IC 843.

Figure 2.14 motivates this conclusion. We have produced mock spectra from the CvD12 models with varying values of [Na/Fe], [Fe/H] and low-mass IMF slope, x,

all convolved to 200kms^{-1}. We measure the FeH and NaI indices from these spectra and compare to our index measurements. The top row of Figure 2.14 shows the IMF slope for each mock spectrum. The second row shows the assumed [Na/Fe] and [Fe/H] abundances. Rows 3 and 4 shows the NaI and FeH indices from the mock spectra, as well as our measurements from NGC 1277 and IC 843. Each panel is plotted against radial position.

In the left two columns, we vary the IMF slope as a function of radius and fix the values of [Na/Fe] and [Fe/H] to those found from spectral fitting in each galaxy. The right two columns show a fixed IMF slope (again, fixed to the values measured using spectral fitting) and vary the abundances of [Na/Fe] and [Fe/H]. In all cases, we assume a constant age of 13 Gyr for NGC 1277 and 10 Gyr for IC 843, as well as an [α/Fe] abundance of +0.25 dex for both galaxies.

We note that this is not a fit to the data; we do not attempt to minimise a χ^2-like function, or infer quantitative values of abundance gradients from this process. We simply vary the assumed IMF and abundance values to best recover the observed measurements. We also note that this exercise is vastly simplified, since we are fixing the values of stellar age, metallicity and [α/Fe] to be held constant, although adding in further complexity would only further increase the degeneracies noted here.

When fixing the chemical abundances and varying the IMF as a function of radius, our mock spectra tend to under predict the NaI index whilst over-predicting FeH in the centre of both galaxies, although both are still consistent at the edge of the error bars. On the other hand, a flat IMF with plausible abundance gradients seems to better match the data, with the very central value of NaI in NGC 1277 the only place where the model and measurements are marginally in tension. Whilst the absolute values of the [Na/Fe] abundance needed to match the NaI measurements in NGC 1277 are very large, we note that the overall gradient of Δ[Na/Fe]=~ -0.3 dex per decade in $\log(R/R_e)$ is plausible (e.g. Alton et al., 2017). We also note there is a different

response to [Na/Fe] overabundances in the CvD12 and E-MILES models, implying that the absolute values of [Na/Fe] abundance needed to match these measurements is likely to be model dependent.

Gradients in [Na/Fe] within individual galaxies have been recently been measured in the context of IMF variations. van Dokkum et al. (2017) used long-slit spectroscopy and full-spectral fitting to measure abundance gradients in six nearby ETGs as well as gradients in the IMF. Furthermore, Alton et al. (2017) also measure a gradient in [Na/Fe] in a stack of 8 nearby ETGs, finding Δ[Na/Fe]=-0.35 dex per decade in $\log(R/R_e)$. Similar abundance gradients were measured for those individual galaxies in the stack with high enough quality data. Interestingly, unlike van Dokkum et al. (2017), they find no evidence for IMF gradients in their data, with the IMF in their stacked spectrum being uniformly Salpeter throughout.

Super solar [Na/Fe] abundance ratios are also not uncommon in massive ETGs. Jeong et al. (2013) find excess NaD line strengths in $\sim$8% of low redshift ($z < 0.08$) SDSS DR7 galaxies, including in ETGs without visible dust lanes, and conclude that [Na/Fe] enhancement, rather than ISM or IMF effects, are the cause. Furthermore, both Worthey et al. (2014) and Conroy et al. (2014) find a trend of increasing [Na/Fe] abundance in galaxies with larger velocity dispersions, of up to ~ 0.4 dex in galaxies with σ=300kms^{-1}, using independent SPS models.

Abundance gradients and IMF gradients are not mutually exclusive, of course, and it is very plausible that a mixture of both exist in NGC 1277 and IC 843. These quantities are notoriously difficult to disentangle, and we would require coverage of a greater number of gravity sensitive absorption features to break the degeneracy and make quantitative statements in these objects.

A key assumption in this work is that the low-mass IMF slope in these objects is a single power law below $M_\odot$. A further explanation of our measurements could be that the IMF varies radially but does not have such a shape. In the "bimodal"

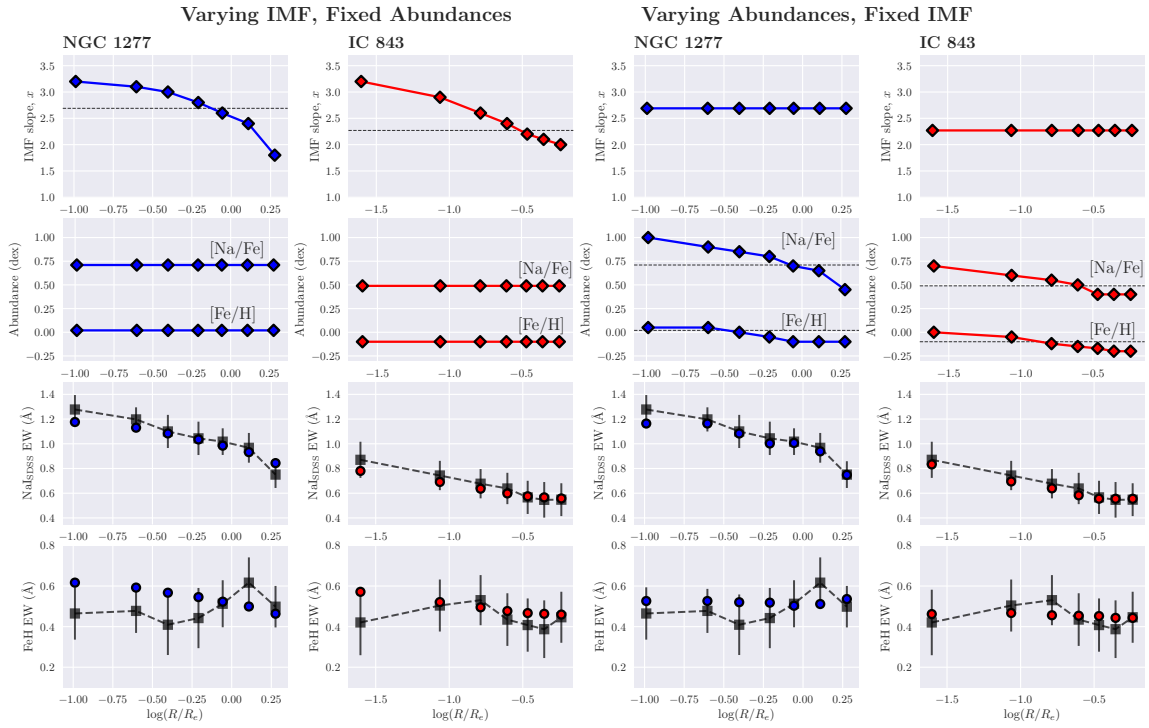

Figure 2.14: A comparison of our index measurements as a function of radius to the CvD12 models. We create model spectra to correspond to the seven radial index measurements we make in each galaxy. Each model spectrum is convolved to 200kms^{-1}, in order to match the index measurements. We assume a constant age and [α/Fe] for each spectrum, then impose either a radially varying IMF and fixed abundance patterns in [Na/Fe] and [Fe/H] (left two columns) or a radially constant IMF combined with abundance gradients (right two columns). Dotted lines show the abundance values and IMF slope found from full spectral fitting in each galaxy. The third and fourth rows show both our measurements (black squares) and these model index measurements (coloured circles) for the NaI and FeH indices. Note that this is not a fit to these data, and we do not aim to draw quantitative conclusions about these abundance or IMF gradients. We find that a radially constant IMF is marginally consistent with our measurements, whilst radial gradients in [Na/Fe] and [Fe/H] are more consistent with the data. It is likely that a combination of IMF and abundance gradients exist in NGC 1277 and IC 843, although we are unable to break this degeneracy and quantify their magnitudes.

parameterisation of Vazdekis et al. (1996), the IMF is flat at masses below 0.2 $M_\odot$ whilst the high mass slope (above 0.6 $M_\odot$) varies. The region in between is connected by spline interpolation. Such an IMF shape introduces a degeneracy between the FeH and NaI indices, by decoupling the very low-mass end of the IMF (where FeH is most sensitive) from the region between $0.2M_\odot < M < 0.6M_\odot$ (where NaI is most sensitive). Qualitatively, this allows a change in NaI strength without the corresponding change in FeH. La Barbera et al. (2016) use this form of the IMF in their study of a nearby massive ETG, finding radially constant measurements of FeH as well as a bimodal IMF gradient. MN15 also use this bimodal IMF parameterisation in their study of NGC 1277. They found evidence for a bottom heavy bimodal IMF of $\Gamma_b = 3$ out to 0.3 R_e, which decreases and flattens off to $\Gamma_b = 2.5$ between 0.8 R_e and 1.4 R_e.

Furthermore, Conroy & van Dokkum (2012b) and van Dokkum et al. (2017) also use a parameterisation of the IMF which is not a single power law. Their IMF is fixed at high masses (above 1 $M_\odot$) and is a two part power law below, with a break at 0.5 $M_\odot$. This form of the low-mass IMF would again allow the NaI and FeH indices to vary independently of each other too, and could explain their behaviour in NGC 1277 and IC 843. Under this form of the IMF, van Dokkum et al. (2017) explicitly show that a lack of gradient in FeH does not imply a radially constant IMF.

With the data available to us, we are unable to rule out the possibility that our spatially resolved NaI and FeH measurements are caused by chemical abundance gradients, radial IMF gradients, or a combination of the two. A wavelength range covering further spectral indices, such as the Na D index and various optical Fe lines, in conjunction with the publicly available state of the art stellar population models, would allow us to make a clearer separation of the effects of the low-mass IMF from abundance gradients.

2.7.2 Other radial studies of FeH and NaI indices

Similar measurements to ours have been found by other authors who have investigated both NaI and FeH indices as a function of radius in a variety of objects. As mentioned previously, Alton et al. (2017) find a strong gradient in NaI and radially flat FeH in a stack of 8 massive ETGs. They find uniform, typically bottom heavy, IMFs in their stack and most of their individual galaxies, with radial changes in index strengths primarily accounted for by abundance gradients. Zieleniewski et al. (2015) studied the central bulge of M31, observing a large decrease in NaI combined with no radial change in FeH, and conclude in favour of a gradient in [Na/Fe] rather than the IMF. Furthermore, Zieleniewski et al. (2017) studied the brightest cluster galaxies (BCGs) in the Coma cluster, measuring a strong gradient in NaI combined with flat FeH profile in the massive ETG NGC 4889, which has a central velocity dispersion of nearly 400kms^{-1}. Other objects in the sample also show weak FeH absorption. Only NGC 4839 displays evidence for a deep Wing-Ford band, although large systematic uncertainty due to residual sky emission prevents the authors from drawing strong conclusions about its stellar population.

McConnell et al. (2016) obtained deep long-slit data on two nearby ETGs, both of which had been part of the Conroy & van Dokkum (2012b) sample. They found strong gradients in NaI but a much weaker decline in FeH, as well as opposite behaviour in NaI/⟨Fe⟩ and FeH/⟨Fe⟩. Again, the authors conclude in favour of a variation in [Na/Fe] over the central ∼300 pc of each galaxy instead of variation in a single power law IMF driving the strong decline in NaI. The authors also argue that the flat FeH profile implies a fixed low-mass slope of the IMF below M $\lesssim 0.4 M_{\odot}$.

Finally, La Barbera et al. (2016, 2017) make resolved measurements of the Wing-Ford band and a number of Na indices to constrain the shape of the low-mass IMF in a nearby ETG. They too find a lack of radial variation in FeH combined with negative

gradients in NaI, NaD and two further Na lines at 1.14 and 2.21 μm, from which they find a gradient in a bimodal IMF combined with a radial change in [Na/Fe].

2.8 Conclusions

We have used the Oxford SWIFT instrument to undertake a study of two low redshift early-type galaxies in order to make resolved measurements IMF sensitive indices in their spectra. We obtained high S/N integral field data of NGC 1277, a fast rotator in the Perseus cluster with a very high central velocity dispersion, and IC 843, also a fast rotator, located in the Coma cluster. Our measurements extend radially to 7.7″ and 6.2″ respectively, corresponding to 2.2 and 0.65 R_e. The SWIFT wavelength coverage, from 6300 Å to 10412 Å, allows resolved measurement of the NaI doublet, CaII triplet, TiO, MgI and FeH spectral features. We conclude:

1. NGC 1277 shows a strong negative gradient in NaI, more marginal negative TiO and CaT gradients and a flat FeH profile. The FeH equivalent widths scatter around 0.42 Å at all radii (corrected to 200kms^{-1}).

2. IC 843 is similar, if less extreme, than NGC 1277. It displays a weaker NaI and TiO gradients, and flat profiles in FeH, CaT and MgI. FeH equivalent widths are a similar strength to NGC 1277, also around 0.4 Å.

3. Similarly to McConnell et al. (2016), Zieleniewski et al. (2017), Alton et al. (2017) and others, we find very different radial trends between the IMF sensitive indices NaI and FeH.

4. In both NGC 1277 and IC 843, our measurements can be explained by a radially constant single power law IMF combined with appropriate abundance gradients. However, a radial gradient in the IMF may also reproduce our results, and our data do not allow us to break this degeneracy, as shown in Figure

2.14. Furthermore, with the spectral range available from SWIFT, gradients in more complicated IMF parameterisations (such as a bimodal or multi-segment IMF) also cannot be excluded. A wavelength range covering absorption indices sensitive to stellar population parameters such as age, [Z/H] and [α/Fe], as well as indices sensitive to elemental abundances (such as NaD and the combination of Fe5250 and Fe5335) are vital to isolate the effects of the IMF.

5. We use our global spectra and state-of-the-art stellar population models to infer global single power-law IMFs in each object. We determine the IMF in each object using three techniques: full spectral fitting using the CvD12 models, as well as fitting the FeH index with corrections for non-solar abundance patterns using the CvD12 and E-MILES models (following Zieleniewski et al., 2017). We find that a super Salpeter slope fits best in NGC 1277, with each technique in agreement. IC 843 is more uncertain, with the spectral fitting consistent with a Salpeter IMF and the index fitting scattering higher.

6. Despite NGC 1277 and IC 843 having only a $\lesssim$ 10% difference in global FeH measurement, and similar population parameters, we find significantly different global IMF slopes when we include further spectral information from between 6600Å and 10,000Å. This may bring into doubt the use of Wing-Ford band to infer an IMF slope when not combined with information from other areas of the spectrum.

7. Our inferred V band stellar mass-to-light ratios are in agreement with published dynamical and spectroscopic determinations. In IC 843, we find a mass-to-light ratio (R_c band) smaller than the dynamical (M/L) from Thomas et al. (2007), despite their conclusion that the dynamics can be fit without a dark matter halo term (i.e that mass follows light). This may imply a non-standard dark matter profile in this object.

3 | The IMF in NGC 1399

The work in this chapter has been published in Vaughan et al. (2018b)

3.1 Motivations

In Chapter 2, we made radial measurements of gravity sensitive absorption features in the spectra of two massive ETGs. One drawback of that work, however, was the limited spectral coverage of the SWIFT instrument; from $\sim$ 6000Å to just beyond 1.04μm. This starting wavelength towards the red end of the visible spectrum means that we were unable to make resolved measurements of many of the classic "Lick" indices (e.g. Hβ, Mgb, <Fe>; Worthey et al., 1994) which are crucial for constraining the stellar age, metallicity and [α/Fe] abundances in a population. Because of this, we were unable to make *quantitative* spatially resolved measurements of the IMF in NGC 1277 or IC 843, instead having to settle for measurements of the IMF in a single, integrated spectrum. In this chapter, we overcome this difficulty by switching instruments to a different IFU. We use the Multi Unit Spectroscopic Explorer (MUSE; Bacon et al., 2010) at the Very Large Telescope, which observes between 4800Å and 9800Å.

The object of study in this chapter NGC 1399, the largest ETG in the Fornax

Cluster. As one the largest nearby massive galaxies, NGC 1399 is well studied in the literature. It has the core-like surface brightness profile characteristic of a supergiant elliptical (Schombert, 1986; Spavone et al., 2017), hosts two jets of radio emission and a pair of X-ray cavities (Killeen et al., 1988; Shurkin et al., 2008; Su et al., 2017) and has a been the subject of a number of dynamical studies in the optical (e.g. Bicknell et al., 1989; Franx et al., 1989; Longo et al., 1994; Graham et al., 1998; Saglia et al., 2000; Gebhardt et al., 2007) and the near infrared (Houghton et al., 2006; Lyubenova et al., 2008).

We use full spectral fitting with the SPS library of Conroy et al. (2018) to determine the low-mass IMF slope, as well as a number of other stellar population parameters, as a function of radius in this galaxy. These models are updated with respect to those used in Chapter 2. In Section 3.2 we present our observations and discuss how the data were reduced. In Section 3.3 we describe our methodology, and present results in 3.4. Our discussion is in Section 3.5, and we draw our conclusions in 3.6.

It should be noted that the Conroy et al. (2018) templates have a different IMF *shape* than those used in Chapter 2. The IMF in these models is parameterised to be a three part power law as follows:

$$\xi(m) = \begin{cases} C_1 m^{-x_1} \text{ for } 0.08\text{M}_\odot \leq m < 0.5\text{M}_\odot \\ C_2 m^{-x_2} \text{ for } 0.5\text{M}_\odot \leq m < 1\text{M}_\odot \\ C_3 m^{-x_3} \text{ for } m \geq 1\text{M}_\odot \end{cases} \tag{3.1}$$

The normalising constants C_i are chosen to ensure the IMF is continuous at each m. In all subsequent analysis, we fix the high-mass slope x_3 to be 2.3. We use the phrase "Milky Way IMF" to refer to the IMF from Kroupa (2002), which has $x_3 = x_2 = 2.3$ and x_1=1.3.

We assume a Planck cosmology of $H_0 = 67.8$ kms^{-1}Mpc^{-1} and $\Omega_\text{m} = 0.308$

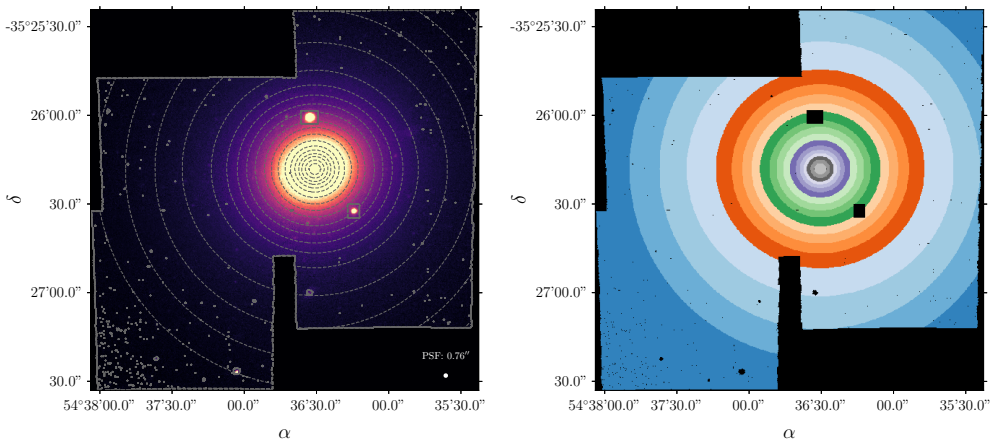

Figure 3.1: The centre of NGC 1399, divided into eighteen annular bins. The annuli extend to 1.3 times the effective radius. Black regions show the locations of missing data, as well as foreground stars and globular clusters which have been masked.

(Planck Collaboration et al., 2016) to give the luminosity distance of NGC 1399 as 21.1 Mpc.

3.2 Observations and Data Reduction

NGC 1399 was observed on the 2nd and 14th of October 2014 with the Multi Unit Spectroscopic Explorer (MUSE) at the European Southern Observatory (ESO), Paranal, for programme 094.B-0903(A) (PI; Zieleniewski). MUSE combines 24 individual Integral Field Units (IFUs) to give a 1×1 arcminute field-of-view with $0.2'' \times 0.2''$ spatial sampling. The wavelength coverage extends from 4750 to 9300 Å.

In order to characterise the instrumental resolution of MUSE observations as a function of wavelength, we fit gaussians to a number of isolated night-sky emission lines present in a sky frame observation. Our results are presented in Figure 3.2, showing good agreement with other characterisations of the MUSE line-spread function from Mentz et al. (2016) and Krajnović et al. (2015). We note that the instrumental resolution is negligible compared to the stellar velocity dispersion in all radial bins of

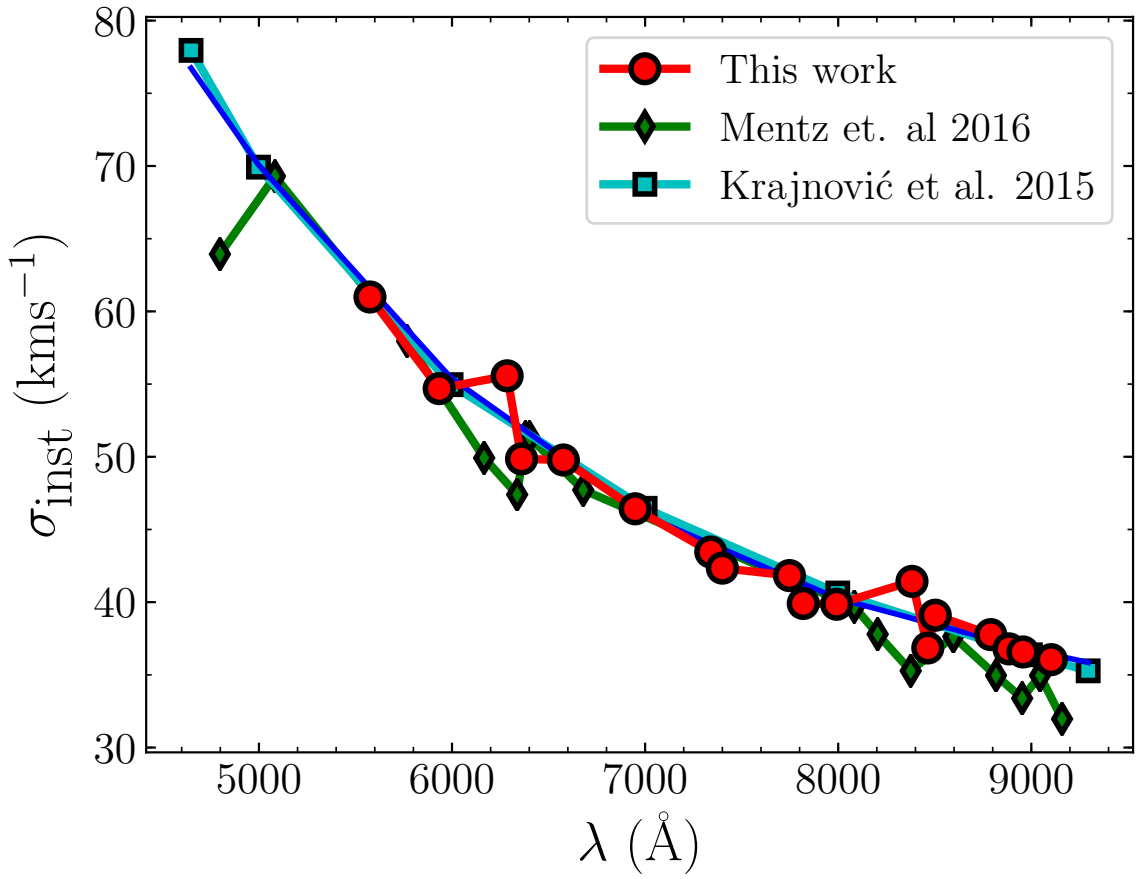

Figure 3.2: MUSE instrumental resolution against wavelength for our data, measured from observations of night sky emission lines, in excellent agreement with measurements from Mentz et al. (2016) and Krajnović et al. (2015). The blue curve shows a third order polynomial fit to our measurements.

NGC 1399, but is an important consideration when measuring the gas velocity dispersion in Section 3.4.2. We use our measurements to create emission line templates which closely match the MUSE line-spread function, having an intrinsic width which varies as a function of the emission line central wavelength. This implies that the best-fit dispersion found from `pPXF` is the true dispersion of the gas, rather than a combination of the gas dispersion and the instrument line-spread function.

The galaxy was observed with 5 exposures, each lasting 900 seconds. Four observations were arranged to give a simple mosaic of roughly 2 × 2 arcminutes square, with the final pointing centred on the middle of the galaxy. Night sky observations,

of the same integration time and offset in declination by 5′, were taken regularly throughout the run to be used as first order sky subtraction.

The data were reduced with the standard MUSE pipeline (version 1.2.1) and ESOREX software (version 3.12) to perform bias and dark current subtraction, flat field division and wavelength calibration. The final cube was corrected for small illumination variations using observations of the twilight sky.[1]

The white dwarf CD-30 17706 was observed for the purposes of flux calibration and telluric correction. The most important area of telluric contamination of our spectra is around the NaI absorption line at $\lambda_{\rm rest} = 8190\,$Å, since the negligible redshift of NGC 1399 places it is in the middle of the telluric absorption region between 8125 and 8346 Å. We carefully scaled the full telluric spectrum to ensure a good removal around this line, and propagated the errors from this process to the final error spectrum for each annulus. After this process, some residual contamination remained between 7160-7330 and 7590-7704 Å, but since they did not fall near any important spectral features we chose to simply mask these regions from future analysis.

As in Chapter 2, subtraction of night-sky emission lines is a crucial step in our analysis. We describe in detail our procedure in Section 3.3.4.

3.3 Analysis

3.3.1 Annular bins

We bin the datacube into eighteen concentric annuli, masking out two bright objects. NGC 1399 also hosts an extensive globular cluster system (e.g. Dirsch et al., 2003; Schuberth et al., 2010), which may contribute non-negligible amounts of flux to the outer bins. To account for these, we subtract a two component Sérsic fit to the light profile of the galaxy and mask any bright residuals before extracting and combining

[1]These steps were performed by Simon Zieleniewski

the individual spectra. An image of the collapsed datacube, the annuli and the pixels which have been masked is shown in Figure 3.1.

A number of recent studies have found a spatial variation in the low-mass IMF between the galaxy centre and one effective radius (R_e), the major axis length of an elliptical aperture which encloses half the galaxy light. NGC 1399, being a cD galaxy (Rusli et al., 2013), resides in a large, extended stellar halo, and its light profile is most often fit with an inner Sérsic profile and one or more outer components (e.g. recently Iodice et al., 2016; Saglia et al., 2016; Spavone et al., 2017). In order to compare to a number of other galaxies with resolved IMF measurements (which are not type cD ellipticals), we use the effective radius of the Sérsic component in our subsequent analysis. This has been measured to be 40″ (de Vaucouleurs et al., 1991; de Carvalho & da Costa, 1988), meaning that our bins extend to $1.3\,R_e$.

Formally, the annular bins each have a signal-to-noise (SN) ratio of well over 1500. However, similarly to the MUSE study of M87 in Sarzi et al. (2018), we find that variation in the residuals around the best fitting template are much greater than one would expect from such a high SN, implying that the true SN ratio of each spectrum is well below this value. S18 attribute this discrepancy to correlations between adjacent pixels introduced during the MUSE data reduction progress, or small instrumental variations between MUSE's 24 integral field units. To account for this under-estimation of the true error in each pixel, we include a parameter in the spectral fitting process to inflate the error-bars appropriately (see Section 3.3.2). The true SN of each spectrum, as found from the ratio of the flux in each spectrum to these rescaled error bars, is shown in Figure 3.3.

3.3.2 Stellar Population Synthesis Models

In order to make inferences about the stellar population in NGC 1399, we fit stellar population synthesis (SPS) models to the spectra in each of the eighteen annular bins.

We use the stellar template library of Conroy et al. (2018), which model variation in the low-mass IMF, stellar age from 1-13.5 Gyr and metallicity from -1.5 to +0.2 dex across the optical to NIR wavelength range (0.37 – 2.4μm). Variation in the individual abundances of 19 elements are also modelled.

The models use the MIST stellar isochrones (Choi et al., 2016; Dotter, 2016) and stellar spectra from the MILES (Sánchez-Blázquez et al., 2006; Falcón-Barroso et al., 2011) and Extended-IRTF (Villaume et al., 2017) libraries. These library stars are interpolated in the parameters $T_{\rm eff}$, $\log g$ and metallicity in order to provide empirical spectra for each point on the appropriate isochrone. A review of stellar population synthesis techniques can be found in Conroy (2013).

A key ingredient in the SPS process is the assumed IMF. For these models, the IMF above 1 $\rm M_{\odot}$ is a power law fixed at the Salpeter value, $x = 2.3$ (Salpeter, 1955). Below this mass, the power law is broken into two components: the slope between 0.08 $\rm M_{\odot} < x <$ 0.5 $\rm M_{\odot}$ and the slope between 0.5 $\rm M_{\odot} < x <$ 1.0 $\rm M_{\odot}$ (as described in equation 3.1). These IMF slopes, x_1 and x_2 respectively, can vary independently and take values between 0.5 and 3.5.

Variations in individual elemental abundances are handled by using response functions (RFs) to correct the base model at a given age, metallicity and IMF. These RFs are based on theoretical stellar atmosphere calculations which include a comprehensive set of molecular and atomic transitions. RFs are available for spectra with abundance variations between -0.3 and +0.3 dex for a variety of common elements, with enhanced [Na/H] abundances available up to +1.0 dex. These RFs assume a form of the IMF, since varying the IMF and self-consistently computing an elemental RF is, at present, computationally infeasible. All analysis in this work uses RFs which assume a Kroupa low-mass IMF (i.e $x_1 = 1.3; x_2 = x_3 = 2.3$ in equation 3.1), although our conclusions are unchanged if, instead, we use the RFs which assume a Salpeter low-mass IMF ($x_1 = x_2 = x_3 = 2.3$).

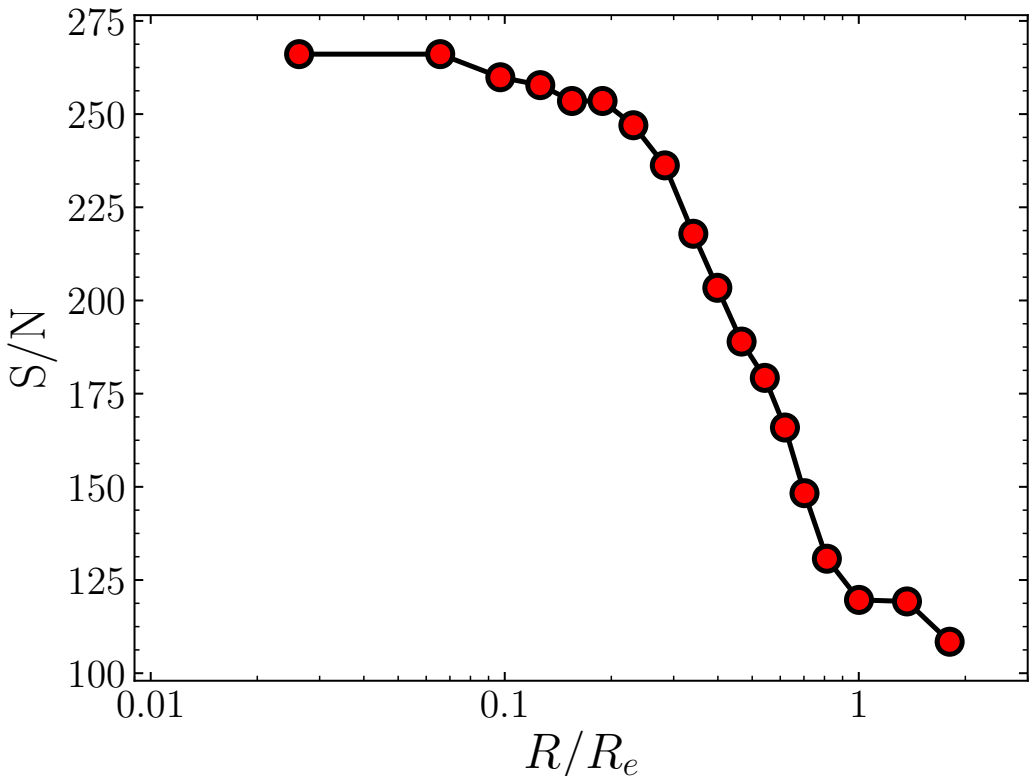

Figure 3.3: True signal-to-noise ratio of the spectrum in each annular bin. These values incorporate the inflation of the error-bars according to the β parameter discussed in Section 3.3.

A full discussion of the models is presented in Conroy et al. (2018).

3.3.3 Spectral Fitting

We fit the models to the data using the PYTHON package `PyStaff` (Python Stellar Absorption Feature Fitting), which is publicly available at `https://github.com/samvaughan/PyStaff`. Below, we outline the steps undertaken during the fitting process.

To ensure that there is a constant velocity difference between pixels which are adjacent in wavelength, we first rebin the data and templates to have an equal sampling in $\ln \lambda$ instead of λ (see e.g Cappellari, 2017). We then linearly interpolate the

SPS models in each dimension, allowing us to make a model at an arbitrary set of parameter values. Free parameters in the model which we choose not to vary are fixed at their initial values. This template is then convolved with a line-of-sight velocity distribution (LOSVD), which, in this case, is simply a gaussian function of width σ and velocity $v_{\rm syst}$. We correct for different continuum shapes between the model spectra and the data by fitting multiplicative Legendre polynomials to the ratio of the template and the data. The order of this polynomial is 8, 10, 10 and 13 respectively for each of the four regions; we have found negligible change to our results by slightly increasing or decreasing these values. The convolved, continuum matched template at arbitrary parameter values is then compared to the data.

Instead of fitting models to the entire spectral range, we split the process into four sections: 4800-5600 Å, 5600-6600 Å, 6600-7500 Å and 7700-9000 Å[2]. These sections are then fit simultaneously. The spectral fitting algorithm has 30 free parameters, which are:

- Recession velocity ($v_{\rm syst}$) and velocity dispersion (σ)
- Stellar age and metallicity [Z/H]
- the low mass IMF slopes x_1 and x_2 (see equation 3.1)
- Individual abundance variations in all 19 individual element abundances available in the SPS models, including Na, Fe, Ca, Mg and Ti[3].
- 4 nuisance parameters regarding the sky subtraction (see Section 3.3.4)
- a parameter, β, to rescale the size of the error bars (see Section 3.3.1)

[2]The small gap between 7500 Å and 7700 Å contains the residuals of a deep telluric absorption feature.

[3]The full list of elements is: Na, Ca, Fe, C, N, Ti, Mg, Si, Ba, O, Cr, Mn, Ni, Co, Eu, Sr, K, V, and Cu

We use the affine-invariant Markov-chain Monte-Carlo (MCMC) code `emcee` (Foreman-Mackey et al., 2013) to explore this parameter space for each of the spectra. For a given set of parameters, θ, we create a model, $f(\theta)$, and compare to the observed spectrum with values D_λ and associated errors σ_λ at each wavelength. This corresponds to the following (log)-likelihood function:

$$\ln p(\theta|D,\sigma) = -\frac{1}{2}\sum_\lambda \left[\frac{(D_\lambda - f(\theta)_\lambda)^2}{s_\lambda^2} + \ln(2\pi s_\lambda^2)\right]$$

with

$$s_\lambda^2 = (1+e^\beta) \times \sigma_\lambda^2$$

for a given value of the nuisance parameter β.

We explore this parameter space with 400 walkers. Each walker takes 30,000 steps, of which we discard the first 25,000 as the "burn-in" period. We are therefore left with $2{\times}10^6$ samples of the posterior in all bins. Each chain is inspected visually for convergence.

3.3.4 Sky Subtraction

First order sky subtraction was performed by subtracting galaxy and sky observations adjacent in time, before the individual data cubes were combined. However, we still found residual sky emission to be prevalent in our observations, especially towards the outskirts of the galaxy. In order to correct for this, we carry out a second sky subtraction during the fitting process (e.g. Weijmans et al., 2009; Zieleniewski et al., 2017; Vaughan et al., 2018a).

We use the dedicated sky-frames taken during the MUSE observations to make four one dimensional sky spectra, containing the emission lines of [O I], the NaI D $\lambda\lambda$5890, 5896 doublet, a forest of OH lines and the ro-vibrational O_2 band respectively

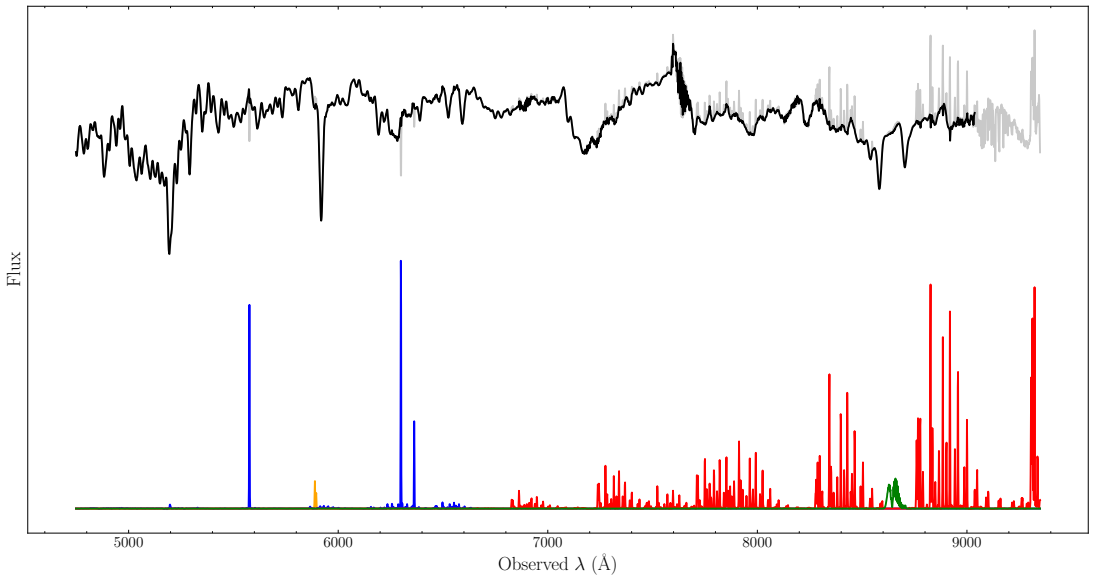

Figure 3.4: A representative galaxy spectrum before (grey) and after (black) the full spectral fitting process, incorporating the sky subtraction technique described in Section 3.3.4. The region redward of 9000 Å is not used in the fit. Below are the four separate one dimensional sky spectra which are used for sky subtraction during the fitting, containing strong [O I] lines (blue), the NaI doublet at 5890 Å (orange), a forest of OH lines (red) and the O_2 band at 8650 Å (green). Note that the grey spectrum, the result of a simple first order sky subtraction, contains under subtracted OH skyline residuals in the red but over subtracted [O I] residuals in the blue.

(using identification from Osterbrock et al., 1996). The absolute fluxes of these spectra are free parameters in the spectral fitting algorithm, allowing each one to be scaled separately before subtraction. We found that this was necessary since first order sky subtraction lead to under-subtracted emission lines in the red end of the spectrum but over subtracted ones towards the blue. A plot of the sky spectra, as well as a galaxy spectrum before and after the full spectral fitting process, is shown in Figure 3.4.

3.4 Results

The fits to the data are very good, with two examples from the central and outer annular bins shown in Figures 3.5 and 3.6. Similarly to van Dokkum et al. (2017,

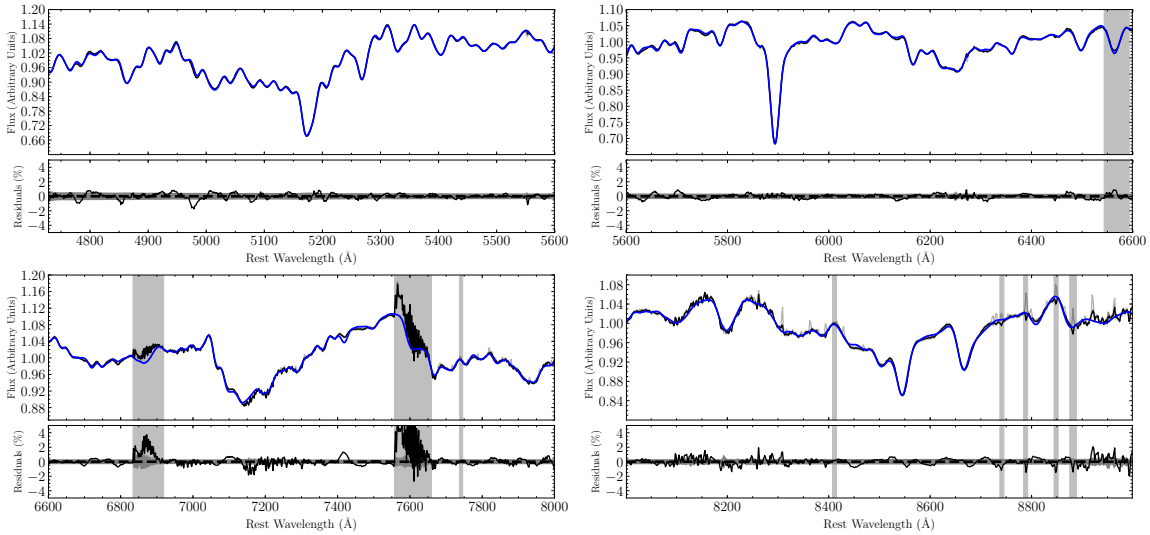

Figure 3.5: The central spectrum of our NGC 1399 observations (black) compared to the best-fit model (blue). Residuals between the data and model are shown below each section of the spectrum. Telluric emission lines in the raw spectrum which have been subtracted during the fit are shown in light grey. Shaded regions show areas of residual telluric absorption or emission which have been excluded from the fit.

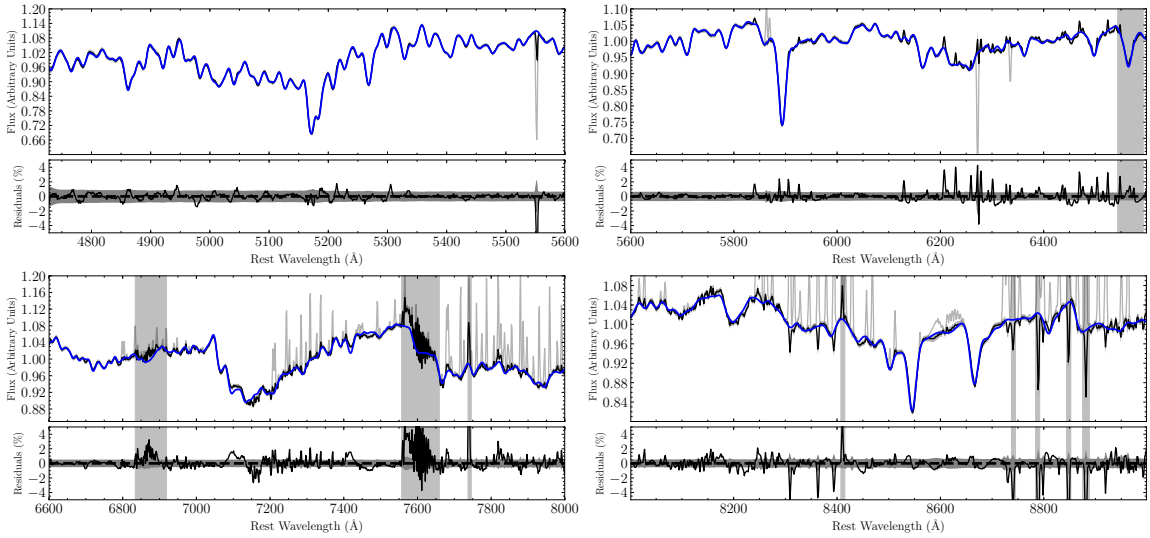

Figure 3.6: As Figure 3.5, but for a spectrum at 20″ (0.5 R_e).

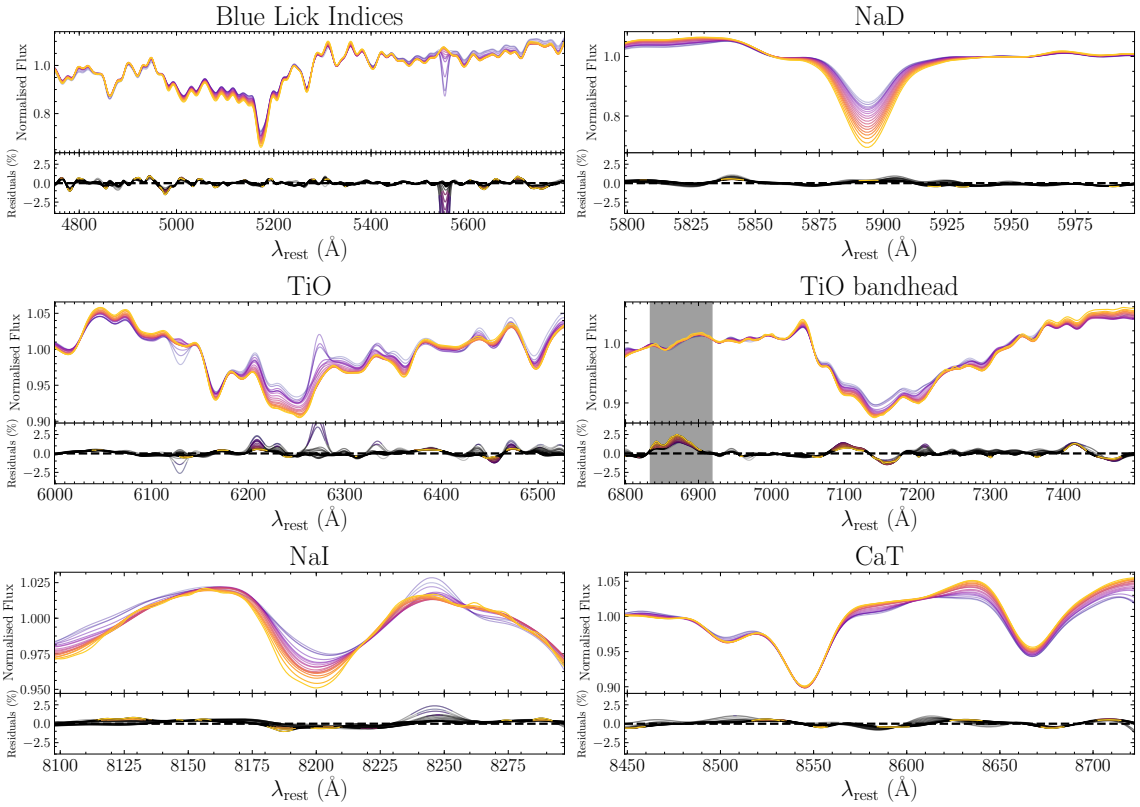

Figure 3.7: Variation in selected areas of the spectra (from the eighteen annular bins) as a function of radius. The data are coloured according to their radius, from yellow (centre) to purple (the outskirts). The spectra have been normalised and convolved to a common velocity dispersion of 350 kms^{-1}. The lower panels show the residuals around the best-fit model. Residuals which are within the 1-σ uncertainties are black, whilst areas of the spectrum which differ from the model by more than this are plotted in colour. The grey shaded region shows an area excluded from the fit due to residual telluric emission or absorption. Note the different y axis scales for each panel.

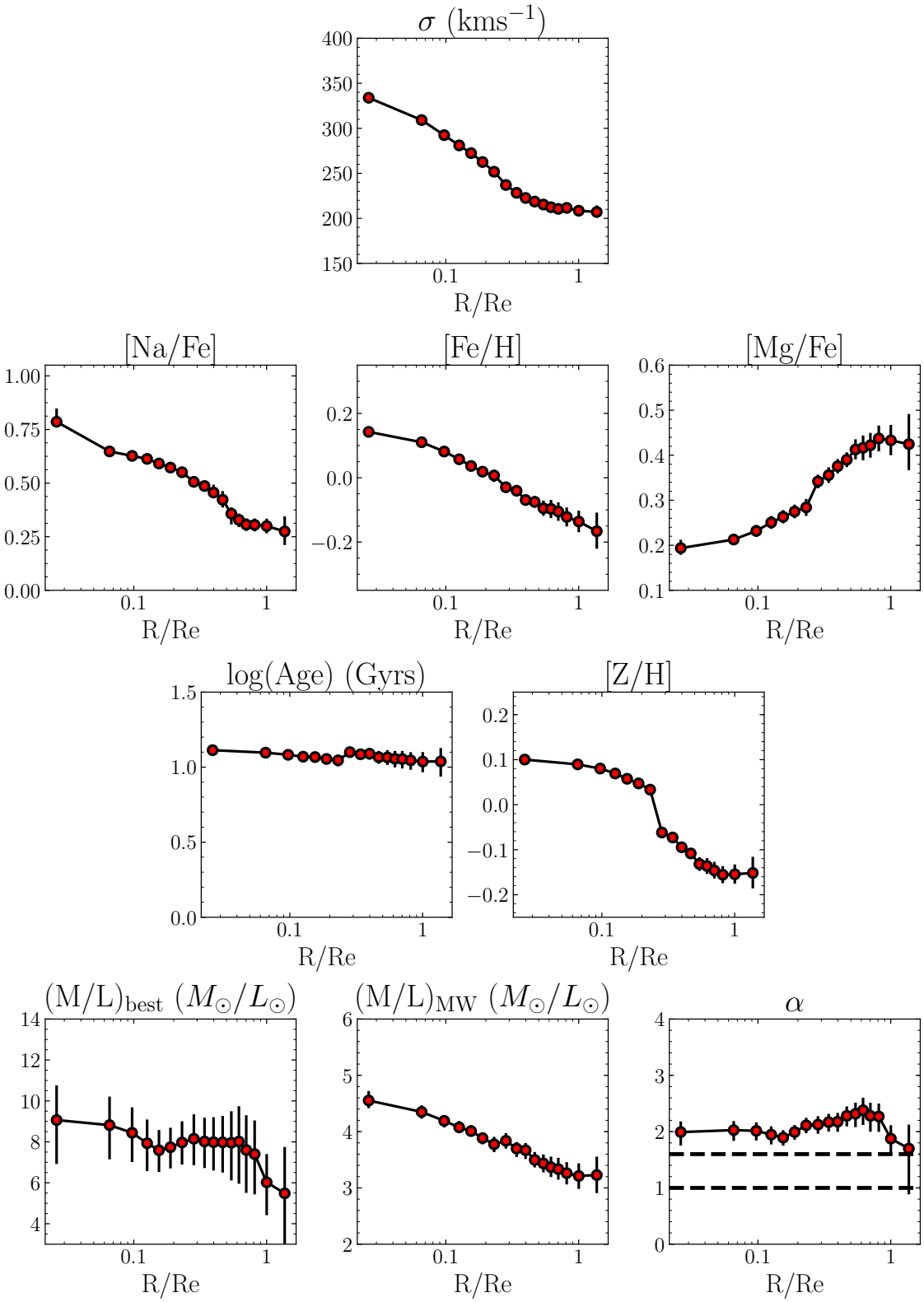

Figure 3.8: Stellar population results as a function of radius from full spectral fitting for NGC 1399. The main result of this work is the bottom right panel, showing the IMF 'mismatch' parameter α shows no gradient out to $\sim$0.7 R_e, before falling and becoming marginally consistent with a Milky Way-like IMF at just larger than R_e.

hereafter vD17), we find residuals to be around the sub percent level across the majority of the spectrum. Figure 3.7 shows the variation as a function of radius for selected spectral features in each of the 18 annular bins, coloured from the centre (yellow) to the outskirts (purple). Also shown are the residuals around the best fitting template as a function of wavelength, with residuals which are greater than the 1-σ error shown in colour.

The strongest radial variation is in the NaD feature at 5890 Å. This line is a well known interstellar medium (ISM) absorption line, which complicates its analysis. However, NGC 1399 has no obvious dust lanes and the line profile is the same as other absorption features in the same spectrum; there are no narrow absorption features which are often associated with ISM contamination (e.g. Schwartz & Martin, 2004). We also find no evidence for ISM contamination in unsharp-masked archival B-band HST images of NGC 1399 (proposal ID 5990; P.I. Grillmair), or in high spatial resolution maps of the NaD line, which we make by measuring the NaD equivalent width in each spaxel in the MUSE observations.

The NaI 8190 and TiO 6230 features also show modest radial variation, both weakening with increasing radius. The CaT is almost exactly uniform across all radii, however, with only a slight change in the blue and red continuum regions of the third absorption feature evident. Mgb at 5160 Å weakens slightly with radius, and there are small changes in the assortment of Fe lines in the blue region of the spectrum. Furthermore, the TiO 7053 band head shows a small change between the centre of NGC 1399 and 0.5 R_e; the band head is slightly stronger in the centre.

3.4.1 IMF Measurements

Figure 3.8 shows stellar population parameters in NGC 1399 derived from spectral fitting. From the top row, the panels show: the velocity dispersion of each bin; the abundances of [Na/Fe], [Fe/H] and [Mg/Fe]; the stellar age and metallicity; and the

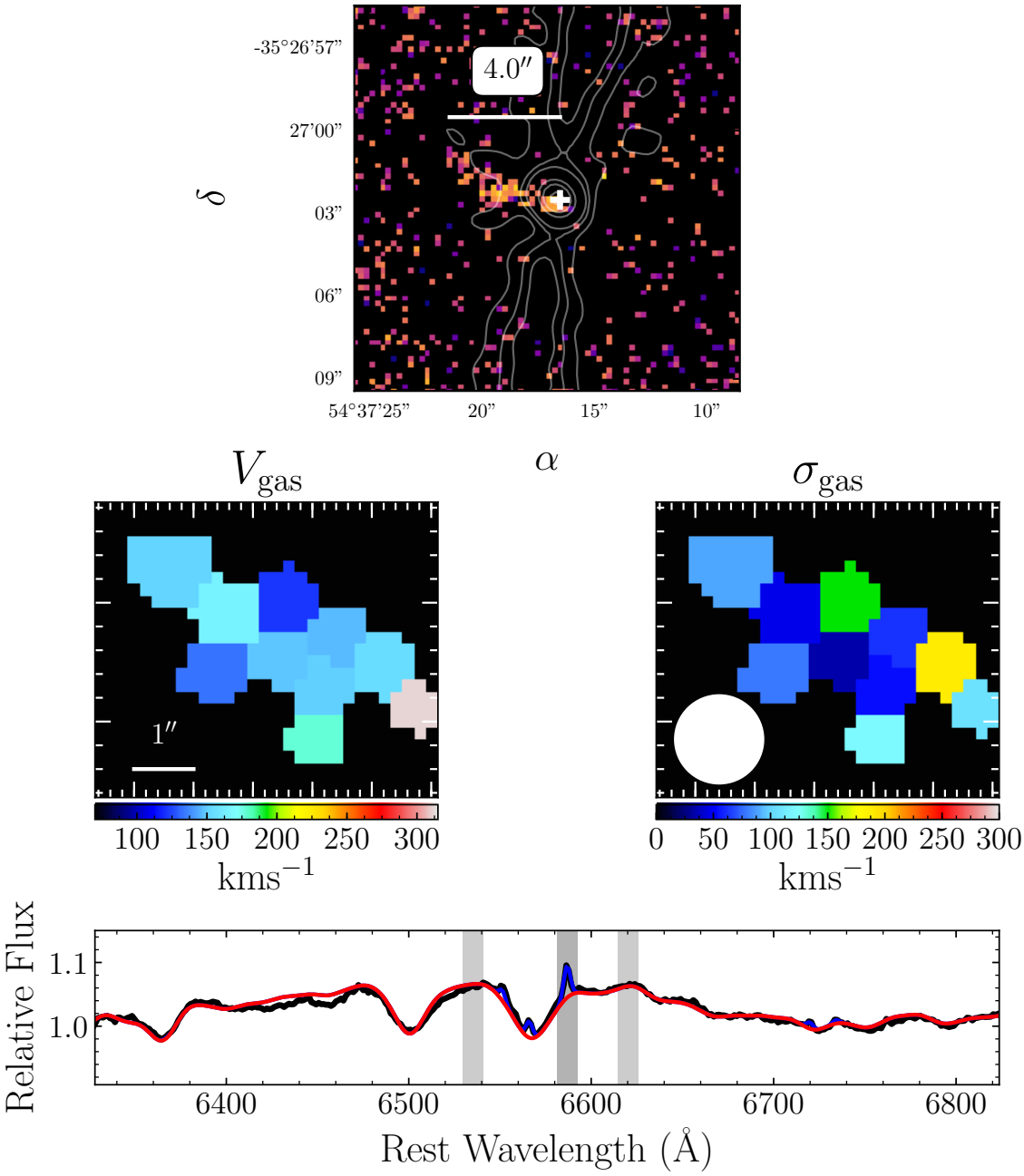

Figure 3.9: The top panel shows a "narrowband" image of the centre of NGC 1399 from the MUSE observations. We sum flux between 6608.0 and 6619.0 Å and subtract an average continuum value from between 6556.0 to 6567.0 Å and 6641.0 and 6652.0 Å (as shown in the bottom panel). We see an obvious filamentary feature extending 4″ from the centre of the galaxy (marked with a white cross). 4.6GHz radio contours of NGC1399's jet, taken from the VLA Archive Survey, are plotted in grey. NGC 1399's large-scale radio jets run in the north-south direction. The inset shows a fit to the kinematics of this gas using `pPXF`, with the seeing radius (of 0.76″) shown in white. The bottom panel shows a representative spectrum from this feature, with fits to the spectrum shown in red (without gas) and blue (with gas). Fits from `pPXF` to all ten spaxels in the filament are shown Figure 3.11.

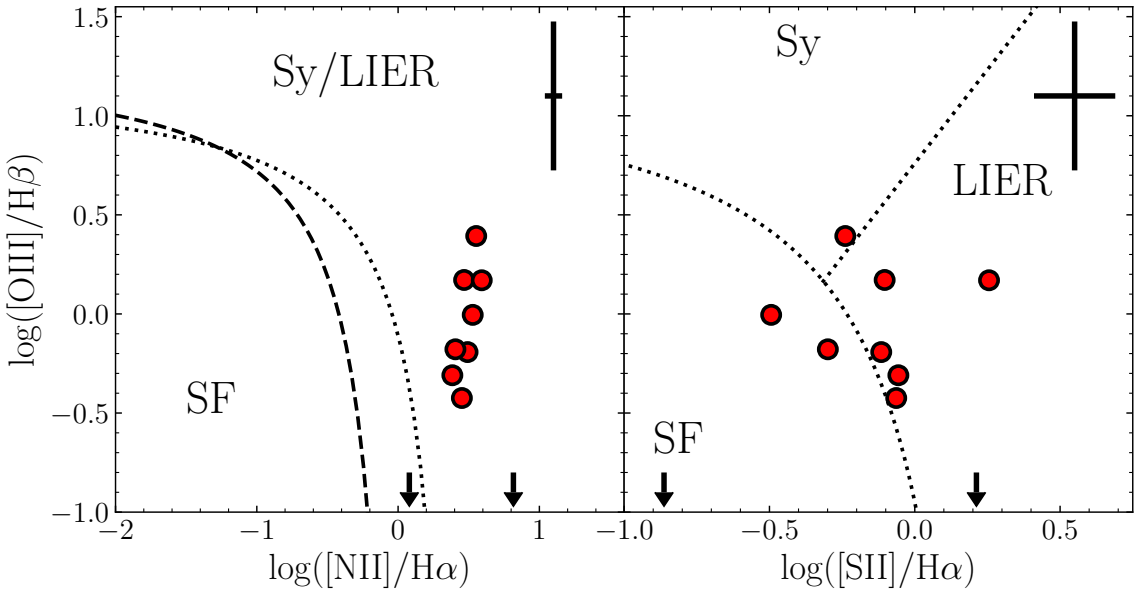

Figure 3.10: Each spaxel in the MUSE observations exhibiting gas emission lines are shown on a BPT diagram. The left plot shows the line ratio [OIII]/Hβ against [NII]/Hα whilst the right diagram shows [OIII]/Hβ against [SII]/Hα. We plot two spaxels with negligible [OIII] emission as upper limits. In the left hand panel, the dashed and dotted lines show the split between star-forming and Seyfert/LIER galaxies from Kauffmann et al. (2003c) and Kewley et al. (2006) respectively. The dashed line in the right panel which separates ionisation caused by star formation, Seyfert radiation and LIERs is also from Kewley et al. (2006). The majority of spaxels reside in the "LIER" region of the graph. This, combined with the spatial location of the emission lines and the clear evidence for an AGN in NGC 1399, leads us to conclude that the ionising radiation is from AGN activity.

best fitting M/L ratio (measured in the V-band), the M/L ratio of a galaxy with the best-fitting age and metallicity but with a Milky Way-like IMF, and the IMF "mismatch" parameter α, the ratio of these two M/L measurements. A population with a Milky Way IMF will have an α value of 1.

The steep gradient in [Na/Fe] and the much shallower radial change in [Fe/H] are evident, along with a modest variation in total metallicity [Z/H] of $\sim$0.2 dex. The small gradient in age shows the galaxy is oldest in the middle. The abundance of [Mg/Fe], a proxy for alpha enhancement, shows a positive gradient, qualitatively similar to (although slightly more pronounced than) the results of e.g. Spolaor et al. (2008), Brough et al. (2007) and Greene et al. (2015) in massive ellipticals. As noted in vD17, the absolute value of the [Mg/Fe] gradient is very sensitive to the library abundances ([X/Fe] and [Fe/H]) of the stars used to generate the SPS model, although this sensitivity does not affect the relative variations between radial bins or the absolute values of the derived IMF constraints. We refer the reader to Conroy et al. (2018) for further discussion of the abundance patterns of the library stars in the models.

The main results of this work are the bottom panels. The first shows that the inferred M/L ratio in NGC 1399 displays a negative gradient as a function of radius, decreasing from $9.0^{+1.69}_{-1.44}\,M_\odot/L_\odot$ in the centre to a value of $5.48^{+4.43}_{-2.27}\,M_\odot/L_\odot$ beyond R_e. The IMF mismatch parameter α takes the value of $1.97^{+0.19}_{-0.16}$ in the very centre, heavier than a Salpeter IMF (and hence a Milky Way IMF), and is flat out to 0.7 R_e. There is tentative evidence that α decreases at radii beyond this, although the error bars on the furthest point are large due to contamination from telluric emission lines. A decrease in α at large radii would be consistent with a number of other studies of nearby ETGs, which find the IMF in the outskirts of similar galaxies to be consistent with that of the Milky Way ($\alpha = 1$).

3.4.2 Emission Lines

Whilst studying the MUSE observations of NGC 1399, we noticed a small region of low-level ionised gas emission extending $\sim 4''$ (404 pc at $D_{\rm L} = 21.1$ Mpc) from the centre of the galaxy. This region is larger than the seeing radius of $0.76''$. The presence of emission lines in the centre of NGC 1399 has been reported before by Ricci et al. (2014), although they were unable to comment on the spatial distribution of the ionised gas.

Further investigation revealed the presence of Hα and [N II] λ6583 emission lines superimposed upon the broad Hα absorption feature. The top panel of Figure 3.9 shows a "narrowband" image created from the MUSE observations, whilst the bottom panel shows a representative spectrum from this region. Also shown are 4.6GHz radio contours, taken from the NRAO VLA Archive Survey[4]. The large-scale radio jet in NGC 1399 is perpendicular to the extended ionised gas emission.

We use the penalised pixel fitting `pPXF` method (Cappellari & Emsellem, 2004a; Cappellari, 2017) to measure the velocity and velocity dispersion of the emission lines. We first aggregate individual spaxels into voronoi-tessellated bins of S/N 300[5], using the method of Cappellari & Copin (2003), and extract a spectrum and error spectrum from each bin. We run `pPXF` using the MILES stellar library (Sánchez-Blázquez et al., 2006; Falcón-Barroso et al., 2011), which contains empirical spectra of nearly 1000 stars in the solar neighbourhood. We also include emission line templates for Hβ, Hα, [SII]λ6716 and [SII]λ6731, and the doublets [OIII]λ5007, [OI]λ6300 and [NII]λ6583. We fix the ratio of the [NII]λ6583 lines to be 3:1, and carefully account for the varying MUSE instrumental resolution at the wavelength of each emission line.

We find, however, that the stars from the MILES library give a poor fit to the region just redward of the Hα absorption feature, most likely due to the non-solar

[4] http://archive.nrao.edu/nvas/

[5] Although the true S/N is likely to be lower than this; see Section 3.3.1

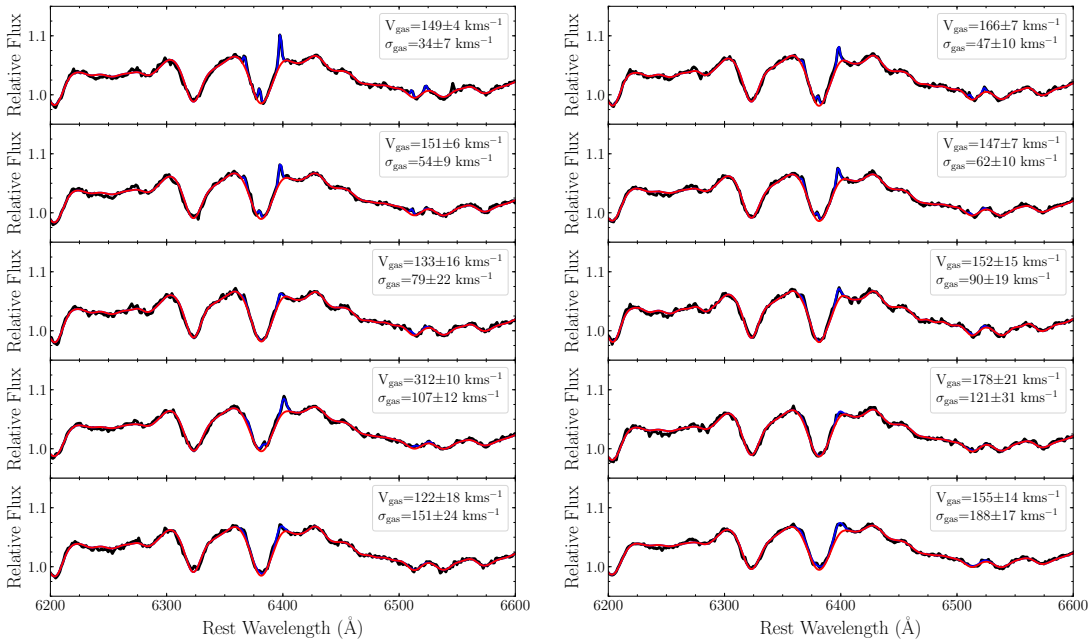

Figure 3.11: Fits to each spaxel in the "filament" of gas shown in Figure 3.9. The data are shown in black. We use `pPXF` to fit the stellar kinematics without gas (red line) and with gas (blue line). Spectra are ordered by velocity dispersion, from narrowest (top left) to broadest (bottom right).

abundance variations in the centre of NGC 1399.[6] To correct for this, we fit each spaxel using just the MILES library and no gas emission lines, in order to measure the residuals between the galaxy and best-fitting template. We then create a response function from the median of these residuals and apply this to each template in the library, before running the fit again with gas emission line templates. This gives a much better fit to the region in question and leads to robust emission line measurements.

The results from `pPXF` are shown in the inset panel of Figure 3.9, with fits to each spaxel shown in Figure 3.11. We find that the emission lines are very weak, with average velocity dispersion of $65 \pm 14 \mathrm{kms}^{-1}$. We also see tentative evidence for a velocity gradient across the filament. The best-fit velocity of the spaxel nearest to the centre of NGC 1399 is $312 \pm 10 \mathrm{kms}^{-1}$, whilst the average velocity of all spaxels in the

[6] We note that the Hα feature was masked during the full spectral fitting process used to measure the IMF, and so such a non-solar abundance does not influence the main conclusions of this work.

filament is of $160 \pm 5 \mathrm{kms}^{-1}$. The average stellar velocity in these bins is $194 \pm 2 \mathrm{kms}^{-1}$.

In order to characterise the source of the ionising radiation, in Figure 3.10 we plot each spaxel on a BPT diagram (Baldwin et al., 1981) based on the line ratios [OIII]/Hβ against [NII]/Hα (left) and [SII]/Hα (right). There was no measurable [OIII] emission in two spaxels, and as such these points are plotted as upper limits. To assess the uncertainties of our line ratio measurements, we add noise to a best-fitting template from the `pPXF` fit and repeat the process of extracting the line fluxes 100 times. A representative error bar for each point is plotted in the upper right corner.

In the left hand panel, we use the classification schemes of Kewley et al. (2006) and Kauffmann et al. (2003c) to differentiate between star-forming regions and areas ionised by Seyfert/LIER (Low Ionisation Emission Region) radiation. Each point lies away from the star-forming region of the diagram, as is expected in the centre of such a passive galaxy. In the right hand panel, using the lines from Kewley et al. (2006), we classify the majority of the points as ionised by a LIER, rather than a Seyfert-like AGN.

Cid Fernandes et al. (2010) introduce the WHAN diagram (the equivalent width of Hα versus [NII]/Hα) to classify ionisation caused by strong, weak and "false" AGN. They classify galaxies with a equivalent width of Hα $< 3\,\text{Å}$ as a "retired" galaxy, i.e. galaxies which have quenched their star formation and are ionised by hot, low-mass evolved stars. The Hα emission lines observed in NGC 1399 are very weak, well below this 3 Å limit, which may suggest that their ionisation is not caused by a low-level weak AGN either. Another possible source of ionising radiation are post asymptotic giant branch (pAGB) stars and hot white dwarfs, which have been shown to be able to account for the ionisation of cold gas observed in ETGs (Binette et al., 1994; Stasińska et al., 2008).

On the other hand, NGC 1399 has been shown unambiguously to contain an AGN

(e.g. Shurkin et al., 2008). Furthermore, O'Connell et al. (2005) report the detection of a transient nuclear point source in the centre of NGC 1399 in deep far-UV spectra from the Hubble Space Telescope (HST) in January 1999. This point source was detectable in earlier HST images taken in 1996, but not those from 1991 or 1993, and had faded by a factor of 4 by mid-2000.

The location of the filament of gas, combined with the recent reported activity of the AGN in NGC 1399, lends weight to the conclusion that the two are related. It is possible that the emission is due to a cloud of cold gas in the process of being accreted onto the central black hole, giving rise to the transient nuclear activity detected in the archival HST images and explaining the difference in velocity between the centre and edge of the filament. In this scenario, the gas cloud's very small equivalent widths may just be a reflection of the (very) low luminosity of the AGN. Follow up high spatial resolution optical spectroscopy would be necessary to investigate this scenario further.

3.5 Discussion

The IMF mismatch parameter, α, has been measured as a function of radius using gravity-sensitive spectral indices in a small number of individual galaxies; see, for example Martín-Navarro et al. (2015a); La Barbera et al. (2016); Conroy et al. (2017), vD17 and S18. The general consensus is such that the phenomenon of bottom heavy IMFs is confined to the cores of massive ETGs, with measurements in their outskirts more consistent with the IMF in our own galaxy. Broadly speaking, therefore, the measurements in NGC 1399 are in agreement with this picture. We measure α to be flat out to $\sim$0.7 R_e before a decrease down to a value which is marginally consistent with a Milky-Way IMF at 1.3 R_e.

Interestingly, however, there are differences in the shapes of the IMF gradients

measured in the works mentioned above. S18 make a comparison between the IMF gradient found in their study of M87 and radial IMF profiles in the massive ETG XSG1 (SDSS J142940.63+002159.0) from La Barbera et al. (2016) and the average IMF measurements in six ETGs from vD17. The IMFs in M87 and XSG1 display very close agreement, with a linear increase in α as a function of $\log R/R_{\rm e}$ from MW-like at 0.3 R_e to $\alpha \sim 2$ in their centres. The vD17 average, on the other hand, has a flatter central profile which reaches $\alpha \sim 2.5$, combined with a steeper rise from MW-like at $\sim$0.3 R_e to $\alpha \sim 2$ at 0.15 R_e. Our measurements of NGC 1399 are more similar to those of vD17, albeit with a bottom-heavy α of >2 measured out to a larger radius (0.7 R_e) than their average, and our measurements around R_e only marginally consistent with the MW within the (admittedly large) error bar. Individual galaxies in van Dokkum et al. (2017) do show quite significant differences from the binned average, however, likely due to the inherently stochastic nature of galaxy formation, with the NGC 1399 results being qualitatively very similar to IMF profile in NGC 1600.

Before too many conclusions are drawn about these differences, it should be noted that the method of IMF analysis, as well as the population synthesis models used to do the analysis and the form of the IMF itself, differs between S18, La Barbera et al. (2016), vD17 and this work. S18 and La Barbera et al. (2016) study the strength of selected regions of spectra sensitive to the IMF (as well as age, [Z/H] and other stellar population parameters). They also use a "bimodal" IMF and the MIUSCAT (Vazdekis et al., 2012) and E-MILES (Vazdekis et al., 2016) models respectively. On the other hand, vD17 and this work analyse the entire spectrum via full spectral fitting, use a two-part power law IMF between 0.08-1$M_\odot$ (see equation 3.1) and stellar models from Conroy et al. (2018). A study of the similarities and differences of these technical prescriptions, by applying both methods of analysis to the same object, is sorely needed.

We do not see a single parameter which correlates well with the α profile. This is

in contrast to S18 and Martín-Navarro et al. (2015c) who see a tight correlation with their bimodal IMF slope Γ_b and [Z/H]. The tightest correlations with α from vD17 are with radius and [Fe/H], neither of which correlate well with α in NGC 1399. We do find, in agreement with both studies, that the local stellar velocity dispersion is not a good tracer of the local IMF.

Spavone et al. (2017) present a photometric study of a number of nearby massive ellipticals, including NGC 1399. They fit the light profile of NGC 1399 out to 30 arcminutes with two Sérsic components and an exponential profile. These correspond physically to three components of a massive ETG; a central component of stars, formed in-situ during the galaxy's formation; a component corresponding to remnants accreted from massive progenitors, which sink rapidly via dynamical friction to smaller radii and which have Sérsic profiles themselves; and a component corresponding to stars accreted from less massive progenitors, which will remain at larger radii and contribute to a galaxy's diffuse outer envelope but add little light to the central regions.

The break between the central Sérsic component and the "accreted" Sérsic component in NGC 1399 occurs at $30\pm6''$ (Spavone et al., 2017, Table 6), very close to the radius where the best fit M/L value recovered from our spectral fitting turns over and begins to decrease ($26''$). This points towards the break in the best-fit M/L and the turn over in the α parameter being caused by the build up of stars formed in different conditions to the central regions, in agreement with the current paradigm of the inside-out formation of ETGs (e.g. Naab, 2013, and references therein).

One significant impact of a non-universal IMF in the centres of massive galaxies is on the dynamical measurements of their black holes. In essence, an unresolved population of low-mass stars adds "unseen" stellar mass above that assumed from a MW IMF, which will end up being attributed to a black hole unless a careful study of the stellar M/L is conducted. A dynamical study of the central regions of NGC 1399

was undertaken by Houghton et al. (2006, hereafter H06), measuring a black hole of mass $1.2^{+0.5}_{-0.6} \times 10^9 M_\odot$. Assuming that mass followed light, H06 derive a best-fit dynamical V-band M/L ratio of 9±1 $M_\odot/L_\odot$, in excellent agreement with the central V-band M/L of $9.0^{+1.69}_{-1.44}$ $M_\odot/L_\odot$ from in this work. As a consequence, this implies that central dark-matter fraction in NGC 1399 is negligible and that the black hole mass estimate from H06 is secure.

3.5.1 [Na/Fe] abundance

The steep gradient in [Na/Fe] abundance is striking. Similar observations have been made in other radial studies of absorption lines sensitive to the abundance of Sodium (e.g. a number of recent studies: La Barbera et al., 2017; van Dokkum et al., 2017; Parikh et al., 2018; Vaughan et al., 2018a), although the explanation for these observed abundance gradients is unclear.

As discussed in section 3.4, we rule out contamination from the interstellar medium (ISM) in our spectra being the cause of the large Na abundance. NGC 1399 has no visible clumps or dust lanes, the profile of the NaD line shows no evidence for the usual sharp absorption features associated with absorption by a cold ISM and we see no evidence for large-scale dust filaments in HST imaging or (seeing-limited) NaD equivalent width maps from MUSE. We therefore turn to a number of possible explanations based on the formation of Na in massive and intermediate mass stars.

Firstly, it is important to note that individual stars in galactic globular clusters have been measured with abundances of [Na/Fe] as high as our measurements in the centre of NGC 1399, ≥0.7 dex (e.g. Gratton et al., 2006; Carretta et al., 2009; Muñoz et al., 2017). Whilst large, therefore, the central [Na/Fe] abundance is certainly not immediately unphysical.

During the lifecycle of a massive star, Na can be injected into the ISM via stellar winds and in type II supernovae (SNe). There is evidence to suggest that the Na

yield from a type II SNe is highly metallicity dependent, with super-solar metallicity SNe producing large [Na/Fe] abundances (Chieffi & Limongi, 2004; Kobayashi et al., 2006), implying that the deaths of massive stars in the high metallicity central regions of NGC 1399 could be the cause. This mechanism for producing large [Na/Fe] abundances would lead to a correlation between [Fe/H] and [Na/Fe], as we observe in NGC 1399 (panels 2 and 3 of Figure 3.8). Such a correlation is not observed, however, in a similar study conducted in La Barbera et al. (2017).

AGB stars are also producers of Na. Indeed, chemical models which only include Na production in type II SNe have been found to underproduce globular cluster [Na/Fe] abundances by factors of 2-3 (e.g. Timmes et al., 1995; Gibson et al., 2005). In AGB stars $\geq 3M_{\odot}$, Na is produced during hot bottom burning by the Ne-Na cycle $^{22}\mathrm{Ne} + p \rightarrow {}^{23}\mathrm{Na} + \gamma$, although the rate of sodium production from this process is highly dependent on the reactions $^{23}\mathrm{Na}{+}p \rightarrow {}^{24}\mathrm{Mg}{+}\gamma$ and $^{23}\mathrm{Na}{+}p \rightarrow {}^{20}\mathrm{Ne}{+}\alpha$ which destroy Na (e.g. Hale et al., 2001). Whilst these reactions have recently been measured in laboratory experiments (Cesaratto et al., 2013), some uncertainty about Na yields from AGB stars remains; a recent study has only been able to match the observed abundance of [Na/O] in globular clusters from models of thermally pulsating AGB stars by significantly reducing these sodium destruction rates (Slemer et al., 2017). As in type II SNe, there is some evidence that the abundance of Na in the ejecta of AGB stars increases with metallicity (Ventura et al., 2013), or in "super" AGB stars in the mass range 6.5-9.0 $M_{\odot}$ (Doherty et al., 2014). In the Milky Way, AGB stars have been found to have a small effect on [Na/Fe] abundance in the disk (Kobayashi et al., 2011), but they may be important in the high metallicity environment of the centres of massive ETGs.

There are also arguments that an increased abundance of [Na/Fe] may reflect the duration of the star formation, in a similar way to [α/Fe]. Tsujimoto et al. (1995) show that type II SNe produce 100 times as much ^{23}Na as type Ia SNe. In the short,

intense bursts of star formation in which the centres of massive ETGs were thought to have formed, therefore, it may be expected to see enhanced [Na/Fe] abundance ratios in what now make up their central regions. Whether this effect is enough to quantitatively match the values measured here and in other studies, however, remains to be seen.

A conclusion to this puzzle would require further study of the production of Na in the extreme conditions which are thought to make up the centre of elliptical galaxies; high densities, super solar metallicities, short formation timescales and a more bottom heavy IMF than the Milky Way.

3.6 Conclusions

We have presented MUSE observations of the central regions of NGC 1399, the largest elliptical galaxy in the Fornax cluster. Using state-of-the-art stellar population synthesis models, we measure the low-mass IMF as a function of radius in this object, as well as the chemical abundances of 19 elements and a number of stellar population parameters. We find that the radial profile of the IMF is bottom heavy in the very centre of NGC 1399, with an IMF mismatch parameter $\alpha = 1.97^{+0.19}_{-0.16}$. We measure a flat radial profile out to $\sim$0.7 R_e before α drops, becoming marginally consistent with a Milky Way IMF within the error bars just beyond R_e. The central V-band M/L implied by our IMF determination is in excellent agreement with the dynamical M/L from Houghton et al. (2006).

Our IMF measurements in NGC 1399 are consistent with the results of radial IMF measurements in other massive ETGs by Martín-Navarro et al. (2015a); La Barbera et al. (2016); Conroy et al. (2017); Parikh et al. (2018) and van Dokkum et al. (2017). Interestingly, the radius at which α begins to decrease (26″) matches the radius where a fit to the light profile in Spavone et al. (2017) transitions between an

"inner" Sérsic component and a Sérsic component the authors attribute to "accreted" stars. NGC 1399 may offer evidence, therefore, for the scenario in which massive ETGs form from the inside out, with stars in their central regions forming first in more extreme conditions at high redshift whilst stars currently residing at larger radii being amassed in a series of minor mergers.

We find a large central abundance of sodium, as often measured in elliptical galaxies, as well as a substantial radial gradient in [Na/Fe]. We argue that the broad shape of the NaD line, combined with the lack of visible dust lanes in NGC 1399 imply this is not due to absorption by the interstellar medium along the line of sight. The cause of this gradient is not clear, although at super-solar metallicities a large abundance of Na may be created by type II supernovae (Chieffi & Limongi, 2004; Kobayashi et al., 2006) and/or produced at higher rates in AGB stars during hot bottom burning (Ventura et al., 2013; Doherty et al., 2014).

We also report on the measurement of a filament of ionised gas extending $\sim 4''$(404 pc) from the very centre of the galaxy. The presence of emission lines in the centre of NGC 1399 was reported previously by Ricci et al. (2014), although this work is the first to resolve their spatial extent. We use `pPXF` to fit and characterise this gas, measuring an average velocity of $160 \pm 5 \mathrm{kms}^{-1}$ and velocity dispersion of 65 ± 14 kms^{-1}. The spaxel closest to the galaxy centre shows a velocity much greater than this (312 ± 10 kms^{-1}), perhaps signalling an infalling/outflowing scenario related to the central black hole. On a BPT diagram the points lie in the "LIER" region, and the equivalent width of Hα is well below the 3 Å limit which Cid Fernandes et al. (2010) use to differentiate "retired" galaxies from true AGN. However, based on the clear evidence for AGN activity in NGC 1399 (e.g. Shurkin et al., 2008) and the central location of the emission, we suggest that (very) low level radiation from the nucleus is the source of ionisation.

4 | KCLASH: The Cluster and Field environments at the build up of the red sequence

4.1 Motivations

It is well known that the average properties of galaxies in the Universe have undergone a number of major transformations in the past 8 Gyrs. Perhaps most dramatically, the co-moving star formation rate density (SFRD) of the Universe has fallen precipitously since its peak at $z \sim 1$–3, known as "cosmic noon" (Lilly et al., 1996; Madau et al., 1996; Hopkins & Beacom, 2006). Similarly, since $z \sim 1$ we have witnessed the build-up of a red sequence of passive galaxies (e.g. Bell et al., 2004; Cooper et al., 2006; Stott et al., 2007) which coincides with the transition of turbulent, highly star-forming, gaseous disk galaxies (Förster Schreiber et al., 2006; Swinbank et al., 2012) to the comparatively quiescent, ordered spirals we see in the Universe today. Exactly how these changes take place, however, is not well understood.

Spectroscopic surveys using fibres, long-slits and multi-object spectroscopy to

study the epoch between $0.2 < z < 1$ have been conducted for many years (Dressler & Gunn, 1992; Cowie et al., 1996; Fisher et al., 1998; Small et al., 1999; Halliday et al., 2004; Eisenstein et al., 2011; Driver et al., 2011; Davidzon et al., 2013; Rosati et al., 2014; Davies et al., 2018). The main advantages of these surveys are their large sample sizes, with modern campaigns collecting tens of thousands of spectra at $z > 0.2$– a prospect which would have been unthinkable just a decade previously. However, fibres and slits have their drawbacks. They lack the spatially resolved capabilities of the now ubiquitous integral field units (IFUs), meanings systematics such as uncertain slit losses and mis-matches in the slit position angle will always be a limiting factor. Furthermore, these effects are compounded at higher redshifts by the messy and asymmetric morphologies of the star-forming galaxies we see, where the thin disks and featureless ellipticals well suited to spatial averaging are scarce (e.g. Genzel et al., 2008; Wisnioski et al., 2011; Nelson et al., 2016b). Since we expect many of the transformative processes important in the past few billion years to be inherently spatially irregular (e.g. major mergers, filamentary gas accretion, ram-pressure stripping, clumpy star formation, outflows), a complete understanding of this epoch can only come from the three-dimensional observations that IFUs can provide.

Understandably, recent ground-breaking IFU surveys have been designed to target the peak of SFRD at $z \sim 1 - 2$ (e.g KROSS, Stott et al. 2016; the KMOS Cluster Survey, Beifiori et al. 2017; KMOS-3D, Wisnioski et al. 2015) or compile large samples of galaxies in the local universe (e.g. MaNGA, Bundy et al. 2015; SAMI, Croom et al. 2012; CALIFA, Sánchez et al. 2012; ATLAS^{3D}, Cappellari et al. 2011). The result of these design choices, however, has left the intermediate period lacking in spatially resolved spectroscopy. The K-CLASH survey aims to fill in this observational gap by building up a sample of galaxies at $0.2 < z < 0.6$ using the K-Band Multi-Object Spectrograph (KMOS: Sharples et al., 2013), targeting galaxies in the well-studied Cluster Lensing and Supernova survey with Hubble (CLASH: Postman et al., 2012)

fields.

The science goals of K-CLASH are two-fold. Firstly, we aim to track the evolution of a number of traditional scaling relations of star-forming galaxies, and compare to their measurements at $z \sim 0$ and $z \sim 1$. K-CLASH will be most competitive when making resolved measurements of galaxy properties, such as investigating gradients of emission line properties or studying dynamical relations such as the Tully-Fisher relation (Tully & Fisher, 1977).

Secondly, K-CLASH will compare the properties of galaxies residing in high-density cluster environments with those evolving in the field. Rich clusters have striking effects on their constituent galaxy population, with relations between the local density and (for example) a galaxy's morphology (Dressler, 1980; Dressler et al., 1997), colour (Pimbblet et al., 2002), age (Smith et al., 2006), stellar mass (Kauffmann et al., 2004) and kinematic morphology (Cappellari et al., 2011). By observing CLASH fields, K-CLASH obtains observations of members of the galaxy cluster as well as observations of interloper field galaxies along the same lines of sight. These field galaxies make an excellent control sample, and we use them as such to explore how a galaxy's environment influences its spatial Hα distribution, the physical conditions of its star forming regions and metallicity in Chapter 5.

This chapter, however, concentrates on describing the K-CLASH survey itself. We begin by discussing the observing strategy, data reduction process and compilation of ancillary photometric data before going on to measure the stellar masses and star formation rates of our targets. We then describe how we select the K-CLASH "field", "cluster" and "outskirts" samples and conclude by constructing the star-forming Main Sequence of our galaxies, showing that our star-forming sample is typical for galaxies at $0.2 < z < 0.6$.

We use a Planck Collaboration et al. (2016) cosmology throughout, with $H_0 = 67.8$ kms^{-1}Mpc^{-1}, $\Omega_m = 0.31$ and $\Omega_\Lambda = 0.69$. A Chabrier (2003) initial mass function

is assumed for all stellar mass and SFR calculations. All magnitudes are in the AB system.

4.2 Observations and Data Reduction

KMOS is a second-generation instrument mounted at the Nasmyth focus of Unit Telescope 1 at the Very Large Telescope, Cerro Paranal, Chile. It comprises 24 IFUs on moveable pick-off arms, which can each be placed individually within a 7.2′ patrol field. Each IFU has a square field of view spanning 2.8″×2.8″, made up of 0.2″ spatial pixels. The light collected by the IFUs is dispersed by one of three identical spectrographs, with resolving power R ∼3000-5000, before being imaged onto one of three Hawaii 2RG detectors optimised for the near-Infrared (NIR) regime. KMOS can make measurements across five spectral bands, from the IZ (0.77 to 1.08 μm) to the K band (1.9 to 2.46 μm). The K-CLASH survey makes all observations in the IZ band, which corresponds to the optical rest-frame of galaxies at $0.2 < z < 0.65$.

Four fields from the CLASH survey were observed with KMOS. The targets are summarised in Table 4.1. Three colour *HST* images of the centres of each cluster are shown in Figure 4.1. The clusters were chosen to be visible from the VLT site, and at a redshift where the wavelengths of Hα and [NII] emission lines avoid regions of strong telluric absorption. We target bright (V <22 for MACS 1931 and $V < 23$ otherwise) galaxies with good photometric redshift estimates (measured by Umetsu et al. 2014, primarily from Subaru Suprime-Cam B, V, R_c, I_c and Z-band photometry– see Section 4.3 for a summary) which placed them between $0.2 < z < 0.6$ and thus observable in the KMOS IZ band. Our observing strategy involved placing the KMOS patrol field in a "pinwheel" pattern over the CLASH field, centred on the brightest-cluster galaxy (BCG), as shown in Figure 4.2. This required that all targets must be within 7′ of the cluster centre. Finally, we preferentially select galaxies which are

blue ($B - V \leq 0.9$ for $z \leq 0.4$ and $V - R_c \leq 0.9$ for $z > 0.4$) and with a photometric redshift which placed them at their cluster redshift, with remaining arms placed on blue galaxies at different photometric redshifts. During each OB, one IFU was placed on the BCG and at least one more on a star in the field of view, in order to measure the KMOS point-spread function (PSF)[1].

K-CLASH observations were carried out over two years between ESO observing periods P97-P100[2]. The cluster was separated into four quadrants, with each quadrant observed for two to three 1.5-hour observing blocks (OBs). This resulted in MACS1311 being observed for 12 hours and the remaining fields for 16.5 hours. Observations within one OB were carried out in a nod-to-sky manner, specifically "OSO-OSO-OS", where "O" refers to an "object" exposure (i.e. a science frame) and "S" refers to a sky frame. Sky frames were chosen to ensure each IFU was free of sources and at least an arcminute away from the cluster core.

Data were reduced with the publicly available ESOREX (Freudling et al., 2013) software[3] with the KMOS instrument pipeline. The pipeline is made up of a set of recipes to perform the standard IFU reduction steps of flat-fielding, illumination correction, wavelength calibration, spectral extraction and datacube reconstruction. Individual object-sky pairs (e.g. an "OS" or "SO" combination) were constructed during the reduction, with the *sky_tweak* option applied. This rescales the intensities of groups of sky emission lines (from the same family of OH vibrational transitions; see e.g. Davies 2007) in an "S" observation to better match those in the data itself, leading to smaller residuals in the final sky-subtracted spectrum.

Reconstructed cubes were flux-calibrated and telluric corrected from observations of standard stars taken throughout the observations. These stars were chosen to be

[1]The observing strategy and target lists were compiled by Alfred Tiley and the rest of the K-CLASH team

[2]proposal IDs IDs 097.A-0397, 098.A-0224, 099.A-0207, and 0100.A-0296; PIs Tiley, Vaughan & Prichard

[3]`https://www.eso.org/sci/software/cpl/download.html`

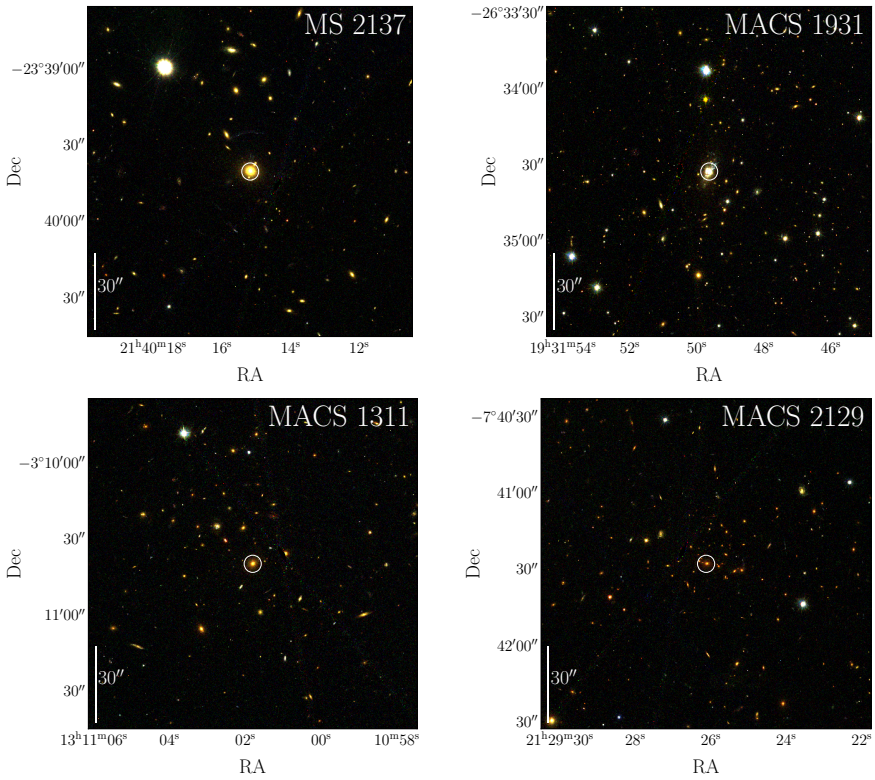

Figure 4.1: Clockwise from top left, the central regions of MS 2137, MACS 1931, MACS 2129 and MACS 1311. Images are RGB composites from *HST* Advanced Camera for Surveys filters F475, F625 and F775 (corresponding to SDSS g, r and i bands respectively). The brightest cluster galaxy is circled in each image.

at similar airmasses to the science targets whilst being close in right ascension and declination.

Combining Observations

Once individual exposures within an OB have been reduced, they must be combined together to give a final datacube for each object. This can be accomplished in a number of ways; here, we discuss the method chosen for the K-CLASH survey.

During planning for each observing run, the coordinates of the target galaxy are saved in the observation's FITS header. In a perfect world, where the KMOS arms can be retracted and replaced on sky with absolute accuracy and shifts between "science" and "sky" observing positions are performed to milli-arcsecond precision, it would

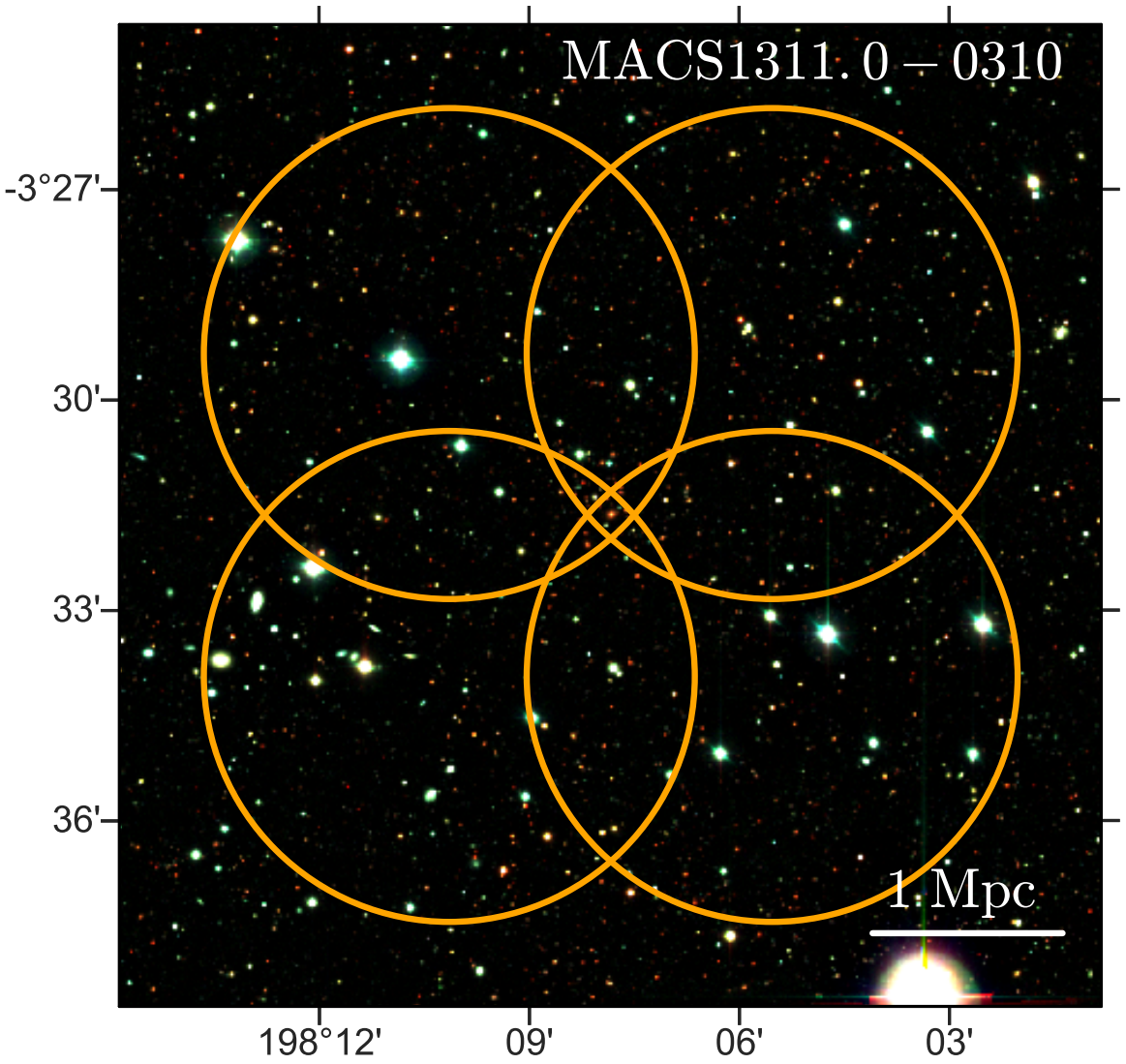

Figure 4.2: Example of the K-CLASH observing pattern for the MACS 1311 field. Each orange circle represents the 7.2′ KMOS patrol field, where individual IFUs can be placed for an OB. The BCG is at the centre of the pattern. Image from Alfie Tiley (private communication), reproduced with permission.

Cluster Name	α_{J2000}	δ_{J2000}	Redshift	$M_{200}(10^{15}M_{\odot}h^{-1})$
MS 2137	21:40:15.18	-23:39:40.7	0.313	1.04 $\pm$0.06$^{(b)}$
MACS 1931	19:31:49.66	-26:34:34.0	0.352	0.46 $\pm$0.03$^{(b)}$
MACS 1311	13:11:01.67	-03:10:39.5	0.494	0.69 $\pm$0.05$^{(b)}$
MACS 2129	21:29:26.06	-07:41:28.8	0.570	3.5 $\pm$ 3.10$^{(a)}$

Table 4.1: Summary of the four CLASH clusters observed with KMOS for the K-CLASH survey. RA, Dec and redshift values are from Postman et al. (2012). Mass measurements are derived from lensing by Sereno & Zitrin 2012 (a) and Merten et al. 2015 (b)

be possible to accurately combine each set of exposures to form the final reduced datacube using this information alone. However, as we show below, this is not the case, and naively combining the observations by their header coordinates tends to reduce the spatial resolution of the resulting datcubes.

To mitigate systematic errors introduced by stacking galaxies on the header coordinates, we measure the position of the bright stars in the field of view (targeted by a KMOS IFU) as a function of exposure number. This is accomplished by fitting a two-dimensional Gaussian profile to the star in each of the five individual 15 minute exposures which make up an OB. Figure 4.3 shows observations of three stars in the top left quadrant of the MACS 1931 field (one in each of the KMOS spectrographs) over two full OBs (10 exposures). The centre of each star moves by more than a pixel ($0.2''$) in the x and y directions during an observing block. To correct for this effect, we use these positions to calculate the shift required to centre the star in the IFU after each integration. We then apply these shifts to all other IFUs before combining their observations together.

This, of course, assumes that the KMOS arms move as one between integrations,

such that an offset measured from one IFU is appropriate for all of the others. Whilst the paths traced out by the centroids in different arms in Figure 4.3 are reassuringly similar to each other, this assumption is unlikely to be completely accurate. Ideally, one would fit a light profile to the observation in each IFU independently, and then use these *individual* shifts during the stacking process to recover the greatest spatial resolution in the final data products. Unfortunately, however, the majority of our targets are too faint to be reliably centred in each 15 minute exposure. For the brighter objects where this is possible, Figure 4.4 shows that applying a shift from one reference star to all other IFUs (a "global" shift) does indeed reduce the variation in position, although does not eliminate it completely. The standard deviation of the x position for the bright objects was on average 0.52 pixels ($0.1''$) before applying such a shift, which reduced to an average of 0.23 pixels afterwards ($0.05''$). We incorporate this residual systematic mis-centering as a source of error when measuring the spatial extent of the Hα emission (see Chapter 5).

Finally, these centred observations were combined using the ESOREX `k_sigma` iterative clipping algorithm. This rejects pixels more than k standard deviations away from the mean before combining the remaining values together and remeasuring the mean, repeating this procedure n times. We used the default choices of $n = 3$ (i.e. 3 iterations) and a $k = 3$ (a 3σ rejection threshold).

4.2.1 Sample Statistics

In total, K-CLASH observed 291 objects across 4 clusters. We detected stellar continuum and/or ionised gas emission (from the Hα or [NII] lines) in 241 galaxies. After integrating the KMOS cube in a $1.2''$ diameter aperture, Hα emission with S/N>3.0 (5.0) was found in 165 (139) objects. When splitting galaxies by colour, we find 217 K-CLASH targets have "blue" colours ($B - V < 0.9$ for $z_{\rm phot} < 0.4$, $V - R < 0.9$ for $z_{\rm phot} > 0.4$), of which we detect continuum light in 176 and Hα emission in 121

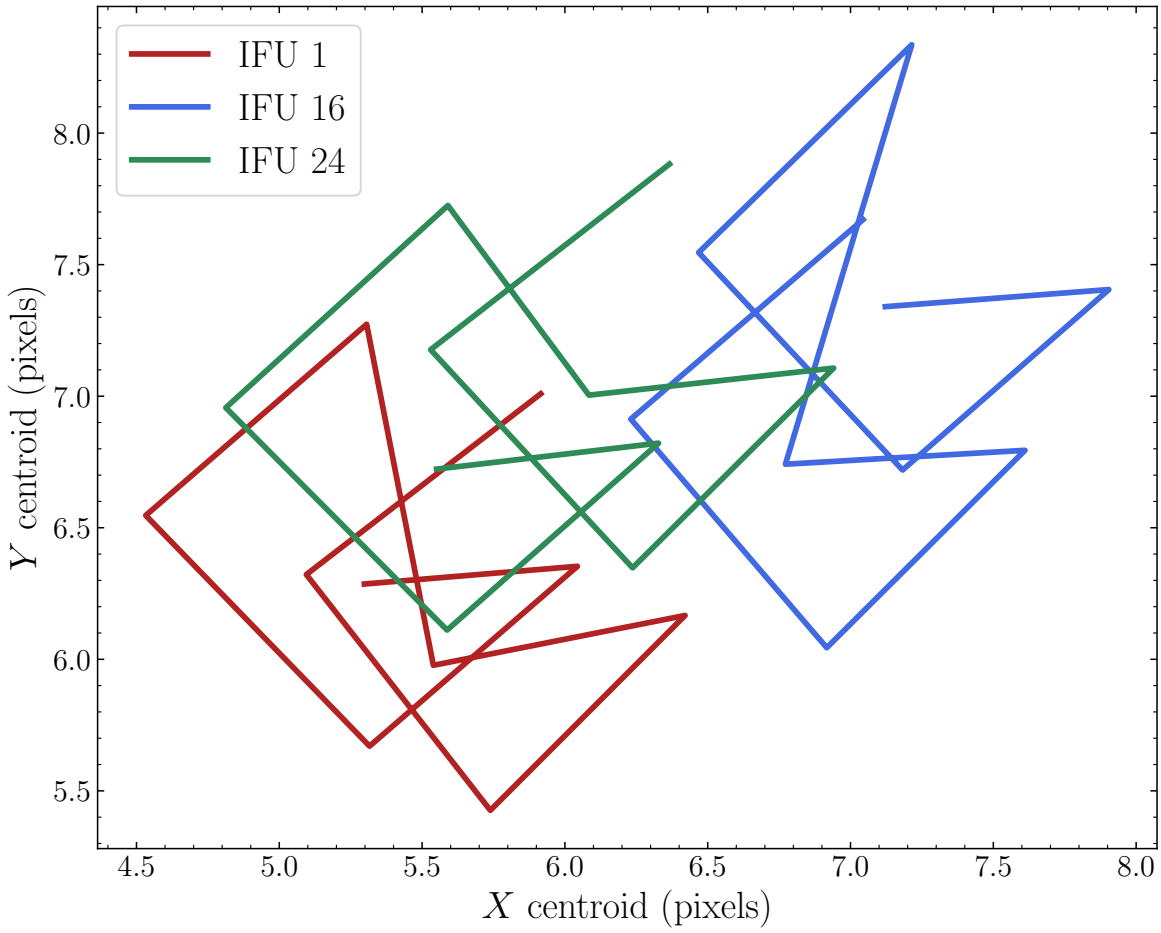

Figure 4.3: Position of the centre of three bright stars observed with KMOS in the MACS 1931 top left quadrant over 10 exposures. The stars move by up to two pixels (0.4″) during the observing block.

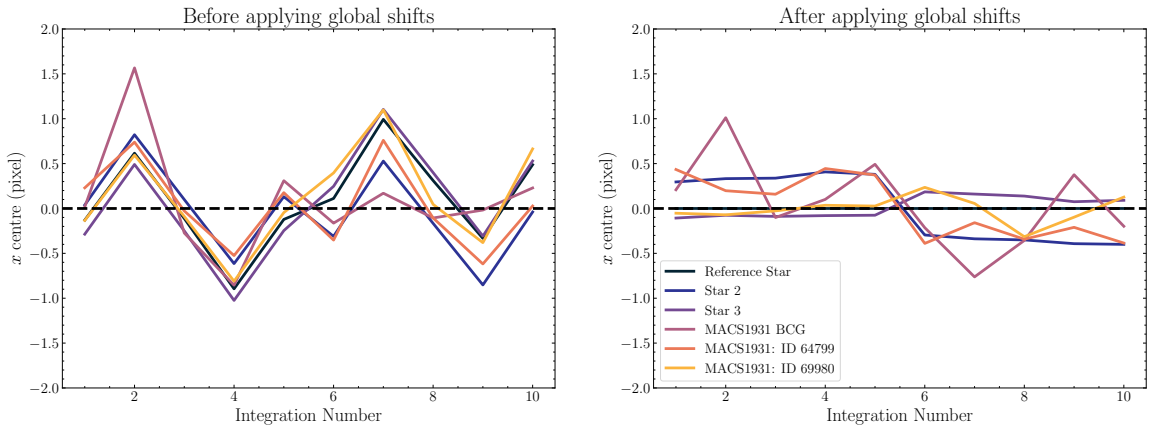

Figure 4.4: The x centroid of a number of stars and bright galaxies in the MACS 1931 top left quadrant for which we were able to accurately measure positions after each 15 minute integration. The panels show the centres of the objects before (left) and after (right) applying the "global" shifts (which accurately centre one of the reference stars) to every IFU.

(55.8%). For those K-CLASH galaxies which are red ($B - V > 0.9$ for $z_{\rm phot} < 0.4$ and $V - R > 0.9$ for $z_{\rm phot} > 0.4$), 65 out of 74 have detectable stellar continuum and 26 have Hα emission (35.1%).

4.3 Photometry

The CLASH fields have been observed at a wide variety of wavelengths, from the optical to the NIR and sub-millimetre. Here, we summarise the photometry available and describe the data used in the forthcoming analysis.

The centre of each CLASH cluster has deep *Hubble Space Telescope* (*HST*) imaging in a number of filters through the CLASH Multi-Cycle Treasury program (*HST* proposal 12065– PI: Postman). However, this imaging is concentrated on the centre of each cluster, and as such only 24 galaxies have measured *HST* photometry. Instead, we turn to the wide-field Suprime-Cam imaging using Subaru (Miyazaki et al., 2002), in the B, V, R_c, I_c and Z photometric filters, for MACS 1931, MACS 2129 and MS 2137. A full description of the Suprime-Cam data reduction and source extraction is

given in Umetsu et al. (2014).

Galaxies in the MACS 1311 field were observed in a different manner. B and V band images were taken with the ESO Wide Field Imager (Baade et al., 1999), Z band images with the Magellan IMACS camera (Dressler et al., 2011) and R_c band images with Suprime-Cam. No I_c band imaging of the MACS 1311 field is available, leaving 78 galaxies with optical photometry in only 4 bands.

All publicly available images have been mosaicked into a single $40'$ square image, with pixel scale $0.2''$. Images in each filter were smoothed to match the PSF of the image with the largest full width at half maximum (FWHM) before they were stacked. The average FWHM across each mosaic ranges between $\sim 0.6''$ in the MACS 2129 field to $1.22''$ towards MACS 1311.

Additionally, we use Spitzer Space Telescope Infrared Array Camera (IRAC: Fazio et al., 2004) observations of the CLASH clusters in the 3.6 and 4.5μm channels[4]. 254 galaxies in our sample are covered by Spitzer pointings. Individual observations were mosaicked into a single image per cluster by the `MOPEX` software package, using the 3.6 μm images as the reference for the 4.5 μm images to ensure identical image sizes and orientations. Further details of the parameters used with `MOPEX` are available on the Spitzer-CLASH website[5].

We extracted photometry from the optical and NIR images using the `astropy` affiliated package `photutils` (Bradley et al., 2019). To ensure consistency throughout, a $4''$ radius circular aperture was used for both the optical and NIR data for all galaxies. We estimated the background level by taking the sigma-clipped median of flux ($\sigma = 3$) in a circular annulus with inner radius $4''$ and outer radius $6''$. Postage-stamp images of a number of K-CLASH galaxies are shown in Figure 4.5.

We note that our measurements are in excellent agreement with the publicly available Spitzer catalogues for these fields. The average difference between the catalogue

[4]https://irsa.ipac.caltech.edu/data/SPITZER/CLASH/
[5]https://irsa.ipac.caltech.edu/data/SPITZER/CLASH/docs/README.CLASHSpitzer

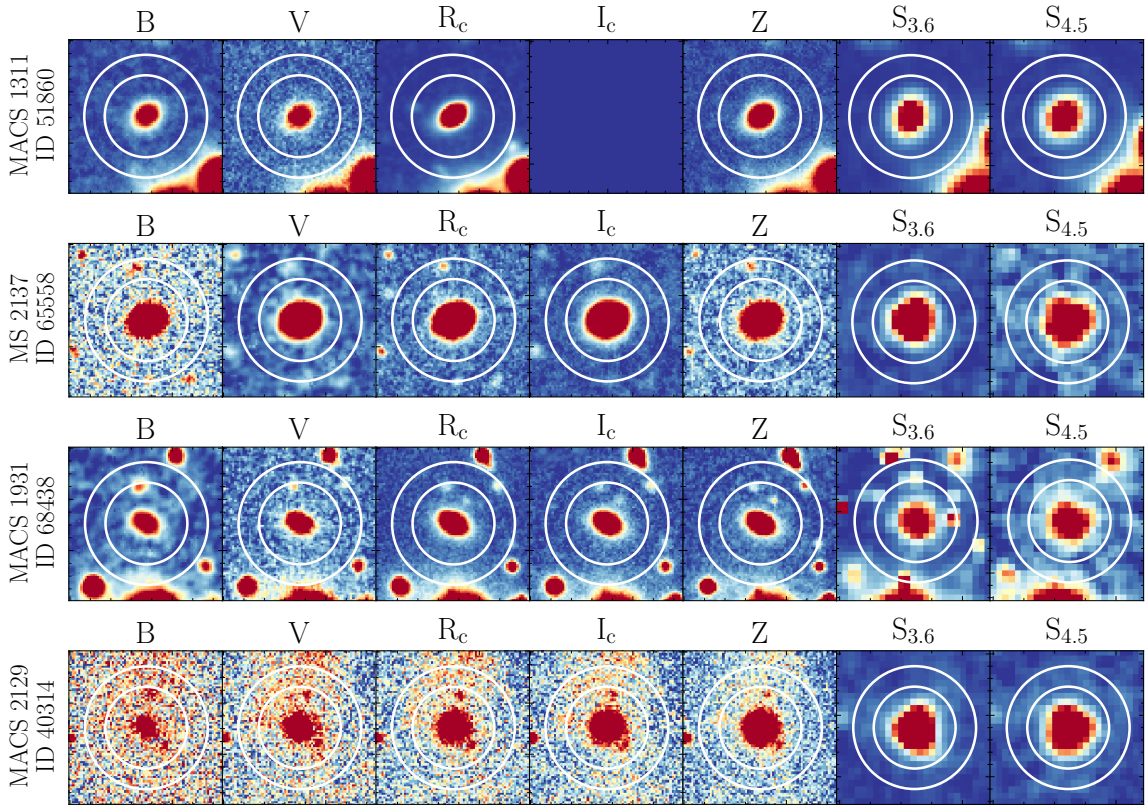

Figure 4.5: Optical and NIR photometry of a number of K-CLASH targets. Each image is 15″ across. We extract flux from the inner aperture of radius 4″, and estimate the background flux level by taking a sigma-clipped median between 4″ and 6″.

"`mag_auto`" magnitudes and our 4″ aperture measurements is -0.001 and 0.008 magnitudes in the 3.6 μm and 4.5 μm bands respectively, with standard deviations 0.36 and 0.37 magnitudes. We assume a conservative uncertainty of 5% on the flux measurement in each band, which incorporates Poisson noise, uncertainties in zero-point calibrations for each instrument and possible contamination from crowded sources.

4.4 Removal of AGN

It is important to distinguish between ionised gas emission which traces recent star formation and ionising photons from Active Galactic Nuclei (AGN). Unfortunately, we cannot place our objects on many of the common emission line diagnostic diagrams used to identify AGN contamination (e.g. the BPT diagram: Baldwin et al., 1981;

Kauffmann et al., 2003c; Kewley et al., 2006) due to the fact the KMOS wavelength range does not encompass the Hβ and [OIII] emission lines for all of our targets. Instead, we turn to ancillary observations and the [NII]/Hα line ratio to select our star-forming sample.

We first cross match our sample with publicly available X-ray imaging from the Chandra ACIS survey of X-ray Point Sources (Wang et al., 2016a), verifying that the Chandra pointings overlap fully with our observations. In total, six of our galaxies have detectable X-ray emission, including three out of four BCGs. We calculate X-ray luminosities of between $10^{42} - 10^{44}$ erg s^{-1} for these objects. These luminosities have not been corrected for absorption by galactic hydrogen along the line of sight, and as such should be treated as lower limits. It should be noted that the observations are far from uniform in exposure time, varying from 10,847 seconds for MACS 2129 to 98,922 seconds for MACS 1931, implying that we may be missing weak X-ray AGN in the shallower fields.

Next, we cross-match our observations with the Wide-field Infrared Survey Explorer (WISE: Wright et al., 2010; Mainzer et al., 2011) "AllWISE" source catalogue[6], requiring an offset of less than 10″ (∼1.5 times the WISE FWHM). 231 K-CLASH objects have observations in the catalogue. Note that four galaxies were not detected in either WISE imaging or NIR Spitzer observations (Section 4.3), meaning they have no NIR photometry. Two of these are detected in Hα emission. We choose not to remove them from our sample, but have verified that our conclusions in this and the following chapter are unchanged if we do so.

We use the WISE observations in bands W_1 and W_2 to select AGN with $W_1 - W_2 > 0.8$, following Stern et al. (2012). 13 objects satisfy this criterion, in which we detect Hα emission in 8. For those objects which are not detected in WISE but are detected in Spitzer, we apply a weak cut on the [3.6]-[4.5] colour, removing 2 objects with [3.6]-

[6]http://wise2.ipac.caltech.edu/docs/release/allwise/

[4.5]>1.0. Unfortunately, we were unable to use the colour-colour cuts from Donley et al. (2012) since neither [5.8] or [8.0] micron observations of our fields were available.

Finally, to remove galaxies with strong contribution from non-stellar excitation sources, we require the nebular emission lines in the integrated 1.2″ aperture spectrum to satisfy $\log([\text{N}\,\text{II}]/\text{H}\alpha) < -0.1$ (similarly to Wisnioski et al., 2018). 38 objects do not satisfy this criterion. We note this selection may still fail to identify galaxies hosting weak AGN surrounded by regions of intense star formation.

In summary, we remove from our sample:

- 6 galaxies detected in X-rays. Of these, 4 are detected in Hα with S/N>5.
- 13 galaxies with WISE colour $W_1 - W_2 > 0.8$. Of these, 8 have Hα with S/N>5.
- 2 galaxies with *Spitzer* colour [3.6]-[4.5]>1.0. One of these is detected in Hα.
- 38 galaxies with $\log([\text{N}\,\text{II}]/\text{H}\alpha) > -0.1$.

4 galaxies are classified as AGN using two or more diagnostics.

It is well known that no single method is able to reliably select all sub-types of AGN in a population, and so using a variety of diagnostics– each of which is sensitive to a different demographic– is the best way to catch as many as possible (see Padovani et al. 2017 for a review). In total, 56 galaxies were selected as AGN by one or more of the above criteria, giving an AGN fraction of $\sim 19\%$. The remaining 235 form the K-CLASH "star-forming" sample. This fraction is very similar to the AGN fraction in the KMOS^{3D} survey (25% for "normal" galaxies at $0.6<z<2.7$ with $9.0<\log(\text{M}/\text{M}_\odot) < 11.7$; Förster Schreiber et al. 2018), and to the multi-wavelength studies of $0.3 < z < 1$ star-forming galaxies by Kartaltepe et al. (2010), who find an AGN fraction between 10-20%.

4.5 Stellar Mass measurements

We derive an estimate of the stellar mass of each galaxy by comparing the K-CLASH photometry to a set of Spectral Energy Distributions (SEDs). This is done using the `LePhare` (Arnouts et al., 1999; Ilbert et al., 2006) and `MagPhys` (da Cunha et al., 2008) routines[7]. Both codes take a model SED, redshift it, calculate the resulting synthetic magnitudes in a set of specified photometric bands and find the best fitting parameters by comparing to the data via χ^2 minimisation. In addition to photometric redshifts and stellar masses, `MagPhys` and `LePhare` can also make an estimate of the dust extinction in the target. Similarly to many other KMOS studies (Wisnioski et al., 2015; Stott et al., 2016; Förster Schreiber et al., 2018), we use the reddening values from SED fitting as a substitute for a measurement of the Balmer decrement in each galaxy. The SED dust extinction estimates assume a Calzetti dust extinction law (Calzetti et al., 2000).

The inputs to `LePhare` and `MagPhys` are optical photometry in the B, V, R_c, I_c and Z bands and NIR photometry in Spitzer IRAC channels 1 and 2 (see Section 4.3). We correct each band for dust extinction in our own galaxy using the reddening maps of Schlafly & Finkbeiner (2011), assuming an extinction to reddening ratio $\mathrm{A_v}/\mathrm{E}(B-V) = 3.1$. The largest corrections, in the B-band, are a factor of ~ 1.4 (~ 0.3 magnitudes).

`MagPhys` requires an estimate of the redshift of each target. For galaxies with a secure Hα detection, this was taken to be its galaxy's spectroscopic redshift. For non-detections, we use the photometric redshifts derived using the Subaru photometry by Umetsu et al. (2014). Similarly, we use the option in `LePhare` to fix the template redshift at the target's spectroscopic redshift if this is known.

We generate SED libraries for `LePhare` using the BC03 (Bruzual & Charlot, 2003)

[7]The `MagPhys` results were obtained by Alfred Tiley (Private Communication)

and PEGASE2 (Fioc & Rocca-Volmerange, 1997) stellar population synthesis models, and compare the derived quantities to those found from `MagPhys` using the BC03 models. These tests, therefore, investigate differences between SED fitting codes using the same and different template libraries.

Figure 4.6 shows the derived histograms of M_* from `LePhare` and `MagPhys`. The upper panel of Figure 4.7 shows a comparison between `MagPhys` and `LePhare` when both use the BC03 libraries. The agreement between the two fitting routines is acceptable, with the mean value of M_* agreeing to less than 0.06dex. The distribution of residuals is non-gaussian, with a small number of outliers with $\Delta M_* < -1$. As such, we fit a Student's T distribution, finding the standard deviation of 0.38 dex between the `MagPhys` and `LePhare` stellar masses and degrees of freedom parameter $\nu = 3.21$.

The lower panel shows a comparison between the stellar masses using the PEGASE2 library with `LePhare`. In this case, the mean value of M_* agrees to better than 0.02dex, but we find an intrinsic scatter of 0.58 dex between the two distributions. As expected, there are a larger number of outliers in this comparison than the previous one (when both codes used the BC03 libraries).

Tests of different SED fitting codes have generally found the deviation in best-fit stellar mass measurements to be around ± 0.2 dex (Mobasher et al., 2015), smaller than we find here. Following their analysis, and in line with a number of high redshift studies (Tiley et al., 2016), we adopt a uniform 0.2 dex uncertainty in M_*. From here, we use masses derived from `LePhare` with the BC03 library for the rest of our analysis, although we have also ensured that using the masses from `MagPhys` do not change our conclusions.

4.6 Integrated Star Formation Rates

Integrated star formation rates (SFR) are calculated from each KMOS datacube. We sum the flux from each spaxel inside an elliptical aperture centred on the galaxy's continuum emission to make a one-dimensional spectrum. The ellipticity is measured by fitting a two-dimensional Sérsic model to the Subaru R_c band image of each galaxy with IMFIT (Erwin, 2015). The area of the aperture is the same as that of a circular aperture with diameter 1.2″. A one-dimensional noise spectrum is constructed by taking the RMS of the spaxels in the error cube. We then measured the Hα and [NII] line fluxes by fitting gaussian emission line templates using `pPXF` (Cappellari & Emsellem, 2004b; Cappellari, 2017). Uncertainties for each galaxy are estimated by adding noise to the best-fit template and re-measuring the fluxes 1000 times.

We then corrected the Hα flux for dust extinction, using the A_v parameters from the SED fitting (Section 4.5). These values correspond to the dust extinction for the stellar continuum in the V-band. However, a number of studies have described additional attenuation towards star-forming regions (Fanelli et al., 1988; Calzetti et al., 1994; Mancini et al., 2011; Wuyts et al., 2013), since HII regions are dustier than the regions surrounding older stellar populations. We therefore apply an extra extinction correction to our nebular line fluxes, following Wuyts et al. (2013):

$$A_{v_{gas}} = A_{v_{stars}}(1.95 - 0.15A_{v_{stars}})$$

and use the Calzetti et al. (2000) dust extinction law to find the dust extinction at the rest-frame wavelength of Hα. To convert Hα luminosities to star formation rates, we use the conversions of Hao et al. (2011) and Murphy et al. (2011), as collated in Kennicutt & Evans (2012):

$$\log_{10}(SFR_{H\alpha}/M_{\odot}yr^{-1}) = \log_{10}(L_{H\alpha}/erg\,s^{-1}) - 41.72$$

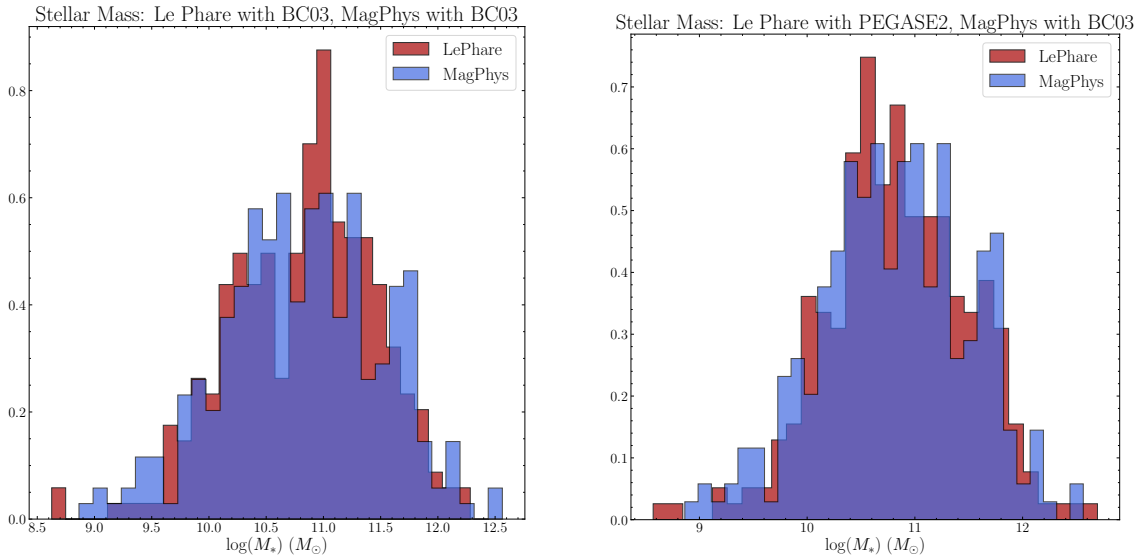

(a) BC03 library

(b) PEGASE2 library

Figure 4.6: A comparison between the derived stellar mass using the `LePhare` and `MagPhys` SED fitting codes. The left panel shows the derived stellar masses using `LePhare` with the BC03 models, whilst the right panel shows `LePhare` with PEGASE2. In each case, `MagPhys` uses the BC03 models. We find very good agreement between the *overall* mass distributions from the two codes in each case. See Figure 4.7 for a comparison on a galaxy by galaxy basis.

For galaxies with Hα signal-to-noise greater than five, we find the average SFR to be 5.4 $M_\odot yr^{-1}$, with standard deviation 2.5 $M_\odot yr^{-1}$. These SFRs are consistent with the SFR-stellar mass relation (known as the "Main Sequence" of star formation) at intermediate redshifts, as we show in Section 4.8.

4.7 Cluster Membership

We now describe our method for selecting which of our targets are members of their galaxy cluster and which are simply field galaxies along the line of sight. The K-CLASH sample of galaxies with spectroscopic redshift determinations is not large or complete enough to define each cluster's v_{esc} profile based on the cluster members themselves, as is commonly done in larger spectroscopic surveys (e.g. Owers et al.,

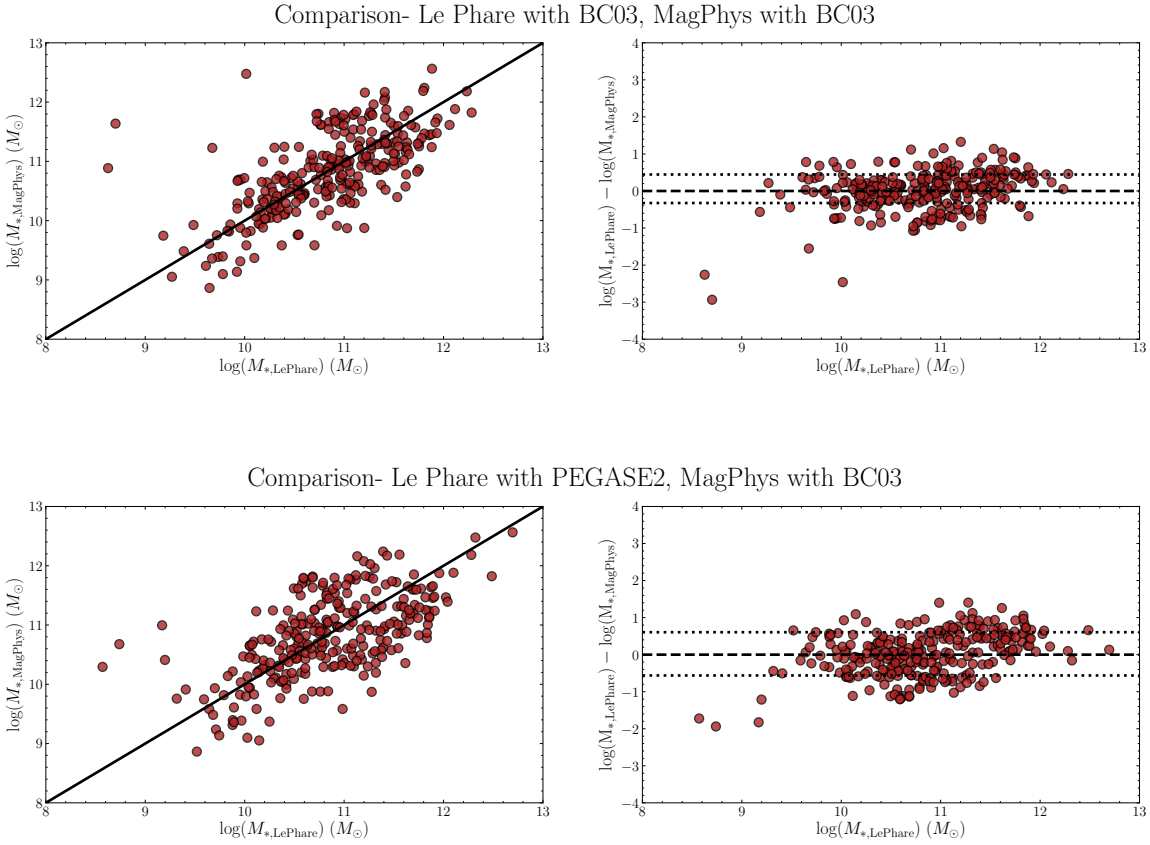

Figure 4.7: A comparison of the stellar masses inferred for the K-CLASH sample using `LePhare` and `MagPhys` using the same SED library (top) and different SED libraries (bottom). The agreement between the two codes is acceptable in each case, but the scatter is quite large.

2017). We therefore turn to previously published values of cluster properties to infer the membership properties of our observations; specifically the NFW halo parameters (virial radius, scale radius and concentration) from Zitrin et al. (2015) and the cluster X-ray properties from Postman et al. (2012).

For each galaxy in the KCLASH sample, we have measurements of its position on the sky (Right Ascension and Declination) and its redshift. These redshifts may be either spectroscopic, from the KMOS observations of objects with Hα emission, or photometric, from the CLASH analysis of the Subaru imaging (Umetsu et al., 2014) or the *HST* observations (Molino et al., 2017). 135 K-CLASH target galaxies were also observed by the CLASH-VLT survey (Monna et al. 2017, Rosati et. al 2019 in prep.), Of these, 69 are not detected in Hα emission by K-CLASH but do have a spectroscopic redshift (from stellar absorption features) from CLASH-VLT.

With these three coordinates per galaxy (RA, Dec, z), we can determine the cluster membership properties for each galaxy in our KCLASH fields, separating those objects which reside in the cluster environment from those which are simply field galaxies observed along our lines of sight.

We first calculated the predicted cluster velocity dispersion (σ_v) using the dispersion-temperature ($\sigma - T$) relation of Girardi et al. (1996)[8] and the cluster X-ray temperature from Postman et al. (2012). We took the redshift ($z_{\rm mean}$) of the cluster to be the spectroscopically measured redshift of the brightest cluster galaxy. For each galaxy we then used its spectroscopic redshift to calculate its velocity with respect to the rest-frame of the cluster as $v_{\rm member} = c(z_{\rm member} - z_{\rm mean})/(1 + z_{\rm mean})$.

Our first approach is then to simply classify galaxies within 2 virial radii from the cluster centre and 3 σ_v of the mean cluster velocity as members. The width of the window was a conservative compromise to account for the possibility that the cluster may not be completely relaxed whilst minimising contamination from non

[8]We verified that using the predicted velocity dispersion assuming a hydrostatic isothermal model ($\sigma^2 = k_{\rm B}T/\mu m_p$) or the σ-T relation from Wu et al. (1999), made negligible difference to our results.

cluster members. Whilst basic, this approach is straightforward and provides a good comparison for the more advanced method below.

The above method does not, however, take into account the uncertainty on cluster-centric velocity, which is especially important for K-CLASH galaxies which only have a photometric redshift. We therefore developed a probabilistic mixture model, separating galaxies as being drawn either from a uniform distribution in (x, y, v) or from a multivariate Gaussian in space and velocity.

We treat the uncertainty in the RA and Dec of each object to be negligible, whilst assuming a conservative uncertainty of $\sigma_z = 0.001$ (350 kms^{-1}, which is 6 pixels at the KMOS spectral resolution) for each galaxy with a spectroscopic redshift. We used the 68% confidence regions from the photometric redshift determinations for galaxies with photometric redshifts.

We then build a mixture model, modelling the cluster as

$$\boldsymbol{x}_i \sim \mathcal{N}(\boldsymbol{\mu}_{x,y}, \boldsymbol{\Sigma}_{x,y}) \times \mathcal{N}(\mu_v, \sigma_v) \tag{4.1}$$

where $\mathcal{N}$ denotes a Normal probability density function. We choose μ_v and σ_v to be the velocity and velocity dispersion of the cluster, $\boldsymbol{\mu}_{x,y}$ to be the cluster centre and $\boldsymbol{\Sigma}_{x,y}$ to be diagonal with $\boldsymbol{\Sigma}_{00} = \boldsymbol{\Sigma}_{11} = R_{200}/\sqrt{8 \ln 2}$, implying the FWHM of the cluster is R_{200}. In this simple example, the cluster is assumed to be axisymmetric (since $\boldsymbol{\Sigma}_{10} = \boldsymbol{\Sigma}_{01} = 0$), but this method can easily be extended to non-symmetric spatial profiles (if known).

Uncertainties are incorporated in the standard hierarchical manner: we model each velocity measurement as drawn from a Normal distribution centred on the intrinsic, *true* velocity value for that galaxy, with standard deviation equal to the measurement uncertainty. We then use this $v_{\rm true}$ value in the mixture model.

Mathematically, this model is described as

$$\theta_v \sim \mathcal{N}(0, 5),\ \tau_v \sim \text{Half Cauchy}(0, 2.5)$$

$$v_{\text{true},i} \sim \mathcal{N}(\theta_v, \tau_v)$$

$$v_{\text{obs},i} \sim \mathcal{N}(v_{\text{true},i}, \sigma_{v,i})$$

$$p_{\text{cluster},i} = p(x_i, y_i, v_{\text{true},i} | \boldsymbol{\mu}_{x,y}, \boldsymbol{\Sigma}_{x,y}, \mu_v, \sigma_v)$$

$$p_{\text{background},i} = p(x_i, y_i, v_{\text{true},i} | \Delta X, \Delta Y, \Delta V)$$

$$\mathcal{L} = \prod_{i=1}^{N} \lambda \times p_{\text{cluster},i} + (1 - \lambda) \times p_{\text{background},i}$$

where $p_{\text{background}}$ is a uniform distribution over $\Delta X, \Delta Y, \Delta V$, the range of values in x, y and z of our sample, λ is the mixture probability and θ_v and τ_v are hyper-parameters. $\mathcal{L}$ is the likelihood function. We place a Normal prior on θ_v, the location of the true velocity value, and a half-Cauchy prior (to ensure it remains positive) on τ_v, the scale parameter of the true velocity distribution. Our results are unchanged if we vary these choices of hyper-priors within sensible ranges, or use a half-Normal prior instead of a half-Cauchy for τ_v.

To reiterate, whilst the usual goal in a mixture model would be infer the parameters of p_{cluster} (i.e. the most likely values for the cluster velocity dispersion and centre), we instead fix these to the values derived from the CLASH survey and use this analysis to derive membership *probabilities* for each galaxy via

$$p_{\text{membership},i} = \frac{\lambda p_{\text{cluster},i}}{(1 - \lambda) p_{\text{background},i} + \lambda p_{\text{cluster},i}} \tag{4.2}$$

This mixture model has unknown parameters λ, θ_v and τ_v, as well as N values $v_{\text{true},i}$, one for each galaxy. We fit this model using `Stan` (Carpenter et al.,

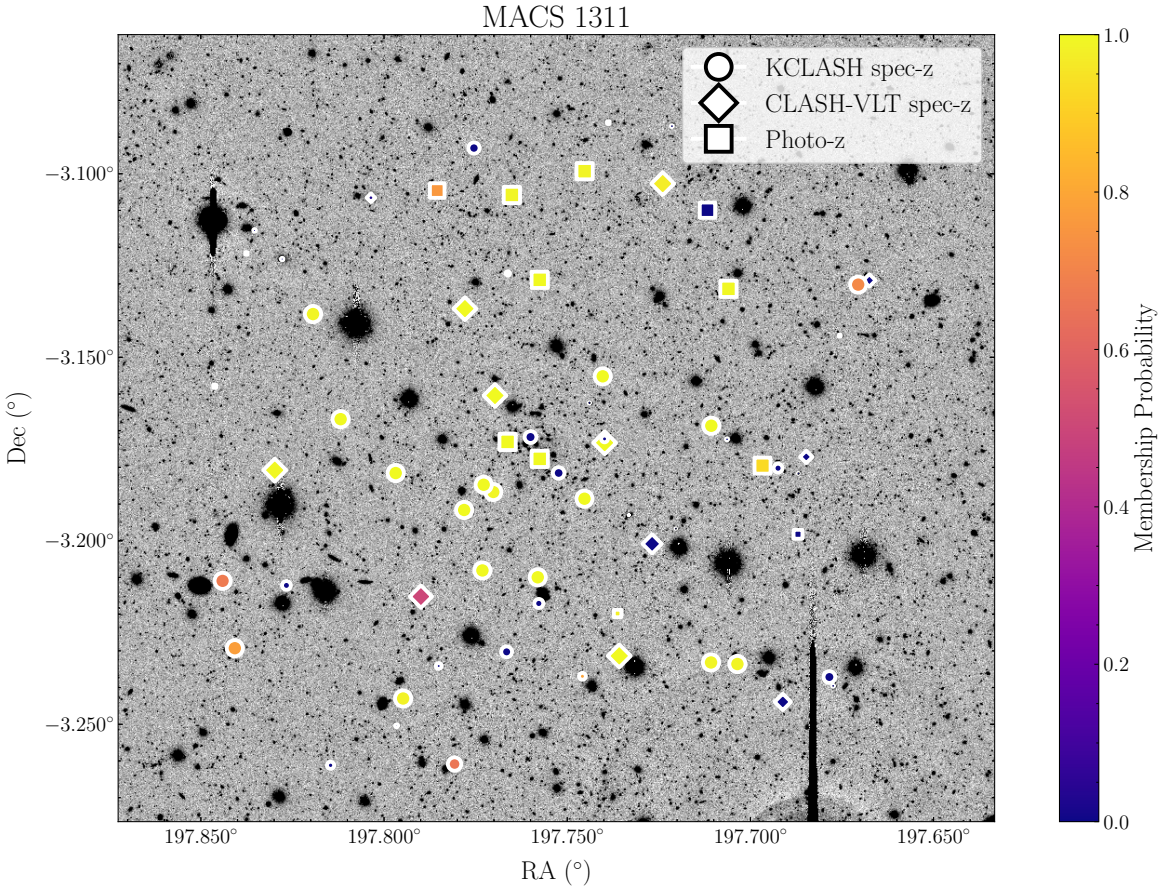

Figure 4.8: All the K-CLASH targets in the MACS 1311 field, plotted over the Subaru Suprime-Cam R_c-band image. Galaxies with a spectroscopic redshift from K-CLASH are shown as circles, whilst those with photometric redshifts are squares. Diamonds refer to redshifts from the CLASH-VLT survey. The size of the symbol decreases as the object's redshift varies from $z = 0.494$, the redshift of the cluster. Each galaxy is coloured by its membership probability, from yellow (likely cluster member) to blue (field).

2017) using its `python` interface (`pyStan`[9]). `Stan` performs full Bayesian inference through Markov-Chain Monte Carlo (MCMC) sampling of the posterior, using an adaptive Hamiltonian Monte Carlo (HMC) algorithm based on the No-U-Turn sampling method of Homan & Gelman (2014). We prefer to use `Stan` and HMC over more familiar MCMC algorithms due to its particular suitability for hierarchical models.

We ran two chains of 5000 steps each, discarding the first 1000 samples as warm-up. We inspected each chain for pathologies, ensuring no divergent transitions, and required that the Gelman-Rubin statistic ($\hat{R}$: Gelman & Rubin, 1992), which estimates MCMC convergence by analysing the difference between multiple chains, was within standard values ($1.0 < \hat{R} < 1.1$).

We tabulate the posterior mean membership probability for each galaxy, as well as a number of posterior percentiles of $p_{\rm membership}$. A plot of the MACS 1311 field, with galaxies colour-coded by membership probability, is shown in Figure 4.8

4.7.1 The Field and Cluster Samples

Using these membership probabilities, we make the following selections:

- Galaxies which are not AGN, have Hα S/N>5 and $p_{\rm membership}$>0.9 form the K-CLASH "Cluster" sample. This selects 22 galaxies.
- Galaxies which are not AGN, have Hα S/N>5 and $p_{\rm membership}$<0.5 form the K-CLASH "Field" sample. This selects 91 galaxies.
- Galaxies which are not AGN, have Hα S/N>5 and $0.5 < p_{\rm membership}$<0.9 form the K-CLASH "Outskirts" sample. This selects 6 galaxies.

These "outskirts" objects are mostly located at R/R_{200}>2.0 with $\Delta V_{\rm galaxy}/\sigma_{\rm cluster}$ very close to 3. A plot of the cluster-centric radius and velocity of all K-CLASH galaxies

[9]PyStan: the Python interface to Stan, Version 2.18.0.0, http://mc-stan.org/users/interfaces/pystan.html

is shown in Figure 4.10. It can be seen that our final cluster sample is, reassuringly, essentially equivalent to the simple cuts of R/R_{200}<2.0 and $\Delta V_{\rm galaxy}/\sigma_{\rm cluster} < 3.0$ mentioned previously. Figure 4.9 shows a histogram of $p_{\rm membership}$ for all K-CLASH galaxies which have Hα S/N>5 and have not been flagged as AGN. We note that reasonable changes to our definition of the field, cluster and outskirts samples (e.g. instead selecting the field sample as $p_{\rm membership}$<0.2) has no effect on our conclusions.

We aim to use K-CLASH to look for evidence of environmental effects in action, by comparing and contrasting properties of the field and cluster samples. However, we must first ensure that our samples are not systematically different in other properties which are known to drive galaxy observables.

Firstly, the samples are slightly mis-matched in stellar mass, with the field sample biased towards more massive objects (as shown in Figure 4.11). The average mass of the field, cluster and outskirts samples are 10.6, 10.3 and 10.7 dex respectively, with standard deviations of 0.5, 0.3 and 0.6 dex.

We therefore create two further samples which we use for comparison with the cluster population:

- Galaxies from the K-CLASH "Field" sample with $9.3 < \log_{10}(\mathrm{M}_*) < 11$ form the "mass-matched Field" sample. This comprises 68 galaxies
- Galaxies from the K-CLASH "Field" sample with $\log_{10}(\mathrm{M}_*) > 11$ form the "high-mass Field" sample. This comprises 23 galaxies

As expected, a two-sided Kolmogorov-Smirnov test fails to reject the hypothesis that the mass-matched field sample and cluster sample are drawn from different distributions ($p = 0.82$).

Figure 4.11 also shows the redshift distribution of each sample. The mass-matched field sample extends to slightly lower and higher redshifts than the cluster galaxies, but the average redshifts are nearly identical ($\langle z_{\rm field} \rangle = 0.448$ and $\langle z_{\rm cluster} \rangle = 0.453$).

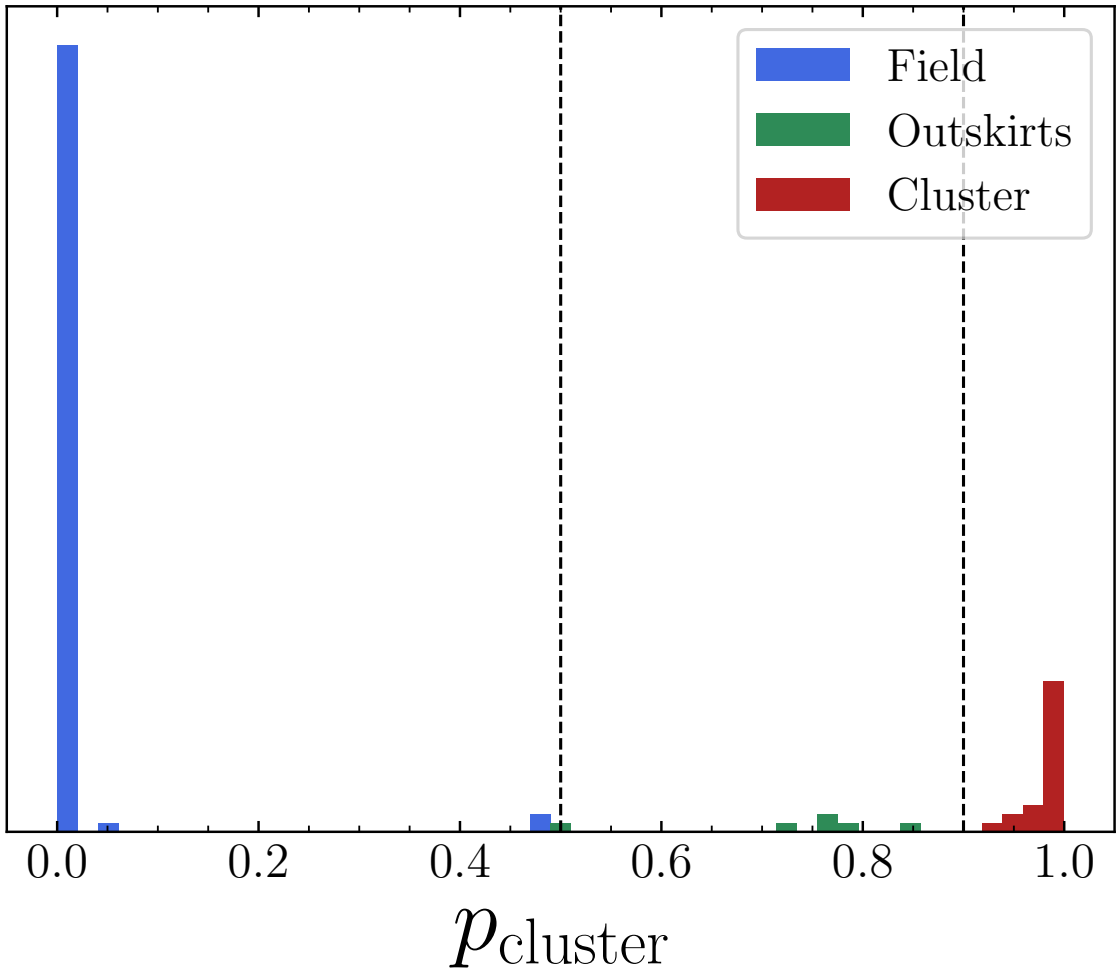

Figure 4.9: The membership probability of all K-CLASH galaxies with Hα S/N>5 and which are not flagged as AGN. Our field sample is in blue ($p_{\rm membership}$<0.5), the cluster sample in red ($p_{\rm membership}$>0.9) and the outskirts sample in green (0.5 < $p_{\rm membership}$<0.9). Dotted lines show $p_{\rm membership}$ = 0.5 and $p_{\rm membership}$ = 0.9. Note that reasonable changes to our selection criteria (e.g. selecting field galaxies as $p_{\rm membership}$<0.2) makes no difference to our overall conclusions.

Since we lack the necessary number of galaxies to create a sample matched in both mass and redshift simultaneously, we simply note that our sample contains an obvious mass-z dependence, and is lacking in low-mass galaxies at high redshift and galaxies more massive than $\log_{10}(M_*) > 10.5$ at $z < 0.3$.

We note that, in total, of the K-CLASH targets with secure spectroscopic redshifts from external sources, 67 reside in their respective galaxy cluster. 45 of these galaxies show little-to-no evidence for very recent star formation, and as such are undetected in Hα from our KMOS observations or have a Hα S/N<5. That such a large fraction of these galaxies are quenched is a consequence of the clear dependence of a galaxy's star formation history on environment: see e.g. Boselli & Gavazzi (2006) and references within. Future analyses could use these objects as upper limits on star formation rates, but we will not do so in this thesis.

4.8 Star Forming Main Sequence

We now plot the star-forming main sequence (MS) of galaxies in the K-CLASH survey. As previously mentioned, the MS is the relationship between star formation rate and stellar mass (see Speagle et al. 2014 for a review and compilation of literature measurements; hereafter S14). For easy comparison with S14, we parameterise the MS as a power law of the form $\log(\mathrm{SFR}) = \alpha \log(M_*) + \beta$.

We fit the relation with a linear "normal" model in `Stan`, incorporating uncertainties on both the x and y variables and estimating the intrinsic scatter. Figure 4.12 shows the fit to all galaxies in the cluster, outskirts and mass-matched field samples, with uncertainties around the best fit line highlighted in orange. Intrinsic scatter is shown in grey. We also plot a number of "consensus" MS relations from the literature, increasing in redshift from $z = 0$ to $z = 1$. Our best-fit parameters are collated in Table 4.2, with a corner plot showing the full posterior in Figure 4.13.

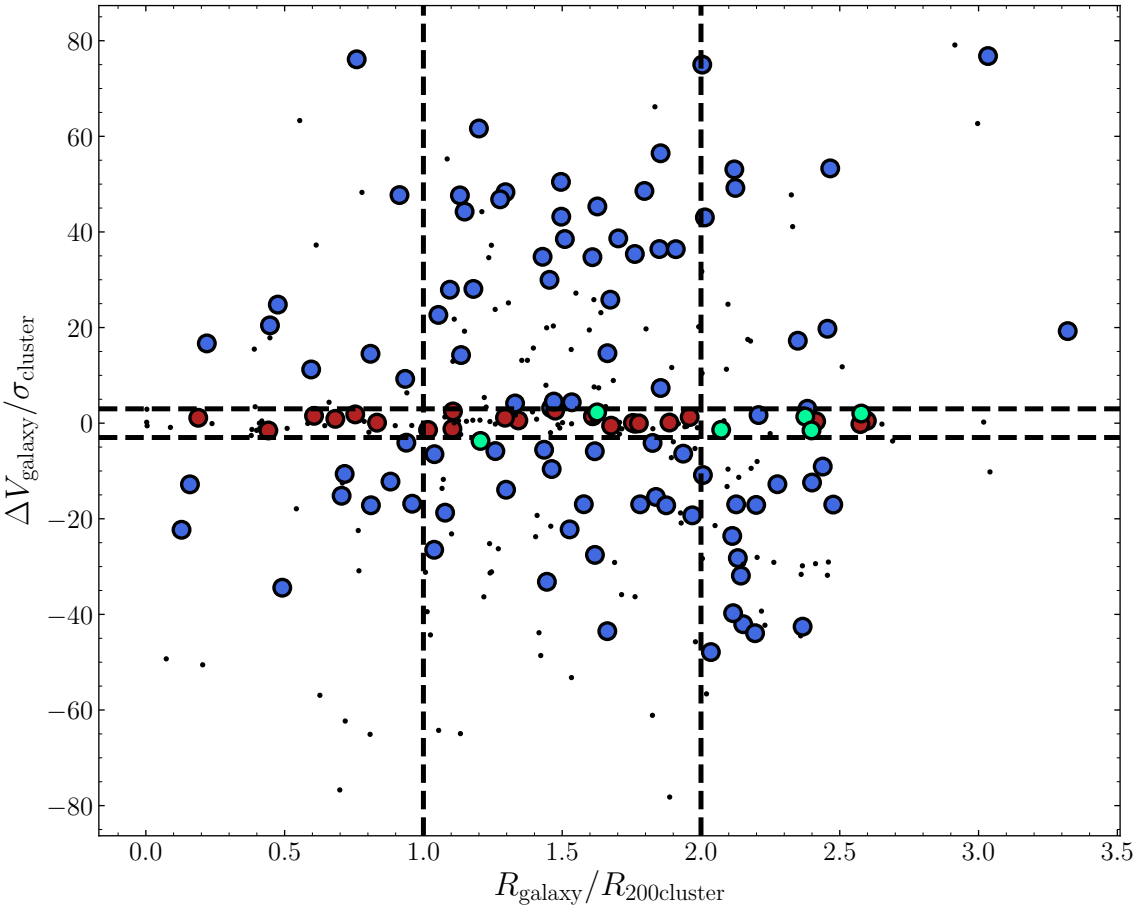

Figure 4.10: A radius-velocity plot for all galaxies in the K-CLASH survey. Galaxies with a spectroscopic redshift from K-CLASH (i.e. Hα detections) are shown as circles, whilst those with photometric redshifts or redshifts from the CLASH-VLT survey are shown as points. Galaxies which form part of the cluster sample are coloured red, the field sample are coloured blue and the outskirts sample are green. We show vertical lines at one and two $R_{\rm galaxy}/R_{\rm 200cluster}$, as well as ± 3 times $\Delta V_{\rm galaxy}/\sigma_{\rm cluster}$.

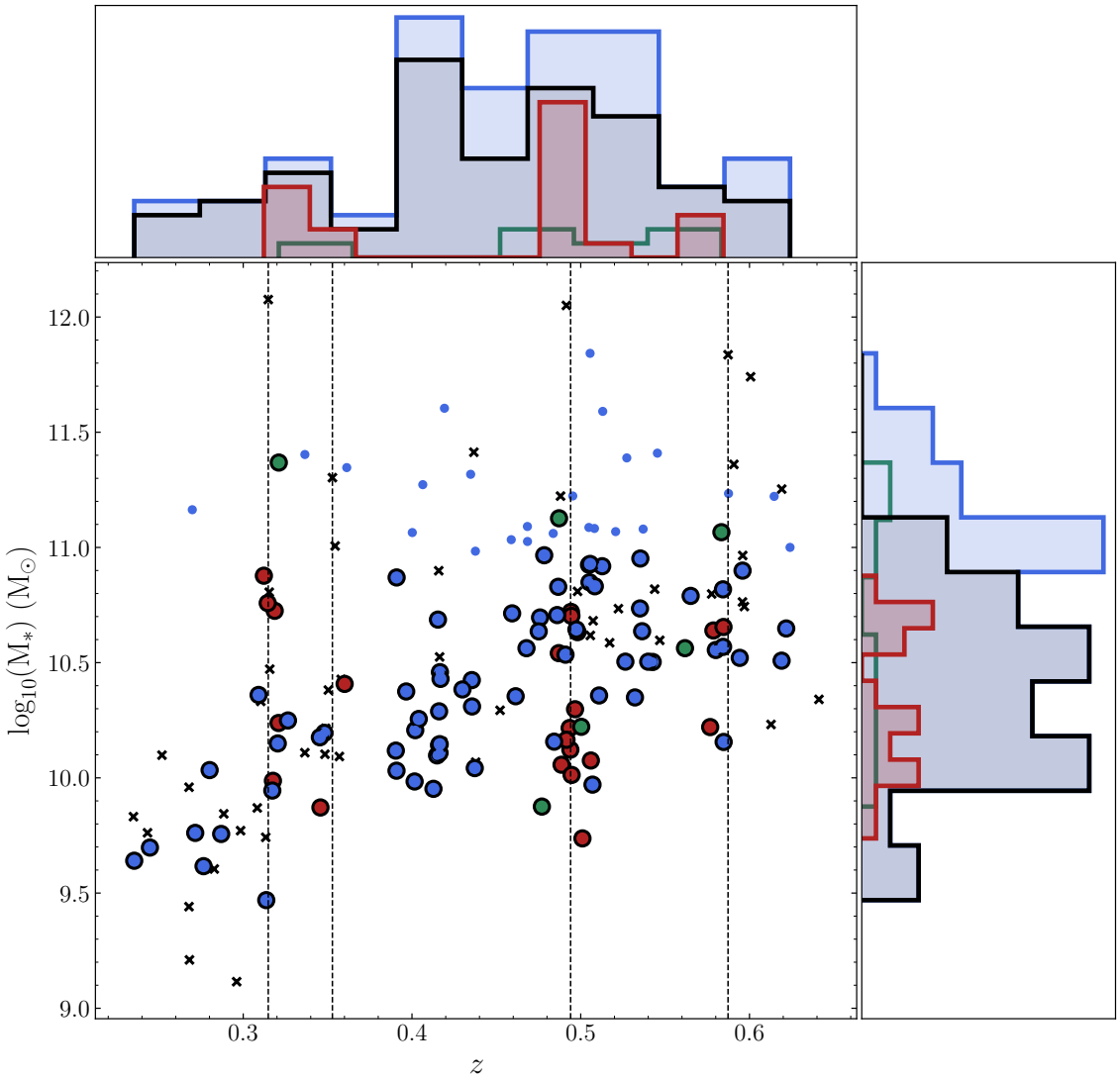

Figure 4.11: The mass and redshift distributions of star-forming samples. The final selection of cluster galaxies (red), mass-matched field galaxies (blue) and outskirts (green) are shown with black outlines. High mass star-forming field galaxies which are not included in the mass-matched sample are shown without an outline. Black crosses are galaxies which have a spectroscopic redshift but are not part of the star-forming sample; they are either below the signal-to-noise cut or classified as AGN. Note that these black crosses are not included in the histograms at the top and on the right. The redshifts of each cluster are marked with dotted lines.

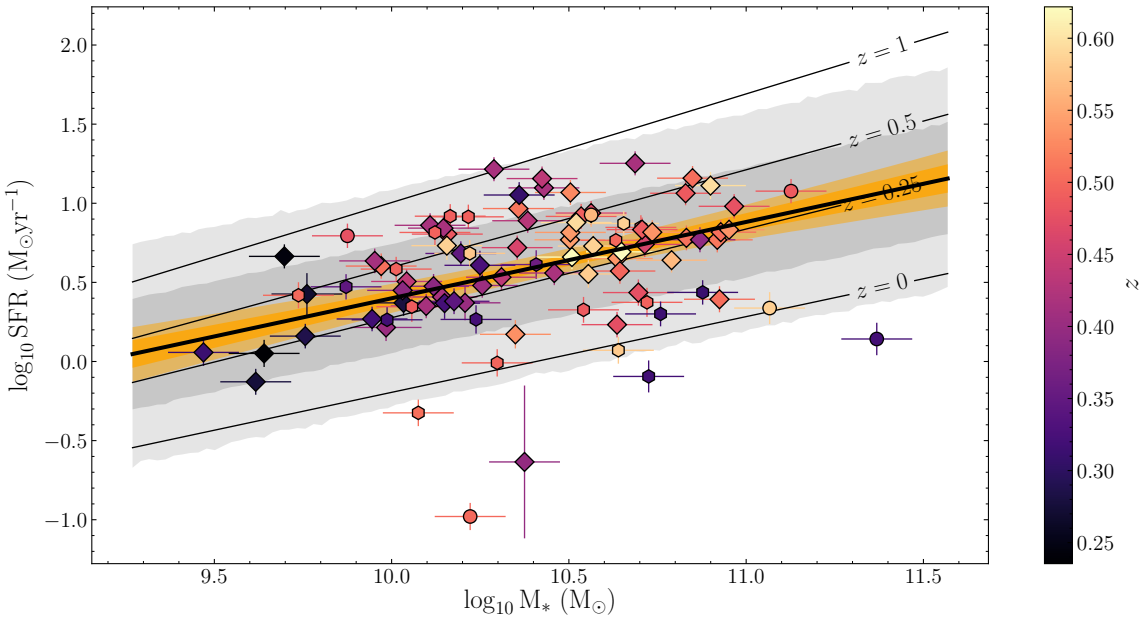

Figure 4.12: The Main Sequence of star formation in the cluster and mass-matched field samples. Field galaxies are plotted as diamonds, the cluster sample as hexagons and the outskirts sample as circles. Each point is coloured by its redshift. The black line shows the best-fit relation from all K-CLASH galaxies, with one- and two-σ uncertainties on the relation shown in orange. Grey shaded regions show the one- and two-σ ranges of intrinsic scatter. Other lines show the "consensus" MS relations compiled from the literature by Speagle et al. (2014) at various redshifts. The intrinsic scatter around the literature relations (not shown) is 0.2 dex, slightly less than the scatter around the K-CLASH relation.

The K-CLASH MS agrees very well with relations in the literature, with the K-CLASH galaxies clearly scattering between the $z = 0.5$ and $z = 0.25$ relations. We do find the slope of the K-CLASH MS relation is slightly shallower than the "consensus" results from S14, which is driven by the SFRs of the most massive galaxies in the sample. We also measure a slightly higher value of intrinsic scatter, which is to be expected given the sample's spread in redshift (the range of redshifts is $0.24 < z < 0.62$). It can be seen that the majority of galaxies below the MS are cluster galaxies (coloured red in Figure 4.13), which we will investigate quantitatively in the next chapter. For now, we simply state that the star formation rates of the star-forming sample mainly lie on the main-sequence at the appropriate redshifts, showing that the K-CLASH selection has resulted in a collection of "normal" star-forming galaxies.

4.9 Concluding Remarks

K-CLASH observations have resulted in 119 spatially resolved data cubes of star-forming galaxies with firm Hα detections (S/N>5), comprising one of the largest samples of IFU observations at intermediate redshifts. In this chapter we have presented the survey, discussing the data reduction, our methods for extracting ancillary photometry, various selections to remove AGN contamination from our sample and our novel method to split galaxies by environment. Our final sample contains 22 cluster galaxies, 91 in the field (with 67 forming our "mass-matched" field sample) and 6 in their cluster outskirts.

We have shown that our observations match the star-forming MS very well at intermediate redshifts, implying that our survey is sampling "normal" star-forming galaxies at $0.2 < z < 0.6$, both in the field and in clusters. In the next chapter, we use the K-CLASH survey to investigate one of its key science goals– how the

α	β	$\Psi_{10.5}$	σ
0.48± 0.07	-4.43± 0.74	0.64±0.04	0.34±0.03

Table 4.2: Best-fit parameters of the K-CLASH MS relation, of the form $\log(\mathrm{SFR}) = \alpha \log(\mathrm{M}_*) + \beta$. $\Psi_{10.5}$ is the (log) SFR of a galaxy with a stellar mass of $10^{10.5}$ $\mathrm{M}_\odot$, measured in dex. σ is the intrinsic scatter around the relation.

environment a galaxy resides in affects its properties.

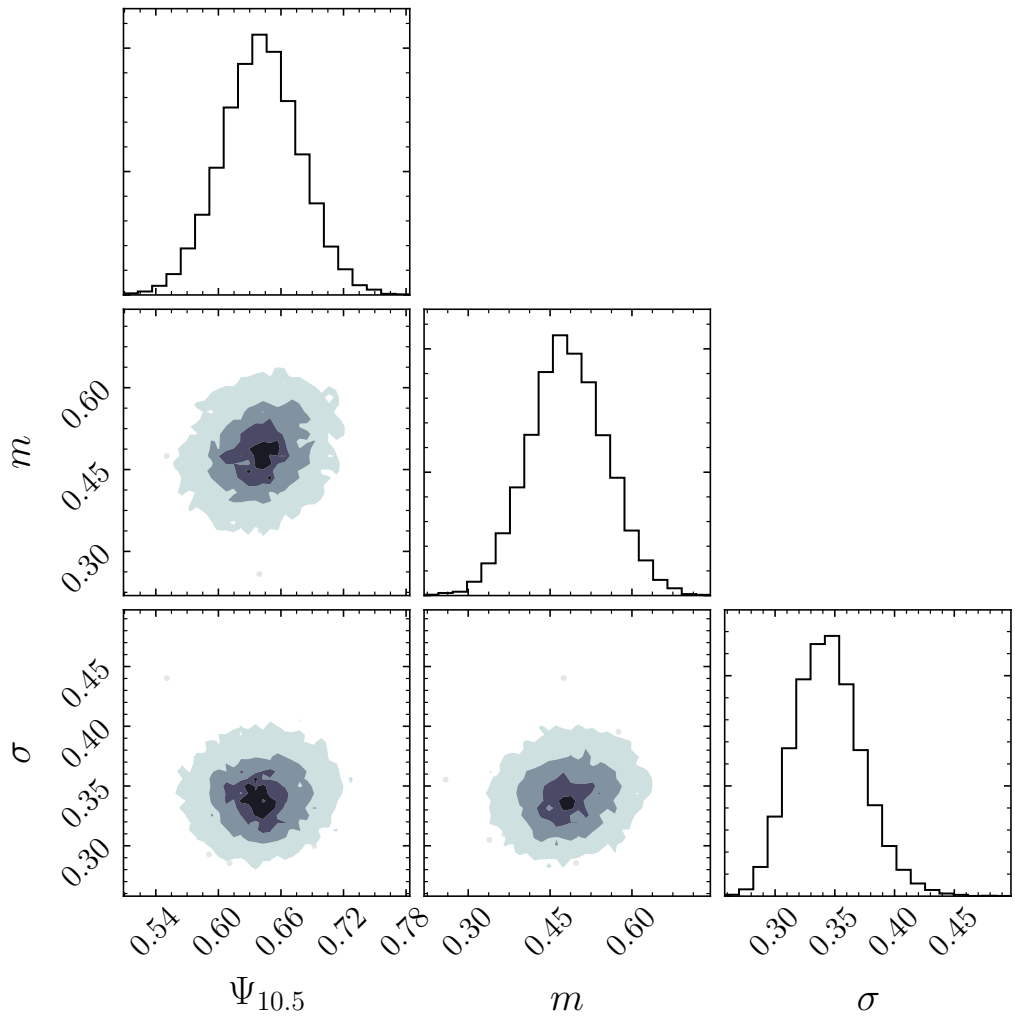

Figure 4.13: The posterior probability distribution of fitting the straight-line $\log_{10}(\mathrm{SFR}) = \mathrm{m}\log_{10}(\mathrm{M}_*/10^{10.5}\mathrm{M}_\odot) + \Psi_{10.5}$ to the MS, with intrinsic scatter σ.

5 | KCLASH: The environmental impact on star-forming galaxies at intermediate redshifts

5.1 Motivation

It has long been understood that the environment in which a galaxy resides plays an important role in its formation and evolution. For many years, we have had strong observational evidence in the local Universe that the physical morphology of a cluster's constituent galaxies is different to the field (Dressler, 1980) and that star-forming galaxies are less common in dense environments (e.g. Gisler, 1978). Current work has extended observations to much higher redshifts, with studies of protoclusters and overdensities between $1.5 < z < 2.5$ becoming common (e.g. Muzzin et al. 2013, Shimakawa et al. 2015, Wang et al. 2016b, Prichard et al. 2017; see Overzier 2016 for a review).

A number of studies have targeted intermediate redshift cluster galaxies, often with spatially unresolved spectroscopy (e.g. recently Rosati et al., 2014; Sobral et al.,

2015; Maier et al., 2016; Morishita et al., 2017). Whilst these studies have the advantage of targeting large numbers of objects and forming statistically significant sample sizes, environmental quenching processes are inherently spatially inhomogeneous. Spectroscopic observations which sample multiple positions at the same time are therefore required to catch these methods of transforming galaxies in the act.

Our view of intermediate to high redshift star-forming galaxies has been revolutionised in the last decade by spatially resolved spectroscopy from the ground (Förster Schreiber et al., 2006; Mancini et al., 2011; Genzel et al., 2011; Wisnioski et al., 2015; Stott et al., 2016; Beifiori et al., 2017) and from space (van Dokkum et al., 2011; Brammer et al., 2012; Schmidt et al., 2014; Treu et al., 2015). These surveys almost exclusively study ionised gas emission, primarily the Hα or [O III]λ5007 lines, resulting in resolved maps of the rate and locations of star formation, two-dimensional maps of the gas kinematics and information on variations in the ISM conditions across individual objects.

There are few studies of this kind, however, which specifically target star formation in cluster members with two-dimensional spectroscopy. Two examples are Vulcani et al. (2015, 2016), who use data from the Grism Lens-Amplified Survey from Space (GLASS) to study the morphology and star formation rates of 76 Hα emitters in 10 CLASH clusters (Postman et al., 2012). They find that Hα emitters are observed with a wide variety of morphologies, including a number undergoing ram-pressure stripping, and that their cluster samples follow a similar mass–star formation rate (SFR) relation to a matched sample of galaxies in the field.

In this chapter, we perform a similar investigation using observations from the K-CLASH survey (presented in Chapter 4). We target 4 clusters from the CLASH sample[1] using the K-band Multi-Object Spectrograph (KMOS; Sharples et al., 2013). Our goal is to find evidence of environmental quenching mechanisms in action, by

[1]Only one, MACS 2129, is also studied in Vulcani et al. (2016)

comparing the properties of cluster and field galaxies observed in a homogeneous way.

In Section 5.2, we study the star-forming Main Sequence relation for field and cluster galaxies. In 5.3 we discuss our method of creating Hα spatial profiles, the R-band continuum images we use, and our fitting method. Section 5.3.1 presents a number of tests regarding the effect of varying S/N, finite IFU size and galaxy location within the IFU on the sizes we measure. The results of our size measurements are shown in Section 5.3.2. In Section 5.4 we lay out our method of measuring emission line fluxes and ratios, as well as our method of stacking spectra of individual galaxies, and discuss the results of our measurements in Section 5.4.1. We place our results into context and discuss the physical implications of our findings in Section 5.5, before drawing our conclusions in Section 5.6.

5.2 The SFR-M$_*$ relation as a function of Environment

In Chapter 4, we presented the star-forming "Main Sequence" (MS) relation for our sample, plotting the integrated star formation rate (SFR) of each galaxy against its stellar mass. Here, we investigate whether the SFRs of galaxies in the cluster sample are significantly different to those in our field sample.

Our measurements are discussed in Section 4.6. To briefly recap, we extract a spectrum from an elliptical aperture centred on the continuum emission in each object. The ellipticity of the aperture is measured from the Subaru R_c band image, and the semi-major axis of the aperture is such that its area is the same as a circular aperture of 1.2″ diameter ($\pi \times \frac{1.2}{2}^2$). We then use `pPXF` (Cappellari & Emsellem, 2004b; Cappellari, 2017) to measure the flux of the Hα emission line, estimating the uncertainty by adding noise to the best-fit template and remeasuring the flux 1000

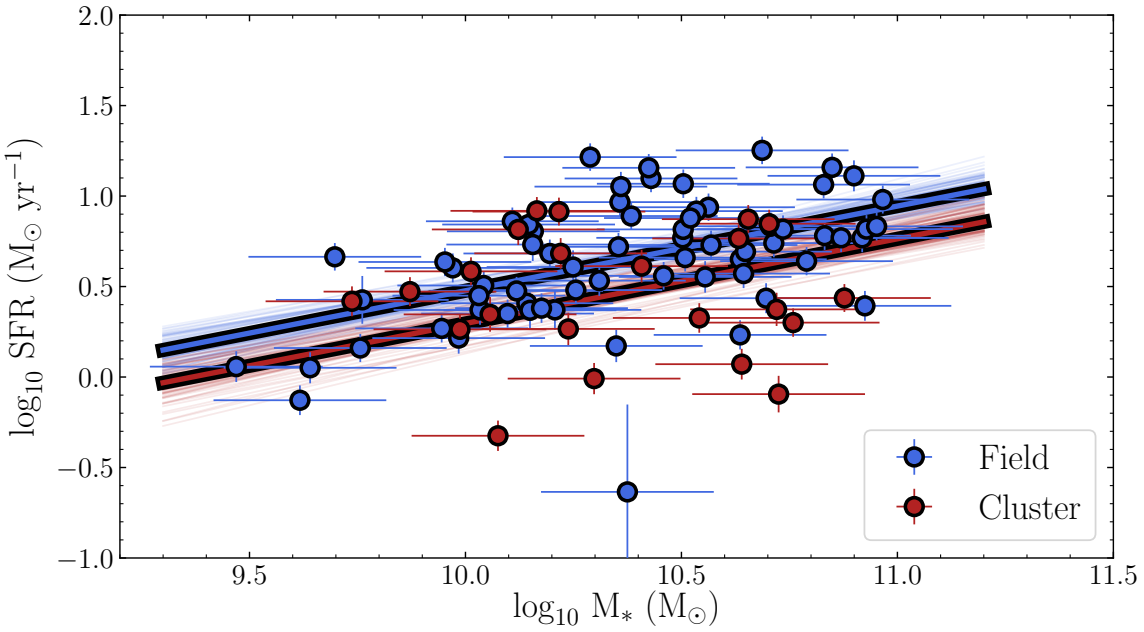

Figure 5.1: The star forming main sequence, split by environment. Field galaxies are shown in blue whilst cluster objects are in red. The best-fit MS relation (fixing the slope for the two populations) are shown as blue and red solid lines. 100 draws from the posterior distribution, shown as thin lines, characterise the uncertainties around each fit.

times. We use the measure of dust-extinction from the SED fitting (Section 4.5) to correct each flux measurement, and use the conversions of Hao et al. (2011) and Murphy et al. (2011) to infer a SFR.

We then fit a straight line of the form $\log_{10}(\mathrm{SFR}) = \alpha \log_{10}\left(\frac{\mathrm{M}}{10^{10.5}}\right) + \Psi_{10.5}$ for the cluster and field samples, forcing the same slope for both (equal to the best-fit slope found for all galaxies in the star-forming sample, measured in Section 4.8) but allowing for independent intercepts. $\Psi_{10.5}$ corresponds to the log(SFR) for a galaxy with log(M) = 10.5. We perform the fit using `Stan` (Carpenter et al., 2017), which performs Hamiltonian Monte Carlo sampling of the posterior probability distribution. This fit incorporates errors on both the x and y variables. Our results are shown in Figure 5.1

We find that $\Psi_{10.5}$ is 0.531±0.065 for the cluster sample and 0.710±0.037 for the

field. Plots of the marginalised posterior of $\Psi_{10.5,\mathrm{cluster}}$ and $\Psi_{10.5,\mathrm{field}}$ are shown in Figure 5.2. This difference ($\Delta\Psi_{10.5}$) of $\sim$ 0.18 dex corresponds to a factor of 1.5 smaller SFRs in star-forming cluster galaxies than the comparison field sample, and is significant at the 2.4σ level.

To investigate how the aperture size influences the difference in Main Sequence intercept, we also extracted spectra from an aperture of area $\pi \times \frac{0.6}{2}^2$ square arcseconds, corresponding to the central regions of each object. We constructed the main sequence in the same way as in Section 5.2, finding that $\Psi_{10.5}$ is -0.131$\pm$0.040 dex in the field sample and -0.268$\pm$0.068 dex for the cluster objects ($\Delta\Psi_{10.5}$ = 0.13 dex, significant at the 1.7σ level).

If the *centres* of the star-forming galaxies in the cluster and field populations had the same star formation rate surface densities (Σ_{SFR}), we'd expect $\Psi_{10.5}$ to be the same value for both samples– i.e. $\Delta\Psi_{10.5}$ would be zero when investigating the smaller apertures. Physically, this would be the case if the environmental effects leading to an offset main sequence in the cluster sample were confined to the outskirts of galaxies.

On the other hand, the environment might be influencing the SFR *throughout* each cluster galaxy, leading to a suppressed Σ_{SFR} at all radii. If this was the case, we'd expect the difference in $\Psi_{10.5}$ to remain the same for the small and large apertures– i.e. $\Delta\Psi_{10.5}$ would be $\sim$ 0.2 dex in both cases.

As it happens, neither of these simple pictures are entirely correct. $\Delta\Psi_{10.5}$ is smaller when using a central aperture than a large one, but not consistent with zero. This is perhaps an indication that, as might be reasonably expected, multiple environmental effects contribute to the quenching of cluster galaxies at the same time. It should also be noted that we are unable to take into account the effects of local variation in dust extinction within each galaxy. The conversion from Hα flux to SFR for both the small and large apertures assumes the same global extinction value. We have also not attempted to construct a *resolved* SFR Main Sequence relation– we do

not attempt to measure the stellar mass inside the smaller aperture, using the total mass of each galaxy in both analyses.

Comparison to other studies

Measuring the SFRs of actively star-forming galaxies in clusters has resulted in a number of contrasting results in the literature. A number of studies find, in agreement with this work, that currently star-forming cluster galaxies have reduced star formation rates compared with the field. In the local Universe, von der Linden et al. (2010) use SDSS observations to show that the typical SFR of non-quiescent galaxies is a factor of 2 lower in the centres of clusters (0.3 dex), whilst Haines et al. (2013) find the average star formation rate of massive cluster galaxies ($M_* > 10^{10}$ $M_\odot$) are $\sim 28\%$ (0.15 dex) lower than the field at $0.15 < z < 0.3$. At similar redshifts to this study ($0.4 < z < 0.8$), Vulcani et al. (2010) and Patel et al. (2009) also find that the SFRs of star-forming galaxies are reduced by factors of 1.5 – 2. The same correlation has been found in galaxy groups as well as clusters; see Schaefer et al. (2019), who find galaxies in high-mass groups have smaller specific SFRs (sSFR) by a factor 0.45 dex compared to those in lower mass groups.

On the other hand, some authors have concluded that a galaxy's environment has no effect on its instantaneous SFR. For example, Peng et al. (2010) found that a galaxy's SFR is completely independent from its environment, and is only influenced by its stellar mass. Similarly, at $z = 0.8$ Sobral et al. (2011) show that the average SFR across cluster galaxies more massive than $10^{10.6}$ $M_\odot$ is the same as in the field, and Darvish et al. (2016) found no difference in the median SFR of field and cluster galaxies between $0 < z < 3$. These authors argue that it is only the *fraction* of star-forming galaxies which decreases with increased environmental density, rather than the star-forming properties of all cluster galaxies as a whole (see also Balogh et al. 2004 and Wetzel et al. 2012)

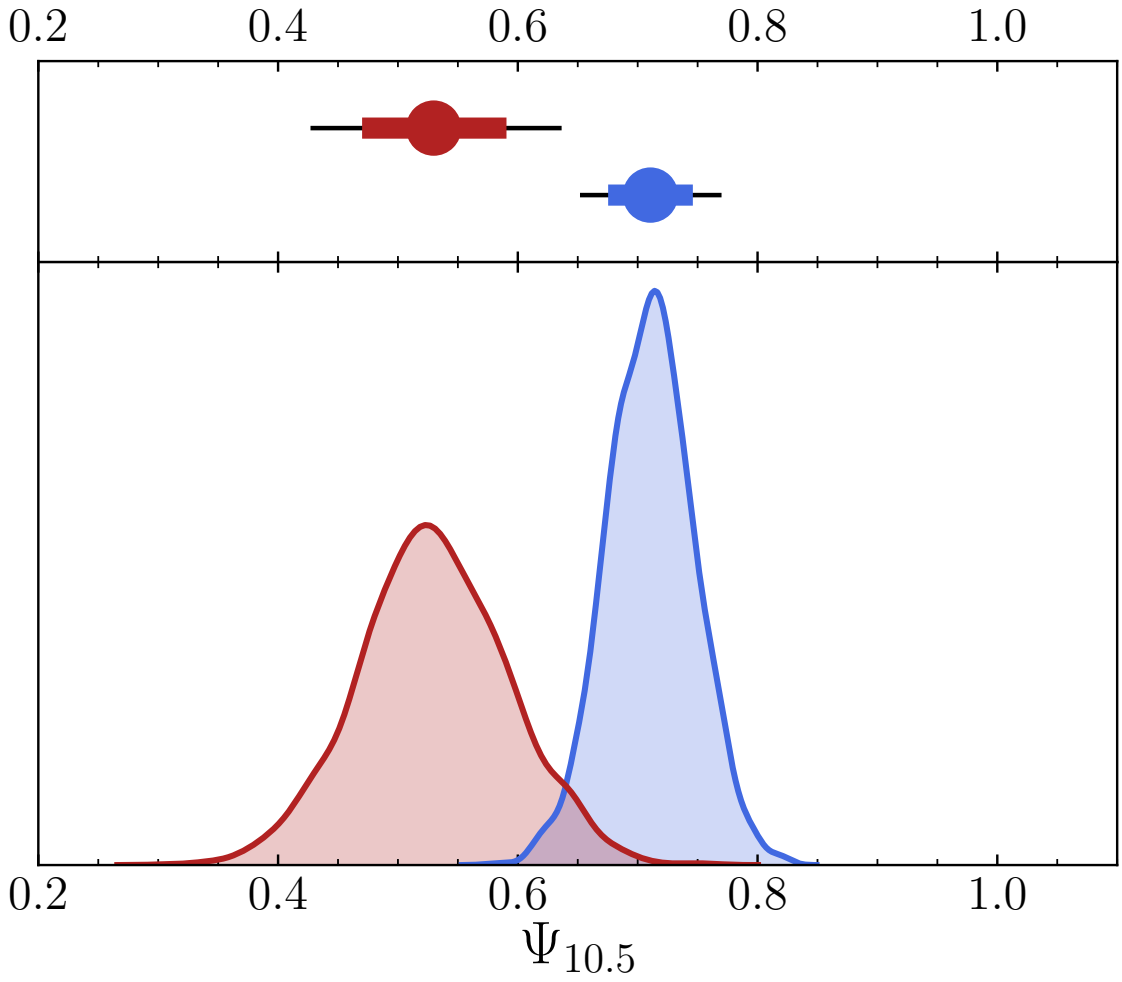

Figure 5.2: The marginalised posterior of $\Psi_{10.5}$ for the cluster and field galaxies. The field values are in blue and the cluster values in red. The top panel shows the 16^{th}-84^{th} percentile range (thick coloured line) and the 5^{th}-95^{th} percentile range (thin black line). The bottom panel shows a kernel-density estimation (KDE) approximation to the posterior.

Since it is clear that cluster environments do quench their star-forming members, observations like these give us information about the timescale of such quenching. If quenching takes place instantaneously, for example, then we'd expect to see identical star-forming main sequence relations, with star-forming cluster galaxies simply dropping out and appearing in the quenched population. On the other hand, if quenching takes place over an appreciable time-scale (∼Gyrs), then we'd see populations of galaxies in the middle of quenching, resulting in the MS relation being offset to lower values of $\Psi_{10.5}$. As discussed in Schaefer et al. (2019), the disagreement between various studies is almost certainly caused by the different star-forming indicators and observational depths– i.e. which galaxies are classified as "star-forming" (see also Taylor et al. 2015).

5.3 Measuring Hα sizes

Utilising the spatially resolved nature of the KMOS observations of each galaxy, we now measure the extent of Hα emission in each object, a proxy for the spatial extent of star formation. In short, this involves measuring the point-spread function (PSF) of the detector, creating an Hα emission line map and then fitting this map with a model light profile.

The KMOS PSF represents the response of the instrument to a point-like input signal. The observing programme required at least one KMOS arm to target a star in the field of view for each observing block (OB), allowing us to measure the PSF. These stellar observations were then reduced in the same way as the science data (Chapter 4), including co-adding multiple observations of the same object over separate OBs. We then collapse the final reduced cube along the wavelength direction to make an image, which we use during the fitting process.

To characterise variation in the PSF, we fit a two dimensional Gaussian model to

each collapsed PSF image. We find the average FWHM of these images across all K-CLASH fields is 0.78″, with standard deviation 0.15″.

The KMOS instrument comprises of three separate spectrographs, which disperse the light from arms 1-8, 9-16 and 17-24 respectively. It has been reported that the PSF can vary slightly between the spectrographs (e.g. Magdis et al., 2016), and so it is important to investigate whether any systematic differences exist which could impact our results. We find that the standard deviation of the average FWHM in each spectrographs is very small, at 0.02″. The best-fitting σ_x and σ_y values for each star observation are shown in Figure 5.3, coloured by the spectrograph it was observed in. We find that the PSF is generally circular, with no evidence that one spectrograph is markedly different from the others. The largest variation in $\sigma_{x,y}$ is around a pixel (0.2″), which is to be expected from variations in the observing conditions between different nights. Where possible, we use the PSF image observed in the same spectrograph as the science data.

We also investigate the wavelength dependence of the KMOS PSF. To do this, we collapse the arm-star observations in a window of width 0.05μm in the wavelength direction (instead of averaging over the entire wavelength range) and proceed as before to fit a two-dimensional Gaussian function. This is repeated six times for increasing central wavelengths. The average results for each spectrograph are shown in Figure 5.4. We find that the PSF improves by around 0.2 spaxels (0.04″) between the start and end of the IZ band spectral range, which is a negligible effect.

To construct the Hα line-map, we sum the flux in the data cube in a small spectral window around the appropriate wavelength and then subtract the stellar continuum. We have found that a width of 10 Å either side of the Hα line centre in the observed frame (rest frame 6563 Å) works well to select the Hα flux whilst disregarding the [NII] lines at 6548 and 6583 Å. The full width of this window corresponds to width in velocity of 750kms^{-1} at an observed wavelength of 0.8μm and 571kms^{-1} at 1.05μm.

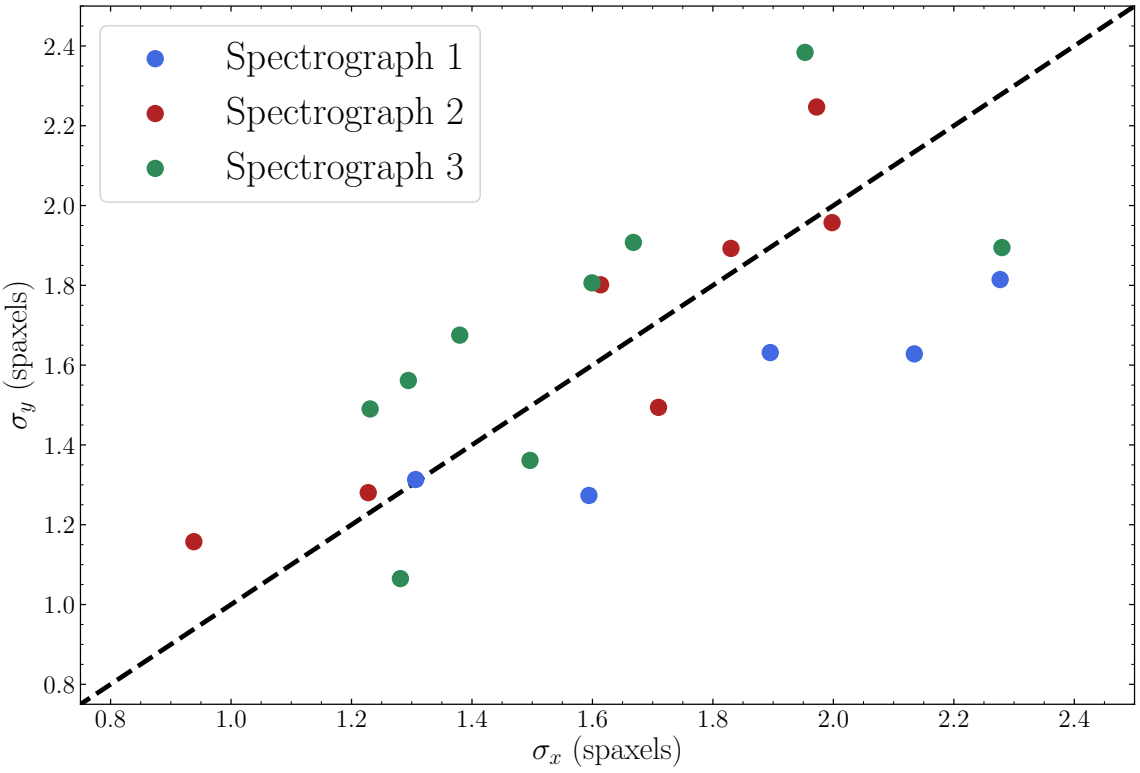

Figure 5.3: The standard deviation (σ_x and σ_y) of the two-dimensional Gaussian fit to each star observed during the K-CLASH survey. Points are coloured by the KMOS spectrograph they were observed in. The standard deviation varies by around a spaxel ($0.2''$) across all observations, consistent with fluctuations in the observing conditions. We see no systematic offset between different spectrographs.

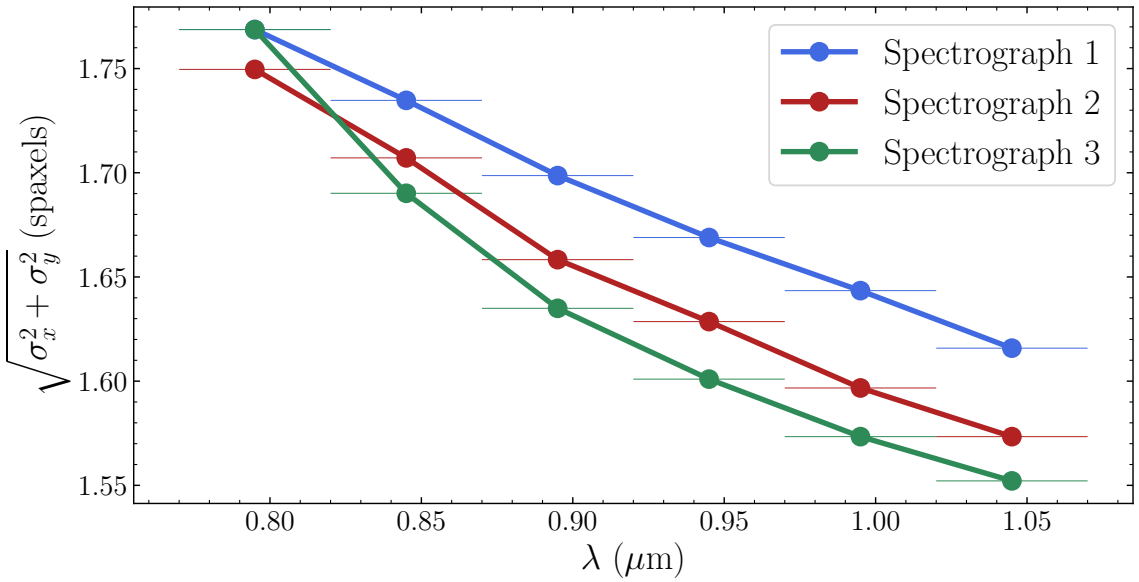

Figure 5.4: The average "circularised" standard deviation ($\sqrt{\sigma_x^2 + \sigma_y^2}$) of the Gaussian fits to each star observed during the K-CLASH survey as a function of wavelength. Points are coloured by the KMOS spectrograph they were observed in. Each image was constructed by collapsing the full data-cube in a window of 0.05μm in the wavelength direction. The size of the PSF varies by around 0.2 spaxels (0.04″) across the IZ spectral range, and less than 0.1 spaxels (0.02″) between spectrographs.

The continuum flux is estimated by fitting a low-order polynomial to each spaxel in the datacube. To avoid bad pixels, skylines and the Hα emission itself biasing the continuum estimation, we iteratively sigma-clip the spectrum during the fitting, discarding outlying pixels and then fitting again to the remaining values. We use a fourth order polynomial, fit with three iterations whilst discarding 2σ outliers, but reasonable changes to these values do not affect our conclusions. An example line map, with representative spectrum showing the continuum and Hα spectral window, is shown in Figure 5.6.

An important consideration in measuring the size of Hα emission is the minimum surface brightness our observations are sensitive to. We estimate the limit to which we can detect Hα emission with KMOS by taking the median noise spectrum in each datacube and integrating this across the same spectral window used for the Hα emission. Our 3σ detection limit is of the order of 1×10^{-15} erg s^{-1} cm^{-2} arcsec^{-2}, which varies from between 4×10^{-15} erg s^{-1} cm^{-2} arcsec^{-2} at worst to 4×10^{-16} erg s^{-1} cm^{-2} arcsec^{-2} for the best observations. This is around three orders of magnitude shallower than the deep stacked Hα images from *HST* grism spectroscopy studied in Nelson et al. (2016b), which reach 1×10^{-18} erg s^{-1} cm^{-2} arcsec^{-2}, and the local MUSE observations of local ram-pressure stripping events from the GASP survey Poggianti et al. (2017) which are sensitive to a limiting surface brightness of 2.5×10^{-18} erg s^{-1} cm^{-2} arcsec^{-2}.

We also convert these Hα surface brightness values to SFR surface densities ($\Sigma_{\rm SFR}$) without correcting for dust extinction (using the relation of Hao et al. 2011 and Murphy et al. 2011; equation 4.6). Figure 5.5 shows the 3σ limiting $\Sigma_{\rm SFR}$ for each galaxy in our sample, which is $\sim$0.04-0.05 M$_\odot$ yr^{-1} kpc^{-2} for galaxies with $\lambda_{\rm H\alpha} > 0.9\mu$m. At low redshift, we see that the decreased sensitivity of the detectors in the KMOS IZ band mean that our observations of galaxies at $z \sim 0.3$ are roughly as deep as those at $z \sim 0.5$. These $\Sigma_{\rm SFR}$ are comparable to those of other IFU studies at

$z \sim 1-2$ (Genzel et al., 2011; Stott et al., 2016), although shallower than *HST* grism studies at intermediate redshifts (e.g. Vulcani et al. 2015 reach 0.01 $M_\odot$ yr^{-1} kpc^{-2}).

Hα spatial profiles

With high resolution broad-band and narrow-band imaging, the spatial structure of continuum light (e.g. Elmegreen & Elmegreen, 2005) and Hα emission (e.g. Shapley, 2011; Nelson et al., 2012) in some high redshift galaxies has been found to be clumpy and disturbed, in contrast to the smooth and ordered star formation seen in spiral galaxies today. For this reason, a number of studies use a curve-of-growth method to estimate the half-light radius of a galaxy's Hα flux (e.g. Nelson et al., 2012; Magdis et al., 2016). This approach has some drawbacks, however. Low signal-to-noise Hα flux at the outskirts of the galaxy may be missed, and the effects of spurious "hot" pixels in the line map are counted as real Hα emission if not properly masked. Furthermore, the seeing-limited nature of our observations means we are also unable to distinguish distinct clumps of Hα emission on scales smaller than the PSF, making these systems appear to follow a smooth, disk-like surface brightness profile. We therefore choose instead to fit model light profiles to our Hα line maps, in a similar way to Nelson et al. (2016b) and Wisnioski et al. (2018). We also note that this choice will have less of an impact on our intermediate redshift study ($0.2<z<0.6$) compared to work at higher redshift.

We fit the Hα surface brightness profiles using the publicly available code IMFIT[2] (Erwin, 2015). IMFIT creates two-dimensional surface brightness profiles and fits these to data through a choice of minimisation techniques. In this case, we use IMFIT to fit exponential disk profiles to our Hα line maps. Each model light profile was convolved with an observation of the PSF (from KMOS arms placed on stars in the field of view) during the fitting process. Three example fits are shown in Figure 5.10. Uncertainties

[2] `http://www.mpe.mpg.de/~erwin/code/imfit/`

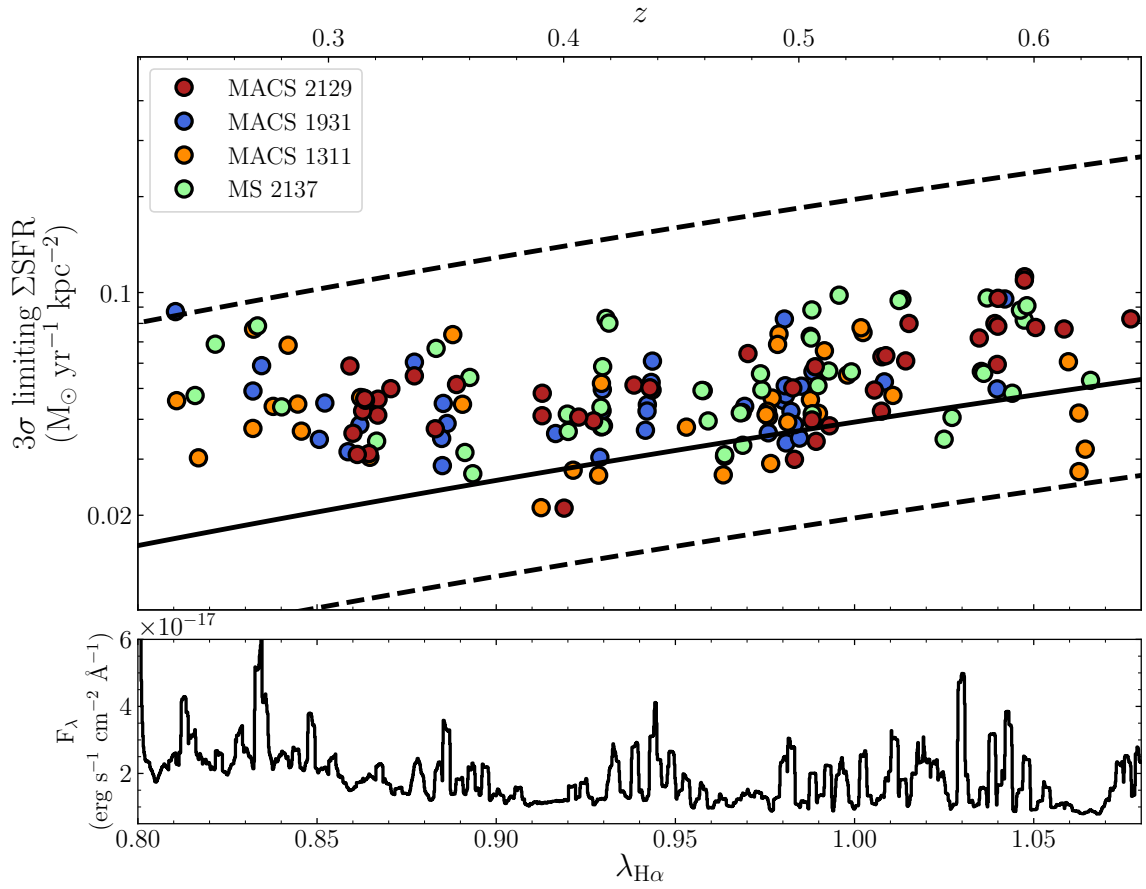

Figure 5.5: Top: The limiting star formation rate surface density ($\Sigma_{\rm SFR}$) as a function of the observed Hα wavelength for each galaxy in our sample. Galaxies are coloured by the CLASH field they are observed in. Solid lines show how a fixed background surface brightness (of 4×10^{-15}, 7.5×10^{-16} and 4×10^{-16} erg s^{-1} cm^{-2} arcsec^{-2}) translates to a variable $\Sigma_{\rm SFR}$ (in M$_\odot$ yr^{-1} kpc^{-2}). Bottom: a representative spectrum showing how the background flux varies as a function of wavelength (due to strong sky emission lines and decreased sensitivity at the blue end of the IZ band). During the creation of the Hα images, we infer the uncertainty in each pixel's flux value by taking the RMS of the noise spectrum in a 20 Å window around Hα. The bottom plot is created by taking a representative noise spectrum and plotting these RMS values (in a rolling 20 Å window) as a function of wavelength. The observations with lowest background noise (around 0.92μm and 1.065μm) correspond to gaps between skylines. Low-z observations are affected by the higher average noise level below 0.9μm due to the decreased KMOS IZ band sensitivity.

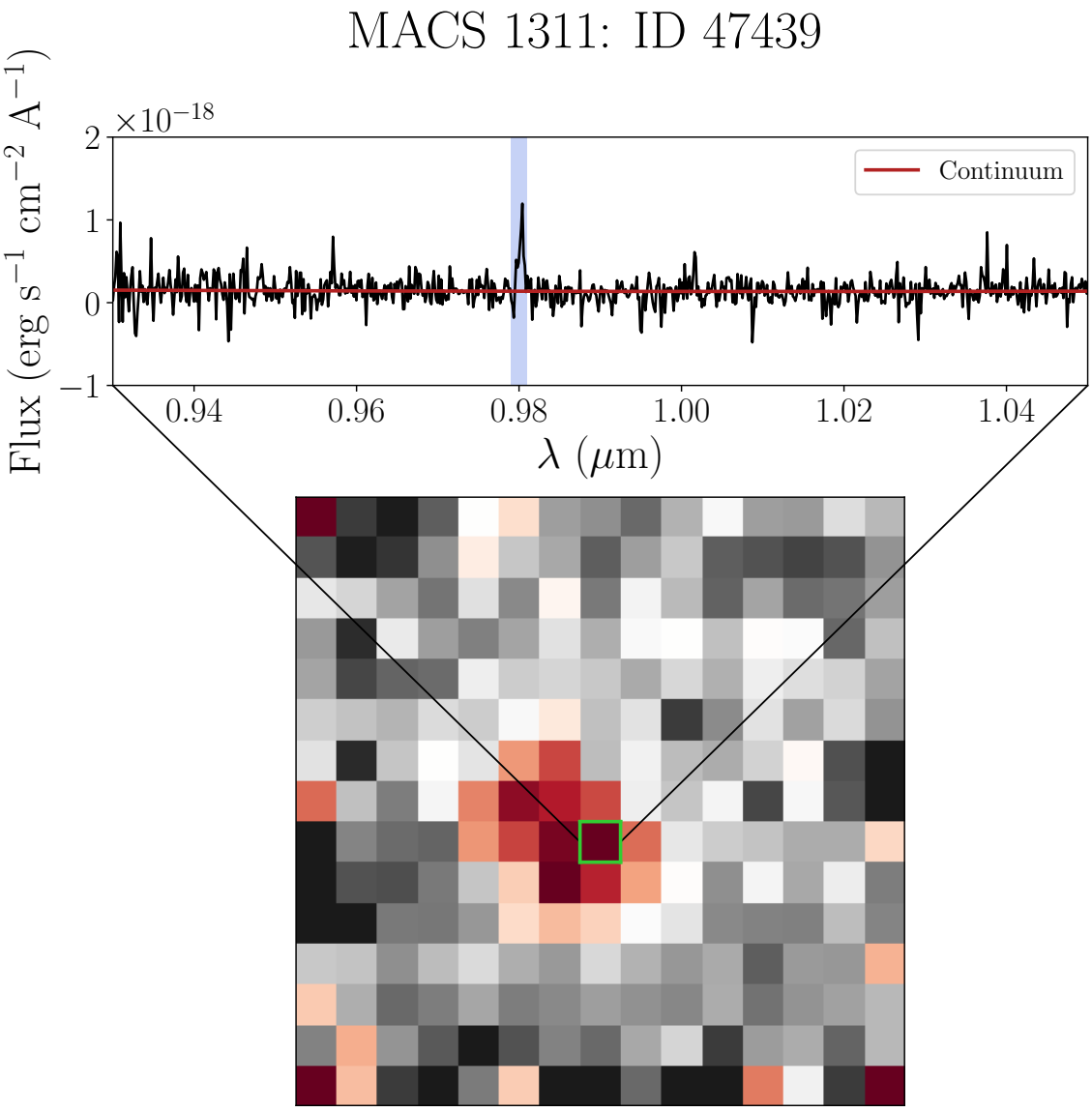

Figure 5.6: An example Hα line map for galaxy MACS 1311: ID 47439. The top panel shows the Hα spectral window (blue) and fit to the continuum (red).

on fitting parameters were estimated using 1000 bootstrap resamples of the original image.

Each KMOS IFU has a field of view of 2.8″ square, which corresponds to 9.5 and 20.3 kpc at the lowest and highest redshifts of our targets respectively. As we show in Section 5.3.1, we are able to recover the size of mock observations larger than the field of view in high S/N data. We also note that, in their study of Hα emitters at $0.3 < z < 0.7$, Vulcani et al. (2016) found no objects with Hα effective radii larger than 10kpc, implying that all of their targets would fit into a KMOS IFU. We therefore conclude that whilst our limited field of view may be missing flux for the most spatially extended Hα emitters, we do not expect this to affect our conclusions.

Continuum imaging

Each K-CLASH field has been targeted with deep Subaru Suprime-Cam observations. Suprime-Cam (Miyazaki et al., 2002) has a 34′x27′ field of view which was mosaic-ed over the cluster to provide much wider field images than are possible with *HST*. The data were reduced and analysed in Umetsu et al. (2014), as well as independently in von der Linden et al. (2014), using reduction methods described in Nonino et al. (2009) and Medezinski et al. (2013). The images are publicly available from the CLASH archive[3].

We use the Suprime-Cam R_c band imaging to measure the surface-brightness profiles of each K-CLASH galaxy, since these bands are available without having been convolved to the same limiting PSF (PSF-matched) before stacking. Instead, the R_c band images we use were stacked individually for each epoch and camera rotation angle, making them most appropriate for measuring galaxy shapes (for a weak lensing analysis) and light profiles.

Similarly to the Hα linemaps, we used IMFIT to fit model profiles to each galaxy

[3] `https://archive.stsci.edu/prepds/clash/`

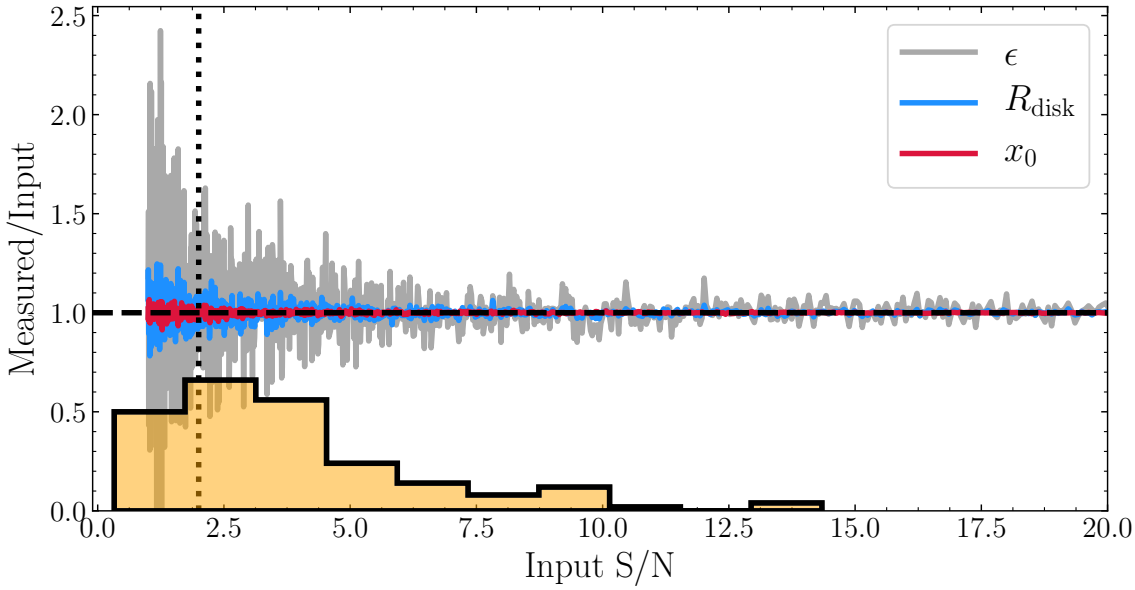

Figure 5.7: Recovering the Hα profiles of mock observations, at various input S/N values of the Hα images. Note the image S/N values are the *average* value within the best-fit half-light radius. The dashed line represents an average image S/N of 2, and the histogram shows the S/N distribution of our Hα images. See Section 5.3.1 for details.

cutout. A median stack of hundreds of stars in each field was used as the PSF estimate during the fitting process. The seeing varied between 0.6-0.9″ in the four K-CLASH fields. In contrast to the Hα spatial modelling, however, we allowed the Sérsic index of the light profile to vary between 1 and 4, corresponding to an exponential disk and peaked, ETG-like profile respectively. Examples for three galaxies are shown in Figure 5.10. Uncertainties were again measured using 1000 bootstrap resamples of the input data.

5.3.1 Signal-to-Noise tests

To test the robustness of our Hα spatial profile measurements, we created mock datacubes with model Hα profiles and fit them in exactly the same way as real observations. The mock cube contains an exponential surface brightness profile convolved with the KMOS PSF, and spectra comprising both continuum and emission line com-

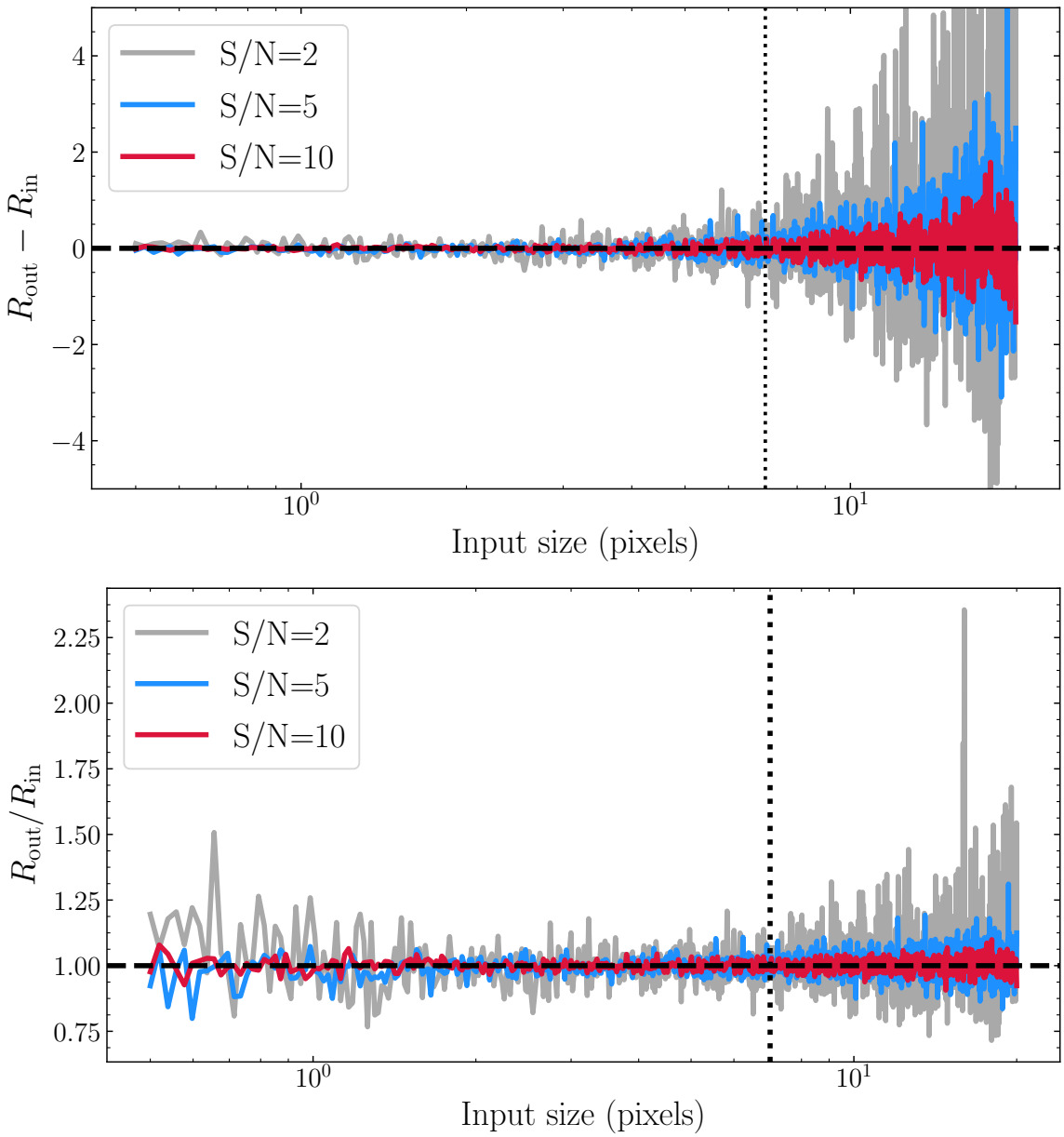

Figure 5.8: Recovering the Hα disk scale length ($R_{\rm disk}$) of mock observations, for various input sizes. The dashed line represents the size of the KMOS IFU for a source placed in the centre (7 pixels). The top panel shows the difference between the input and output scale lengths, whilst the bottom shows the *fractional* difference between $R_{\rm out}$ and $R_{\rm in}$. See Section 5.3.1 for details.

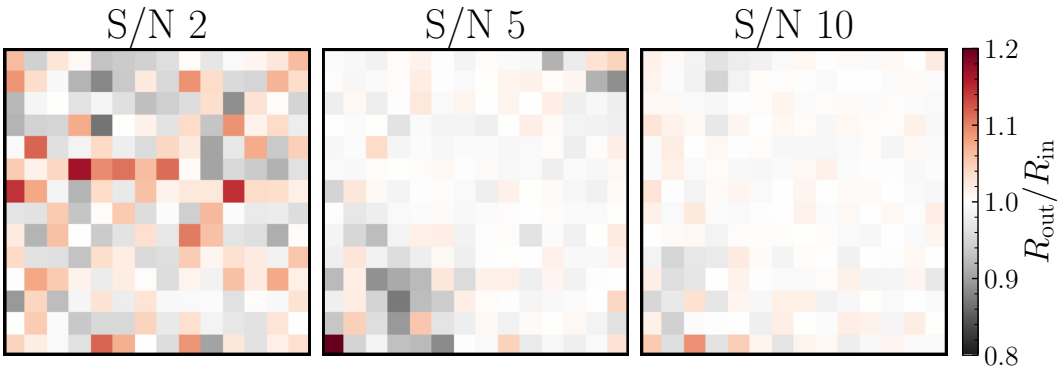

Figure 5.9: Recovering the Hα disk scale length ($R_{\rm disk}$) of mock observations, for various locations on the IFU. The model is a source of $R_{\rm disk} = 3$, $\epsilon = 0.2$ and position angle 135°. See Section 5.3.1 for details.

ponents. Random noise is added to a given signal-to-noise level. We fix the linewidth of the Hα emission to be 100kms^{-1} and the peak height to be twice the level of the continuum. Note that these simulations do not model the effect of sky-subtraction residuals on our measurement process.

These results are shown in Figures 5.7, 5.8 and 5.9. Figure 5.7 shows that estimating $R_{\rm disk}$ requires a larger S/N than simply finding the Hα flux centre, but is easier than constraining the galaxy ellipticity (ϵ). A histogram of the S/N ratio of our data is shown in orange. We find that to recover the input disk scale radius ($R_{\rm disk}$) to an accuracy better than 10%, we require the average S/N within the best-fit half-light radius to be greater than 2. For an exponential surface brightness profile, this implies that the peak S/N ratio is ~ 10.

To investigate the effect of the finite KMOS IFU size, we then placed a mock galaxy in the centre of a cube and varied the input $R_{\rm disk}$, at a range of average S/N ratios. Figure 5.8 shows that our ability to recover $R_{\rm disk}$ is good for all galaxies which fit in the IFU, before declining for objects with $R_{\rm disk} > 7$ pixels. This is most pronounced for low S/N objects. The *fractional* error, however, as shown in the bottom panel of Figure 5.8, remains fairly constant for all input sizes.

Finally, we assess the impact of mis-centred Hα emission by placing our mock observation at various positions across the IFU. We create a model galaxy with $\epsilon = 2$, $R_{\rm disk} = 3$ and position angle 135° and then place it at each (x, y) location. We measure the best-fitting $R_{\rm disk}$ 10 times, and show the average ratio of $R_{\rm out}/R_{\rm in}$ for S/N of 2, 5 and 10 in Figure 5.9. We find that the effect of small offsets from the centre has no effect on our ability to recover the input size. The largest uncertainties occur when the mis-centring is large (i.e. the object is in the corner of the IFU), which we ensured does not occur for any of our observations.

Whilst not exhaustive, these tests show that we can robustly measure $R_{\rm disk}$ for a variety of S/N values, sizes and locations on the IFU, and allow us to make an informed decision on the minimum S/N ratio to use in our analysis. It should be stressed that these tests are conducted under more favourable conditions than the real analysis, since they are fitting a model which we know to be the true representation of the data, and do not include systematic uncertainties such as skyline residuals in the spectral dimension or "hot" pixels in the Hα images.

Final Sample

Our sample has, up to now, been selected to have Hα S/N greater than 5 in a spectrum integrated over a 1.2″ diameter aperture. We now enforce further constraints that the reduced χ^2 value for the Hα and continuum fit should be less than 3, as well as requiring that the average Hα SN within the best-fit half-light radius is greater than 2 (as motivated by our tests in Section 5.3.1). Finally, we visually inspect each map and remove two poor fits maps from the high-mass field sample and two from the field sample. We also remove a field galaxy whose R_c band image is obscured by the diffraction spike from a bright star. We are then left with 46 field galaxies, 12 cluster galaxies, 2 galaxies in the outskirts sample and 10 in the high-mass field sample.

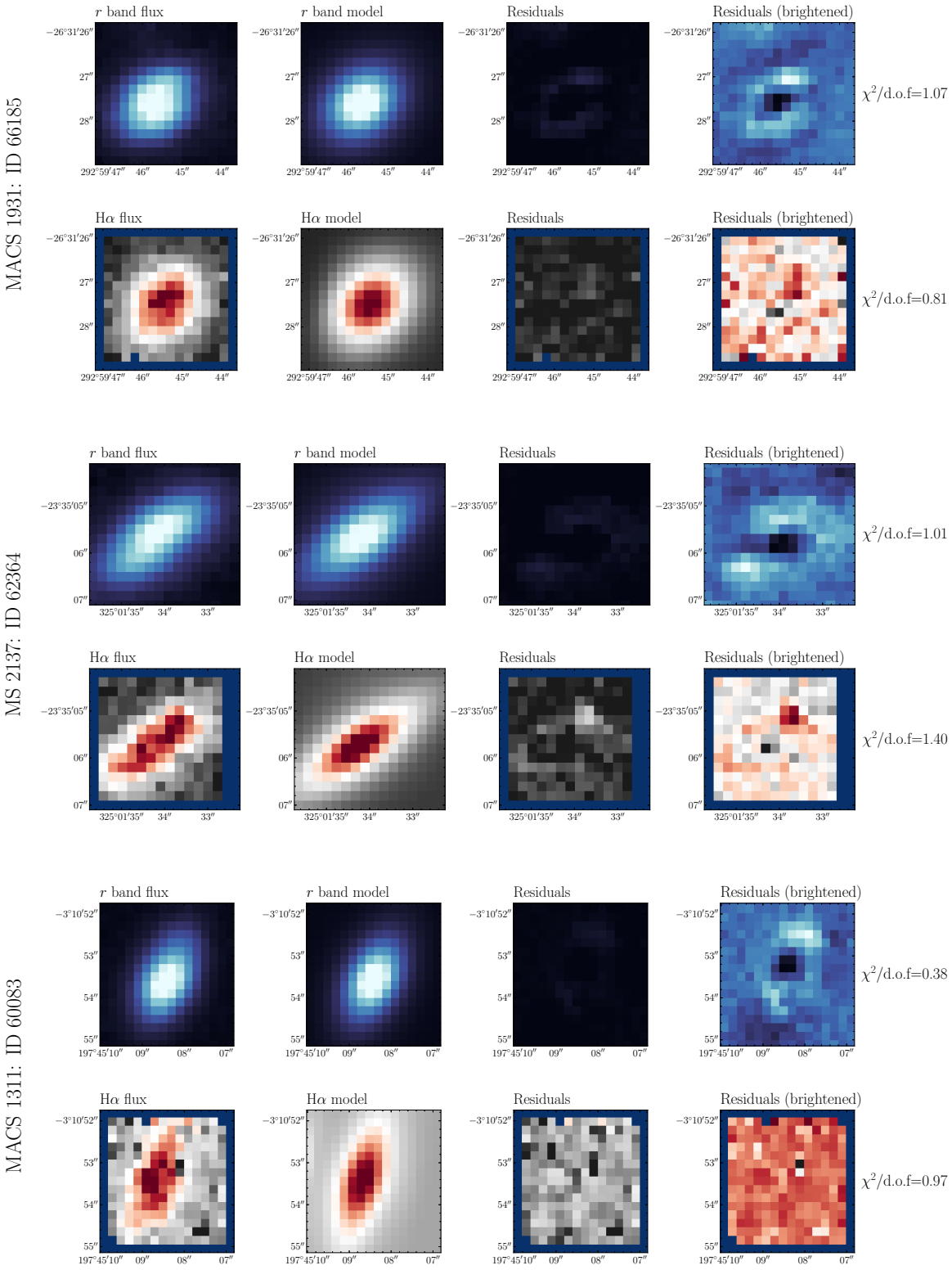

Figure 5.10: Examples of fits to the r-band flux and Hα emission of three K-CLASH galaxies. From left to right, the columns show the data, model and residuals from the fit. The final column shows the same residuals with the colormap scaled to show faint structure. Pixels coloured dark blue in the Hα maps have been masked from the fitting; these are mostly confined to the edges of each image. Each panel from the same galaxy has an identical spatial scale.

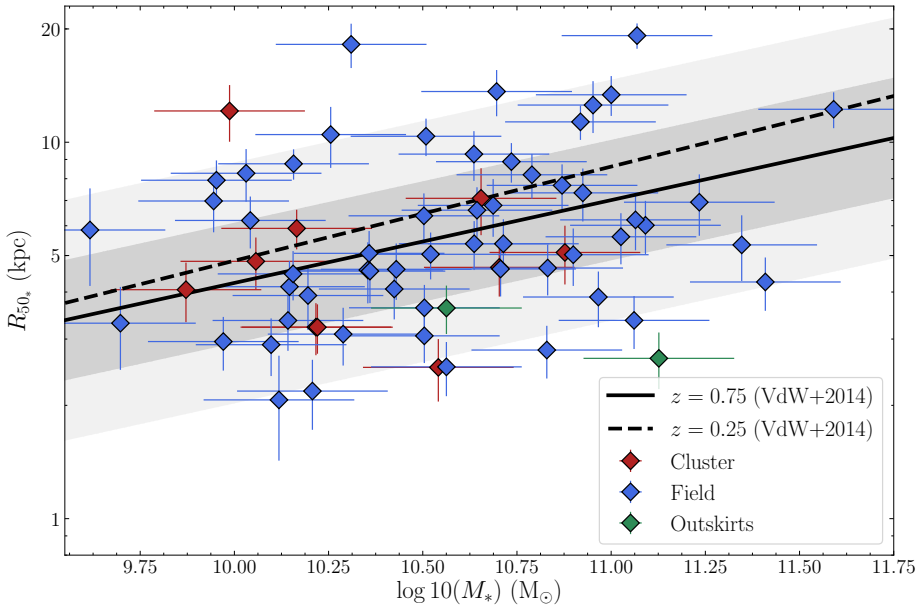

Figure 5.11: The mass-size relation for our sample, split by environment. Solid and dashed lines are the fits from van der Wel et al. (2014) at $z = 0.75$ and $z = 0.25$ respectively. Shaded areas show the 1-σ and $2-\sigma$ scatter around the $z = 0.75$ relation; the scatter around the $z = 0.25$ relation is similar.

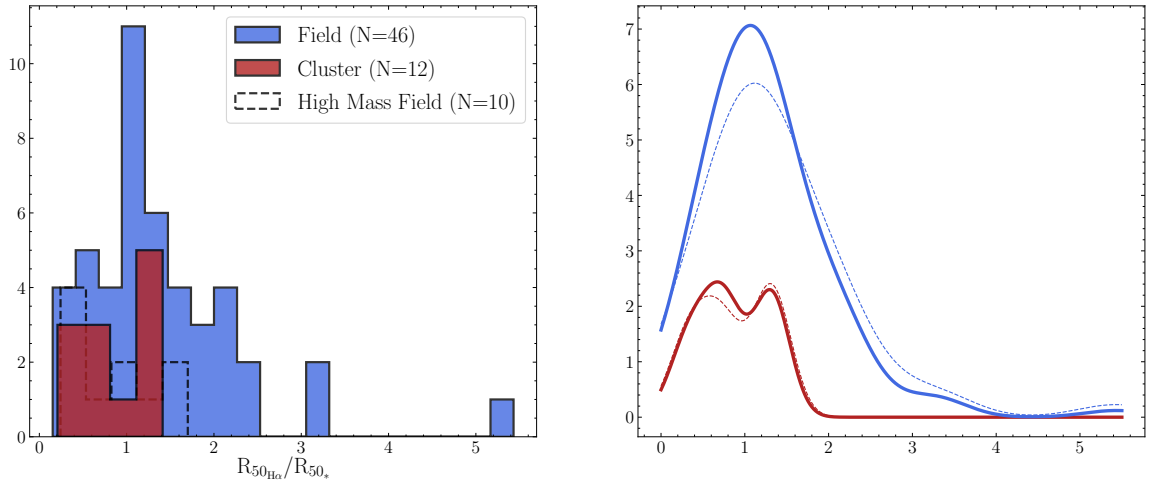

Figure 5.12: Left: Histogram of the ratio of Hα size to continuum size, split into cluster and field samples. We also show the size ratio for the high mass field sample (dashed line). Right: Gaussian kernel density estimation (KDE) of the same data. In this representation, we have weighted each data-point by its S/N ratio, accounting for the uncertainty in each size measurement. The dashed lines show the KDE without this weighting.

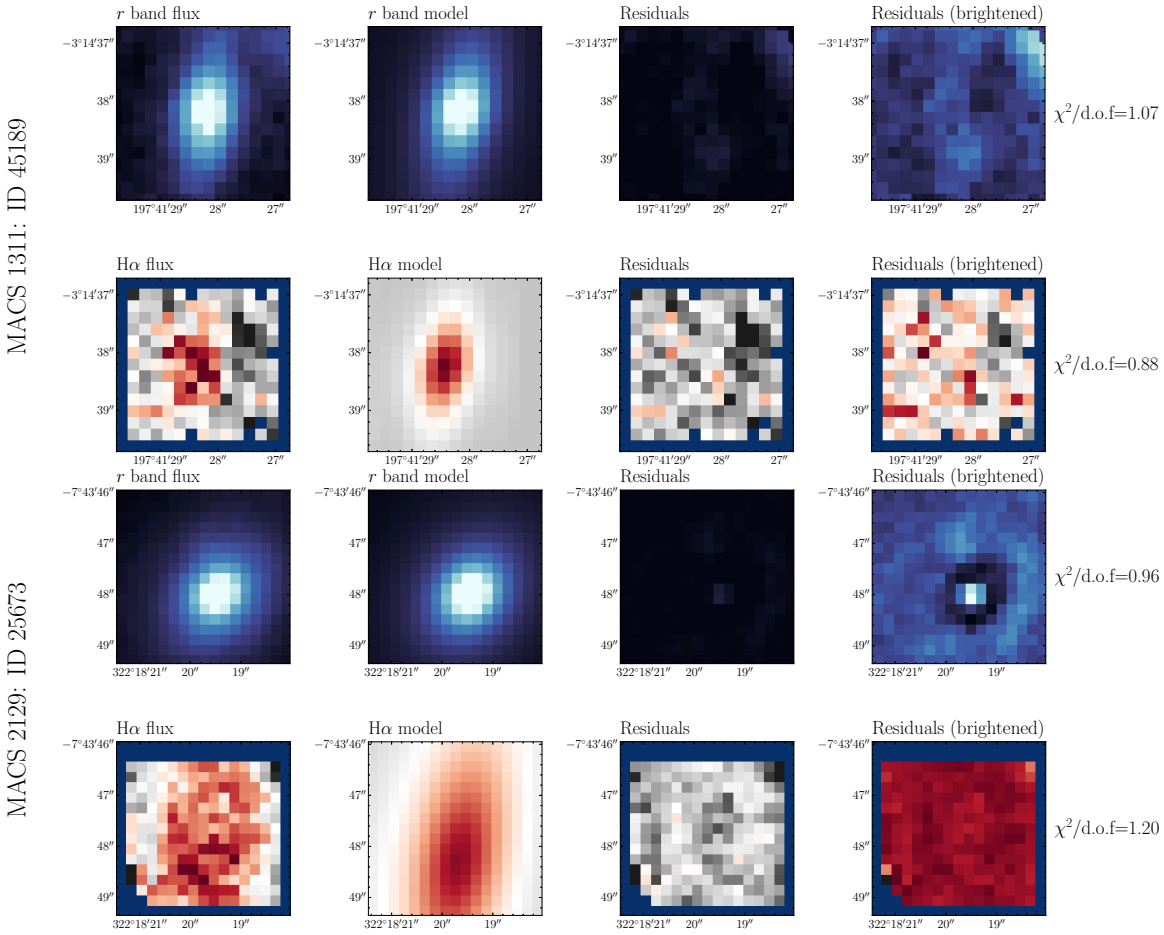

Figure 5.13: Two examples of very centrally concentrated Hα (top) and very extended Hα (bottom) compared to the stellar continuum light.

5.3.2 Results

Three example fits are shown in Figure 5.10. Images of the remaining galaxies in the sample are shown in Appendix B. The average ratio of Hα size to R_c-band continuum size is 1.22±0.09, with a range between 0.26 and 5.43. Our measurements agree well with the mass-(continuum) size relation at intermediate redshifts (van der Wel et al., 2014), as shown in Figure 5.11, and the ratios are consistent with the $z \sim 1$ galaxies of Nelson et al. (2016b) and "compact" SFGs of Wisnioski et al. (2018) at $z \sim 0.7 - 3.7$.

Figure 5.12 shows the ratio of Hα size to continuum size, split by environment, whilst Figure 5.13 shows two examples of galaxies with small and large size ratios. The inverse-variance-weighted average ratio of $r_{50_{\mathrm{H}\alpha}}/r_{50_{R_c}}$ is 0.86 ± 0.12 for the cluster galaxies and 1.26 ± 0.14 for the field sample, where the quoted uncertainty is the standard error on the mean (the standard deviation of the sampling distribution). The smaller ratio in the cluster galaxies is driven by their smaller $r_{50_{H\alpha}}$ values on average: 4.96 ± 0.64kpc compared to 5.86 ± 1.11kpc in the field. The two samples have more consistent $r_{50_{R_c}}$ averages within the uncertainties, of 4.96 ± 2.25 kpc in the cluster sample and 5.22 ± 2.57 kpc in the field

Our study is very similar to the one by Bamford et al. (2007). Their work measured the radial extent of rest frame B band light and a number of emission lines ([O II]λ3727, Hβ, [O III]λ4959 and [O III]λ5007) in 19 cluster and 50 field galaxies at $0.25 < z < 1$. They found that the ratio of emission line to stellar scale length in cluster galaxies was 0.92±0.07 and 1.22±0.06 in field galaxies, in comparison to 0.86 ± 0.12 and 1.26 ± 0.14 from our sample. We also find agreement with Schaefer et al. (2017), who studied the scale-radius ratio in a low redshift sample of 201 star-forming galaxies in the SAMI survey. They found that at larger local environmental densities, the fraction of galaxies with centrally concentrated Hα emission ($r_{50_{\mathrm{H}\alpha}}/r_{50_{R_c}}$) increases.

Further evidence for truncated Hα disks in the local galaxy clusters has also been

reported by Koopmann & Kenney (2004), using narrowband Hα observations of the Virgo cluster. They found $r_{\mathrm{H}\alpha}/r_R = 0.91 \pm 0.05$ and 1.18 ± 0.10 in their cluster and field samples respectively, again in excellent agreement with the values found in this study– showing a lack of redshift evolution in the average ratio. Koopmann & Kenney (2004), and follow up by Crowl & Kenney (2008), also found that the star formation rates in the centres of these truncated spirals were comparable to a matched field sample, showing that these galaxies were undergoing stripping of their outskirts rather than experiencing a global reduction in star formation.

On the other hand, Vulcani et al. (2015, 2016) find a small number of cluster galaxies at redshift $0.3 < z < 0.7$ with *extended* Hα sizes compared to the stellar continuum, using *Hubble Space Telescope (HST)* grism observations and rest-frame UV, optical and infra-red *HST* imaging. Of galaxies with "spiral" morphologies in their sample, 7 out of 25 show Hα sizes more than twice their size in the *HST* $F475W$ band. They also conclude that these objects have been ram-pressure stripped, leading to an extended star-forming halo around the stellar light and complicated morphologies.

As discussed in Section 5.3, the limiting SFR surface density of our observations is ~ 0.05 M$_\odot$ yr^{-1} kpc^{-2}, 5 times shallower than the studies in Vulcani et al. (2015, 2016) which reach 0.01 M$_\odot$ yr^{-1} kpc^{-2}. The reason for the apparent disagreement between the studies, therefore, is likely due to the fact that we are missing extended low surface brightness Hα emission from the outskirts of disturbed galaxies.

Statistical Significance

Our cluster sample is not very large. Is it likely that the distribution we observe for the cluster galaxies is actually the same as that for the field sample, with small number statistics conspiring to make them appear different?

To investigate whether or not this was the case, we begin by fitting the values of $\log_{10}(r_{50_{\mathrm{H}\alpha}}/r_{50_{R_c}})$ for the field galaxies with a Student's T distribution. This was

accomplished using MCMC sampling via `Stan` (Carpenter et al., 2017) in order to infer the full posterior distributions of the Student's T location, width and "normality" parameters[4] (μ, σ and ν, respectively). We find $\mu = 0.07 \pm 0.04$, $\sigma = 0.27 \pm 0.04$ and $\nu = 16.6^{+11.2}_{-10.9}$. The data and this fit are shown in the left panel of Figure 5.14.

We then simulate making 12 "measurements" from this distribution and compare these to our observations. Note that these simulations take into account the uncertainty on the best-fit parameters. We find that the simulated "field" measurements have a maximum value of $\log_{10}(r_{50_{\mathrm{H}\alpha}}/r_{50_{R_c}})$ which is *smaller* than the value we observe in our cluster galaxies in only 196 of 50,000 draws (less than 0.4% of the time). We therefore conclude that the distribution of size ratios in the field and cluster galaxies is intrinsically different, at the 3.4σ level. The histogram of maximum $\log_{10}(r_{50_{\mathrm{H}\alpha}}/r_{50_{R_c}})$ values is shown in the right panel of Figure 5.14.

What else could lead to small $r_{50_{\mathrm{H}\alpha}}/r_{50_{R_c}}$ ratios?

Previously, we have made the association of small $r_{50_{\mathrm{H}\alpha}}/r_{50_{R_c}}$ ratios with the removal of Hα-emitting gas at larger galaxy radii, or global reduction in SFR in cluster galaxies. Here, we discuss other factors or processes which could lead to a similar result whilst also explaining why their contribution is expected to be small.

The source of Hα flux we want to measure are stars more massive than ~ 20 M$_\odot$ and younger than 5-10 Myrs in individual star-forming regions (see e.g. Kennicutt 1998 and Calzetti 2013 for reviews). We then want to make the association of Hα flux and star formation. Under the assumption that each HII region is optically thick to ionising radiation ("Case B"– every energetic photon from a massive star ionises an atom of Hydrogen, which then recombines and produces a cascade of emission lines, with Hα and Hβ the most prominent), a simple relation between Hα flux and star formation rate exists (Osterbrock & Ferland, 2006). However, the effects of dust,

[4] As the normality parameter (also known as the "degrees of freedom") tends to infinity, the Student's T distribution tends towards a Gaussian.

AGN and photo-ionisation from evolved stars or shocks can confound this simple picture.

Firstly, dust attenuation and extinction will suppress Hα and continuum flux, absorbing photons to be re-emitted at longer wavelengths. Is it possible that a difference in dust properties between cluster and field galaxies is driving the observed trends to small $r_{50_{\mathrm{H}\alpha}}/r_{50_{R_c}}$ in dense environments? The R_c band in which we measure our continuum sizes is centred on 6500Å, meaning that it traces flux from between 4000-5500Å in the rest-frame of our sources, 1000 - 2500Å bluer than rest frame Hα. Dust reddening is a function of emitted wavelength, with stronger extinction at shorter wavelengths (e.g. Calzetti et al., 2000), naively implying that dust will tend to attenuate the stellar continuum light more than the Hα emission. On the other hand, however, a number of studies have described additional attenuation towards star-forming regions (e.g. Fanelli et al., 1988; Calzetti et al., 1994; Mancini et al., 2011), finding that Hα emission is further attenuated by a factor of ~ 2 compared to the continuum at the same wavelength ($\mathrm{A_{V,H\alpha}} = \mathrm{A_{V,cont}}/0.44$). This is due to the fact that HII regions, where young stars are found, are inherently dustier than the regions surrounding older stellar populations.

Using the Calzetti extinction law (Calzetti et al., 2000) and taking these two effects into account, the Hα emission is reddened more than the R_c-band continuum light[5]. It is therefore possible that a difference in global dust properties between environments could lead to smaller observed size ratios, if cluster galaxies are more obscured than their field counterparts. Using the global extinction estimates from the SED fitting (Section 4.5), however, we find the average value of $\mathrm{A_V}$ to be *lower* for cluster galaxies than those in the field by 0.3 magnitudes. We also observe no correlation between $\mathrm{A_V}$ and size ratio (correlation coefficient ρ=0.06), implying that galaxies with smaller size ratios are not systematically more attenuated.

[5]for a representative extinction of $\mathrm{A_V}$=1 magnitude, Hα is reddened by 1.87 magnitudes compared to 1.36 magnitudes for the continuum, for a source at z=0.6

It should be noted that the KMOS wavelength range available to us makes it impossible to make *local* extinction corrections to our Hα maps, although differences in the spatial distribution of dust conspiring to suppress the $r_{50_{\mathrm{H}\alpha}}/r_{50_{R_c}}$ ratio in cluster but not field galaxies is unlikely. We also note that whilst it is also well known that dust extinction correlates with stellar mass (e.g. Reddy et al., 2006; Momcheva et al., 2013; Nelson et al., 2016a) and star formation rate (at fixed stellar mass– e.g. Reddy et al., 2006, 2010; Wuyts et al., 2011), we have avoided any systematic effects from these correlations by matching our field and cluster samples in mass, and demonstrating in Section 5.2 that the difference in SFR as a function of environment at fixed mass is small (<0.2 dex).

Secondly, we consider Hα flux from active galactic nuclei. The effect of AGN would be to add extra flux in the centre of each galaxy, leading to peaked radial flux profiles and small inferred sizes. Narrow-line AGN especially would tend to impact the Hα flux more than continuum measurements and bias the inferred $r_{50_{\mathrm{H}\alpha}}/r_{50_{R_c}}$ to small values. Whilst we have endeavoured to remove all AGN contamination from our sample (Section 4.4), without further observations of the $H\beta$ and [OII] emission lines in each galaxy we cannot guarantee the purity of our selection, and the presence of weak AGN surrounded by star-forming regions especially cannot be ruled out. In the local Universe, the fraction of luminous AGN in high density environments is lower than in the field (Kauffmann et al., 2004; Popesso & Biviano, 2006), although it has shown strong evolution since $z > 1$ to the present day (Martini et al., 2013). For weaker AGN, the fractions tend to be comparable (Best et al., 2005; Haggard et al., 2010). We therefore expect the effect of AGN interlopers which have been missed by our selection cuts to be small, but also– importantly– comparable for the field and cluster sample.

Finally, photo-ionisation from sources such as planetary nebulae and post-AGB stars can contribute to Hα emission (Binette et al., 1994; Sarzi et al., 2010). Re-

gions where such emission is an important fraction of the total ionising photon flux have come to be known as Low Ionisation Emitting Regions or "LIERS" (Belfiore et al., 2016). The usual way to identify LIERs is with a BPT diagram, and as such we are unable to remove spectra with LIER-like line ratios from our samples. However, the average redshift of the cluster and field samples is comparable, and so to a first approximation the galaxy ages– and hence contribution from evolved stellar populations– should be similar. Furthermore, the total fraction of ionising radiation from post-AGB stars is largest for old, quiescent populations, so for the currently star-forming galaxies in our sample their contribution is expected to be small (Byler et al., 2017).

We therefore take our result at face value: above the limiting surface brightness for our observations, galaxies residing in clusters have smaller $r_{50_{\mathrm{H}\alpha}}/r_{50_{R_c}}$ values than those in the field. This is mainly driven by the population of galaxies we observe to be currently forming stars at large radii compared to their older stellar populations, which are absent from a similar sample in high density environments.

5.4 Emission Line Analysis

Having found a difference in the *extent* of star formation between the cluster and field environments, we now assess whether the *conditions* in star-forming regions differ too. To do this, we investigate similarities and differences in the emission line spectra of galaxies in the cluster, mass-matched field sample and a high mass field sample.

As discussed in Section 5.2, we extract flux from an elliptical aperture centred on the continuum centre of each object. We measure the fluxes of the Hα, [NII] $\lambda6548, \lambda6584$ and [SII] $\lambda6716, \lambda6731$ emission lines. This was accomplished by performing a fit (with a single velocity component) to each spectrum using `ppxf` (Cappellari & Emsellem, 2004b; Cappellari, 2017). The [NII] doublet was fit with a single

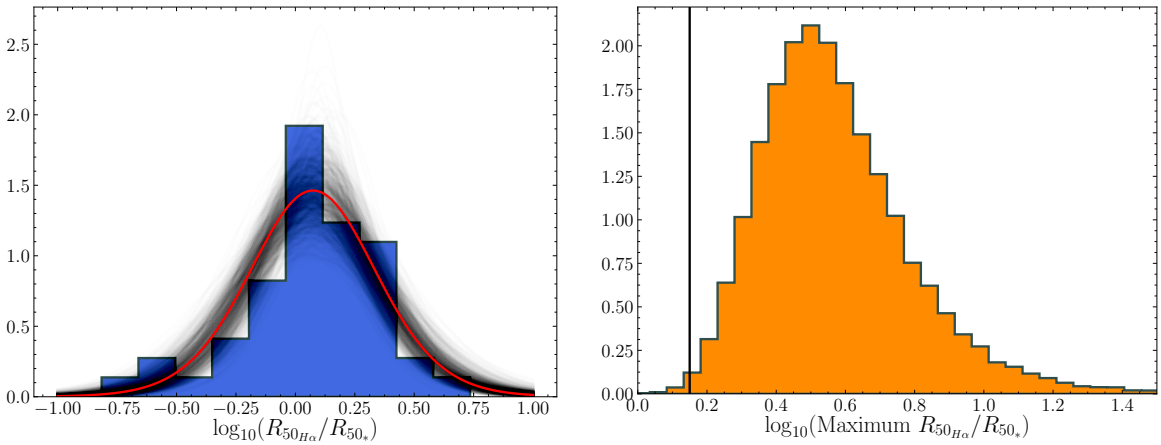

Figure 5.14: Left: The histogram of the ratio $\log_{10}(r_{50_{\mathrm{H}\alpha}}/r_{50_{R_c}})$ for the field galaxy sample, with the best-fit Student's T distribution overlaid. Black lines show 1000 random draws from the posterior distributions of μ, σ and the "normality" parameter, ν. Right: Assuming that our cluster galaxies follow the same "size ratio" distribution as the field sample, how likely are we to make observations similar to those in Figure 5.12? Here, we plot the maximum value of $\log_{10}(r_{50_{\mathrm{H}\alpha}}/r_{50_{R_c}})$ in 50,000 simulations of 12 "measurements" from the best-fit distribution showing that we only see a maximum value as small as that observed in our cluster sample ($10^{0.12}$) in 196 (less than 0.4% of the time).

template of two Gaussians, fixed at a ratio of 3 (Osterbrock & Ferland, 2006). The [S II] lines were fit with individual templates, but we use the "`limit_doublets`" keyword in `ppxf` to limit the ratio of the two lines to be between between 0.44 and 1.44, the values allowed by a physical analysis of atomic transitions involved (Osterbrock & Ferland, 2006). We estimate uncertainties by adding random noise to the best-fit template and reperforming the fit 1000 times per galaxy. Our measurements for each K-CLASH galaxy are collected in Table C.1.

We also investigate a stack of the spectra in the cluster, field and high-mass field samples. The process of stacking increases the S/N with respect to the spectra of individual galaxies, and allows us to make more robust measurements of the relatively faint [SII] doublet.

During the stacking procedure, we interpolate each spectrum to be uniformly sampled in $\log\lambda$, then fit a Gaussian to find the centroid of the Hα emission line,

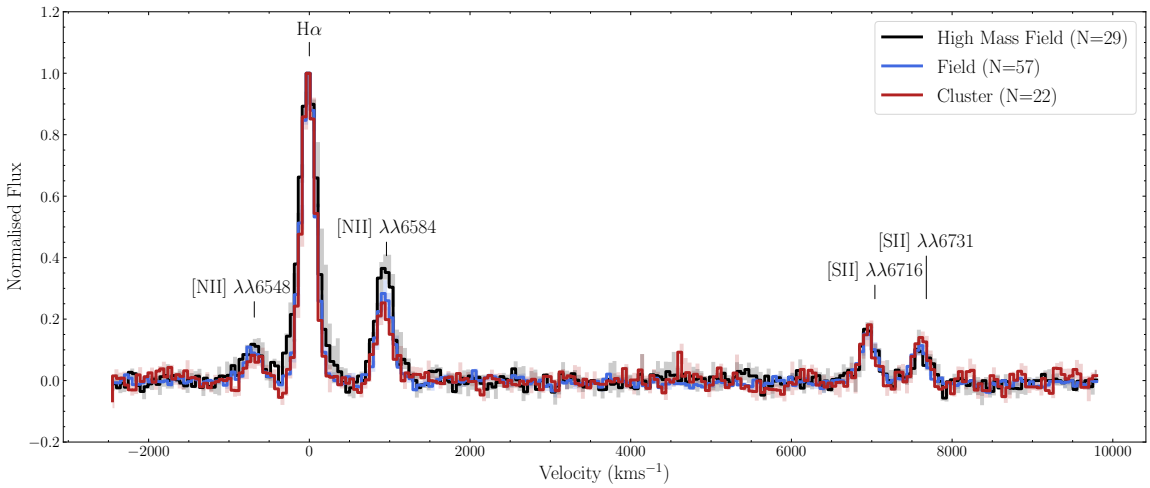

Figure 5.15: Median stacked spectra for the field, cluster and high-mass field samples. Note that these spectra have slightly different velocity dispersions ($\sigma_{\rm cluster} = 85{\rm kms}^{-1}$, $\sigma_{\rm field} = 91{\rm kms}^{-1}$ and $\sigma_{\rm hm\ field} = 111{\rm kms}^{-1}$) and have *not* been convolved to a matching σ.

shift it to its rest frame and divide by the peak Hα flux. We normalise the stellar continuum shape by dividing out an 4$^{\rm th}$ order polynomial fit and combine all spectra into a median stack. Our conclusions are unchanged if we sigma-clip the spectra before combining. The final stacked spectra for the three samples are shown in Figure 5.15.

We perform 10,000 bootstrap resamples to assess the uncertainty in each stack. If N objects contribute to a stack, we randomly draw N spectra from the sample (with replacement) and recombine them. The final error spectra are estimated by taking the standard deviation of the bootstrap samples at each wavelength slice. We measure the emission lines in the same manner as for each galaxy individually, with measurement uncertainties estimated by 10,000 bootstrap resamples of each spectrum in the stack.

5.4.1 Results

The stacked spectra for the samples are shown in Figure 5.15. The mass-matched field and cluster show very similar average spectra on the whole, with the clearest

difference the high [NII]/Hα ratio in the high-mass field sample. This adds to the findings of a number of other studies who show that the environment a galaxy resides in plays only a small role in setting the conditions of its interstellar medium (e.g. Mouhcine et al., 2007; Cooper et al., 2008; Pilyugin et al., 2017; Wu et al., 2017).

A number of characteristics of star-forming regions can be investigated using emission line fluxes and line ratios. Firstly, we measure the gas-phase metallicity, $12 + \log(\mathrm{O/H})$, of our sample. A number of methods exist to covert emission line measurements to metallicities, although it is well known that large discrepancies exist between metallicities estimated with different conversion techniques (e.g. Pilyugin, 2001; Liang et al., 2007; Kewley & Ellison, 2008). Here, we choose to derive the gas-phase metallicity using the ratio of [NII]λ6584/Hα and the polynomial conversion from Pettini & Pagel (2004):

$$12 + \log(\mathrm{O/H}) = 9.37 + 2.03\mathrm{N} + 1.26\mathrm{N}^2 + 0.32\mathrm{N}^3 \tag{5.1}$$

where $N = \log_{10}([\mathrm{NII}]\lambda6584/\mathrm{H}\alpha)$.

We measure an [NII]λ6584/Hα ratio of 0.254±0.018 for the cluster stacked spectrum, 0.311±0.012 for the mass-matched field stack and 0.367±0.017 for the high-mass field stack. These results are summarised in Table 5.1. These correspond to $12 + \log(\mathrm{O/H}) = 8.552 \pm 0.023$, 8.603 ± 0.017 and 8.641 ± 0.027 for the cluster, field and high-mass field samples respectively. A corner plot of the bootstrapped Hα and [NII] measurements for the field and cluster stack, as well as histograms representing the uncertainty in the inferred total gas-phase metallicities, are shown in Figure 5.16.

We also use Equation 5.1 to construct the mass-metallicity (MZ) relationship for our individual galaxies in the star-forming samples (Lequeux et al., 1979; Tremonti et al., 2004). This is shown in the top panel of Figure 5.17. Contours show the local MZ relation for 236,114 galaxies from the 12th data release of the Sloan Digital Sky Survey (SDSS; Alam et al., 2015). Emission line measurements are from Thomas

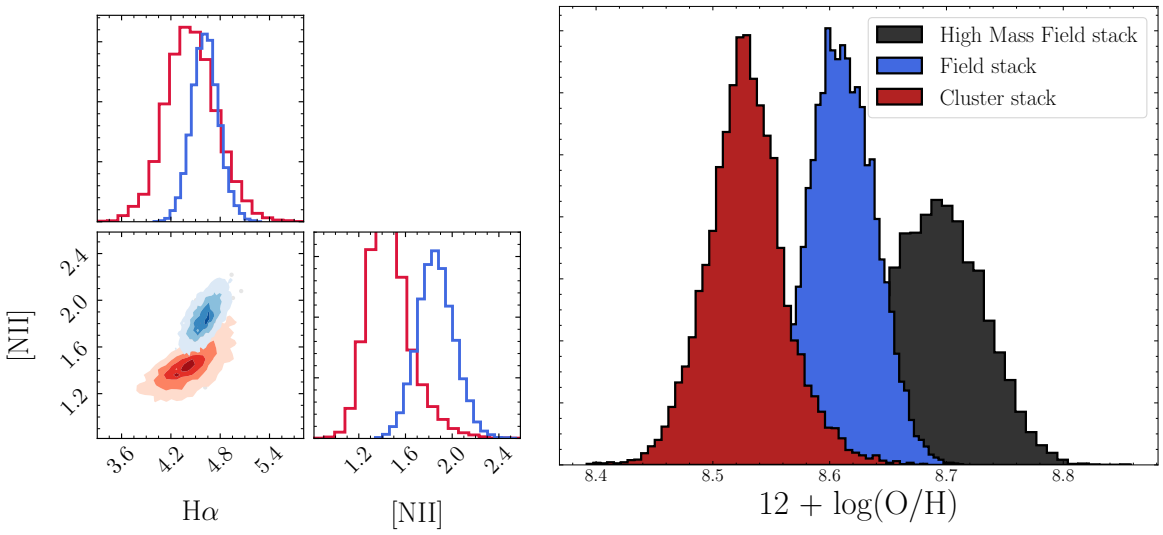

Figure 5.16: Left: measurements of the Hα and [NII] integrated line fluxes from 10,000 bootstrap-resampled spectra of the cluster (red) and field (blue) stacks (arbitrary units). The velocity dispersion of the field stack is slightly higher than the cluster stack, leading to a larger Hα flux, despite both peak heights being normalised to 1. Right: inferred metallicities for the cluster, field and high-mass field samples, from the bootstrapped spectra. We use the conversion of Pettini & Pagel (2004) (see Section 5.4)

et al. (2013), with stellar masses estimated using the technique of Maraston et al. (2009) assuming a Kroupa IMF (Kroupa, 2001). We measure metallicities for the SDSS sample using Equation 5.1. The average redshift of the sample is 0.06, with galaxies selected to be in the "star-forming" region of the BPT diagram.

Following Maiolino et al. (2008), we fit a relation of the form

$$12 + \log(\mathrm{O/H}) = -0.0864(\log M - M_0)^2 + K_0 \tag{5.2}$$

with free parameters M_0 and K_0. We perform the fit using `Stan`, incorporating errors in the x and y directions and intrinsic scatter around the relation. For the entire K-CLASH sample, we find $M_0 = 11.93 \pm 0.19$ and $K_0 = 8.88 \pm 0.05$, with an intrinsic scatter of $\sigma = 0.13 \pm 0.01$ dex.

In the bottom panel of Figure 5.17, we split our sample by environment and fit to

the field and cluster samples separately. In general, the two populations lie on similar MZ relations. We do find a lack of high metallicity cluster galaxies more massive than $10^{10.5}$ $M_{\odot}$, meaning that the cluster MZ relation is flatter than that for the field sample. In light of the small size and lack of completeness of our cluster sample, however, we do not draw strong conclusions from this result.

The fact that the field and cluster MZ relations are similar is in agreement with Maier et al. (2016), who found a difference in the MZ relation between field galaxies and cluster members of another CLASH cluster at $z \sim 0.4$ to be less than 0.1dex. Similarly, for local galaxies, Mouhcine et al. (2007) find only small differences between the gas-phase metallicity of galaxies with masses greater than $10^{9.5}$ as a function of environmental density. On the other hand, after removing the trend between environment, colour and luminosity, Cooper et al. (2008) find a weak but significant trend between between metallicity and environment, with more metal-rich galaxies residing in higher densities. Ellison et al. (2009) also find an elevation of 0.04 dex in metallicity between a sample of 1318 cluster galaxies and a matching field sample, but also a stronger trend between *local* density and metallicity, rather than simply membership of a cluster.

Emission Line Ratios

The ratio of [S II]λ6716 / [S II]λ6731 is a well-known electron density diagnostic tool (Osterbrock & Ferland, 2006; Proxauf et al., 2014). The root cause of this is the fact that both lines have nearly the same ionisation energy. This means that, in the low density regime, the ratio of the two lines is simply given by the ratio of the Einstein A coefficients of the two transitions. As the electron density increases, collisional de-excitation affects the emission line with the longest metastable lifetime first– in this case, [S II]λ6731. In the high density limit, the ratio of the two lines is given by the ratio of their lifetimes. The [S II] lines also have the useful quality that differential

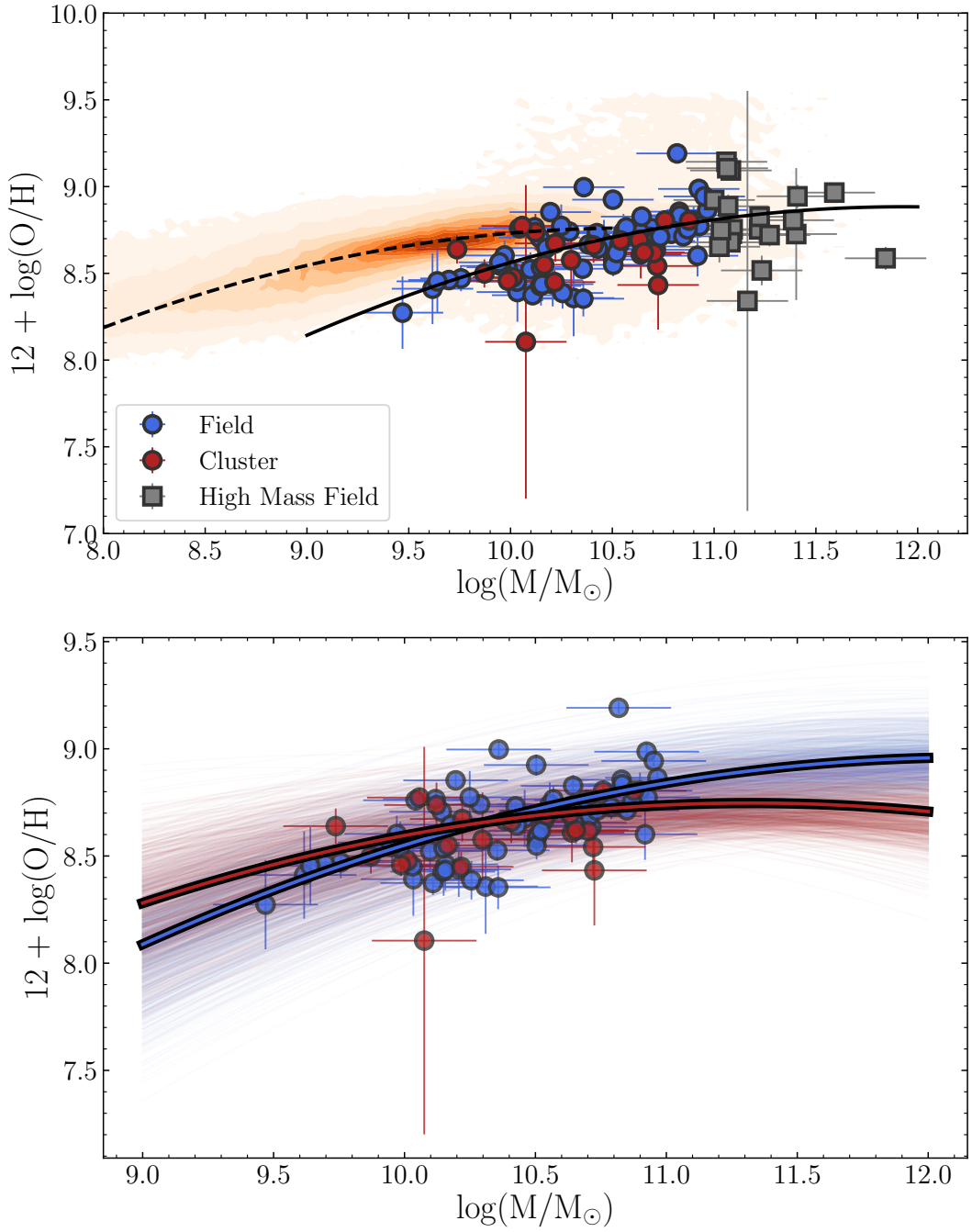

Figure 5.17: Top: The mass-metallicity (MZ) relation for K-CLASH star-forming galaxies. We use the polynomial conversion of Pettini & Pagel (2004) to infer 12 + log(O/H) from measurements of Hα/[NII]. Cluster galaxies are shown in red, field galaxies in blue and high-mass field galaxies in grey. The orange contours show star-forming local galaxies from the 12$^{\text{th}}$ data release of the Sloan Digital Sky Survey, with emission line measurements from Thomas et al. (2013) and stellar masses estimated by Maraston et al. (2009). Lines show a polynomial fit to each population of the form of Equation 5.2, following Maiolino et al. (2008) Bottom: The K-CLASH sample split by environment. We fit Equation 5.2 to the cluster and field samples individually. Thin lines are 1000 individual draws from the relevant posterior distribution, showing the uncertainty in the fits.

reddening effects are negligible, due to their close proximity in wavelength.

The values of the line ratio in the very low ($n_e < 10$ cm^{-3}) and high ($n_e > 10^4$ cm^{-3}) density limits are 1.44 and 0.44 respectively. In the K-CLASH sample, we find 34 individual galaxies which have [S II]λ6716 / [S II]λ6731 values at this low density limit and 2 at the high density limit. Assuming an electron temperature of 10,000K and using the empirical calibration of Proxauf et al. (2014), we find that the average electron density in the cluster stacked spectrum is $n_e = 67^{+100}_{-57}$ cm^{-3}, the field sample is 19^{+48}_{-9} cm^{-3} and the high mass field sample is < 10 cm^{-3}.

Among the individual objects, the distribution of cluster and field electron density values are very similar, with a KS test showing that none of the three distributions are significantly different. Figure 5.18 shows the derived electron densities and a comparison between the [S II]λ6716/[S II]λ6731 and $\log_{10}$([N II]$_{\lambda6584}$/Hα) ratios. We find a correlation between the [S II] ratio and $\log_{10}$[N II]$_{\lambda6584}$/Hα) in that that objects with high electron densities (smaller [S II] ratio) are preferentially found at higher metallicity (larger $\log_{10}$([N II]$_{\lambda6584}$/Hα) values).

These comparable electron density results across both environments are in agreement with Kewley et al. (2016), who found no differences between the electron densities of a sample of 13 galaxies in a $z = 2.1$ cluster and a number of $z \sim 2$ field galaxies. Darvish et al. (2015), on the other hand, do find an environmental dependence of electron density, with galaxies residing in large-scale filamentary structures at a similar redshift to our sample ($z \sim 0.5$) showing much smaller electron density values than a similar sample residing in the field. Similarly, Sobral et al. (2015) study a merging cluster at $z \sim 0.2$ and find that cluster galaxies show a lower electron density than field objects with similar properties. We see a small difference in [S II] ratio in the high S/N stacked spectra, but this is in the other direction to the studies of Darvish et al. (2015) and Sobral et al. (2015); the cluster stacked spectrum has a marginally *higher* electron density than the mass-matched field stack.

Two further variables important for understanding the state of the ISM are the so-called "ionisation parameter", describing the ionisation state of the gas, and the hardness of the ionising radiation.

Assuming a spherical geometry, the ionisation parameter q can be defined in terms of the Stromgren radius, R_s as

$$q = \frac{Q_H}{4\pi R_s^2 n_H} \tag{5.3}$$

where Q_H is the flux of ionising photons with energy above the ionisation potential of hydrogen and n_H is the number density of hydrogen ions (Strömgren, 1939). The usual assumption is to take n_H to be equal to the electron density, n_e. Physically, q represents the maximum possible velocity for an ionisation front driven by the local radiation field (Levesque et al., 2010), and is related to the dimensionless ratio of ionising photon density to the density of electrons (U; Osterbrock & Ferland, 2006) by $q \equiv cU$.

The [NII]λ6584/[SII]λ6716, 6731[6] ratio is sensitive to the ionisation parameter, because the ionisation potential of the [N II] and [S II] lines is significantly different (Kewley & Dopita, 2002; Kewley et al., 2016). The [S II]/Hα ratio is sensitive to the radiation hardness, since the [S II] line forms in a partially ionised zone. Harder far-UV spectra increase the size of the partially ionised region, which leads to larger [S II] flux whilst not changing the Hα emission (Levesque et al., 2010).

However, both of these line ratios are also dependent on age, metallicity and abundance effects (e.g. Levesque et al., 2010; Dopita et al., 2013). We would require measurements of further strong emission lines to break these degeneracies (which can be done with, for example, [N II]/[S II] versus [O III]/Hβ and [S II]/Hα versus [O III]/Hβ diagrams to separate the effects of metallicity, and a model star formation history fit to the galaxy photometry to assess the age of the HII regions). In the

[6] [SII]λ6716, 6731 is the total flux of the [S II] doublet.

	Cluster	Field	High Mass Field
[SII]λ6716 / [SII]λ6731	1.32 ± 0.11	$1.41^{+0.03}_{-0.05}$	$1.44^{+0.00}_{-0.1}$
[NII]λ6584/Hα	0.25 ± 0.025	0.30 ± 0.02	0.354 ± 0.037
[SII]λ6716, 6731/Hα	0.33 ± 0.04	0.32 ± 0.03	0.21 ± 0.04
[N II]λ6584/[SII]λ6716, 6731	1.0 ± 0.16	1.27 ± 0.14	2.20 ± 0.52
$12 + \log(\mathrm{O/H})$	8.552 ± 0.023	8.603 ± 0.017	8.641 ± 0.027
$n_e\,(\mathrm{cm}^{-3})$	$67^{+100.0}_{-57}$	19^{+48}_{-9}	< 10

Table 5.1: Emission line ratios and derived quantities for the stacked spectra.

absence of further emission lines to make quantitative measurements, therefore, we simply state that we find qualitatively similar values of [N II]/[S II] and [S II]/Hα for the cluster and mass-matched field samples. This implies that the ISM conditions are similar between the two environments. The largest differences can be seen as a function of mass, with the high-mass field stacked spectrum showing significantly lower [S II]/Hα and higher [N II]/[S II] ratios.

5.5 Discussion

This chapter has been split into three parts, each studying different aspects of the properties of cluster and field galaxies at $0.3 < z < 0.6$. Firstly, we find that the average SFR in cluster galaxies is offset to lower values compared to their field counterparts, by a factor of ~ 1.5 (0.18 dex). Secondly, the average scale-length ratio ($r_{50_{\mathrm{H}\alpha}}/r_{50_{R_c}}$) of star forming cluster galaxies is smaller than that of field star-forming galaxies which are matched in mass. Thirdly, the integrated spectra of cluster and field galaxies are very similar, with no strong variations in emission-line ratios or ISM

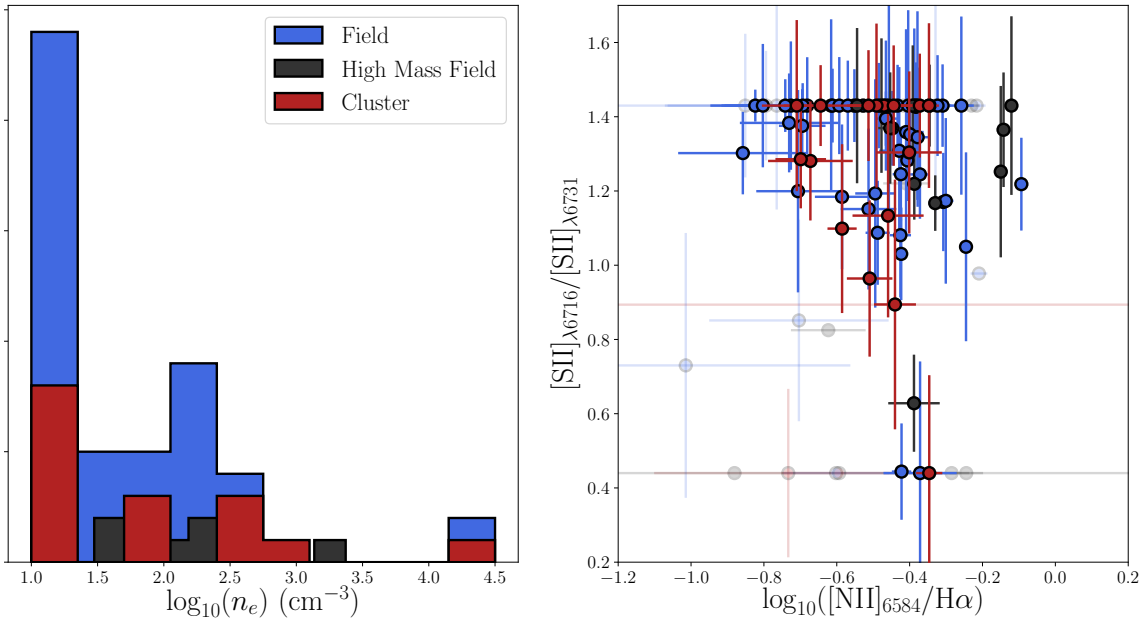

Figure 5.18: Left: The electron density in the field, cluster and high mass field samples, estimated from the [S II]λ6716/[S II]λ6731 line ratio and the calibration from Proxauf et al. (2014). Right: The [S II]λ6716/[S II]λ6731 ratio against $\log_{10}$([N II]$_{\lambda6584}$/Hα) for the three samples. Each solid point has [S II] and [NII] S/N greater than 3, whilst faded points have S/N less than 3.

conditions.

We find $r_{50_{\mathrm{H}\alpha}}/r_{50_{R_c}}$ equal to 0.86 ± 0.12 for the cluster galaxies and 1.27 ± 0.13 for the field sample. Whilst significantly different, both averages are close to unity, which shows that Hα emission is generally taking place in the disks of the galaxies in our sample, and traces the location of older stellar populations well. This is consistent with the findings of other studies at similar redshifts (Vulcani et al., 2015, 2016; Nelson et al., 2016b). The spatially resolved Hα maps and R_c band imaging give snapshots of a galaxy's star formation history at two points in time– instantaneously (timescales $\lesssim 20$ Myrs) and a few Gyrs previously. Galaxies with $r_{50_{\mathrm{H}\alpha}}/r_{50_{R_c}} > 1$, therefore, are actively growing in size in an inside-out manner, whilst those with $r_{50_{\mathrm{H}\alpha}}/r_{50_{R_c}} < 1$ are instead building up mass in their central regions.

The fact that the average scale length ratio is smaller in cluster galaxies than their field counterparts points to an environmental effect, and can be explained in two ways. Firstly, gas could be being heated or removed, and star formation quenched, solely in the outskirts of galaxy disks. Secondly, star formation could be being regulated globally in the galaxy disks, with the outskirts simply dropping outside our detection limits before the centres. These two processes are referred to as 'truncation' of galaxy disks and disk 'anaemia' respectively.

In Section 5.2, we find that cluster galaxies reside on a star-forming main sequence which is offset to lower SFRs by $\sim$0.2 dex compared to the field (significant at the 2.4σ level). The SFRs were integrated in an aperture of area $\pi \times \frac{1.2}{2}^2$ square arcseconds, however. When we instead used an aperture of $\pi \times \frac{0.6}{2}^2$ square arcseconds, the offset reduced to 0.13 dex (1.7σ). As discussed in Section 5.2, if ram-pressure stripping was the only process taking place, we'd expect the main-sequence offset to disappear in the smaller aperture. If a process to reduce the SFR at all radii were occurring, we'd expect the main-sequence offset to be identical in both cases. Since the data fall in between these two simple pictures, we infer that it is actually a combination of both

of these effects taking place.

Star formation can be suppressed by heating the ISM, either to stop it being able to collapse and form stars or by removing it from the galaxy altogether via evaporation (e.g. Cowie & McKee, 1977). This heat can be supplied to the ISM by the intracluster medium (ICM) via the process of thermal conduction (Spitzer & Härm, 1953; Sarazin, 1986; Narayan & Medvedev, 2001). Simulations conducted in Vijayaraghavan & Sarazin (2017a,b) study the effect of thermal conduction and ram-pressure stripping on cluster galaxies, finding that the gas-removal efficiency of thermal conduction is sensitive to the cluster's magnetic field. In the absence of magnetic fields, thermal conduction removes gas on timescales of $\sim$ 100 Myrs, whilst the inclusion of orderly (rather than turbulent) magnetic fields can slow this timescale to comparable or longer than that of ram-pressure stripping ($\sim$Gyrs). Crucially, in this scenario, gas can be heated globally in a galaxy, since the mean-free path of the electrons which carry out the heating is 1-10 kpc (comparable to the galactic disk scale lengths).

We find this environmental quenching mechanism to likely be more important than disk strangulation in our sample. Strangulation occurs when a galaxy's halo of cold gas is removed. In the absence of a supply of cold gas, galaxies continue to form stars until they run out of the gas residing in their disks (e.g. Larson et al., 1980; Peng et al., 2015). A key observational signature of this process is that the galaxies also become more metal enriched, since their gas reservoirs are not being diluted by pristine halo gas. Maier et al. (2016) find strangulation consistent with their measurements of the chemical enrichment of galaxies in a CLASH cluster at $z = 0.3972$, but in this work we do not find that cluster galaxies below the main-sequence are at a preferentially higher metallicity than those currently on the main-sequence. There is no significant correlation between between distance from the main-sequence and a galaxy's metallicity, for the cluster or field populations (with Pearson correlation

coefficient $\rho_{x,y} = 0.37$, p value $p = 0.08$ for the cluster population, $\rho_{x,y} = 0.12$, $p = 0.32$ for the field).

In terms of quenching at large radii, there are two possible candidates to strip gas from the outskirts of galaxy disks; ram pressure stripping (Gunn & Gott, 1972) and viscous stripping (Nulsen, 1982). Ram pressure stripping occurs when the pressure of the ICM "wind" experienced by a galaxy (due to its motion through the ICM) exceeds the galaxy's gravitational restoring force. On the other hand, viscous stripping occurs due to the Kelvin-Helmholtz instability induced when two viscous fluids flow past each other (in this case, the ICM flowing past the galaxy's gas disk). Viscous stripping is also known as "continuous stripping", since it leads to a slow, constant loss of gas from a galaxy, but has been found not to significantly change the radius of an object's gas disk in simulations (Roediger & Brüggen, 2007).

Of the many hydrodynamical simulations of ram-pressure stripping available in the literature, the study by Bekki (2014) is most appropriate to compare to here. They use hydrodynamical simulations of ram pressure to investigate the ratio of Hα to optical disk scale lengths of galaxies passing through dense environments. They find that whilst the precise evolution of $r_{50_{\mathrm{H}\alpha}}/r_{50_{R_c}}$ for individual star-forming galaxies in clusters depends sensitively on the cluster halo mass and galaxy disk inclination with respect to the cluster core, in general ram pressure stripping leads to disk galaxies in massive clusters tending to smaller $r_{50_{\mathrm{H}\alpha}}/r_{50_{\mathrm{optical}}}$ size ratios, as found in this work. They also find that the central star formation of these galaxies can be both moderately enhanced (during pericentre passage, primarily for edge on systems), suppressed or completely quenched (both after pericentre passage).

Local studies have recently unveiled the complexity of galaxies undergoing gas stripping processes. The GASP project (GAs Stripping Phenomena in galaxies with MUSE; Poggianti et al. 2017 and references therein) studies 114 nearby galaxies in group and cluster environments which show evidence of recent stripping by ram pres-

sure or turbulent processes. Truncated gas disks are common in the galaxies published so far, with most observations also showing evidence of spectacular tails of ionised gas (Poggianti et al., 2017; Gullieuszik et al., 2017; Moretti et al., 2018), although these are not ubiquitous (Fritz et al., 2017). The 3σ limiting surface brightness of the GASP observations is 2.5×10^{-18} erg s^{-1} cm^{-2} arcsec^{-1} (Poggianti et al., 2017), with the tidal tails having surface brightness values of $\lesssim 1 \times 10^{-16}$ erg s^{-1} cm^{-2} arcsec^{-1} (e.g. Gullieuszik et al., 2017), below the average K-CLASH limiting surface brightness ($\sim 1 \times 10^{-15}$ erg s^{-1} cm^{-2} arcsec^{-1}). We estimate that we would require nine hours on source to obtain a 3σ detection of an Hα emission line at 1μm with surface brightness 1×10^{-16} erg s^{-1} cm^{-2} arcsec^{-1}, 3.6 times longer than the typical K-CLASH galaxy observation.

Despite their differences in $r_{50_{\mathrm{H}\alpha}}/r_{50_{R_c}}$, we find the emission line properties of our cluster and field targets to be very similar. We find no differences between the distributions of electron density values (measured from the ratio of [S II] doublet lines) between the field and cluster samples, and the two populations follow similar mass-metallicity (MZ) relations. The cluster MZ relation is flatter than that for the field, due to an absence of high mass metal rich cluster galaxies. However, as discussed in Section 5.4.1 our small and incomplete sample prevents us from drawing strong conclusions from this observation.

This implies that the environmental effects at work are not evident in the centres of these galaxies, where most of the emission line flux we measure in our integrated spectrum originates. As a galaxy progresses through the dense ICM, its gaseous halo and disk are compressed towards the cluster centre and stripped on the opposite side. Physically, one might expect to see a variation in gas density between the leading and trailing edges of the object, which could be evident in the ratio of [S II] doublet lines. Spatially resolved maps of the [S II] line ratio have been studied in local AGN, starburst galaxies and ULIRGs (e.g. Bennert et al., 2006; Sharp & Bland-Hawthorn,

2010; Westmoquette et al., 2011; Kakkad et al., 2018), but not for objects undergoing ram-pressure stripping, for which the GASP project provides an excellent data set. It is tempting to ascribe the marginally smaller [S II] doublet ratio (corresponding to increased electron densities) in the cluster galaxy stacked spectrum to the compression effect of ram pressure stripping, but further observations of those objects in which we observe high electron densities, perhaps with adaptive optics to spatially resolve the emission, would be needed to confirm this.

5.6 Conclusions

Using IFU observations from the K-CLASH survey discussed in Chapter 4, we have studied the effect of environment on star-forming galaxies in 4 CLASH clusters at $0.3 < z < 0.6$. We make comparisons to a mass-matched sample residing in the field along the line of sight at similar redshifts, as well as a high-mass population with $M_* > 10^{11}$ $M_\odot$.

Our analysis is broken into three sections. Firstly, we measure the integrated star formation properties of our objects, by constructing the star formation rate – stellar mass relation (the "main sequence" of star formation). Secondly, we infer the radial extent of star formation by fitting exponential disk models to the Hα surface brightness profiles, as well as Sérsic profiles to R_c-band imaging from Suprime-Cam. Thirdly, we investigate the physical ISM conditions in our sample by measuring emission line ratios in an integrated spectrum from each galaxy, as well as stacking these spectra together to improve the signal-to-noise ratio. We summarise our conclusions below.

1. Cluster galaxies follow a SFR main sequence relation which is offset to lower SFRs than in the field population. The size of this offset is 0.18 dex, which is significant at the 2.4σ level.

2. The average ratio of the half-light radius of the Hα emission compared to R-band continuum emission ($r_{50_{\mathrm{H}\alpha}}/r_{50_{R_c}}$) is 1.22 ± 0.09, showing that star formation is generally taking place throughout stellar disks at these redshifts.

3. When separating by environment, we find $r_{50_{\mathrm{H}\alpha}}/r_{50_{R_c}}$=0.86±0.12 in the cluster sample and 1.27 ± 0.13 in the field sample.

4. The physical conditions of the ISM in the centres of each galaxy are very similar between the field and cluster samples. Using the conversion of Pettini & Pagel (2004), we measure a gas-phase metallicity for each object from the [N II]λ6584/Hα ratio. Both the cluster and field samples follow similar mass-metallicity relations, although our sample lacks the size or completeness to make strong statements about the small differences we do observe.

5. Using the ratio of the [S II]λ6716, 6731 lines, we infer an electron density in each galaxy. The distribution of these values is similar between the field and cluster samples, with a Kolmogorov-Smirnov test failing to distinguish between the two. The stacked cluster spectrum does show a marginally smaller [S II]λ6716, 6731 ratio than the stacked field spectrum, implying a larger electron density. We tentatively attribute this to the effects of gas compression due to ram pressure from the intra-cluster medium, but would require deeper follow up observations to confirm this result.

6. In the cluster galaxies, we are unable to distinguish between a *global* reduction in SFR due to heating of the ISM (thermal conduction) and the quenching of star formation solely in the outskirts due to ram-pressure stripping (or both). However, we see the similar emission line ratios between cluster and field to be implying that environmental quenching processes which tend to increase a galaxy's gas-phase metallicity (e.g. strangulation) are likely to be sub-dominant.

6 | Conclusions

Hey, what else can we do now?
Except roll down the window and let
the wind blow back your hair

Bruce Springsteen

In this thesis we have studied the stellar populations of both star-forming and quiescent galaxies, at low redshift and at $0.3 < z < 0.6$. Here, we summarise our conclusions from each previous chapter and set out future projects to build on the work presented in this thesis.

The IMF

In Chapter 2, we made radial measurements of stellar initial mass function (IMF) sensitive absorption features in the spectra of two massive early-type galaxies, NGC 1277 and IC 843. Using the Oxford Short Wavelength Integral Field SpecTrogaph (SWIFT; Thatte et al. 2006), we obtained resolved measurements of the NaI0.82 and FeH0.99 indices, among others, finding both galaxies show strong gradients in NaI absorption combined with flat FeH profiles (with equivalent widths ~ 0.4Å). We paid particular attention to the sky subtraction process during the analysis, as this is crucial for

measurement of the Wing-Ford band at 0.99μm. We show that these measurements may be explained by radial gradients in the IMF, appropriate abundance gradients in [Na/Fe] and [Fe/H], or a combination of the two, and that our data was unable to break this degeneracy.

We also use full spectral fitting (combined with measurements from the literature) to infer global properties from an integrated spectrum of each object, deriving a power-law IMF slope consistent with Salpeter in IC 843 ($x = 2.27 \pm 0.17$) but steeper than Salpeter in NGC 1277 ($x = 2.69 \pm 0.11$), despite their similar FeH equivalent widths. Independently, we also fit the strength of the FeH feature and compare to the E-MILES and CvD12 stellar population libraries to infer the IMF, finding agreement between the models. The IMF values derived in this way are in close agreement with those from spectral fitting in NGC 1277 ($x_{\rm CvD12} = 2.59^{+0.25}_{-0.48}$, $x_{\rm E-MILES} = 2.77 \pm 0.31$), but are less consistent in IC 843, with the IMF derived from FeH alone leading to steeper slopes than when fitting the full spectrum ($x_{\rm CvD12} = 2.57^{+0.30}_{-0.41}$, $x_{\rm E-MILES} = 2.72 \pm 0.25$). We also used these IMF determinations to infer stellar mass-to-light ratios which were consistent with previously published dynamical and spectral studies.

Chapter 2 highlighted the importance of a large wavelength coverage for breaking the degeneracy between abundance and IMF variations, and brings into doubt the use of the Wing-Ford band as an IMF index if used without other spectral information (see also the Appendix of van Dokkum et al. 2017).

In Chapter 3, we improve on the IMF determinations of Chapter 2 by utilising updated SSP models (from Conroy et al., 2018) and an instrument with a more suitable wavelength range. We presented observations of NGC 1399 using the Multi Unit Spectroscopic Explorer (MUSE; Bacon et al. 2010), and performed full spectral fitting to measure the low-mass IMF, as well as a number of individual elemental abundances, as a function of radius. We find that the IMF in NGC 1399 is heavier than the Milky Way in its centre and remains radially constant at a super-Salpeter

slope out to 0.7 R_e. At radii larger than this, the IMF slope decreases to become marginally consistent with a Milky Way IMF just beyond R_e. The inferred central V-band M/L ratio is in excellent agreement with the previously reported dynamical M/L measurement from Houghton et al. (2006). The measured radial form of the M/L ratio may be evidence for a two-phase formation in this object, with the central regions forming differently to the outskirts (e.g. see Naab et al., 2009; Hopkins et al., 2009).

We also reported measurements of a spatially resolved filament of ionised gas extending 4″ (404 pc at $D_L = 21.1$ Mpc) from the centre of NGC 1399, with very small equivalent width and low velocity dispersion (65 ± 14 kms^{-1}). The location of the emission, combined with an analysis of the emission line ratios, lead us to conclude that NGC 1399's AGN as the source of ionising radiation.

In both Chapters 2 and 3, we found that our targets had low-mass IMF slopes significantly steeper than we measure in the Milky Way. We also show in Chapter 3 that the bottom heavy IMF we measure is not radially constant, in agreement with other work. This ties in with the idea that compact high-redshift galaxies being the progenitors of the cores of nearby massive ETGs (Naab et al., 2009; Hopkins et al., 2009; van de Sande et al., 2013), with their the outskirts having been accreted via minor mergers over time.

To date, we have been unable to robustly test these theories by measuring the IMF beyond the local Universe. The *James Webb Space Telescope* will provide unrivalled measurements of high-redshift galaxies after its launch, and will be able to perform absorption line spectroscopy of bright high-redshift quiescent galaxies. The prospect of measuring gravity-sensitive absorption features in these spectra are very slim- since the contribution of low-mass stars to the total flux of young stellar populations is much less than 1%- but studies will be able to measure the dynamical mass of their targets, and compare to the stellar masses derived *assuming* a Chabrier/Salpeter IMF. If

the IMF is bottom-heavy in compact high-redshift galaxies, we should find evidence for large M/L ratios (with the caveat that this effect is difficult to disentangle with variation in the central dark-matter fraction). Such studies have already provided evidence for IMF variation in the local Universe (Cappellari et al., 2012), and there is a good possibility we will see quantitative verification of high-redshift bottom heavy IMFs (and galaxy evolution models in general) in the next decade.

K-CLASH

Chapter 4 introduced the K-CLASH survey. K-CLASH observes four intermediate redshift galaxy clusters (from the Cluster Lensing and Supernova survey with Hubble-CLASH; Postman et al. 2012) using the K-band Multi-Object Spectrograph (KMOS; Sharples et al. 2013). K-CLASH provides spatially resolved spectroscopy of galaxies at $0.3 < z < 0.6$ which reside in dense cluster environments, as well as in the field along the line of sight.

In this chapter, we discussed the K-CLASH observing strategy and the KMOS data reduction process. We measured the photometry of our targets in optical Suprime-Cam B, V, R_c, I_c and Z filters, as well as *Spitzer* 3.6μm and 4.5μm bands, and compared and contrasted the stellar masses derived using two publicly available SED fitting codes (`LePhare` and `MagPhys`).

We then described the steps undertaken to identify all Active Galactic Nuclei (AGN) in our observations, in order to select a sample of purely star-forming galaxies. Firstly, all galaxies with X-ray detections in the Chandra ACIS survey (Wang et al., 2016a) were removed. We then classified all galaxies with WISE colours $W_1 - W_2 > 0.8$ as AGN, following Stern et al. (2012). Finally, we removed objects with $\log([\mathrm{NII}]/\mathrm{H}\alpha) > -0.1$, in a similar manner to Wisnioski et al. (2018). In total, 56 galaxies were classified as AGN, which constitute 19% of our targeted galaxies. Of the remaining star-forming galaxies, we measure 119 with secure (S/N>5) detections

of Hα in their integrated spectra.

Chapter 4 also summarises our method for determining whether each galaxy actually resides in a CLASH cluster. Firstly, we take measurements of R_{200} from Postman et al. (2012) and $\sigma_{\rm cluster}$ from the $kT - \sigma$ relation of Girardi et al. (1996). We then use the right ascension, declination and redshift of each K-CLASH galaxy to find all objects within two virial radii of the brightest cluster galaxy's (BCG) location on the sky and within three times the cluster velocity dispersion around its redshift. These are named "cluster" galaxies.

We also build a more statistically robust mixture model, describing galaxies as being drawn from a uniform distribution on the sky (which represent the background population) or from a Normal distribution in RA, Dec and cluster-centric velocity, v (which represents the galaxy cluster population itself). The cluster spatial distribution was taken to be axisymmetric, with FWHM of R_{200}, and have a standard deviation of $\sigma_{\rm cluster}$ in the velocity dimension. Every K-CLASH galaxy is then assigned a probability of belonging to each distribution.

This method naturally takes into account uncertainties in the redshift information for each galaxy, and gives membership probabilities rather than a binary member/not classification. We found that classifying galaxies in this way gave the same results as the first, simpler method, if we select all galaxies with probability of being drawn from the cluster $p_{\rm cluster} > 0.9$. Whilst we have not investigated extensions to this formalism here, future work could easily adapt this technique to model non-axisymmetric cluster mass distributions or use the derived membership probabilities as variables or weighting parameters in an analysis. Our final sample contains 22 cluster galaxies, 91 in the field (with 67 forming our "mass-matched" field sample) and 6 in their cluster outskirts ($0.5 < p_{\rm cluster} < 0.9$).

Finally, we constructed the star-forming "Main Sequence" (MS) for the K-CLASH sample, which plots a galaxy's stellar mass against integrated star-formation rate. We

find that the K-CLASH MS agrees well with relations from the literature, showing that we are sampling "normal" star-forming galaxies at these redshifts.

In Chapter 5, we used the K-CLASH star-forming sample to investigate the similarities and differences between cluster and field environments. We begin by fitting the MS to the cluster and field populations separately. This allows us to measure the average star-formation rate for a galaxy of mass $10^{10.5}$ $M_{\odot}$, which we call $\Psi_{10.5}$. We find $\Psi_{10.5}$ to be 0.18 dex lower in the cluster population than in the field, which is significant at the 2.4σ level.

Next, we measure the spatial extent of Hα emission in the field and cluster populations by fitting exponential disk surface brightness profiles. We compare to the size of galaxies in the SuprimeCam R_c band, and find that the distribution of the size ratio $r_{50_{\mathrm{H}\alpha}}/r_{50_{R_c}}$ is 0.86±0.12 for the cluster galaxies and 1.26±0.14 in the field. This shows that cluster galaxies have more centrally concentrated Hα emission than in the field, which is significant at the 3.4σ level. Finally, we compare the emission line ratios between field and cluster galaxies, finding similar properties between the two populations.

We are unable to disentangle the effects of a global reduction in SFR from a cessation in star-formation solely at the edges of the cluster galaxies. A global reduction in SFR could be caused by the intracluster medium (ICM) heating the cold interstellar medium (ISM) of a cluster member, inhibiting its ability to form stars throughout the disk. Ram pressure stripping, on the other hand, causes a reduction in SFR solely in the outskirts, as gas which may be used to form new stars is removed from the galaxy entirely. Deeper observations, to look for low luminosity Hα emission or evidence of stripped Hα tails (similar to the low-redshift "jellyfish" galaxies studied in the GASP program; Poggianti et al. 2017), would be required to separate these possibilities.

6.1 Future Work

We now set out the prospects to expand on the work presented in this thesis.

6.1.1 The consistency between different SSP models used to measure the IMF

As discussed in Chapters 2 and 3, there are a number of simple stellar population (SSP) models which are used to infer the low-mass IMF. In this thesis, we have used models from Conroy & van Dokkum (2012a, CvD12) and Röck et al. (2016, E-MILES) in Chapter 2 and Conroy et al. (2018) in Chapter 3. These models are built from different isochrones, make different assumptions about stellar physics, and allow the user to vary different population parameters and individual elemental abundance patterns.

The shapes of the IMFs can also vary between models, from single and multi-segment power laws to the "bimodal" IMF available in the E-MILES models. Similarly, studies to infer the IMF in integrated galaxy spectra have been conducted with a number of different instruments (and therefore wavelength ranges), implying they each measure a slightly different subset of the optical and NIR spectral regions. Finally, a number of studies fit the IMF using only the measurements of selected spectral indices (e.g. Ferreras et al., 2013; La Barbera et al., 2013; Spiniello et al., 2014; Martín-Navarro et al., 2015b,c; Spiniello et al., 2015a; La Barbera et al., 2016; Zieleniewski et al., 2017; Alton et al., 2017; Parikh et al., 2018; Alton et al., 2018; Sarzi et al., 2018) whilst some fit models to the entire spectrum simultaneously (van Dokkum & Conroy, 2010, 2012; Conroy & van Dokkum, 2012b; van Dokkum et al., 2017; Conroy et al., 2017; Newman et al., 2017; Vaughan et al., 2018a,b).

Performing consistency checks between the various models, methods and IMF shapes would be very helpful to the community. The best way to accomplish this

would be to take a number of publicly available spectra observed with a long-slit spectrograph with very wide wavelength coverage (e.g. LRIS on Keck or X-Shooter at the ELT). The study would then measure the IMF via full spectral fitting as well as from fitting absorption features, and would use both the Conroy et al. (2018) and E-MILES models. Studies of this kind with limited scope have been conducted before (e.g. Spiniello et al., 2015b), but the SSP models compared have since changed dramatically.

Secondly, it would be very interesting to investigate how the derived IMF varies as the wavelength over which the models are fit is restricted. It is clear, for example, that with the wavelength range of SWIFT in Chapter 2 it is impossible to constrain all the necessary parameters self consistently. But what is the shortest wavelength range for which this *is* possible? A comprehensive study of the self-consistency of different fitting methods, SSP models and wavelength ranges would shore up the foundations of this area of research.

6.1.2 The kinematics of cluster and field galaxies with K-CLASH

An obvious avenue to pursue with the K-CLASH IFU observations would be to investigate the ionised gas kinematics of galaxies at $z \sim 0.5$, in a similar way to a number of other KMOS studies at $z > 1$ (e.g. Tiley et al., 2016; Übler et al., 2017; Mason et al., 2017).

Whilst investigating the possibility of measuring the Tully-Fisher relation (TF; Tully & Fisher, 1977), we found that the KMOS IFU size would be a limiting factor in the analysis. As described in Freeman (1970), for a purely exponential disk the peak of the velocity curve occurs at 2.2 times the disk scale radius (1.67 times the effective radius). Assuming that the surface brightness of the ionised gas follows that of the stellar light, around half of our targets have $2.2r_{\rm disk}$ larger than $1.4''$ (half the

size of the KMOS IFU). This would imply that we would miss the peak of the rotation curve for a large proportion of our targets, reducing our sample size with which to measure the TF.

Instead, it would be interesting to investigate whether there are any dynamical differences between cluster and field galaxies in K-CLASH. This project would involv measuring the kinematics of the cluster and field samples using `pPXF`, and fitting the kinematics with a model velocity field (assuming an exponential disk surface brightness profile; Freeman 1970). Three example velocity maps of cluster galaxies in the MACS 1311 observations are shown in Figure 6.1. By studying the residuals around the best-fit model, we would look for evidence of outflows, disturbed kinematics or dynamical evidence of ram-pressure stripping in action.

In addition, the sample size of this analysis would also be larger than just the K-CLASH star-forming sample. 53 galaxies were flagged as active galactic nuclei (AGN) due to their X-ray flux, near infra-red colours or high [NII]/Hα ratio (Chapter 4). Since we would be studying the dynamical properties of the galaxies, rather than the *source* of the ionising photons, these objects with resolved kinematics would be included in a study alongside the 119 galaxies studied so far.

6.1.3 K-CLASH BCGs

As part of the survey design, a KMOS IFU was placed on the brightest cluster galaxy (BCG) during observations of every quadrant, such that they have an exposure time four times longer than the rest of the sample. Two of these objects have very strong emission line detections, allowing for possibilities of measurements of ionised gas kinematics and resolved emission line ratio diagnostics. The BCGs of MACS 2129 and MACS 1311 are quiescent, with no nebular emission detected in our KMOS observations (or publicly available MUSE data). We could, however, use our K-CLASH data to place a strong upper limit on the SFR in these objects.

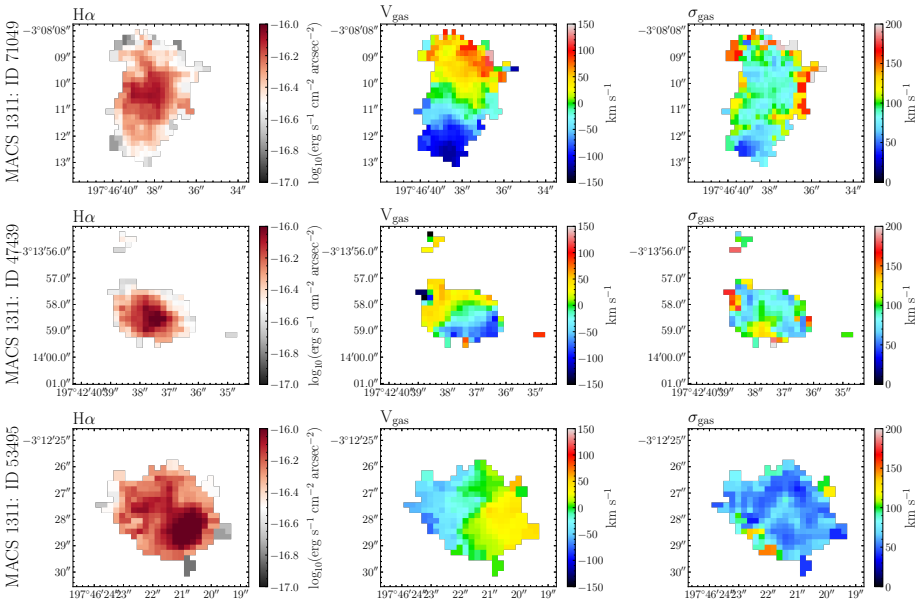

Figure 6.1: From left to right: Hα flux, velocity and velocity dispersion maps for three members of the MACS 1311 cluster. We Voronoi bin the KMOS observations to a S/N ratio of 5, then extract kinematics using `pPXF`. Future work may investigate whether the kinematics of cluster members are more disturbed than those in the field by comparing to a simple exponential disk model.

Furthermore, a wealth of ancillary data exists for these targets. Since they are in the centres of their respective clusters, they are also covered by 17 *Hubble Space Telescope* filters, as well as the 5 Subaru bands and 3.6μm and 4.5μm *Spitzer* imaging discussed in Chapter 4. These data could be used to constrain the star-formation histories of these objects very precisely. Publicly available MUSE observations can also be found for each in the ESO archives, which would open up the possibility of measuring stellar absorption features and spatially resolved Hβ and [O II]λ5007 fluxes. We could then make resolved BPT diagrams (Baldwin et al., 1981) and place each spaxel on the star-forming sequence with *local* corrections for dust extinction using measurements of the Balmer decrement.

These BCGs live in special places in the Universe, and the wide range of data available would make it possible to place strong constraints on their star-formation histories and the evolutionary paths they have followed to date.

A | Appendix to Chapter 2

A.1 Index Measurements

We present all the radial index measurements from NGC 1277 and IC 843 in Tables A.1 and A.2. Our measurement methodology is discussed in Section 2.3.

A.2 Fitting the FeH feature

In order to make quantitative measurements of the IMF in each galaxy, we compare our results to the CvD12 and E-MILES stellar population models. The aim is to create a spectrum with the same stellar population parameters and FeH measurement as the global spectrum for both galaxies, and then read off the IMF slope of that spectrum. The two sets of models allow for changes in separate population parameters, meaning that the analysis which starts with a base template from the CvD12 models is slightly different to the case where we start with a base spectrum from the E-MILES models. Both cases are described below.

Table A.1: All index measurements in NGC 1277. As discussed in Section 2.3, these measurements were taken at the intrinsic velocity dispersion of the radial bin and then corrected to 200 kms^{-1} for both galaxies. All results are equivalent widths, in units of Å and found using the formalism of Cenarro et al. (2001), except for that of TiO which is a ratio of the blue and red pseudo-continuua.

$\log(R/R_e)$	CaT (Å)	FeH (Å)	MgI (Å)	NaI (Å)	TiO
-0.99	6.94 ± 0.34	0.46 ± 0.13	0.36 ± 0.16	1.28 ± 0.12	1.0809 ± 0.0062
-0.60	6.78 ± 0.29	0.48 ± 0.11	0.25 ± 0.12	1.20 ± 0.10	1.0795 ± 0.0053
-0.40	6.71 ± 0.40	0.41 ± 0.15	0.33 ± 0.15	1.10 ± 0.13	1.0788 ± 0.0069
-0.21	6.73 ± 0.40	0.44 ± 0.15	0.42 ± 0.15	1.04 ± 0.14	1.0764 ± 0.0070
-0.06	6.61 ± 0.32	0.51 ± 0.12	0.68 ± 0.11	1.02 ± 0.11	1.0754 ± 0.0057
0.11	6.18 ± 0.36	0.62 ± 0.12	0.57 ± 0.12	0.97 ± 0.12	1.0679 ± 0.0061
0.28	6.11 ± 0.31	0.50 ± 0.10	0.57 ± 0.11	0.75 ± 0.11	1.0622 ± 0.0052
Global	6.82 ± 0.13	0.45 ± 0.05	0.56 ± 0.07	1.07 ± 0.05	1.0729 ± 0.0030

Table A.2: All index measurements in IC 843. See the caption of Table A.1 for details

$\log(R/R_e)$	CaT (Å)	FeH (Å)	MgI (Å)	NaI (Å)	TiO
-1.60	7.34 ± 0.40	0.42 ± 0.16	0.58 ± 0.13	0.87 ± 0.15	1.0718 ± 0.0070
-1.06	7.28 ± 0.33	0.50 ± 0.13	0.54 ± 0.10	0.74 ± 0.12	1.0686 ± 0.0057
-0.79	7.17 ± 0.33	0.53 ± 0.12	0.57 ± 0.10	0.68 ± 0.12	1.0683 ± 0.0056
-0.60	7.36 ± 0.35	0.43 ± 0.13	0.58 ± 0.09	0.64 ± 0.13	1.0663 ± 0.0058
-0.47	7.24 ± 0.37	0.41 ± 0.13	0.54 ± 0.09	0.57 ± 0.13	1.0647 ± 0.0060
-0.35	7.20 ± 0.41	0.39 ± 0.14	0.54 ± 0.10	0.55 ± 0.14	1.0661 ± 0.0064
-0.24	6.97 ± 0.37	0.45 ± 0.13	0.58 ± 0.09	0.55 ± 0.13	1.0621 ± 0.0057
Global	7.24 ± 0.14	0.41 ± 0.05	0.58 ± 0.04	0.66 ± 0.05	1.0671 ± 0.0024

A.2.1 CvD12

We interpolate the base set of CvD12 models of varying IMF slope as a function of age and FeH equivalent width. These base spectra are at solar metallicity, [α/Fe]=0 and have solar elemental abundance ratios, whilst spanning IMF slopes from bottom-light to $x = 3.5$. To accurately account for the different metallicities, α-abundances and [Na/Fe] ratios in each galaxy, we apply linear response functions to the CvD spectra.

The correction is defined as follows. To deal with varying continuum levels between spectra with different IMF slopes, we use multiplicative rather than additive response functions. For a spectrum with a non-solar α-abundance ratio, $S(\Delta\alpha)$,

$$S(\Delta\alpha) = x_\alpha S(\Delta\alpha = 0.0)$$

where x_α is the linear response function. We also Taylor expand $S(\Delta\alpha)$ to give

$$S(\Delta\alpha) \approx S(\Delta\alpha = 0.0) + \frac{dS}{d\alpha}\Delta\alpha$$

which leaves

$$x_\alpha = (1 + \frac{d\ln S}{d\alpha}\Delta\alpha)$$

We approximate the gradient term using a model spectrum from CvD12 at enhanced [α/Fe]=+0.3:

$$\begin{aligned}\frac{d\ln S}{d\alpha}\Delta\alpha &\approx \frac{1}{S(\Delta\alpha = +0.0)}\frac{S(\Delta\alpha = +0.3) - S(\Delta\alpha = +0.0)}{10^{0.3} - 1}(10^{\Delta\alpha} - 1) \\ &= \left(\frac{S(\Delta\alpha = +0.3)}{S(\Delta\alpha = +0.0)} - 1\right)\frac{10^{\Delta\alpha} - 1}{10^{0.3} - 1} \\ &= f_\alpha\end{aligned}$$

A similar correction is applied for [Fe/H] and [Na/Fe] abundance variations. The final set of spectra are therefore:

$$S_{\rm final} = S_0 \cdot x_\alpha \cdot x_{\rm Na} \cdot x_{\rm Fe}$$

$$\ln S_{\rm final} = \ln S_0 + f_\alpha + f_{\rm Na} + f_{\rm Fe}$$

It is important to note that the CvD12 spectra with non-elemental abundances (e.g those with [Fe/H]=+0.3 dex) are calculated from a Chabrier IMF, whereas we find the IMFs in these galaxies from this analysis to be heavier than this. Another unavoidable source of uncertainty in the use of these models concerns the fact that the response of the IMF sensitive indices strong in very low-mass stars (such as FeH) to quantities like [α/Fe] are computed from theoretical atmospheric models which may

not converge. For further discussion of this point, see CvD12 section 2.4.

A.2.2 E-MILES

A similar process was carried out for the E-MILES spectra. We interpolate a grid of templates of varying IMF, age, metallicity and [Na/Fe] enhancement. Since the E-MILES models are all at solar [α/Fe] abundance, we use a response function from the CvD12 models to approximate an α-enhanced spectrum.

A complication here is that a CvD12 model template at [α/Fe]=+0.3 is not at solar metallicity, because the CvD12 models are computed at fixed [Fe/H] and not fixed [Z/H]. Using the relation from Trager et al. (2000),

$$[\mathrm{Fe/H}] = [\mathrm{Z/H}] - 0.93 \times [\alpha/\mathrm{Fe}]$$

and so CvD12 template with [α/Fe]=+0.3 also has [Z/H]=0.279. We must therefore apply an [α/Fe] response function to a base spectrum of metallicity

$$[\mathrm{Z/H}]_{\mathrm{spectrum}} = [\mathrm{Z/H}]_{\mathrm{galaxy}} - 0.93 \times [\alpha/\mathrm{Fe}].$$

rather than simply $[\mathrm{Z/H}]_{\mathrm{galaxy}}$. This means, therefore, that the base template used for NGC 1277 has [Z/H]=-0.079, whilst the base template for IC 843 has [Z/H]=-0.197.

B | Additional Plots for Chapter 5

Figures B.1, B.2 and B.3 show all the Hα and R_c band fits from Chapter 5 for the cluster, field and high-mass field samples respectively. See Section 5.3 for details.

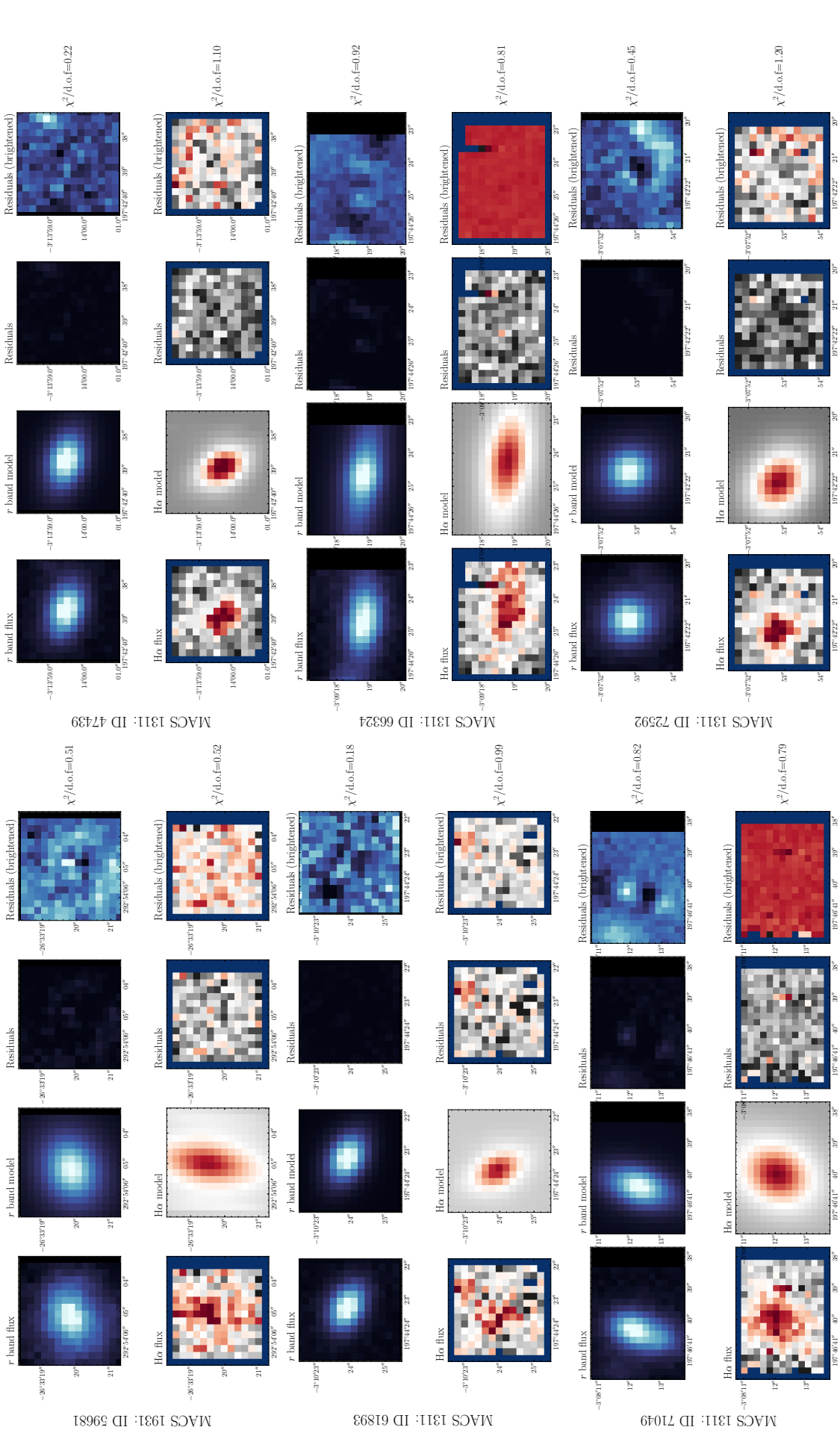

Figure B.1: Cluster galaxies- Hα and R_c band fits. See Section 5.3 for details

Figure B.1: (continued) Cluster galaxies- Hα and R_c band fits. See Section 5.3 for details

.

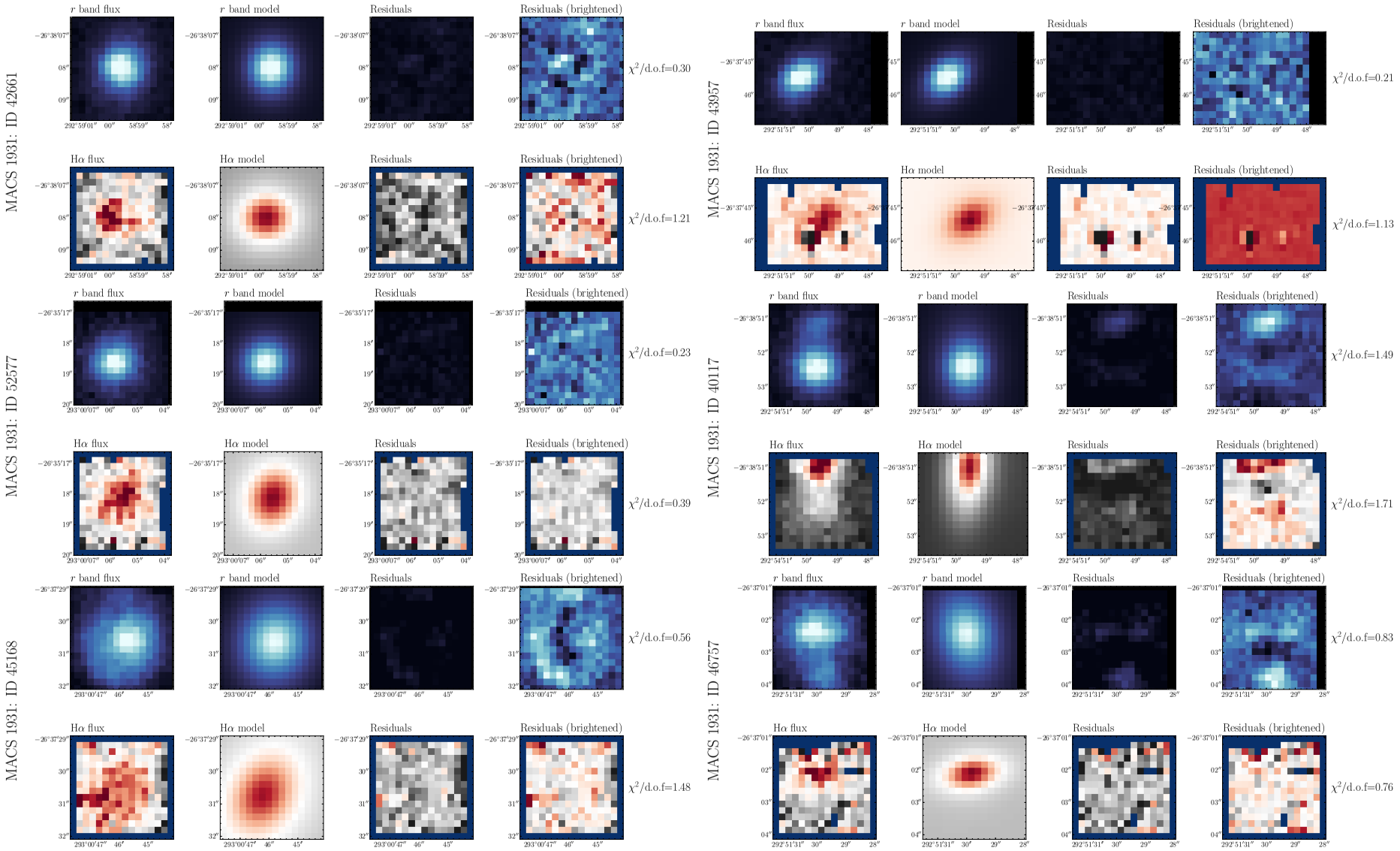

Figure B.2: Field galaxies- Hα and R_c band fits. See Section 5.3 for details

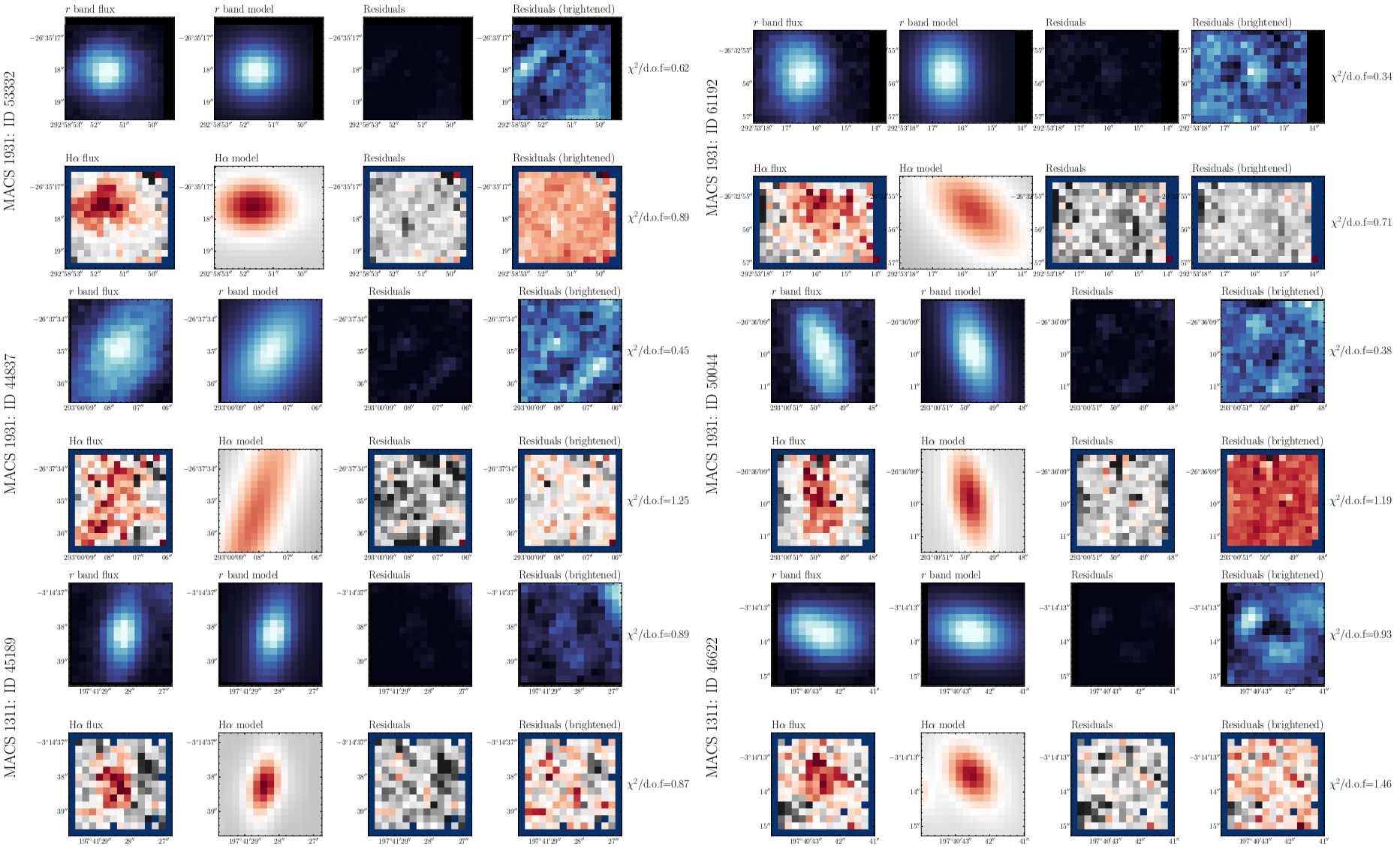

Figure B.2: (continued) Field galaxies- Hα and R_c band fits. See Section 5.3 for details

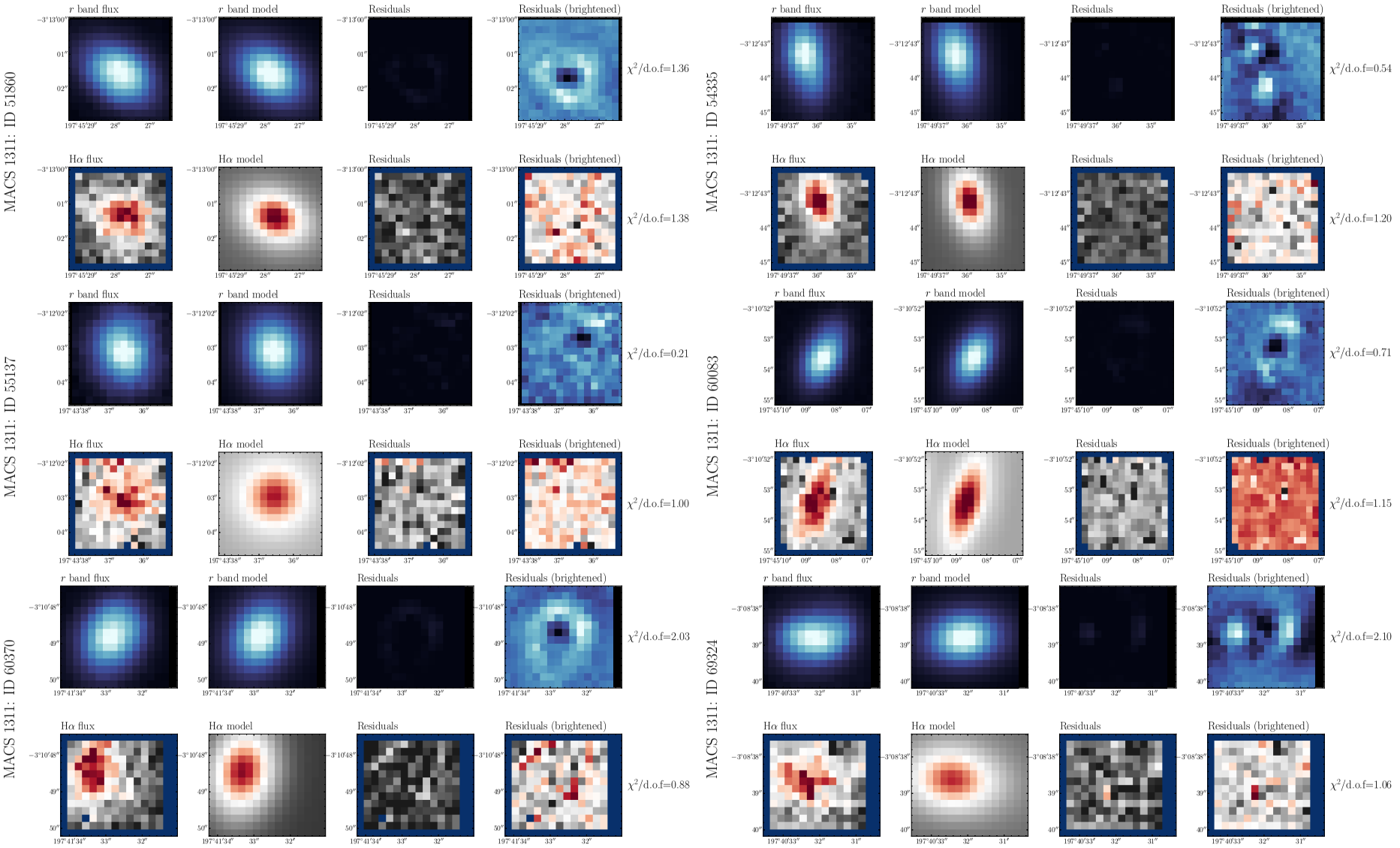

Figure B.2: (continued) Field galaxies- Hα and R_c band fits. See Section 5.3 for details

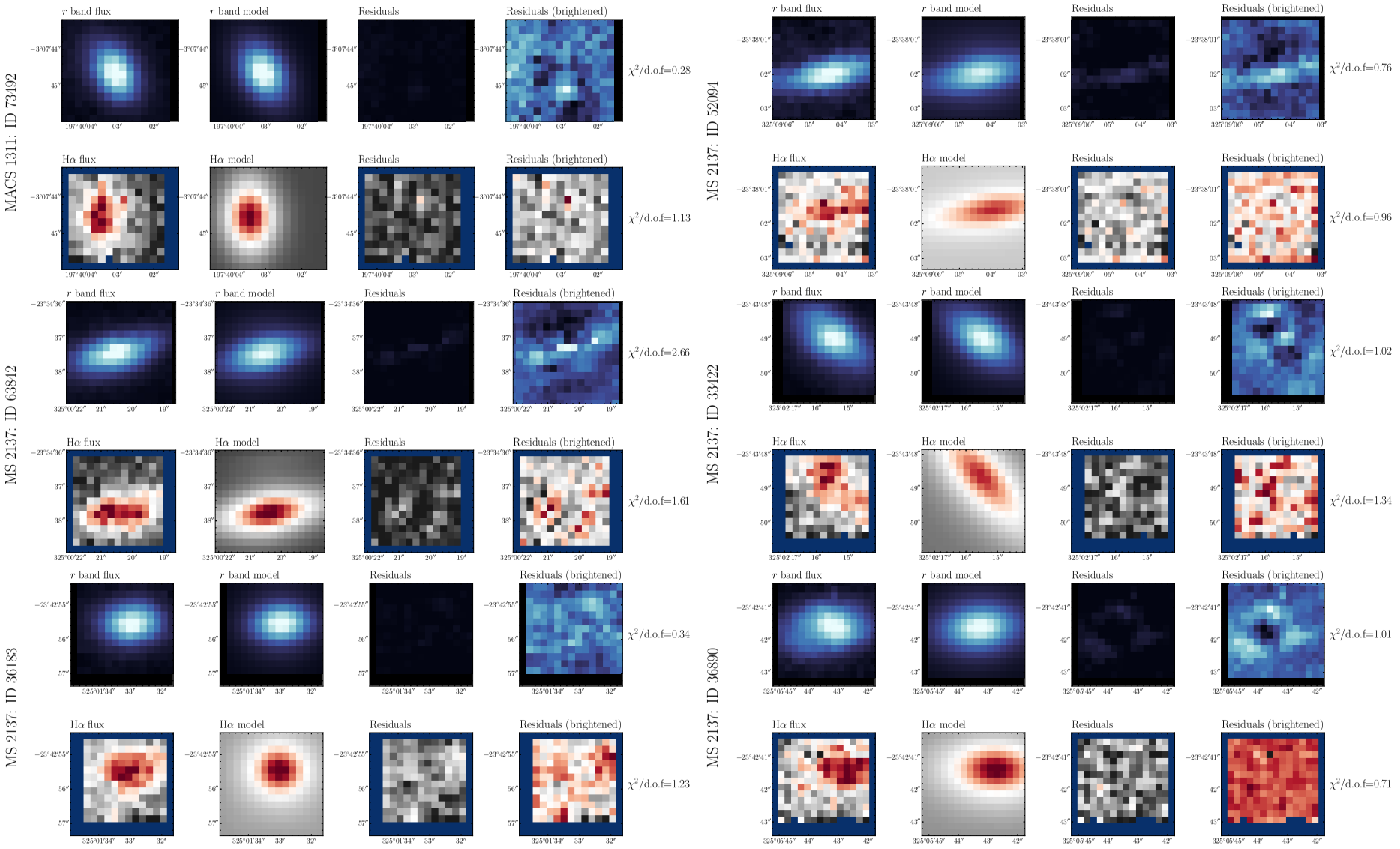

Figure B.2: (continued) Field galaxies- Hα and R_c band fits. See Section 5.3 for details

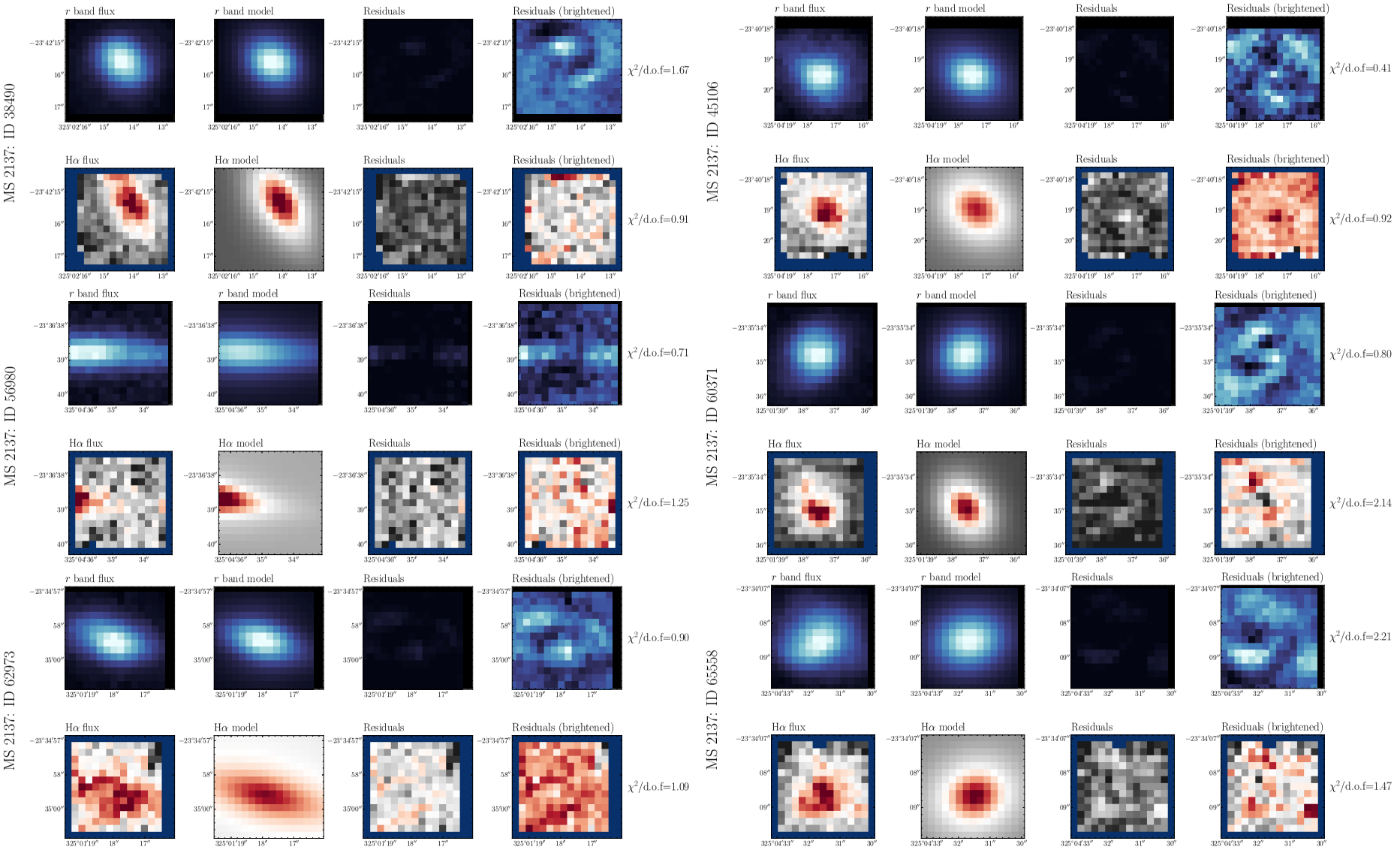

Figure B.2: (continued) Field galaxies- Hα and R_c band fits. See Section 5.3 for details

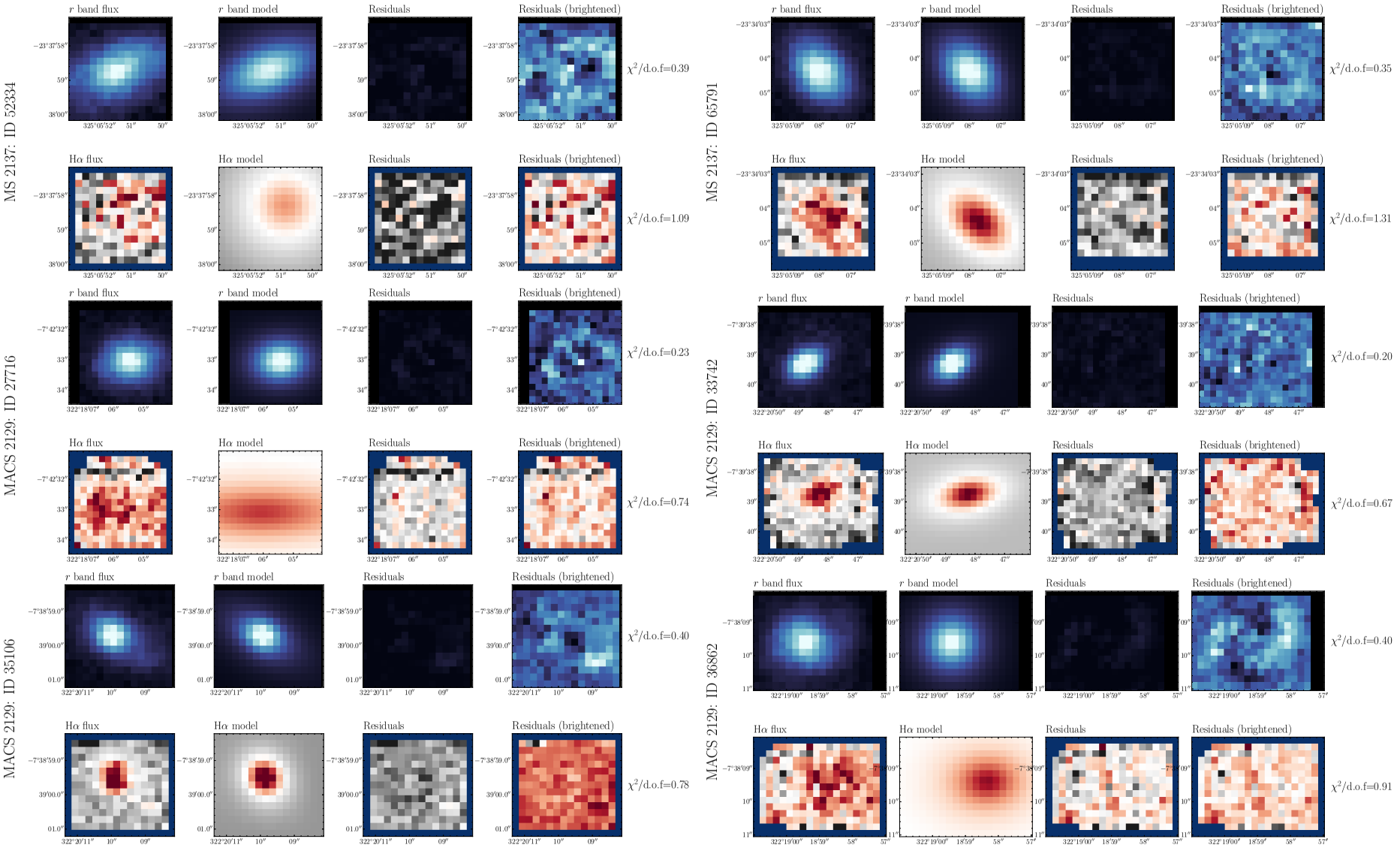

Figure B.2: (continued) Field galaxies- Hα and R_c band fits. See Section 5.3 for details

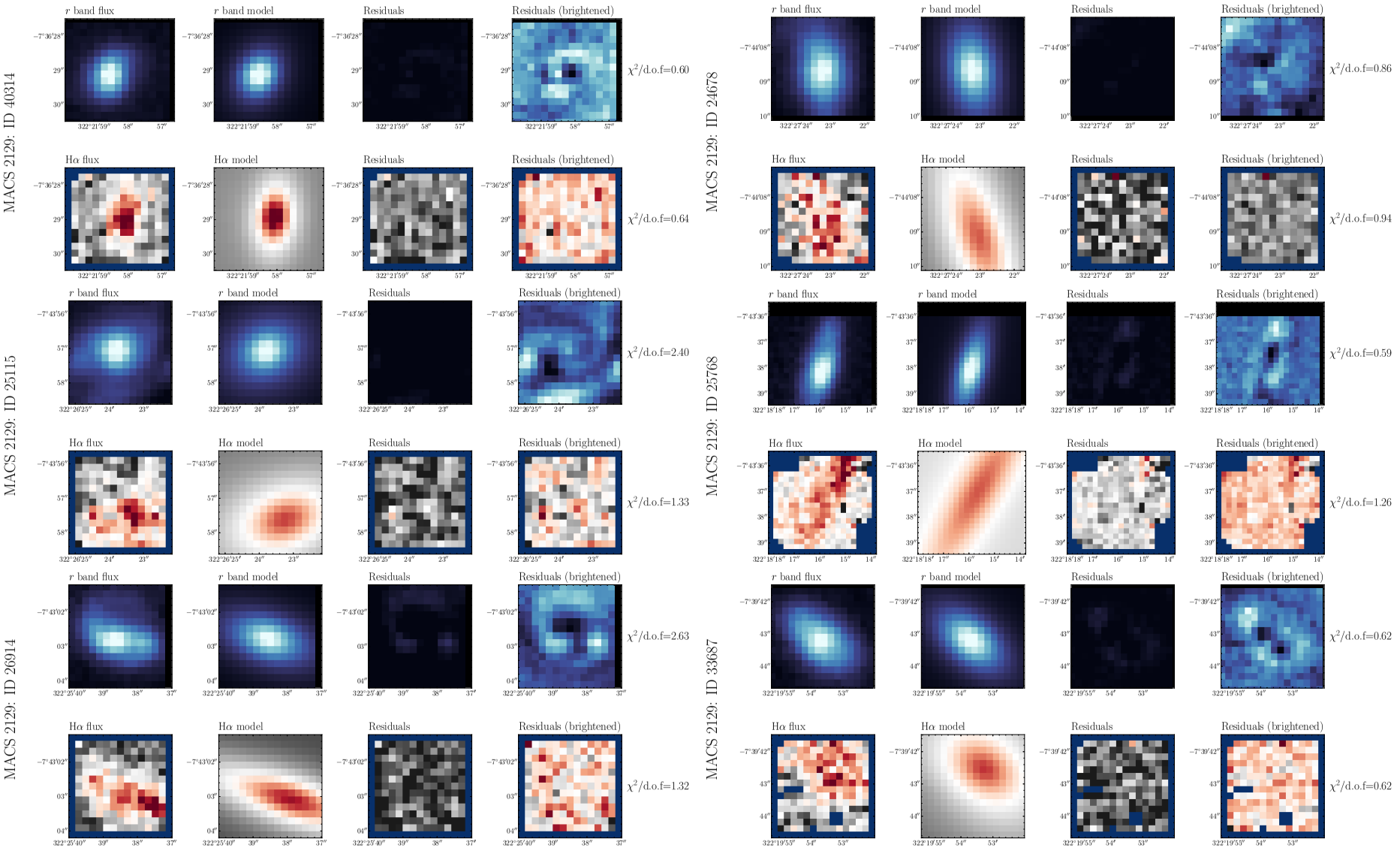

Figure B.2: (continued) Field galaxies- Hα and R_c band fits. See Section 5.3 for details

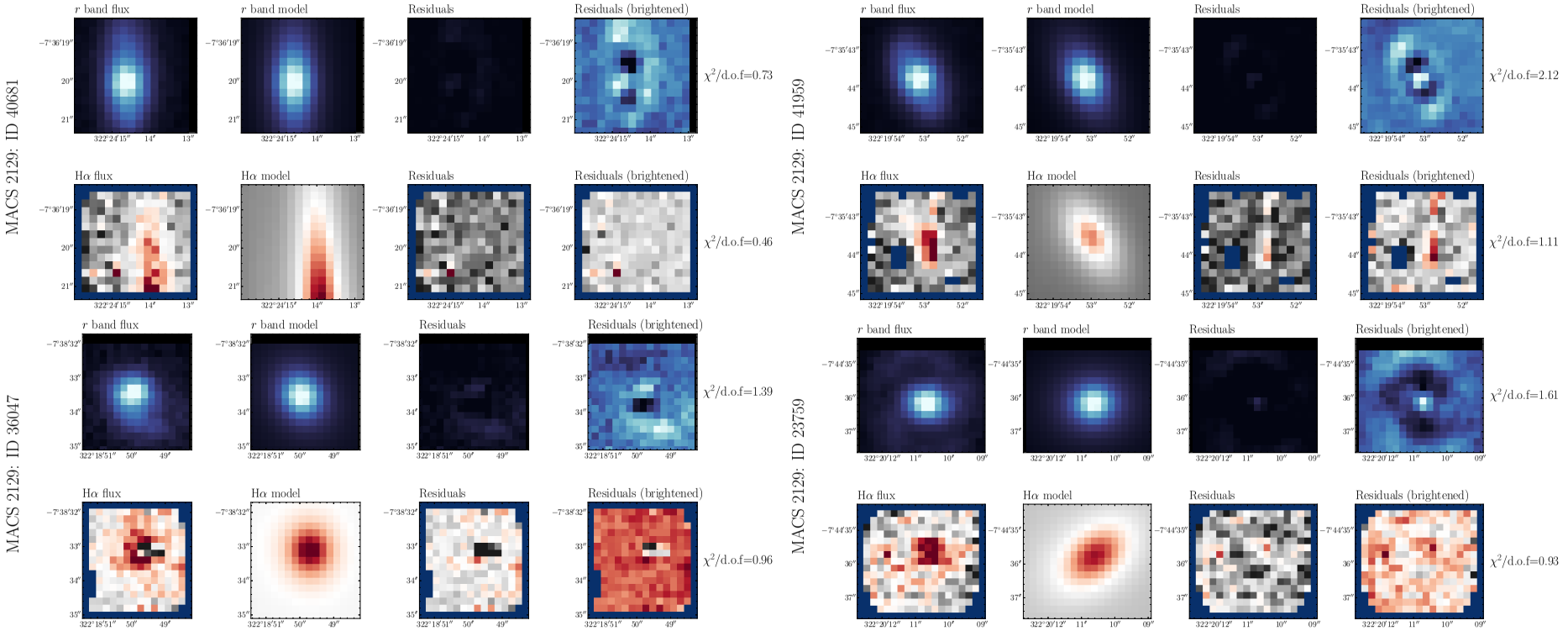

Figure B.2: (continued) Field galaxies- Hα and R_c band fits. See Section 5.3 for details

.

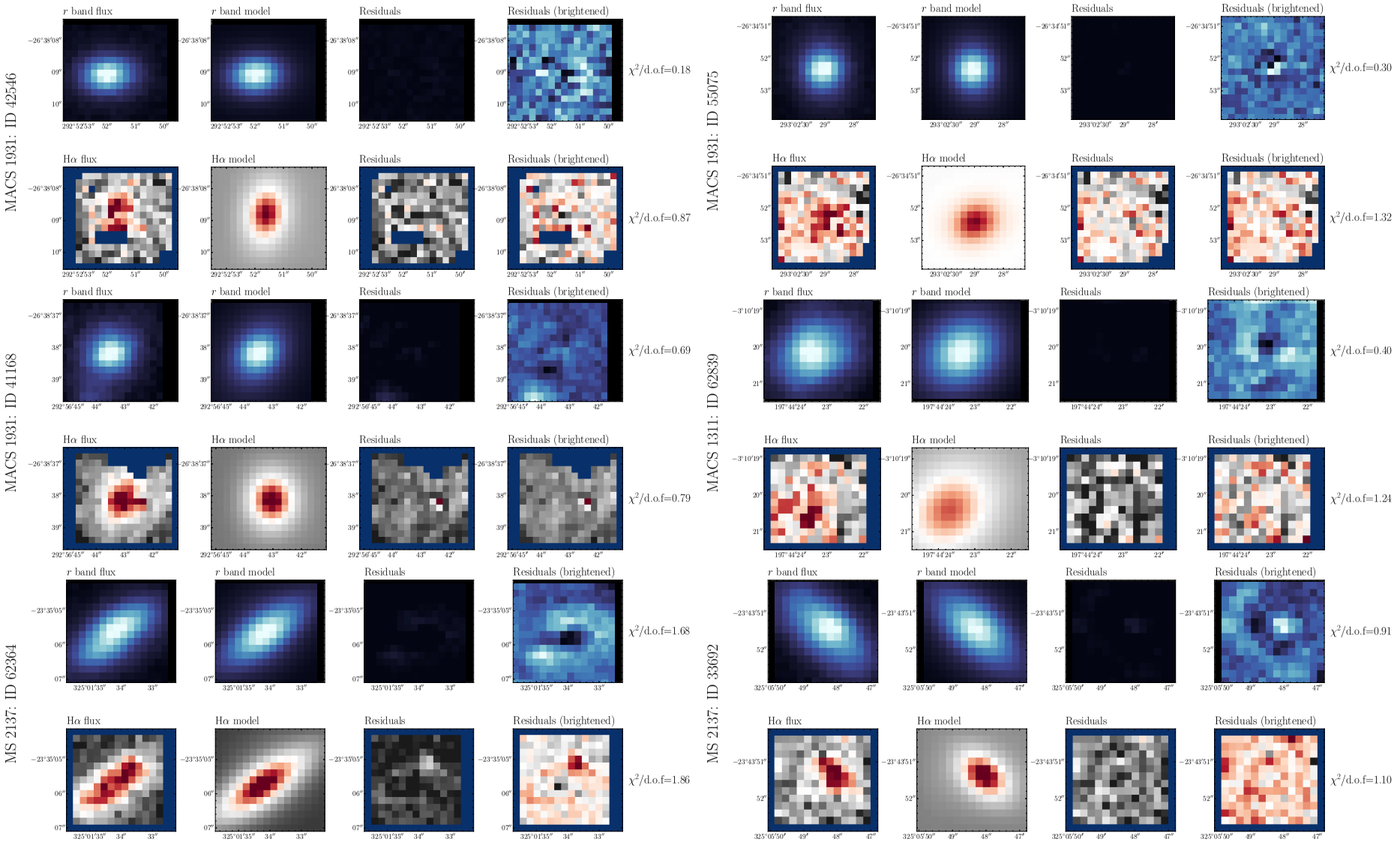

Figure B.3: High mass field galaxies- Hα and R_c band fits.. See Section 5.3 for details

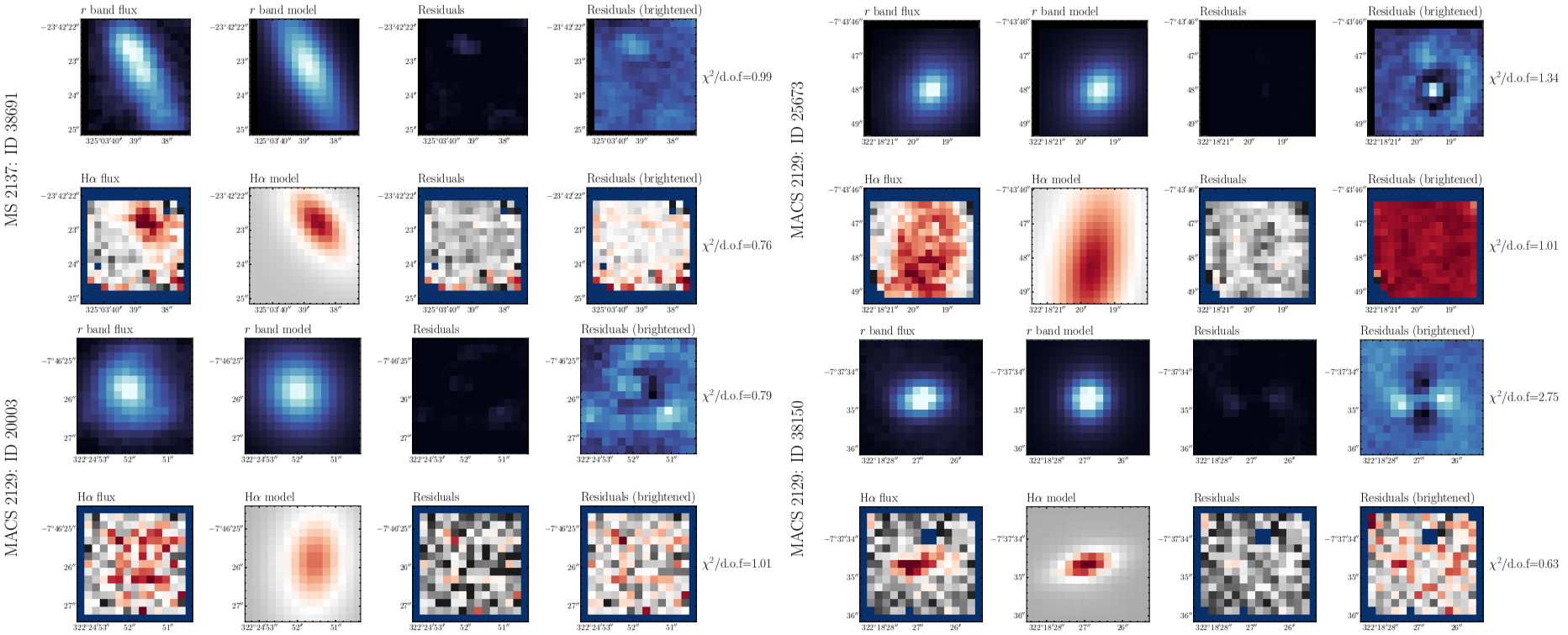

Figure B.3: (continued) High mass field galaxies- Hα and R_c band fits.. See Section 5.3 for details

.

C | Emission Line Measurements from Chapter 5

Table C.1 presents emission line measurements from the field, cluster and high-mass field samples. We give the galaxy's K-CLASH ID, RA, Dec, emission line fluxes in units of 10^{-17} erg s^{-1} cm^{-2}, the ratio of the two [SII] lines and the galaxy's gas-phase metallicity derived using the ratio [NII]/Hα and the conversion of Pettini & Pagel (2004). See Section 5.4 for details.

Table C.1: All emission line measurements from the field, cluster and high-mass field samples. We give the galaxy's K-CLASH ID, RA, Dec, and emission line fluxes in units of 10^{-17} erg s^{-1} cm^{-2}. [SII] is the total flux of both lines, and R([SII]) gives their ratio. $12 + \log(\mathrm{O/H})$ is the gas-phase metallicity derived using the ratio [NII]/Hα and the conversion of Pettini & Pagel (2004). See Section 5.4 for details.

Name	RA	Dec	Hα	[NII]	[SII]	R([SII])	12 + log(O/H)
Cluster							
MS2137_56177	$21^h39^m49.4803^s$	$-23°36'57.3186''$	11.18±0.40	6.66±0.44	2.26±0.46	1.43±0.21	8.80±0.03
MS2137_37505	$21^h39^m55.1913^s$	$-23°42'30.8138''$	11.13±0.55	6.46±0.55	2.44±0.52	0.44±0.26	8.79±0.04
MS2137_35655	$21^h40^m05.6514^s$	$-23°43'08.5099''$	5.19±0.58	0.44±0.43	1.85±0.66	0.44±0.00	8.20±0.46
MS2137_30037	$21^h40^m11.8787^s$	$-23°45'03.0168''$	4.35±0.67	1.23±0.62	3.69±0.69	0.44±0.18	8.48±0.27
MS2137_57911	$21^h40^m21.5796^s$	$-23°36'32.7128''$	9.99±0.57	2.96±0.28	3.31±0.32	1.20±0.16	8.49±0.06
MACS2129_21295	$21^h29^m23.3718^s$	$-7°45'47.1174''$	2.18±0.19	0.66±0.17	0.00±0.11	0.00±0.00	8.50±0.14
MACS2129_36201	$21^h29^m24.8728^s$	$-7°38'28.2711''$	6.91±0.31	2.92±0.28	2.16±0.23	1.00±0.18	8.63±0.05
MACS2129_30535	$21^h29^m28.1183^s$	$-7°41'18.4732''$	3.39±0.30	1.45±0.27	1.54±0.29	1.16±0.27	8.64±0.10
MACS1931_59681	$19^h31^m36.3461^s$	$-26°33'19.8955''$	9.57±0.59	3.13±0.40	3.70±0.40	1.43±0.10	8.53±0.07
MACS1931_58042	$19^h31^m59.6628^s$	$-26°33'49.095''$	4.98±0.57	2.22±0.39	1.15±0.37	1.43±0.31	8.66±0.10
MACS1311_60491	$13^h10^m47.2056^s$	$-3°10'46.309''$	2.51±0.21	0.10±0.21	1.48±0.26	0.75±0.24	8.08±1.22
MACS1311_47520	$13^h10^m48.85^s$	$-3°14'00.9477''$	3.90±0.16	1.05±0.17	1.56±0.18	1.43±0.13	8.46±0.09
MACS1311_72592	$13^h10^m49.4371^s$	$-3°07'52.8503''$	11.65±0.30	4.07±0.23	4.22±0.52	1.15±0.21	8.55±0.03
MACS1311_47439	$13^h10^m50.5788^s$	$-3°13'59.4334''$	6.26±0.22	1.64±0.19	1.04±0.21	1.35±0.23	8.45±0.06
MACS1311_61893	$13^h10^m57.5469^s$	$-3°10'23.8928''$	2.24±0.16	1.01±0.20	1.18±0.19	1.43±0.16	8.66±0.10
MACS1311_66324	$13^h10^m57.6725^s$	$-3°09'18.6966''$	5.83±0.28	3.03±0.29	1.65±0.40	1.30±0.29	8.73±0.05

Continued on next page

Name	RA	Dec	Hα	[NII]	[SII]	R([SII])	12 + log(O/H)
Field							
MACS1311_53495	$13^h11^m05.5549^s$	$-3°12'29.1551''$	7.16±0.26	2.77±0.18	2.21±0.29	1.37±0.16	8.59±0.04
MACS1311_71049	$13^h11^m06.7002^s$	$-3°08'12.3431''$	3.17±0.43	1.63±0.51	1.81±0.51	0.89±0.34	8.72±0.16
MACS1311_57540	$13^h11^m06.7517^s$	$-3°11'29.8366''$	3.52±0.27	1.57±0.23	1.36±0.26	1.43±0.19	8.66±0.08
MACS1311_63737	$13^h11^m14.8426^s$	$-3°10'00.7298''$	1.86±0.18	0.08±0.19	0.73±0.22	1.43±0.29	8.08±1.48
MACS1311_70482	$13^h11^m16.6509^s$	$-3°08'17.6288''$	4.97±0.48	2.58±0.46	2.20±0.48	1.19±0.29	8.73±0.10
MACS1311_60701	$13^h11^m19.1583^s$	$-3°10'50.7537''$	2.41±0.29	0.92±0.22	0.00±0.15	0.00±0.00	8.59±0.14
MS2137_63842	$21^h40^m01.3717^s$	$-23°34'37.526''$	32.98±0.70	8.95±0.42	10.01±0.55	1.43±0.06	8.46±0.03
MS2137_62973	$21^h40^m05.201^s$	$-23°34'58.4526''$	5.75±0.29	3.89±0.28	3.07±0.33	1.43±0.12	8.87±0.04
MS2137_36183	$21^h40^m06.1961^s$	$-23°42'55.5614''$	7.35±0.26	3.06±0.25	2.75±0.30	1.43±0.10	8.62±0.05
MS2137_60371	$21^h40^m06.5071^s$	$-23°35'34.8647''$	10.07±0.17	5.02±0.18	2.57±0.19	1.07±0.13	8.71±0.02
MS2137_42239	$21^h40^m06.9066^s$	$-23°41'06.186''$	4.82±0.25	2.28±0.30	1.75±0.32	1.43±0.19	8.68±0.07
MS2137_38490	$21^h40^m08.9565^s$	$-23°42'15.658''$	12.23±0.24	7.98±0.30	3.46±0.27	1.17±0.13	8.85±0.02
MS2137_33422	$21^h40^m09.029^s$	$-23°43'49.0631''$	11.88±0.42	3.04±0.53	5.62±0.46	1.07±0.13	8.44±0.09
MS2137_34910	$21^h40^m10.9533^s$	$-23°43'30.9805''$	8.77±0.82	2.84±0.83	6.46±1.17	0.89±0.28	8.52±0.16
MS2137_57202	$21^h40^m13.7975^s$	$-23°36'34.0213''$	4.62±0.42	0.60±0.34	1.76±0.38	1.11±0.30	8.27±0.27
MS2137_45106	$21^h40^m17.176^s$	$-23°40'19.5847''$	5.11±0.16	2.08±0.18	0.00±0.00	0.00±0.00	8.62±0.05
MS2137_65558	$21^h40^m18.1104^s$	$-23°34'08.4926''$	9.85±0.22	4.70±0.22	2.88±0.25	1.33±0.12	8.69±0.02
MS2137_56980	$21^h40^m18.3234^s$	$-23°36'38.896''$	4.97±0.18	1.08±0.18	1.46±0.24	1.43±0.17	8.40±0.08
MS2137_65791	$21^h40^m20.5328^s$	$-23°34'04.3921''$	7.63±0.38	2.55±0.30	2.37±0.29	1.32±0.15	8.54±0.07
MS2137_54196	$21^h40^m21.4058^s$	$-23°37'25.9604''$	9.95±0.42	2.16±0.38	2.80±0.35	1.43±0.13	8.40±0.09
MS2137_36890	$21^h40^m22.8847^s$	$-23°42'41.6313''$	6.67±0.33	2.90±0.29	2.24±0.41	1.02±0.30	8.64±0.06

Continued on next page

Name	RA	Dec	Hα	[NII]	[SII]	R([SII])	12 + log(O/H)
Field							
MS2137_52334	$21^h40^m23.4294^s$	$-23°37'58.768''$	3.26±0.25	2.54±0.24	0.44±0.28	1.43±0.00	8.96±0.04
MS2137_29492	$21^h40^m31.3988^s$	$-23°45'21.1027''$	3.97±0.16	2.19±0.15	1.53±0.20	1.32±0.17	8.76±0.04
MS2137_52094	$21^h40^m36.3105^s$	$-23°38'01.9172''$	7.84±0.58	1.05±0.65	0.91±0.41	1.43±0.00	8.28±0.29
MS2137_36702	$21^h40^m37.5219^s$	$-23°42'47.5912''$	5.45±0.10	2.34±0.09	0.00±0.00	0.00±0.00	8.64±0.02
MACS2129_27716	$21^h29^m12.3642^s$	$-7°42'33.0641''$	4.94±0.29	2.13±0.27	3.26±0.44	1.13±0.21	8.64±0.07
MACS2129_25768	$21^h29^m13.0662^s$	$-7°43'38.0373''$	9.45±0.32	2.46±0.41	2.71±0.49	1.25±0.26	8.45±0.09
MACS2129_21443	$21^h29^m13.5522^s$	$-7°45'40.6633''$	1.73±0.19	0.00±0.22	0.44±0.37	1.43±0.00	0.00±0.00
MACS2129_36047	$21^h29^m15.3218^s$	$-7°38'33.7037''$	6.93±0.81	1.77±0.25	3.62±0.37	1.41±0.11	8.44±0.09
MACS2129_36862	$21^h29^m15.9588^s$	$-7°38'09.6531''$	4.74±0.44	3.01±0.44	1.47±0.41	1.24±0.33	8.84±0.07
MACS2129_18582	$21^h29^m18.3369^s$	$-7°47'08.174''$	3.38±0.34	2.41±0.38	0.59±0.25	1.02±0.00	8.91±0.07
MACS2129_41959	$21^h29^m19.5382^s$	$-7°35'43.7574''$	15.02±1.06	13.01±0.92	2.98±0.77	1.33±0.28	9.03±0.03
MACS2129_33687	$21^h29^m19.5749^s$	$-7°39'43.2721''$	5.10±0.33	3.05±0.40	1.20±0.42	1.43±0.00	8.80±0.06
MACS2129_35106	$21^h29^m20.6499^s$	$-7°38'59.8173''$	6.76±0.30	1.98±0.32	2.25±0.36	1.43±0.17	8.49±0.09
MACS2129_23759	$21^h29^m20.7149^s$	$-7°44'36.2214''$	5.72±0.25	3.94±0.27	1.20±0.27	0.88±0.32	8.88±0.03
MACS2129_33742	$21^h29^m23.2496^s$	$-7°39'39.3617''$	5.24±0.32	2.09±0.29	1.21±0.35	1.43±0.29	8.61±0.08
MACS2129_40314	$21^h29^m27.8956^s$	$-7°36'29.0833''$	10.54±0.41	6.63±0.40	3.23±0.50	1.14±0.23	8.83±0.03
MACS2129_18941	$21^h29^m33.9374^s$	$-7°46'58.864''$	2.86±0.43	1.05±0.40	0.00±0.28	0.00±0.00	8.57±0.21
MACS2129_37582	$21^h29^m36.8256^s$	$-7°37'48.7449''$	4.76±0.57	2.95±0.70	1.65±0.62	0.44±0.00	8.82±0.11
MACS2129_40681	$21^h29^m36.9725^s$	$-7°36'19.9449''$	7.79±0.43	3.90±0.50	3.81±0.76	1.27±0.26	8.71±0.07
MACS2129_20461	$21^h29^m39.1178^s$	$-7°46'12.9447''$	5.70±0.39	2.69±0.28	2.44±0.32	1.43±0.13	8.68±0.06
MACS2129_21812	$21^h29^m42.4328^s$	$-7°45'31.0436''$	11.01±0.32	5.10±0.31	4.02±0.26	1.43±0.07	8.67±0.03

Continued on next page

Name	RA	Dec	Hα	[NII]	[SII]	R([SII])	12 + log(O/H)
Field							
MACS2129_26914	$21^h29^m42.5734^s$	$-7°43'02.6024''$	7.53±0.16	3.80±0.19	2.22±0.19	1.23±0.14	8.71±0.03
MACS2129_25115	$21^h29^m45.5848^s$	$-7°43'57.0224''$	6.34±0.23	3.20±0.23	2.21±0.21	1.28±0.14	8.71±0.04
MACS2129_24678	$21^h29^m49.5536^s$	$-7°44'08.5168''$	7.32±0.31	2.65±0.34	2.33±0.27	1.43±0.12	8.57±0.07
MACS2129_35364	$21^h29^m49.9397^s$	$-7°38'53.0998''$	4.98±0.28	2.84±0.31	1.17±0.27	1.43±0.22	8.78±0.06
MACS1931_46757	$19^h31^m25.9965^s$	$-26°37'02.7411''$	4.08±0.23	1.60±0.36	1.12±0.35	1.43±0.33	8.60±0.12
MACS1931_43957	$19^h31^m27.35^s$	$-26°37'45.4899''$	7.38±1.36	1.95±0.33	2.29±0.41	1.43±0.17	8.45±0.13
MACS1931_46297	$19^h31^m29.8585^s$	$-26°37'07.895''$	13.93±0.46	6.85±0.35	3.83±0.47	0.50±0.14	8.70±0.03
MACS1931_61192	$19^h31^m33.1029^s$	$-26°32'55.7827''$	4.78±0.38	3.69±0.49	1.49±0.43	1.43±0.00	8.95±0.05
MACS1931_40117	$19^h31^m39.3106^s$	$-26°38'52.1673''$	9.31±0.28	2.65±0.23	2.73±0.27	1.41±0.10	8.48±0.05
MACS1931_75118	$19^h31^m45.2764^s$	$-26°28'52.2201''$	14.71±0.43	6.52±0.67	3.21±0.38	1.43±0.12	8.65±0.05
MACS1931_46041	$19^h31^m51.2368^s$	$-26°37'18.8734''$	6.74±0.50	1.29±0.43	2.23±0.33	1.43±0.15	8.36±0.17
MACS1931_48927	$19^h31^m53.5728^s$	$-26°36'20.6074''$	3.73±0.35	1.40±0.31	0.68±0.60	0.44±0.00	8.58±0.13
MACS1931_53332	$19^h31^m55.4321^s$	$-26°35'18.1446''$	8.58±0.25	2.96±0.27	2.56±0.29	1.35±0.14	8.55±0.05
MACS1931_42661	$19^h31^m55.9709^s$	$-26°38'08.0242''$	4.72±0.19	1.52±0.31	1.14±0.28	1.43±0.25	8.52±0.11
MACS1931_52577	$19^h32^m00.3845^s$	$-26°35'18.6073''$	5.35±0.22	2.68±0.33	1.27±0.23	1.43±0.19	8.71±0.06
MACS1931_44837	$19^h32^m00.5072^s$	$-26°37'34.9815''$	4.14±0.33	3.05±0.32	1.54±0.26	1.43±0.16	8.92±0.05
MACS1931_45168	$19^h32^m03.0601^s$	$-26°37'30.4931''$	4.40±0.20	2.16±0.22	1.10±0.24	1.43±0.23	8.70±0.05
MACS1931_50044	$19^h32^m03.3146^s$	$-26°36'09.8873''$	5.08±0.34	2.63±0.39	2.39±0.27	1.43±0.12	8.73±0.08
MACS1311_73492	$13^h10^m40.2078^s$	$-3°07'44.5824''$	18.77±0.38	10.78±0.67	6.83±0.40	1.29±0.09	8.78±0.03
MACS1311_69324	$13^h10^m42.1425^s$	$-3°08'38.7729''$	11.23±0.40	8.62±0.40	3.65±0.39	1.42±0.11	8.95±0.02
MACS1311_46622	$13^h10^m42.8256^s$	$-3°14'13.6766''$	5.96±0.26	3.41±0.33	2.59±0.24	1.35±0.12	8.78±0.05

Continued on next page

Name	RA	Dec	Hα	[NII]	[SII]	R([SII])	12 + log(O/H)
Field							
MACS1311_55862	$13^h10^m44.8818^s$	$-3°11'53.6397''$	15.15±0.29	3.90±0.38	4.56±0.21	1.42±0.05	8.45±0.05
MACS1311_45189	$13^h10^m45.8766^s$	$-3°14'38.1121''$	3.50±0.31	0.83±0.26	1.60±0.26	1.43±0.16	8.42±0.17
MACS1311_60370	$13^h10^m46.1892^s$	$-3°10'48.8157''$	14.53±0.44	3.83±0.60	5.14±0.38	1.43±0.08	8.45±0.08
MACS1311_55137	$13^h10^m54.4381^s$	$-3°12'03.0703''$	5.11±0.23	2.40±0.16	0.68±0.18	1.14±0.34	8.68±0.04
MACS1311_41309	$13^h10^m57.3681^s$	$-3°15'33.9608''$	3.74±0.93	0.00±0.48	0.00±0.44	0.00±0.00	0.00±0.00
MACS1311_60083	$13^h11^m00.5612^s$	$-3°10'53.5442''$	14.70±0.37	7.84±0.33	4.36±0.28	1.27±0.10	8.74±0.02
MACS1311_51860	$13^h11^m01.8627^s$	$-3°13'01.5223''$	14.23±0.26	6.39±0.37	3.55±0.28	1.07±0.14	8.66±0.03
MACS1311_48247	$13^h11^m08.4182^s$	$-3°14'02.8933''$	0.22±0.25	0.05±0.24	2.41±0.56	0.44±0.21	8.43±2.36
MACS1311_40938	$13^h11^m15.5033^s$	$-3°15'40.3141''$	0.00±0.58	10.69±0.85	12.64±0.46	1.43±0.21	0.00±0.00
MACS1311_54335	$13^h11^m18.3949^s$	$-3°12'43.8257''$	15.53±0.34	7.81±0.51	5.15±0.45	1.15±0.15	8.71±0.03
High Mass Field							
MS2137_55197	$21^h39^m50.1336^s$	$-23°37'19.9467''$	13.49±0.37	8.15±0.25	1.96±0.21	1.43±0.11	8.81±0.02
MS2137_44219	$21^h39^m55.2426^s$	$-23°40'38.2318''$	3.12±0.22	1.66±0.28	7.82±0.55	0.75±0.13	8.74±0.09
MS2137_62364	$21^h40^m06.2806^s$	$-23°35'05.7012''$	15.78±0.31	8.60±0.35	4.77±0.26	1.21±0.10	8.75±0.02
MS2137_44854	$21^h40^m07.0811^s$	$-23°40'25.1702''$	5.62±0.42	3.08±0.39	1.38±0.47	1.34±0.33	8.76±0.07
MS2137_38691	$21^h40^m14.5848^s$	$-23°42'23.3554''$	5.63±0.43	3.87±0.58	0.65±0.46	0.44±0.00	8.88±0.07
MS2137_33692	$21^h40^m23.2207^s$	$-23°43'51.4954''$	5.30±0.24	5.13±0.26	2.72±0.32	1.38±0.14	9.11±0.02
MS2137_42396	$21^h40^m25.0853^s$	$-23°41'19.1847''$	20.94±0.26	13.68±0.26	8.72±0.38	1.19±0.07	8.85±0.01
MACS2129_25673	$21^h29^m13.2965^s$	$-7°43'47.9505''$	6.41±0.33	5.19±0.48	1.15±0.47	1.43±0.00	8.99±0.04
MACS2129_38150	$21^h29^m13.7943^s$	$-7°37'34.7542''$	3.85±0.32	3.06±0.46	0.67±0.38	0.44±0.00	8.97±0.06
MACS2129_25978	$21^h29^m18.1025^s$	$-7°43'35.5194''$	5.38±0.38	3.02±0.38	3.54±0.49	1.43±0.16	8.77±0.07

Continued on next page

Name	RA	Dec	Hα	[NII]	[SII]	R([SII])	12 + log(O/H)
High Mass Field							
MACS2129_30717	$21^h29^m27.3312^s$	$-7°41'16.2885''$	7.70±0.20	7.15±0.30	2.70±0.22	1.31±0.11	9.08±0.01
MACS2129_22204	$21^h29^m34.4976^s$	$-7°45'20.16''$	8.22±0.54	4.38±0.48	0.78±0.46	1.43±0.00	8.74±0.06
MACS2129_34913	$21^h29^m38.6115^s$	$-7°39'06.6705''$	9.14±0.36	4.34±0.23	2.30±0.25	1.23±0.17	8.68±0.03
MACS2129_20003	$21^h29^m39.4636^s$	$-7°46'25.804''$	2.49±0.15	1.12±0.16	1.04±0.17	1.43±0.18	8.66±0.08
MACS1931_44841	$19^h31^m28.3173^s$	$-26°37'31.9048''$	7.37±0.44	6.80±0.43	3.09±0.53	1.32±0.22	9.08±0.02
MACS1931_58566	$19^h31^m30.0472^s$	$-26°33'43.2764''$	4.88±0.26	1.78±0.23	1.46±0.29	1.43±0.20	8.57±0.07
MACS1931_42546	$19^h31^m31.4641^s$	$-26°38'09.1276''$	5.48±0.47	5.30±0.40	0.67±0.50	1.43±0.00	9.11±0.03
MACS1931_48595	$19^h31^m44.1844^s$	$-26°36'34.1628''$	4.00±2.62	0.77±1.51	0.48±0.76	0.44±0.00	8.36±1.03
MACS1931_41168	$19^h31^m46.9059^s$	$-26°38'38.288''$	8.78±0.30	5.54±0.43	0.00±0.00	0.00±0.00	8.83±0.04
MACS1931_56753	$19^h31^m47.0525^s$	$-26°34'06.9293''$	1.15±0.78	0.00±0.47	0.00±0.34	0.00±0.00	0.00±0.00
MACS1931_55075	$19^h32^m09.9358^s$	$-26°34'52.2899''$	3.44±0.37	0.00±0.21	0.00±0.19	0.00±0.00	0.00±0.00
MACS1311_62839	$13^h10^m57.5553^s$	$-3°10'20.0946''$	6.92±0.41	2.44±0.30	0.67±0.30	0.91±0.00	8.56±0.07
MACS1311_64971	$13^h10^m58.5439^s$	$-3°09'44.7349''$	12.78±4.81	7.61±5.20	0.17±0.73	1.43±0.00	8.80±0.35
MACS1311_49192	$13^h11^m03.969^s$	$-3°13'49.0115''$	3.30±0.44	0.33±0.40	0.05±0.27	1.43±0.00	8.23±0.56

Bibliography

Abramson L. E., Gladders M. D., Dressler A., Oemler Augustus J., Poggianti B., Vulcani B., 2016, ApJ, 832, 7

Alam S., et al., 2015, The Astrophysical Journal Supplement Series, 219, 12

Alton P. D., Smith R. J., Lucey J. R., 2017, MNRAS, 468, 1594

Alton P. D., Smith R. J., Lucey J. R., 2018, MNRAS, 478, 4464

Anderson T. W., Darling D. A., 1954, Journal of the American Statistical Association, 49, 765

Arnouts S., Cristiani S., Moscardini L., Matarrese S., Lucchin F., Fontana A., Giallongo E., 1999, MNRAS, 310, 540

Baade D., et al., 1999, The Messenger, 95, 15

Babcock H. W., 1953, Publications of the Astronomical Society of the Pacific, 65, 229

Bacon R., et al., 2001, MNRAS, 326, 23

Bacon R., et al., 2010, in Ground-based and Airborne Instrumentation for Astronomy III. p. 773508, doi:10.1117/12.856027

Baldry I. K., Balogh M. L., Bower R. G., Glazebrook K., Nichol R. C., Bamford S. P., Budavari T., 2006, MNRAS, 373, 469

Baldry I. K., Glazebrook K., Driver S. P., 2008, MNRAS, 388, 945

Baldwin J. A., Phillips M. M., Terlevich R., 1981, PASP, 93, 5

Balogh M. L., Baldry I. K., Nichol R., Miller C., Bower R., Glazebrook K., 2004, ApJ, 615, L101

Bamford S. P., Milvang-Jensen B., Aragón-Salamanca A., 2007, MNRAS, 378, L6

Barnabè M., Spiniello C., Koopmans L. V. E., Trager S. C., Czoske O., Treu T., 2013, MNRAS, 436, 253

Bastian N., Covey K. R., Meyer M. R., 2010, ARA&A, 48, 339

Becker B. J., 2001, Journal for the History of Astronomy, 32, 43

Beifiori A., et al., 2017, ApJ, 846, 120

Bekki K., 2014, MNRAS, 438, 444

Belfiore F., et al., 2016, MNRAS, 461, 3111

Bell E. F., McIntosh D. H., Katz N., Weinberg M. D., 2003, The Astrophysical Journal Supplement Series, 149, 289

Bell E. F., et al., 2004, ApJ, 608, 752

Bennert N., Jungwiert B., Komossa S., Haas M., Chini R., 2006, A&A, 456, 953

Bernardi M., Shankar F., Hyde J. B., Mei S., Marulli F., Sheth R. K., 2010, MNRAS, 404, 2087

Bertola F., Capaccioli M., 1975, ApJ, 200, 439

Best P. N., Kauffmann G., Heckman T. M., Brinchmann J., Charlot S., Ivezić Ž., White S. D. M., 2005, MNRAS, 362, 25

Bicknell G. V., Bruce T. E. G., Carter D., Killeen N. E. B., 1989, ApJ, 336, 639

Binette L., Magris C. G., Stasińska G., Bruzual A. G., 1994, A&A, 292, 13

Binney J., 1978, MNRAS, 183, 501

Blanton M. R., Moustakas J., 2009, Annual Review of Astronomy and Astrophysics, 47, 159

Boselli A., Gavazzi G., 2006, Publications of the Astronomical Society of the Pacific, 118, 517

Bosma A., 1978, PhD thesis, -

Bosma A., 1981, AJ, 86, 1825

Bowen I. S., 1938, ApJ, 88, 113

Bradley L., et al., 2019, astropy/photutils: v0.6, doi:10.5281/zenodo.2533376, `https://doi.org/10.5281/zenodo.2533376`

Brammer G. B., et al., 2012, The Astrophysical Journal Supplement Series, 200, 13

Brinchmann J., Charlot S., White S. D. M., Tremonti C., Kauffmann G., Heckman T., Brinkmann J., 2004, MNRAS, 351, 1151

Brough S., Proctor R., Forbes D. A., Couch W. J., Collins C. A., Burke D. J., Mann R. G., 2007, MNRAS, 378, 1507

Bruzual G., Charlot S., 2003, MNRAS, 344, 1000

Bundy K., et al., 2015, ApJ, 798, 7

Butcher H., Oemler A. J., 1978, ApJ, 219, 18

Butcher H., Oemler A. J., 1984, ApJ, 285, 426

Byler N., Dalcanton J. J., Conroy C., Johnson B. D., 2017, ApJ, 840, 44

Cairns H., Harney B. Y., 2004, Dark Sparklers: Yidumduma's Aboriginal Astronomy. Hugh Cairns

Calzetti D., 2013, Star Formation Rate Indicators. p. 419

Calzetti D., Kinney A. L., Storchi-Bergmann T., 1994, ApJ, 429, 582

Calzetti D., Armus L., Bohlin R. C., Kinney A. L., Koornneef J., Storchi-Bergmann T., 2000, ApJ, 533, 682

Cano-Díaz M., et al., 2016, ApJ, 821, L26

Cappellari M., 2016, Annual Review of Astronomy and Astrophysics, 54, 597

Cappellari M., 2017, MNRAS, 466, 798

Cappellari M., Copin Y., 2003, MNRAS, 342, 345

Cappellari M., Emsellem E., 2004a, PASP, 116, 138

Cappellari M., Emsellem E., 2004b, Publications of the Astronomical Society of the Pacific, 116, 138

Cappellari M., et al., 2007, MNRAS, 379, 418

Cappellari M., et al., 2011, MNRAS, 413, 813

Cappellari M., et al., 2012, Nature, 484, 485

Cappellari M., et al., 2013, MNRAS, 432, 1862

Carpenter B., et al., 2017, Journal of Statistical Software, Articles, 76, 1

Carretta E., et al., 2009, A&A, 505, 117

Cenarro A. J., Cardiel N., Gorgas J., Peletier R. F., Vazdekis A., Prada F., 2001, MNRAS, 326, 959

Cenarro A. J., Gorgas J., Vazdekis A., Cardiel N., Peletier R. F., 2003, MNRAS, 339, L12

Cesaratto J. M., et al., 2013, Phys. Rev. C, 88, 065806

Chabrier G., 2003, PASP, 115, 763

Chieffi A., Limongi M., 2004, ApJ, 608, 405

Choi J., Dotter A., Conroy C., Cantiello M., Paxton B., Johnson B. D., 2016, ApJ, 823, 102

Cid Fernandes R., Stasińska G., Schlickmann M. S., Mateus A., Vale Asari N., Schoenell W., Sodré L., 2010, MNRAS, 403, 1036

Clauwens B., Schaye J., Franx M., 2016, MNRAS, 462, 2832

Clough S. A., Shephard M. W., Mlawer E. J., Delamere J. S., Iacono M. J., Cady-Pereira K., Boukabara S., Brown P. D., 2005, J. Quant. Spec. Radiat. Transf., 91, 233

Cohen J. G., 1978, ApJ, 221, 788

Conroy C., 2013, ARA&A, 51, 393

Conroy C., Gunn J. E., 2010, ApJ, 712, 833

Conroy C., van Dokkum P., 2012a, ApJ, 747, 69

Conroy C., van Dokkum P. G., 2012b, ApJ, 760, 71

Conroy C., Gunn J. E., White M., 2009, ApJ, 699, 486

Conroy C., White M., Gunn J. E., 2010, ApJ, 708, 58

Conroy C., Graves G. J., van Dokkum P. G., 2014, ApJ, 780, 33

Conroy C., van Dokkum P. G., Villaume A., 2017, ApJ, 837, 166

Conroy C., Villaume A., van Dokkum P. G., Lind K., 2018, ApJ, 854, 139

Conselice C. J., 2006, MNRAS, 373, 1389

Cooper M. C., et al., 2006, MNRAS, 370, 198

Cooper M. C., Tremonti C. A., Newman J. A., Zabludoff A. I., 2008, MNRAS, 390, 245

Couture J., Hardy E., 1993, ApJ, 406, 142

Cowie L. L., McKee C. F., 1977, ApJ, 211, 135

Cowie L. L., Songaila A., Hu E. M., Cohen J. G., 1996, AJ, 112, 839

Crommelin A. C. D., 1918, Journal of the Royal Astronomical Society of Canada, 12, 33

Croom S. M., et al., 2012, MNRAS, 421, 872

Crowl H. H., Kenney J. D. P., 2008, AJ, 136, 1623

Curtis H. D., 1917, Publications of the Astronomical Society of the Pacific, 29, 206

Darvish B., Mobasher B., Sobral D., Hemmati S., Nayyeri H., Shivaei I., 2015, ApJ, 814, 84

Darvish B., Mobasher B., Sobral D., Rettura A., Scoville N., Faisst A., Capak P., 2016, ApJ, 825, 113

Davidzon I., et al., 2013, A&A, 558, A23

Davies R. I., 2007, MNRAS, 375, 1099

Davies R. L., Efstathiou G., Fall S. M., Illingworth G., Schechter P. L., 1983, ApJ, 266, 41

Davies L. J. M., et al., 2018, MNRAS, 480, 768

Dirsch B., Richtler T., Geisler D., Forte J. C., Bassino L. P., Gieren W. P., 2003, AJ, 125, 1908

Djorgovski S., Davis M., 1987, ApJ, 313, 59

Doherty C. L., Gil-Pons P., Lau H. H. B., Lattanzio J. C., Siess L., 2014, MNRAS, 437, 195

Donley J. L., et al., 2012, ApJ, 748, 142

Dopita M. A., Sutherland R. S., Nicholls D. C., Kewley L. J., Vogt F. P. A., 2013, The Astrophysical Journal Supplement Series, 208, 10

Dotter A., 2016, ApJS, 222, 8

Dressler A., 1980, ApJ, 236, 351

Dressler A., Gunn J. E., 1992, The Astrophysical Journal Supplement Series, 78, 1

Dressler A., Lynden-Bell D., Burstein D., Davies R. L., Faber S. M., Terlevich R., Wegner G., 1987, ApJ, 313, 42

Dressler A., et al., 1997, ApJ, 490, 577

Dressler A., et al., 2011, Publications of the Astronomical Society of the Pacific, 123, 288

Dreyer J. L. E., 1888, Memoirs of the Royal Astronomical Society, 49, 1

Driver S. P., et al., 2011, MNRAS, 413, 971

Ebeling H., Stephenson L. N., Edge A. C., 2014, ApJ, 781, L40

Eisenstein D. J., et al., 2011, AJ, 142, 72

Ellison S. L., Simard L., Cowan N. B., Baldry I. K., Patton D. R., McConnachie A. W., 2009, MNRAS, 396, 1257

Elmegreen B. G., Elmegreen D. M., 2005, ApJ, 627, 632

Emsellem E., 2013, MNRAS, 433, 1862

Emsellem E., et al., 2007, MNRAS, 379, 401

Erwin P., 2015, ApJ, 799, 226

Faber S. M., 1972, A&A, 20, 361

Faber S. M., French H. B., 1980, Lick Observatory Bulletin, 823, 1

Faber S. M., Jackson R. E., 1976, ApJ, 204, 668

Faber S. M., Dressler A., Davies R. L., Burstein D., Lynden Bell D., Terlevich R., Wegner G., 1987, in Faber S. M., ed., Nearly Normal Galaxies. From the Planck Time to the Present. p. 175

Fabian A. C., 2012, Annual Review of Astronomy and Astrophysics, 50, 455

Falcón-Barroso J., Sánchez-Blázquez P., Vazdekis A., Ricciardelli E., Cardiel N., Cenarro A. J., Gorgas J., Peletier R. F., 2011, A&A, 532, A95

Fanelli M. N., O'Connell R. W., Thuan T. X., 1988, ApJ, 334, 665

Fazio G. G., et al., 2004, ApJS, 154, 10

Ferrarese L., Merritt D., 2000, ApJ, 539, L9

Ferrarese L., Ford H. C., Jaffe W., 1996, ApJ, 470, 444

Ferré-Mateu A., Trujillo I., Martín-Navarro I., Vazdekis A., Mezcua M., Balcells M., Domínguez L., 2017, MNRAS,

Ferreras I., La Barbera F., de la Rosa I. G., Vazdekis A., de Carvalho R. R., Falcón-Barroso J., Ricciardelli E., 2013, MNRAS, 429, L15

Fioc M., Rocca-Volmerange B., 1997, A&A, 326, 950

Fisher D., Fabricant D., Franx M., van Dokkum P., 1998, ApJ, 498, 195

Fixsen D. J., 2009, ApJ, 707, 916

Foreman-Mackey D., Hogg D. W., Lang D., Goodman J., 2013, PASP, 125, 306

Förster Schreiber N. M., et al., 2006, ApJ, 645, 1062

Förster Schreiber N. M., et al., 2018, arXiv e-prints, p. arXiv:1807.04738

Franx M., Illingworth G., Heckman T., 1989, ApJ, 344, 613

Freedman W. L., et al., 2001, ApJ, 553, 47

Freeman K. C., 1970, ApJ, 160, 811

Freeman K. C., 1999, in Davies J. I., Impey C., Phillips S., eds, Astronomical Society of the Pacific Conference Series Vol. 170, The Low Surface Brightness Universe. p. 3

Freudling W., Romaniello M., Bramich D. M., Ballester P., Forchi V., García-Dabló C. E., Moehler S., Neeser M. J., 2013, A&A, 559, A96

Fritz J., et al., 2017, ApJ, 848, 132

Gaffney V., et al., 2013, Internet Archaeology, 34

Gebhardt K., et al., 2000, ApJ, 539, L13

Gebhardt K., et al., 2007, ApJ, 671, 1321

Gelman A., Rubin D. B., 1992, Statist. Sci., 7, 457

Genzel R., et al., 2008, ApJ, 687, 59

Genzel R., et al., 2011, ApJ, 733, 101

Gibson B. K., Fenner Y., Kiessling A., 2005, Nuclear Physics A, 758, 259

Girardi M., Fadda D., Giuricin G., Mardirossian F., Mezzetti M., Biviano A., 1996, ApJ, 457, 61

Gisler G. R., 1978, MNRAS, 183, 633

Gladders M. D., Oemler A., Dressler A., Poggianti B., Vulcani B., Abramson L., 2013, ApJ, 770, 64

Graham A. W., Colless M. M., Busarello G., Zaggia S., Longo G., 1998, A&AS, 133, 325

Gratton R. G., Lucatello S., Bragaglia A., Carretta E., Momany Y., Pancino E., Valenti E., 2006, A&A, 455, 271

Greene J. E., Janish R., Ma C.-P., McConnell N. J., Blakeslee J. P., Thomas J., Murphy J. D., 2015, ApJ, 807, 11

Gullieuszik M., et al., 2017, ApJ, 846, 27

Gunn J. E., Gott J. Richard I., 1972, ApJ, 176, 1

Guth A. H., 1981, Phys. Rev. D, 23, 347

Hafez I., Stephenson R., Orchiston W., 2011, Abdul-Rahman al-Sufi and his Book of the Fixed Stars. pp 121–138

Haggard D., Green P. J., Anderson S. F., Constantin A., Aldcroft T. L., Kim D.-W., Barkhouse W. A., 2010, ApJ, 723, 1447

Haines C. P., et al., 2013, ApJ, 775, 126

Hale S. E., Champagne A. E., Iliadis C., Hansper V. Y., Powell D. C., Blackmon J. C., 2001, Phys. Rev. C, 65, 015801

Halliday C., et al., 2004, A&A, 427, 397

Hamacher D. W., 2018, The Australian Journal of Anthropology, 29, 89

Hao C.-N., Kennicutt R. C., Johnson B. D., Calzetti D., Dale D. A., Moustakas J., 2011, ApJ, 741, 124

Harms R. J., et al., 1994, ApJ, 435, L35

Haynes R., 1996, Explorers of the southern sky : a history of Australian astronomy. Cambridge ; New York : Cambridge University Press

Hearin A. P., Watson D. F., 2013, MNRAS, 435, 1313

Homan M. D., Gelman A., 2014, J. Mach. Learn. Res., 15, 1593

Hopkins A. M., Beacom J. F., 2006, ApJ, 651, 142

Hopkins P. F., Bundy K., Murray N., Quataert E., Lauer T. R., Ma C.-P., 2009, MNRAS, 398, 898

Houghton R. C. W., Magorrian J., Sarzi M., Thatte N., Davies R. L., Krajnović D., 2006, MNRAS, 367, 2

Hubble E. P., 1925, Popular Astronomy, 33, 252

Hubble E. P., 1926, ApJ, 64, 321

Hubble E., 1929, Proceedings of the National Academy of Science, 15, 168

Huggins W., 1865, Proceedings of the Royal Society of London Series I, 14, 39

Huggins W., Miller W. A., 1864, Philosophical Transactions of the Royal Society of London Series I, 154, 437

Ilbert O., et al., 2006, A&A, 457, 841

Illingworth G., 1977, ApJ, 218, L43

Iodice E., et al., 2016, ApJ, 820, 42

Jeong H., Yi S. K., Kyeong J., Sarzi M., Sung E.-C., Oh K., 2013, ApJS, 208, 7

Kakkad D., et al., 2018, A&A, 618, A6

Kaltenegger L., Traub W. A., 2009, ApJ, 698, 519

Kartaltepe J. S., et al., 2010, ApJ, 709, 572

Kauffmann G., et al., 2003a, MNRAS, 341, 33

Kauffmann G., et al., 2003b, MNRAS, 341, 54

Kauffmann G., et al., 2003c, MNRAS, 346, 1055

Kauffmann G., White S. D. M., Heckman T. M., Ménard B., Brinchmann J., Charlot S., Tremonti C., Brinkmann J., 2004, MNRAS, 353, 713

Kausch W., et al., 2014, in Manset N., Forshay P., eds, Astronomical Society of the Pacific Conference Series Vol. 485, Astronomical Data Analysis Software and Systems XXIII. p. 403 (arXiv:1401.7768)

Keenan P. C., Hynek J. A., 1945, ApJ, 101, 265

Kelson D. D., 2014, arXiv e-prints, p. arXiv:1406.5191

Kennicutt Robert C. J., 1998, Annual Review of Astronomy and Astrophysics, 36, 189

Kennicutt R. C., Evans N. J., 2012, Annual Review of Astronomy and Astrophysics, 50, 531

Kewley L. J., Dopita M. A., 2002, The Astrophysical Journal Supplement Series, 142, 35

Kewley L. J., Ellison S. L., 2008, ApJ, 681, 1183

Kewley L. J., Groves B., Kauffmann G., Heckman T., 2006, MNRAS, 372, 961

Kewley L. J., et al., 2016, ApJ, 819, 100

Killeen N. E. B., Bicknell G. V., Ekers R. D., 1988, ApJ, 325, 180

Kirchhoff G., Bunsen R., 1860, Annalen der Physik, 186, 161

Kobayashi C., Umeda H., Nomoto K., Tominaga N., Ohkubo T., 2006, ApJ, 653, 1145

Kobayashi C., Karakas A. I., Umeda H., 2011, MNRAS, 414, 3231

Koopmann R. A., Kenney J. D. P., 2004, ApJ, 613, 866

Kormendy J., Ho L. C., 2013, Annual Review of Astronomy and Astrophysics, 51, 511

Krajnović D., et al., 2015, MNRAS, 452, 2

Kravtsov A. V., Borgani S., 2012, ARA&A, 50, 353

Kroupa P., 2001, MNRAS, 322, 231

Kroupa P., 2002, Science, 295, 82

La Barbera F., Ferreras I., Vazdekis A., de la Rosa I. G., de Carvalho R. R., Trevisan M., Falcón-Barroso J., Ricciardelli E., 2013, MNRAS, 433, 3017

La Barbera F., Vazdekis A., Ferreras I., Pasquali A., Cappellari M., Martín-Navarro I., Schönebeck F., Falcón-Barroso J., 2016, MNRAS, 457, 1468

La Barbera F., Vazdekis A., Ferreras I., Pasquali A., Allende Prieto C., Röck B., Aguado D. S., Peletier R. F., 2017, MNRAS, 464, 3597

Larkin J., et al., 2006, in Society of Photo-Optical Instrumentation Engineers (SPIE) Conference Series. p. 62691A, doi:10.1117/12.672061

Larson R. B., Tinsley B. M., Caldwell C. N., 1980, ApJ, 237, 692

Leavitt H. S., Pickering E. C., 1912, Harvard College Observatory Circular, 173, 1

Lequeux J., Peimbert M., Rayo J. F., Serrano A., Torres-Peimbert S., 1979, A&A, 500, 145

Levesque E. M., Kewley L. J., Larson K. L., 2010, AJ, 139, 712

Liang Y. C., Hammer F., Yin S. Y., Flores H., Rodrigues M., Yang Y. B., 2007, A&A, 473, 411

Lilly S. J., Le Fevre O., Hammer F., Crampton D., 1996, ApJ, 460, L1

Linde A. D., 1982, Physics Letters B, 108, 389

Longo G., Zaggia S. R., Busarello G., Richter G., 1994, A&AS, 105, 433

Lyubenova M., Kuntschner H., Silva D. R., 2008, A&A, 485, 425

Lyubenova M., et al., 2016, MNRAS, 463, 3220

Madau P., Ferguson H. C., Dickinson M. E., Giavalisco M., Steidel C. C., Fruchter A., 1996, MNRAS, 283, 1388

Magdis G. E., et al., 2016, MNRAS, 456, 4533

Magorrian J., et al., 1998, AJ, 115, 2285

Maier C., et al., 2016, A&A, 590, A108

Mainzer A., et al., 2011, ApJ, 731, 53

Maiolino R., et al., 2008, A&A, 488, 463

Mancini C., et al., 2011, ApJ, 743, 86

Mannucci F., Cresci G., Maiolino R., Marconi A., Gnerucci A., 2010, MNRAS, 408, 2115

Maraston C., Strömbäck G., Thomas D., Wake D. A., Nichol R. C., 2009, MNRAS, 394, L107

Martín-Navarro I., Barbera F. L., Vazdekis A., Falcón-Barroso J., Ferreras I., 2015a, MNRAS, 447, 1033

Martín-Navarro I., La Barbera F., Vazdekis A., Ferré-Mateu A., Trujillo I., Beasley M. A., 2015b, MNRAS, 451, 1081

Martín-Navarro I., et al., 2015c, ApJ, 806, L31

Martini P., et al., 2013, ApJ, 768, 1

Mason C. A., et al., 2017, ApJ, 838, 14

McConnell N. J., Lu J. R., Mann A. W., 2016, ApJ, 821, 39

McGaugh S. S., Schombert J. M., Bothun G. D., de Blok W. J. G., 2000, ApJ, 533, L99

Medezinski E., et al., 2013, ApJ, 777, 43

Mentz J. J., et al., 2016, MNRAS, 463, 2819

Merten J., et al., 2015, ApJ, 806, 4

Messier C., 1781, Technical report, Catalogue des Nébuleuses et des Amas d'Étoiles (Catalog of Nebulae and Star Clusters)

Miyazaki S., et al., 2002, Publications of the Astronomical Society of Japan, 54, 833

Mobasher B., et al., 2015, ApJ, 808, 101

Molino A., et al., 2017, MNRAS, 470, 95

Momcheva I. G., Lee J. C., Ly C., Salim S., Dale D. A., Ouchi M., Finn R., Ono Y., 2013, AJ, 145, 47

Monna A., et al., 2017, MNRAS, 466, 4094

Moretti A., et al., 2018, MNRAS, 475, 4055

Morishita T., et al., 2017, ApJ, 835, 254

Mouhcine M., Baldry I. K., Bamford S. P., 2007, MNRAS, 382, 801

Mountford C. P., 1976, Nomads of the Australian desert. Melbourne : Rigby

Muñoz C., Villanova S., Geisler D., Saviane I., Dias B., Cohen R. E., Mauro F., 2017, A&A, 605, A12

Murphy E. J., et al., 2011, ApJ, 737, 67

Muzzin A., Wilson G., Demarco R., Lidman C., Nantais J., Hoekstra H., Yee H. K. C., Rettura A., 2013, ApJ, 767, 39

Naab T., 2013, in Thomas D., Pasquali A., Ferreras I., eds, IAU Symposium Vol. 295, The Intriguing Life of Massive Galaxies. pp 340–349 (arXiv:1211.6892), doi:10.1017/S1743921313005334

Naab T., Johansson P. H., Ostriker J. P., 2009, ApJ, 699, L178

Narayan R., Medvedev M. V., 2001, ApJ, 562, L129

Nelson E. J., et al., 2012, ApJ, 747, L28

Nelson E. J., et al., 2016a, ApJ, 817, L9

Nelson E. J., et al., 2016b, ApJ, 828, 27

Newman A. B., Smith R. J., Conroy C., Villaume A., van Dokkum P., 2017, ApJ, 845, 157

Nicastro F., Mathur S., Elvis M., 2008, Science, 319, 55

Noeske K. G., et al., 2007, ApJ, 660, L43

Nonino M., et al., 2009, The Astrophysical Journal Supplement Series, 183, 244

Norris R. P., 2016, Publications of the Astronomical Society of Australia, 33, e039

Nulsen P. E. J., 1982, MNRAS, 198, 1007

O'Connell R. W., Martin J. R., Crane J. D., Burstein D., Bohlin R. C., Landsman W. B., Freedman I., Rood R. T., 2005, ApJ, 635, 305

Osterbrock D. E., Ferland G. J., 2006, Astrophysics of gaseous nebulae and active galactic nuclei

Osterbrock D. E., Fulbright J. P., Martel A. R., Keane M. J., Trager S. C., Basri G., 1996, Publications of the Astronomical Society of the Pacific, 108, 277

Overzier R. A., 2016, Astronomy and Astrophysics Review, 24, 14

Owers M. S., Couch W. J., Nulsen P. E. J., Rand all S. W., 2012, ApJ, 750, L23

Owers M. S., et al., 2017, MNRAS, 468, 1824

Padovani P., et al., 2017, Astronomy and Astrophysics Review, 25, 2

Parikh T., et al., 2018, MNRAS, 477, 3954

Patel S. G., Holden B. P., Kelson D. D., Illingworth G. D., Franx M., 2009, ApJ, 705, L67

Peeples M. S., Shankar F., 2011, MNRAS, 417, 2962

Peng Y.-j., et al., 2010, ApJ, 721, 193

Peng Y., Maiolino R., Cochrane R., 2015, Nature, 521, 192

Perlmutter S., et al., 1999, ApJ, 517, 565

Pettini M., Pagel B. E. J., 2004, MNRAS, 348, L59

Pilyugin L. S., 2001, A&A, 374, 412

Pilyugin L. S., Grebel E. K., Zinchenko I. A., Nefedyev Y. A., Mattsson L., 2017, MNRAS, 465, 1358

Pimbblet K. A., Jensen P. C., 2012, MNRAS, 426, 1632

Pimbblet K. A., Smail I., Kodama T., Couch W. J., Edge A. C., Zabludoff A. I., O'Hely E., 2002, MNRAS, 331, 333

Planck Collaboration et al., 2016, A&A, 594, A13

Poggianti B. M., et al., 2009, ApJ, 693, 112

Poggianti B. M., et al., 2017, ApJ, 844, 48

Popesso P., Biviano A., 2006, A&A, 460, L23

Postman M., et al., 2012, ApJS, 199, 25

Press W. H., Schechter P., 1974, ApJ, 187, 425

Price J., Phillipps S., Huxor A., Smith R. J., Lucey J. R., 2011, MNRAS, 411, 2558

Prichard L. J., et al., 2017, ApJ, 850, 203

Proxauf B., Öttl S., Kimeswenger S., 2014, A&A, 561, A10

Puiseux P., 1912, L'Astronomie, 26, 31

Rawle T. D., et al., 2014, MNRAS, 442, 196

Reddy N. A., Steidel C. C., Fadda D., Yan L., Pettini M., Shapley A. E., Erb D. K., Adelberger K. L., 2006, ApJ, 644, 792

Reddy N. A., Erb D. K., Pettini M., Steidel C. C., Shapley A. E., 2010, ApJ, 712, 1070

Ricci T. V., Steiner J. E., Menezes R. B., 2014, MNRAS, 440, 2442

Riess A. G., et al., 1998, AJ, 116, 1009

Riess A. G., et al., 2011, ApJ, 730, 119

Roberts M. S., 1966, ApJ, 144, 639

Röck B., Vazdekis A., Ricciardelli E., Peletier R. F., Knapen J. H., Falcón-Barroso J., 2016, A&A, 589, A73

Roediger E., Brüggen M., 2007, MNRAS, 380, 1399

Rosati P., et al., 2014, The Messenger, 158, 48

Rubin V. C., Ford W. Kent J., 1970, ApJ, 159, 379

Rubin V. C., Ford W. K. J., Thonnard N., 1980, ApJ, 238, 471

Rusli S. P., Erwin P., Saglia R. P., Thomas J., Fabricius M., Bender R., Nowak N., 2013, AJ, 146, 160

Saglia R. P., Kronawitter A., Gerhard O., Bender R., 2000, AJ, 119, 153

Saglia R. P., et al., 2016, ApJ, 818, 47

Salpeter E. E., 1955, ApJ, 121, 161

Sánchez-Blázquez P., et al., 2006, MNRAS, 371, 703

Sánchez S. F., et al., 2012, A&A, 538, A8

Sarazin C. L., 1986, Reviews of Modern Physics, 58, 1

Sarzi M., et al., 2010, MNRAS, 402, 2187

Sarzi M., Spiniello C., La Barbera F., Krajnović D., van den Bosch R., 2018, MNRAS, 478, 4084

Schaefer A. L., et al., 2017, MNRAS, 464, 121

Schaefer A. L., et al., 2019, MNRAS, 483, 2851

Schawinski K., et al., 2014, MNRAS, 440, 889

Schechter P. L., Gunn J. E., 1979, ApJ, 229, 472

Schiavon R. P., Barbuy B., Rossi S. C. F., Milone A. 1997a, ApJ, 479, 902

Schiavon R. P., Barbuy B., Singh P. D., 1997b, ApJ, 484, 499

Schlafly E. F., Finkbeiner D. P., 2011, ApJ, 737, 103

Schmidt K. B., et al., 2014, ApJ, 782, L36

Schombert J. M., 1986, ApJS, 60, 603

Schuberth Y., Richtler T., Hilker M., Dirsch B., Bassino L. P., Romanowsky A. J., Infante L., 2010, A&A, 513, A52

Schwartz C. M., Martin C. L., 2004, ApJ, 610, 201

Sereno M., Zitrin A., 2012, MNRAS, 419, 3280

Sérsic J. L., 1963, Boletin de la Asociacion Argentina de Astronomia La Plata Argentina, 6, 41

Shapley H., 1919, Publications of the Astronomical Society of the Pacific, 31, 261

Shapley A. E., 2011, Annual Review of Astronomy and Astrophysics, 49, 525

Sharp R. G., Bland-Hawthorn J., 2010, ApJ, 711, 818

Sharples R., et al., 2013, The Messenger, 151, 21

Sharratt M., 1996, Galileo : decisive innovator. Cambridge, University Press, Cambridge New York, NY, USA

Shen S., Mo H. J., White S. D. M., Blanton M. R., Kauffmann G., Voges W., Brinkmann J., Csabai I., 2003, MNRAS, 343, 978

Shimakawa R., Kodama T., Tadaki K.-i., Hayashi M., Koyama Y., Tanaka I., 2015, MNRAS, 448, 666

Shurkin K., Dunn R. J. H., Gentile G., Taylor G. B., Allen S. W., 2008, MNRAS, 383, 923

Slemer A., et al., 2017, MNRAS, 465, 4817

Slipher V. M., 1913, Lowell Observatory Bulletin, 1, 56

Slipher V. M., 1914, Lowell Observatory Bulletin, 2, 66

Small T. A., Ma C.-P., Sargent W. L. W., Hamilton D., 1999, ApJ, 524, 31

Smethurst R. J., et al., 2015, MNRAS, 450, 435

Smith R. J., 2014, MNRAS, 443, L69

Smith R. J., Hudson M. J., Lucey J. R., Nelan J. E., Wegner G. A., 2006, MNRAS, 369, 1419

Smith R. J., et al., 2010, MNRAS, 408, 1417

Smith R. J., Lucey J. R., Conroy C., 2015, MNRAS, 449, 3441

Sobral D., Best P. N., Smail I., Geach J. E., Cirasuolo M., Garn T., Dalton G. B., 2011, MNRAS, 411, 675

Sobral D., Stroe A., Dawson W. A., Wittman D., Jee M. J., Röttgering H., van Weeren R. J., Brüggen M., 2015, MNRAS, 450, 630

Spavone M., et al., 2017, A&A, 603, A38

Speagle J. S., Steinhardt C. L., Capak P. L., Silverman J. D., 2014, The Astrophysical Journal Supplement Series, 214, 15

Spiniello C., Trager S., Koopmans L. V. E., Conroy C., 2014, MNRAS, 438, 1483

Spiniello C., Barnabè M., Koopmans L. V. E., Trager S. C., 2015a, MNRAS, 452, L21

Spiniello C., Trager S. C., Koopmans L. V. E., 2015b, ApJ, 803, 87

Spinrad H., Taylor B. J., 1971, ApJS, 22, 445

Spitzer L., Härm R., 1953, Phys. Rev., 89, 977

Spolaor M., Forbes D. A., Proctor R. N., Hau G. K. T., Brough S., 2008, MNRAS, 385, 675

Stasińska G., et al., 2008, MNRAS, 391, L29

Stern D., et al., 2012, ApJ, 753, 30

Stott J. P., Smail I., Edge A. C., Ebeling H., Smith G. P., Kneib J. P., Pimbblet K. A., 2007, ApJ, 661, 95

Stott J. P., et al., 2016, MNRAS, 457, 1888

Strateva I., et al., 2001, AJ, 122, 1861

Strömgren B., 1939, ApJ, 89, 526

Su Y., Nulsen P. E. J., Kraft R. P., Forman W. R., Jones C., Irwin J. A., Randall S. W., Churazov E., 2017, ApJ, 847, 94

Swinbank A. M., Smail I., Sobral D., Theuns T., Best P. N., Geach J. E., 2012, ApJ, 760, 130

Taylor E. N., et al., 2015, MNRAS, 446, 2144

Thatte N., Tecza M., Clarke F., Goodsall T., Lynn J., Freeman D., Davies R. L., 2006, in Society of Photo-Optical Instrumentation Engineers (SPIE) Conference Series. p. 62693L, doi:10.1117/12.670859

Thomas D., Maraston C., Bender R., 2003, MNRAS, 343, 279

Thomas J., Saglia R. P., Bender R., Thomas D., Gebhardt K., Magorrian J., Corsini E. M., Wegner G., 2007, MNRAS, 382, 657

Thomas D., Maraston C., Johansson J., 2011a, MNRAS, 412, 2183

Thomas J., et al., 2011b, MNRAS, 415, 545

Thomas D., et al., 2013, MNRAS, 431, 1383

Tiley A. L., et al., 2016, MNRAS, 460, 103

Timmes F. X., Woosley S. E., Weaver T. A., 1995, ApJS, 98, 617

Tinsley B. M., 1968, ApJ, 151, 547

Trager S. C., Faber S. M., Worthey G., González J. J., 2000, AJ, 120, 165

Tremonti C. A., et al., 2004, ApJ, 613, 898

Treu T., Auger M. W., Koopmans L. V. E., Gavazzi R., Marshall P. J., Bolton A. S., 2010, ApJ, 709, 1195

Treu T., et al., 2015, ApJ, 812, 114

Trujillo I., et al., 2004, ApJ, 604, 521

Trujillo I., Ferré-Mateu A., Balcells M., Vazdekis A., Sánchez-Blázquez P., 2014, ApJ, 780, L20

Tsujimoto T., Nomoto K., Yoshii Y., Hashimoto M., Yanagida S., Thielemann F.-K., 1995, MNRAS, 277, 945

Tully R. B., Fisher J. R., 1977, A&A, 500, 105

Übler H., et al., 2017, ApJ, 842, 121

Umetsu K., et al., 2014, ApJ, 795, 163

Vaughan S. P., Davies R. L., Zieleniewski S., Houghton R. C. W., 2018a, MNRAS, 475, 1073

Vaughan S. P., Davies R. L., Zieleniewski S., Houghton R. C. W., 2018b, MNRAS, 479, 2443

Vazdekis A., Casuso E., Peletier R. F., Beckman J. E., 1996, ApJS, 106, 307

Vazdekis A., Ricciardelli E., Cenarro A. J., Rivero-González J. G., Díaz-García L. A., Falcón-Barroso J., 2012, MNRAS, 424, 157

Vazdekis A., Koleva M., Ricciardelli E., Röck B., Falcón-Barroso J., 2016, MNRAS, 463, 3409

Ventura P., Di Criscienzo M., Carini R., D'Antona F., 2013, MNRAS, 431, 3642

Vijayaraghavan R., Sarazin C., 2017a, ApJ, 841, 22

Vijayaraghavan R., Sarazin C., 2017b, ApJ, 848, 63

Villaume A., Conroy C., Johnson B., Rayner J., Mann A. W., van Dokkum P., 2017, ApJS, 230, 23

Vulcani B., Poggianti B. M., Finn R. A., Rudnick G., Desai V., Bamford S., 2010, ApJ, 710, L1

Vulcani B., et al., 2015, ApJ, 814, 161

Vulcani B., et al., 2016, ApJ, 833, 178

Walsh J. L., van den Bosch R. C. E., Gebhardt K., Yıldırım A., Richstone D. O., Gültekin K., Husemann B., 2016, ApJ, 817, 2

Wang S., Liu J., Qiu Y., Bai Y., Yang H., Guo J., Zhang P., 2016a, The Astrophysical Journal Supplement Series, 224, 40

Wang T., et al., 2016b, ApJ, 828, 56

Watson F., 2004, Stargazer : the life and times of the telescope / Fred Watson. Allen and Unwin Crows Nest, N.S.W

Weijmans A.-M., et al., 2009, MNRAS, 398, 561

Weitzel L., Krabbe A., Kroker H., Thatte N., Tacconi-Garman L. E., Cameron M., Genzel R., 1996, Astronomy and Astrophysics Supplement Series, 119, 531

Westmoquette M. S., Smith L. J., Gallagher J. S. I., 2011, MNRAS, 414, 3719

Wetzel A. R., Tinker J. L., Conroy C., 2012, MNRAS, 424, 232

Wing R. F., Ford Jr. W. K., 1969, PASP, 81, 527

Wisnioski E., et al., 2011, MNRAS, 417, 2601

Wisnioski E., et al., 2015, ApJ, 799, 209

Wisnioski E., et al., 2018, ApJ, 855, 97

Worthey G., Faber S. M., Gonzalez J. J., Burstein D., 1994, ApJS, 94, 687

Worthey G., Tang B., Serven J., 2014, ApJ, 783, 20

Wright E. L., et al., 2010, AJ, 140, 1868

Wu X.-P., Xue Y.-J., Fang L.-Z., 1999, ApJ, 524, 22

Wu P.-F., Zahid H. J., Hwang H. S., Geller M. J., 2017, MNRAS, 468, 1881

Wuyts S., et al., 2011, ApJ, 738, 106

Wuyts S., et al., 2013, ApJ, 779, 135

Yıldırım A., van den Bosch R. C. E., van de Ven G., Husemann B., Lyubenova M., Walsh J. L., Gebhardt K., Gültekin K., 2015, MNRAS, 452, 1792

Zhong J., et al., 2015, Research in Astronomy and Astrophysics, 15, 1154

Zhuravleva I., Churazov E., Kravtsov A., Lau E. T., Nagai D., Sunyaev R., 2013, MNRAS, 428, 3274

Zieleniewski S., Houghton R. C. W., Thatte N., Davies R. L., 2015, MNRAS, 452, 597

Zieleniewski S., Houghton R. C. W., Thatte N., Davies R. L., Vaughan S. P., 2017, MNRAS, 465, 192

Zitrin A., et al., 2015, ApJ, 801, 44

da Cunha E., Charlot S., Elbaz D., 2008, MNRAS, 388, 1595

de Carvalho R. R., da Costa L. N., 1988, The Astrophysical Journal Supplement Series, 68, 173

de Vaucouleurs G., 1953, MNRAS, 113, 134

de Vaucouleurs G., de Vaucouleurs A., Corwin Herold G. J., Buta R. J., Paturel G., Fouque P., 1991, Third Reference Catalogue of Bright Galaxies

van Dokkum P. G., 2001, PASP, 113, 1420

van Dokkum P. G., 2008, ApJ, 674, 29

van Dokkum P. G., Conroy C., 2010, Nature, 468, 940

van Dokkum P. G., Conroy C., 2012, ApJ, 760, 70

van Dokkum P. G., et al., 2011, ApJ, 743, L15

van Dokkum P., Conroy C., Villaume A., Brodie J., Romanowsky A. J., 2017, ApJ, 841, 68

van de Hulst H. C., Raimond E., van Woerden H., 1957, Bulletin of the Astronomical Institutes of the Netherlands, 14, 1

van de Sande J., et al., 2013, ApJ, 771, 85

van den Bosch R. C. E., Gebhardt K., Gültekin K., van de Ven G., van der Wel A., Walsh J. L., 2012, Nature, 491, 729

van der Wel A., et al., 2014, ApJ, 788, 28

von der Linden A., Wild V., Kauffmann G., White S. D. M., Weinmann S., 2010, MNRAS, 404, 1231

von der Linden A., et al., 2014, MNRAS, 439, 2